The University of Osaka
Institutional Knowledge Archive

Title	Pulse shape discrimination method to suppress neutron-induced background in the J-PARC KOTO experiment
Author(s)	杉山, 泰之
Citation	大阪大学, 2016, 博士論文
Version Type	VoR
URL	https://doi.org/10.18910/59521
rights	
Note	

The University of Osaka Institutional Knowledge Archive : OUKA

https://ir.library.osaka-u.ac.jp/

The University of Osaka

Pulse shape discrimination method to suppress neutron-induced background in the J-PARC KOTO experiment

Yasuyuki SUGIYAMA

Department of Physics, Graduate School of Science
Osaka University

May, 2016

Abstract

The purpose of the KOTO experiment is to search for new physics that brakes the CP symmetry beyond the Standard Model of the elementary particle physics, by discovering the $K_L \to \pi^0 \nu \bar{\nu}$ decay and measuring its branching ratio.

I have developed the data acquisition system for the KOTO experiment, and integrated veto detectors into the system.

To suppress the background caused by neutrons hitting the CsI calorimeter, I have developed a new method to reject neutron-induced clusters based on the pulse shapes of the CsI calorimeter. The method can reject 92% of background events with two neutron-induced clusters while keeping 90% of the signal acceptance.

Combined with other methods, the background caused by neutrons is suppressed to the level below the branching ratio of $K_L \to \pi^0 \nu \bar{\nu}$ predicted by the Standard Model.

Acknowledgement

I would like to show my special thank to Dr. Hiroki Matsuda for his kindness, friendship and the support at KEK, J-PARC and ELPH. I enjoyed the chat with him about the hobbies such as TV animations and games.

Finally, I would like to thank my family, Yasuhisa, Atsuko, and Sumiko Sugiyama for various supports throughout my life.

<div align="right">

May, 2016
Kyoto, Japan.
Yasuyuki Sugiyama

</div>

Contents

CONTENTS

Chapter 1

Introduction

When particles and anti-particles were created in the early universe, naive expectation from the symmetries of physics would be that particles and anti-particles should have been generated in equal amounts. However, all the matter around us is made of particles. This can be explained if the symmetry between particles and anti-particles, called "CP symmetry", is broken. In the Standard Model (SM) of particle physics, the symmetry is broken in the weak interactions for quarks. The broken symmetry is explained by the Cabibbo-Kobayashi-Maskawa (CKM) model [1, 2]. However, the amount of asymmetry predicted by the SM is not large enough to explain the difference in the abundance of particles. This is why we are looking for new physics that can break the CP symmetry.

$K_L \to \pi^0 \nu \overline{\nu}$ is a rare decay mode of the long-lived neutral K meson, K_L. This decay directly breaks the CP symmetry. Its branching ratio is predicted by the SM with a small theoretical uncertainty. If a measurement of the branching ratio is different from the theoretical prediction, it signifies new physics beyond the SM. Thus $K_L \to \pi^0 \nu \overline{\nu}$ is one of the most sensitive probes to search for the physics beyond SM that breaks the CP symmetry.

Although there were several experiments to search for $K_L \to \pi^0 \nu \overline{\nu}$, the decay has not been discovered yet. The KOTO experiment [3] is a rare kaon-decay experiment at J-PARC [4, 5] in Ibaraki, Japan. Its goal is to discover the $K_L \to \pi^0 \nu \overline{\nu}$ decay and measure its branching ratio.

This thesis describes the improvement of the Data Acquisition (DAQ) system for the KOTO experiment, which was needed to conduct the first physics data taking in May 2013. This thesis also describes the study to discriminate photon-induced clusters and neutron-induced clusters on the CsI Calorimeter to suppress background events caused by neutrons.

1.1 CP violation in the Standard Model

The SM is based on CPT symmetry, the combined symmetry of three fundamental symmetries in the Quantum Field Theory:

- Charge conjugation (C): transformation between particle and anti-particle,

- Parity (P): $\vec{x} \to -\vec{x}$

- T: Time reversal, $t \to -t$.

Although CPT is conserved, CP symmetry is broken in weak interaction.

In the SM, the Lagrangian of the charged current in the weak interaction involving W boson is

$$\mathcal{L}_{CC} = -\frac{g_w}{2} \left\{ \overline{u_i}\gamma^\mu V_{ij} d_j W_\mu^+ + \overline{d_j}\gamma^\mu V_{ij}^* u_i W_\mu^- \right\}, \tag{1.1}$$

where $i, j = 1, 2, 3$ are generation numbers, u_i and d_i are left-handed up-type quark and down-type quark, respectively, and $W^\pm$ denote the W bosons. The V_{ij} is an element of 3×3 unitary Cabbibo-Kobayashi-Maskawa matrix (CKM matrix) V_{CKM} [2] which connects the mass eigenstate and weak eigenstate of the up-type quarks and down-type quarks:

$$V_{CKM} = \begin{pmatrix} V_{ud} & V_{us} & V_{ub} \\ V_{cd} & V_{cs} & V_{cb} \\ V_{td} & V_{ts} & V_{tb} \end{pmatrix}. \tag{1.2}$$

L.Wolfenstein parametrized [6] the matrix by setting $\lambda = |V_{us}| = 0.22$,

$$V_{CKM} = \begin{pmatrix} 1 - \lambda^2/2 & \lambda & A\lambda^3(\rho - i\eta) \\ -\lambda & 1 - \lambda^2/2 & A\lambda^2 \\ A\lambda^3(1 - \rho - i\eta) & -A\lambda^2 & 1 \end{pmatrix} + \mathcal{O}(\lambda^4), \tag{1.3}$$

where A, ρ, λ, and η are independent real parameters. The parameter η represents the imaginary part of the CKM matrix elements which causes CP violation.

1.2 $K_L \to \pi^0 \nu\overline{\nu}$

1.2.1 $K_L \to \pi^0 \nu\overline{\nu}$ in the Standard Model

Figure 1.1 shows the Feynman diagrams of the $K_L \to \pi^0 \nu\overline{\nu}$ decay. Each diagram has an electroweak loop with a virtual top quark.

The amplitude of $K_L \to \pi^0 \nu\overline{\nu}$ can be expressed as:

$$\begin{aligned} A(K_L \to \pi^0 \nu\overline{\nu}) &\sim A(K^o \to \pi^0 \nu\overline{\nu}) - A(\bar{K}^o \to \pi^0 \nu\overline{\nu}) \\ &\propto V_{td}^* V_{ts} - V_{ts}^* V_{td} \\ &= 2Im\left(V_{ts}^* V_{td}\right) \\ &\propto \eta. \end{aligned} \tag{1.4}$$

Thus the branching ratio of $K_L \to \pi^0 \nu\overline{\nu}$ decay is proportional to η^2 and the decay is induced directly by CP violation in the weak interaction. By measuring the branching ratio of $K_L \to \pi^0 \nu\overline{\nu}$ decay, we can directly measure η in the K meson decay. The SM predicts the branching ratio $\mathrm{BR}(K_L \to \pi^0 \nu\bar{\nu})$ to be $(2.43 \pm 0.39 \pm 0.06) \times 10^{-11}$ [8]. The first error is related to the uncertainties in the input parameters, and the second error is related to theoretical uncertainty. The theoretical uncertainty on the prediction is only 2.5%. If a measurement of the branching ratio is different from the theoretical prediction, it signifies new physics beyond the Standard Model.

Because its branching ratio is predicted to be small with a small theoretical uncertainty, $K_L \to \pi^0 \nu\overline{\nu}$ decay is one of the best probes to examine the SM and to search for physics beyond the SM.
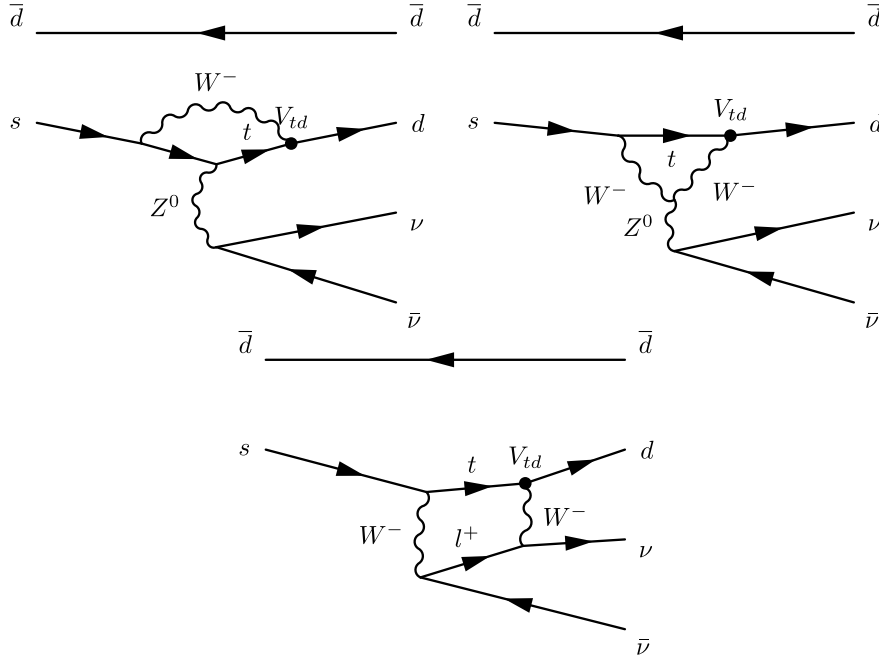
Figure 1.1: Feynman diagrams of $K_L \to \pi^0 \nu \bar{\nu}$ decay. This figure is taken from [7].

1.2.2 $K_L \to \pi^0 \nu \bar{\nu}$ in physics beyond the Standard Model

The branching ratio of $K_L \to \pi^0 \nu \bar{\nu}$ can put a strong restriction on new physics beyond the SM alone or with the branching ratios of its iso-symmetrical partner, $K^+ \to \pi^+ \nu \bar{\nu}$. Here I will describe the effect of the measurement of the branching ratio of $K_L \to \pi^0 \nu \bar{\nu}$ to new physics beyond SM.

1.2.2.1 $K^+ \to \pi^+ \nu \bar{\nu}$ decay and Grossman-Nir bound

The branching ratio of $K^+ \to \pi^+ \nu \bar{\nu}$ can set a restriction to the branching ratio of $K_L \to \pi^0 \nu \bar{\nu}$. A model-independent upper bound on the BR($K_L \to \pi^0 \nu \bar{\nu}$), called the Grossman-Nir bound [9], is derived as

$$BR(K_L \to \pi^0 \nu \bar{\nu}) < 4.4 \times BR(K^+ \to \pi^+ \nu \bar{\nu}).$$

This relation between the decay modes of neutral and charged kaons is obtained from isospin symmetry arguments.

The branching ratio of $K^+ \to \pi^+ \nu \bar{\nu}$ was measured by BNL E787/E949 group as BR($K^+ \to \pi^+ \nu \bar{\nu}$) = $(1.7 \pm 1.1) \times 10^{-10}$ [10, 11]. This branching ratio of $K^+ \to \pi^+ \nu \bar{\nu}$ sets an upper limit on BR($K_L \to \pi^0 \nu \bar{\nu}$) of 1.46×10^{-9} (90% C.L.) [3].

1.2.2.2 $K_L \to \pi^0 \nu \bar{\nu}$ and $K^+ \to \pi^+ \nu \bar{\nu}$ decays and physics beyond the SM

The combination of the measurement of the branching ratio of $K_L \to \pi^0 \nu \bar{\nu}$ and $K^+ \to \pi^+ \nu \bar{\nu}$ decays can put a strong restriction on new physics beyond the SM. Figure 1.2 shows the two branching ratios with a contributions from new physics models [12]. Some physics models predict that there is correlation between the branching ratio of these two decay modes. There are also possibility to have the branching ratio of $K_L \to \pi^0 \nu \bar{\nu}$ much larger than SM but below

the Grossman-Nir bound. Even if the $K_L \rightarrow \pi^0 \nu \overline{\nu}$ is not observed, the improvement of the upper limit of $BR(K_L \rightarrow \pi^0 \nu \overline{\nu})$ can put constraints on such new-physics models.
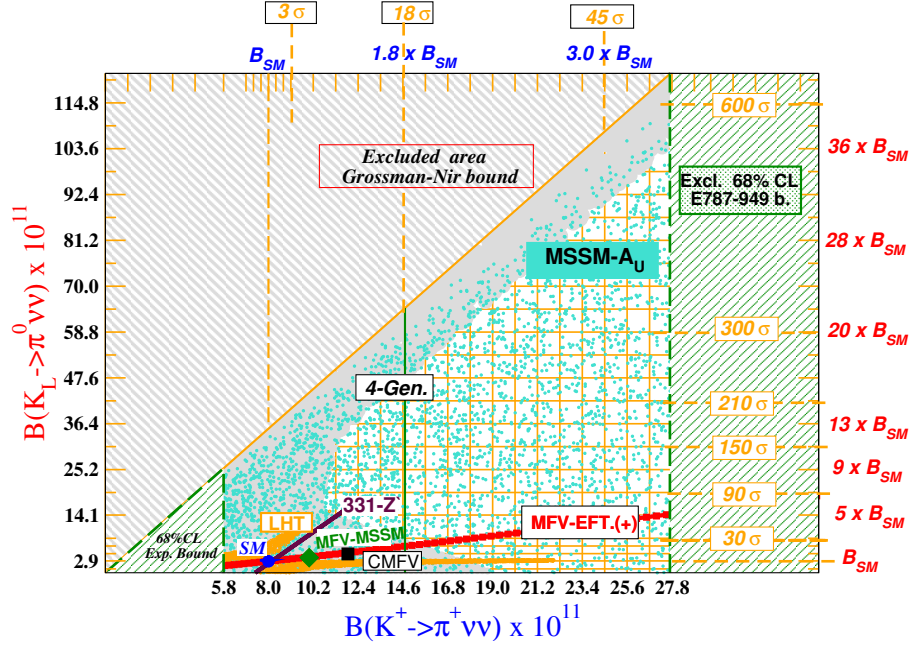
Figure 1.2: Correlation between the branching ratios of $K_L \rightarrow \pi^0 \nu \overline{\nu}$ and $K^+ \rightarrow \pi^+ \nu \overline{\nu}$ with new physics models beyond SM [12].

1.2.3 History of $K_L \rightarrow \pi^0 \nu \overline{\nu}$ search

There were several experiments to search for $K_L \rightarrow \pi^0 \nu \overline{\nu}$, as shown in Fig. 1.3. However, $K_L \rightarrow \pi^0 \nu \overline{\nu}$ decay has not been discovered yet due to its small branching ratio, and only upper limits on the branching ratio were given. The current experimental upper limits is 2.6×10^{-8} at the 90% confidence level (C.L.) given by the KEK E391a experiment [13] which was the first dedicated experiment to search for $K_L \rightarrow \pi^0 \nu \overline{\nu}$.

1.3 The KOTO experiment

In this section, the basic concept of the KOTO experiment is described. The detailed design of KOTO experiment will be described in Chapter 2

1.3.1 The KOTO experiment

The KOTO experiment [3] is a new kaon-decay experiment at J-PARC [4, 5] in Ibaraki, Japan. Its goal is to discover the $K_L \rightarrow \pi^0 \nu \overline{\nu}$ decay and measure its branching ratio. The KOTO experiment is a successor of KEK E391a experiment and was designed to improve the sensitivity of E391a by three orders of magnitude.
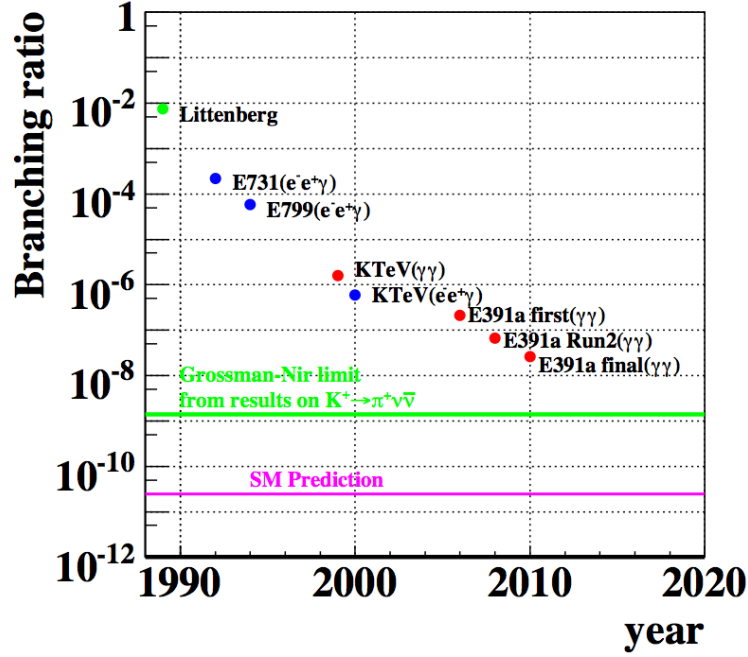
Figure 1.3: The history of the search for $K_L \to \pi^0 \nu \bar{\nu}$. Each point shows the 90% C.L upper limit of $\mathrm{Br}(K_L \to \pi^0 \nu \bar{\nu})$. Blue (Red) points show the results of the analysis using $\pi^0 \to e^+ e^- \gamma$ ($\pi^0 \to \gamma\gamma$). The pink line shows the prediction in the SM and the green line shows the Grossman-Nir limit set by $K^+ \to \pi^+ \nu \bar{\nu}$ decay experiment. This figure is taken from [7].

1.3.2 Signature of $K_L \to \pi^0 \nu \bar{\nu}$

The experimental difficulty in observing the $K_L \to \pi^0 \nu \bar{\nu}$ decay is due to the lack of charged particles both in the initial and the final states. The two photons from the π^0 decay are the only observable decay products because ν is difficult to detect.

Other K_L decay modes such as $K_L \to 3\pi^0$, $K_L \to 2\pi^0$, $K_L \to \pi^+ \pi^- \pi^0$, and $K_L \to \pi^\pm l^\mp \nu$ ($l = e, \mu$) have extra photons or charged particles. Two-photon system from $K_L \to \pi^0 \nu \bar{\nu}$ has a finite transverse momentum P_T due to missing neutrinos while two photons from $K_L \to \gamma\gamma$ has zero P_T.

The signature of $K_L \to \pi^0 \nu \bar{\nu}$ is thus "$\pi^0 \to \gamma\gamma$ ($P_T \neq 0$) with nothing else".

1.3.3 Background sources and its reduction

There are two types of backgrounds: K_L decay background, and the beam-interaction background. If extra particles from other K_L decay modes are not detected, it becomes a source of the background. If a π^0 is produced by a beam particle interacting with detector materials, it can also be a source of background.

1.3.3.1 Background from K_L decay modes

Table 1.1 shows a list of the branching ratios of K_L decay modes. Among the top four decay modes, three decay modes have charged particles in the final state. To reject those modes, the detectors are required to have a high efficiency to detect charged particles. The $K_L \to 2\pi^0$ and

$K_L \to 3\pi^0$ decays can be backgrounds if extra photons are missed. In particular, $K_L \to 2\pi^0$ is thought to be a major source of backgrounds.

The $K_L \to \gamma\gamma$ has only two photons in the final state, as $K_L \to \pi^0\nu\overline{\nu}$. The $K_L \to \gamma\gamma$ decay mode has zero transverse momentum and can be rejected by requiring large P_T. This decay mode can be a background if the transverse momentum is miscalculated.

Table 1.1: A list of the branching ratios of K_L decay modes. The $K_L \to \pi^0\nu\overline{\nu}$, top four decay modes and relevant two decay modes are listed. The branching ratio of $K_L \to \pi^0\nu\overline{\nu}$ by the Standard Model is quoted from [8] and other values are quoted from [14].

K_L decay modes	Branching ratio	particles in the final state
$K_L \to \pi^\pm e^\mp \nu_e$ (K_{e3} mode)	$40.55 \pm 0.11\%$	charged particles
$K_L \to \pi^\pm \mu^\mp \nu_\mu$ ($K_{\mu3}$ mode)	$27.04 \pm 0.07\%$	charged particles
$K_L \to \pi^+\pi^-\pi^0$	$12.54 \pm 0.05\%$	charged particle
$K_L \to 3\pi^0$	$19.52 \pm 0.12\%$	six photons
$K_L \to 2\pi^0$	$(8.64 \pm 0.06) \times 10^{-4}$	four photons
$K_L \to \gamma\gamma$	$(5.47 \pm 0.04) \times 10^{-4}$	two photons
$K_L \to \pi^0\nu\overline{\nu}$	$(2.43 \pm 0.39) \times 10^{-11}$	two photons

1.3.3.2 Background from the interaction between beam and detector materials

In the neutral beam, there are many neutrons produced by hadronic interaction at a production target. If a neutron in the beam interact with any materials, it can produce π^0 or η which decay into two photons and mimic a $K_L \to \pi^0\nu\overline{\nu}$ decay event.

interaction with residual gas

The residual gas in the decay region and the detector components around beam can be sources of the background. To reduce the interaction between neutrons and residual gas, the decay region must be kept in a high vacuum with the level of $O(10^{-5})$ Pa.

interaction with detector materials

If a neutron in the beam hits the detector materials, π^0 or η can be generated and two photons will be produced. This background can be rejected by calculating the decay vertex position of $\pi^0 \to \gamma\gamma$. However, if we miscalculate the decay vertex position, it can be a source of background. To reduce this background, the amount of material around the beam must be minimized, and the detectors are required to have good energy resolution.

1.3.4 The concept

The KOTO experiment shares its concept with its predecessor experiment, KEK E391a. The experimental concept of KOTO experiment is shown in Fig. 1.4 and is described as follows.

1. Use of a well collimated K_L beam to have decays on the beam axis.

   Because K_L is a neutral particle, we cannot track the trajectory of K_L, and it is difficult to reconstruct the decay vertex of K_L. By collimating K_Ls, we can assume that the K_L have small transverse momenta and will decay on the beam axis. With this assumption, the decay vertex is reconstructed.
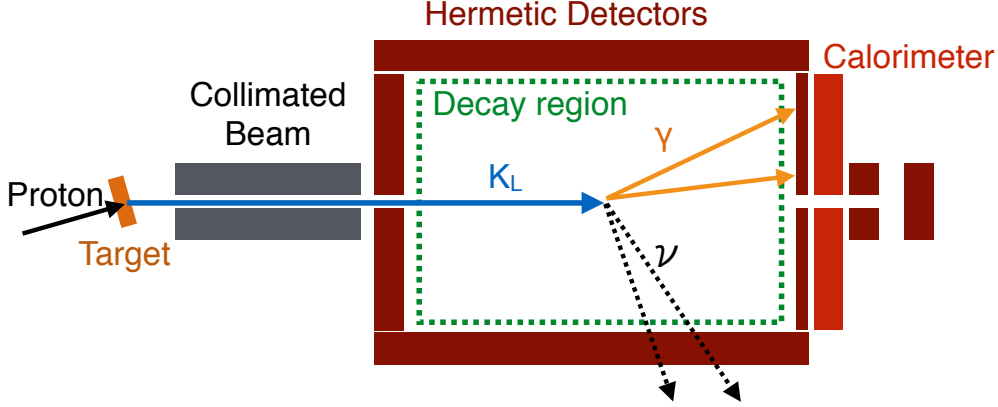
Figure 1.4: A conceptual view of the KOTO experiment.

2. Detect two photons from π^0 with a calorimeter and reconstruct the decay vertex of π^0.

   Two photons from a π^0 decay are the sole observable particles in this decay. By measuring the energies and incident positions of the two photons, the decay vertex Z_{vtx} and transverse momentum P_T of the π^0 can be calculated. An electromagnetic Calorimeter made of Cesium Iodide crystals (CsI calorimeter) was used to measure the energies and incident positions of the two photons with good energy and position resolutions.

3. Require large transverse momentum P_T due to the momentum taken away by two neutrinos.

   $K_L \to \gamma\gamma$ decay can be discriminated by using the P_T of two-photon system.

4. Cover the decay volume with hermetic veto detector subsystems to veto extra particles.

   Other decay modes of K_L such as $K_L \to 3\pi^0$, $K_L \to 2\pi^0$, $K_L \to \pi^+\pi^-\pi^0$, and $K_L \to \pi^\pm l^\mp \nu$ $(l = e, \mu)$ have extra photons or charged particles. To reject these decay mode, the decay volume is covered by hermetic veto detector subsystems with high detection efficiencies for photons and charged particles.

1.4 Purpose and Outline of the Thesis

The purposes of this thesis are the followings.

1. Develop trigger logic required to take $K_L \to \pi^0 \nu\bar{\nu}$ events.

2. Study the difference in pulse shape between neutron events and photon events and establish a method to discriminate them.

1.4.1 Development of trigger logic

In the original design, the Data Acquisition (DAQ) system of KOTO experiment used the information only from the CsI calorimeter for making triggers. In this case, most of the collected events will be the background events from K_L decays such as $K_L \to \pi^0\pi^0$, $K_L \to \pi^0\pi^0\pi^0$, and $K_L \to \pi^\pm l^\mp \nu$ $(l = e, \mu)$. To reject those events and to take only the events with the activity only

in the CsI calorimeter, the integration of the veto detector subsystems into the DAQ system was required. I developed new trigger logics and implemented into the KOTO DAQ system to use the information from all the detector subsystems for the trigger decision.

1.4.2 Pulse shape study

During the analysis of first physics run to search for $K_L \rightarrow \pi^0 \nu \overline{\nu}$, we found some background events after applying all the kinematic cuts. Most of those background events could be rejected by requiring the cluster shape on the CsI calorimeter to be consistent with typical cluster shape of photon induced cluster. Remained background events are thus thought to be induced by neutrons instead of photons. Though most of the background events were rejected by the cut on cluster shape, one event still remained after all the cuts. To suppress the background induced by neutrons even more, we needed a new method with a new perspective other than the cluster shape was required. I studied the pulse shape of the CsI calorimeter for photon-induced clusters and neutron-induced clusters, and found a difference between them. I developed a new method to discriminate between neutron-induced clustes and photon-induced clusters.

1.4.3 Outline of this thesis

In this chapter, the basic information about CP symmetry, $K_L \rightarrow \pi^0 \nu \overline{\nu}$ decay, KOTO experiment, and the purpose of my thesis are described. The apparatus of KOTO experiment is described in Chapter 2. The improvement to KOTO DAQ system that I have developed is described in Chapter 3. The analysis of $K_L \rightarrow \pi^0 \nu \overline{\nu}$ is described in Chapter 4. The pulse shape study for photon and neutron events, and the impact of this thesis for $K_L \rightarrow \pi^0 \nu \overline{\nu}$ analysis in the KOTO experiment are described in Chapter 5. The mechanism to make differences in pulse shapes, and other methods for further reduction of background events are discussed in Chapter 6. Chapter 7 concludes this thesis.

Chapter 2

KOTO experiment

In this chapter, I will describe the J-PARC facility and the apparatus of the KOTO experiment. I will first describe the J-PARC accelerator facilities and the hadron experimental facility. The KOTO detector and the data acquisition system will be also described. At the end, the summary of the physics data taking runs for KOTO taken in May 2013 and 2015 is described.

2.1 J-PARC

The Japan Proton Accelerator Research Complex (J-PARC) [4, 5] is a high-intensity proton accelerator facility in Ibaraki, Japan. A bird's-eye view of the entire J-PARC facility is shown in Fig. 2.1.

J-PARC consists of three accelerator facilities: a linear accelerator (LINAC) [15], a 3 GeV Rapid Cycle Synchrotron (RCS) [16], and the Main Ring (MR) [17]. The protons from those accelerator facilities are used in three experimental facilities: the Material and Life science experimental Facility (MLF), the Neutrino Experimental facility (NU) [18], and the Hadron Experimental facility (HD-hall) [19, 20].

2.1.1 Accelerator facilities

Table 2.1 shows main parameters of the J-PARC accelerator facilities. Negative hydrogen ions (H$^-$) are extracted from the ion source and accelerated up to 400 MeV [21] by the LINAC and delivered to RCS. H$^-$ ions are converted to protons by a charge-exchanging foil and the produced protons are injected to RCS. RCS accelerates protons up to 3 GeV at a repetition cycle of 25 Hz. A portion of 3-GeV protons are delivered to MR for further acceleration, and most of the protons are delivered to MLF. The MR accelerates protons from 3 GeV up to 30 GeV. The accelerated protons are extracted via two different methods: a fast extraction (FX) within 5 μs to NU using kicker magnets, and a slow extraction over 2 s to HD-hall using a resonant extraction. As of December 2015, the MR achieved operation with beam power of 330 kW for FX and 43 kW for SX.

2.1.2 The Hadron Experimental Facility (HD-hall)

The primary proton beam extracted from MR is delivered to the Hadron Experimental Facility (HD-hall) through the beam switchyard (SY). Figure 2.2 shows the layout of the SY and HD-hall. The length of SY is about 200 m along the primary beam line. The 30-GeV protons are
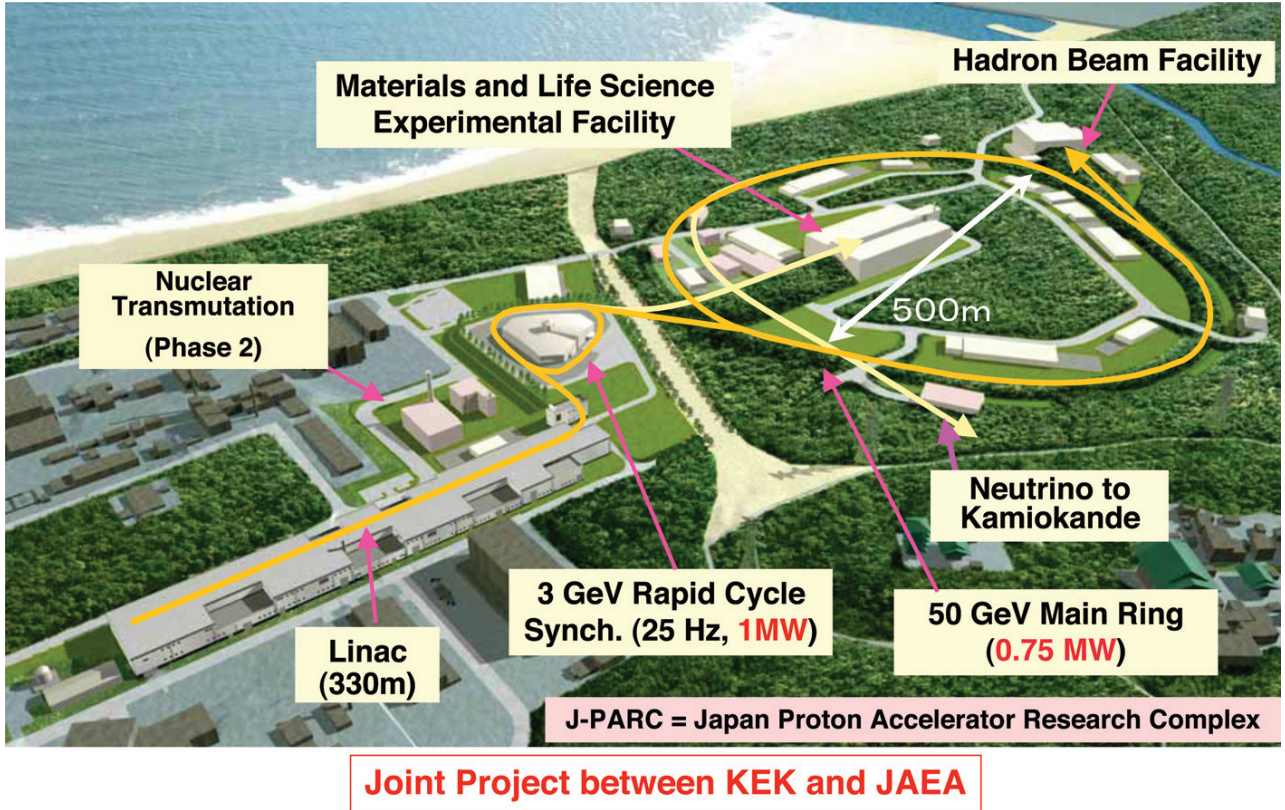
Figure 2.1: A bird's-eye view of the entire J-PARC facility. This figure is obtained from [5].

Table 2.1: A list of parameters of J-PARC accelerator facilities.

LINAC	
Ion species	Negative hydrogen ions
Repetion cycle	25Hz
Extraction Beam Energy	400MeV
RCS	
Circumference	348.333 m
Repetion cycle	25Hz
Extraction Beam Energy	3 GeV
MR	
Circumference	1567.5 m
Beam cycle	2.56 s (FX), 5.52, 6.0 s (SX)
Extraction Beam Energy	30 GeV
Achieved Beam Power	330 kW (FX), 43 kW (SX)
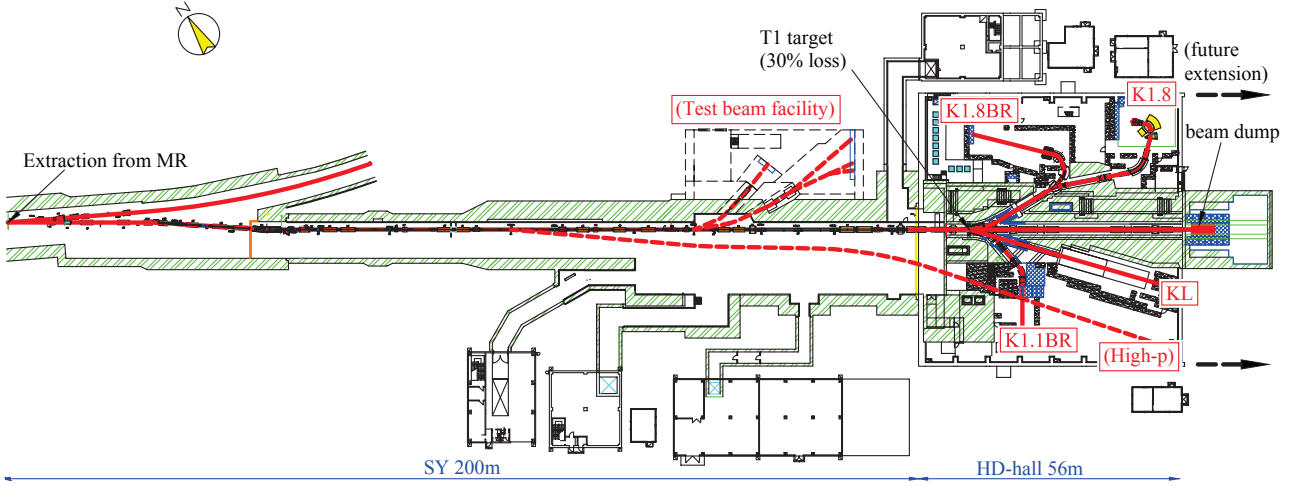
Figure 2.2: Layout of the primary beam line and the hadron experimental facility. The extracted proton beam is delivered to the hadron experimental facility (HD-hall) through the beam switchyard (SY). The solid lines represent the beam line in operation and dashed line shows the additional beam line planned for the future extention. This figure is taken from [19].

extracted to SY over 2 s. The beam was extracted every 6 s in the runs before the summer of 2015 and 5.52 s after then. A beam extraction in one cycle is called "spill".

Figure 2.3 shows the layout of the hadron experimental hall and its secondary beam lines. The dimensions of the HD-hall are 60 m × 56 m.

The protons delivered to the HD-hall are injected to a production target, called T1 target, located in the HD-hall. Figures 2.4 and 2.5 show the photograph and structural drawing of the T1 target used in 2013 and 2015, respectively. The T1 target consists of gold blocks bonded on a copper block for with a water cooling mechanism [22].

The secondary particles produced at the T1 target are delivered to the secondary beam lines which share the T1 target. Currently, there are three beam lines for charged particles and one beam line for neutral particles.

2.2   Beamline

The KOTO experiment uses a neutral beam line, called "KL" beam line, in the HD-hall. Figure 2.6 shows the layout of the KL beam line. This beam line is 21 m long toward 16° direction from the primary proton beam line. As shown in Fig. 2.6, the beam also has to go through many equipments for another beam lines which share the same T1 target. Figure 2.7 shows the components in the KL beam line. The KL beam line consists of a photon absorber, a sweeping magnet, a beam plug, and two long collimators.

The particles extracted from the T1 target are collimated by two collimators. The length of the first collimator is 4 m and the length of the second collimator is 5 m . They are made of iron except for their edge regions. The edge regions are made of tungsten to increase mass-thickness. The collimators were designed to make a narrow beam and to suppress halo neutrons produced by the multiple-scattering of the beam neutrons [24].

Photons coming from the T1 target are stopped by a 7 cm lead block, called "Photon
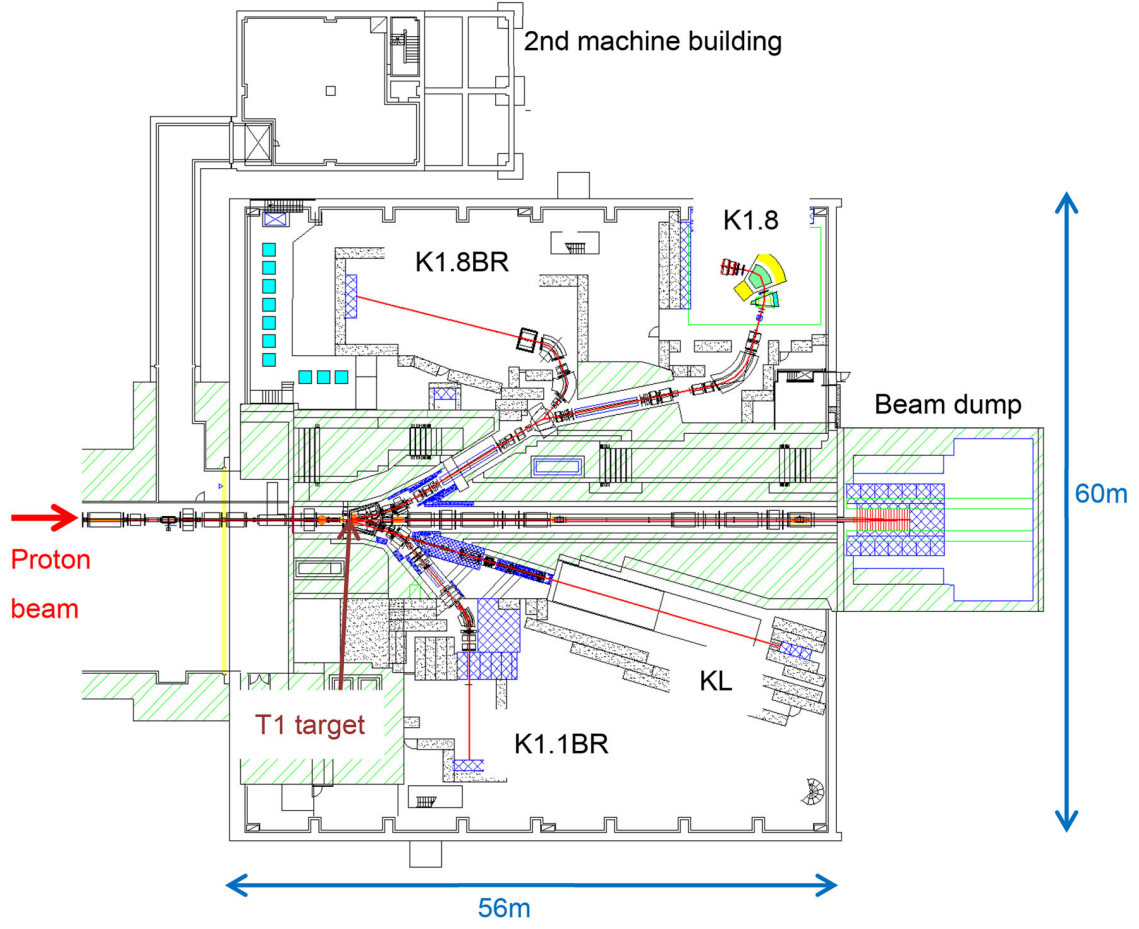
Figure 2.3: Layout of the the hadron experimental facility. This figure is taken from [22].
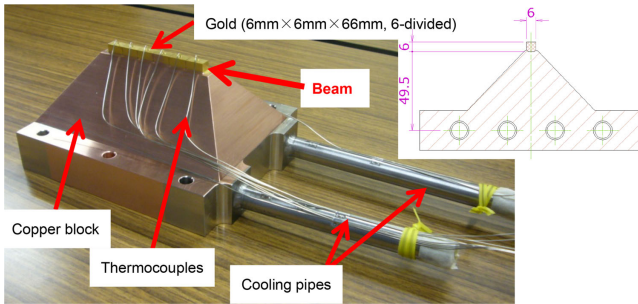
Figure 2.4: Photograph of the T1 target in May 2013 before the installation and its crosssectional drawing. A gold target is bonded to a copper block with cooling water pipes. This figure is taken from [22].
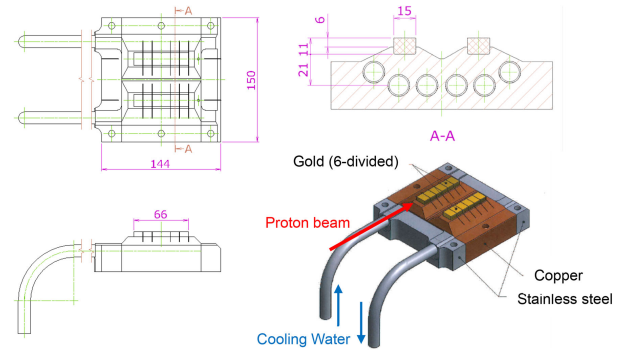
Figure 2.5: Structural drawings of the new T1 target used from the 2015 beam operation. New T1 target consists of two gold targets with wider cross section. This figure is taken from [22].
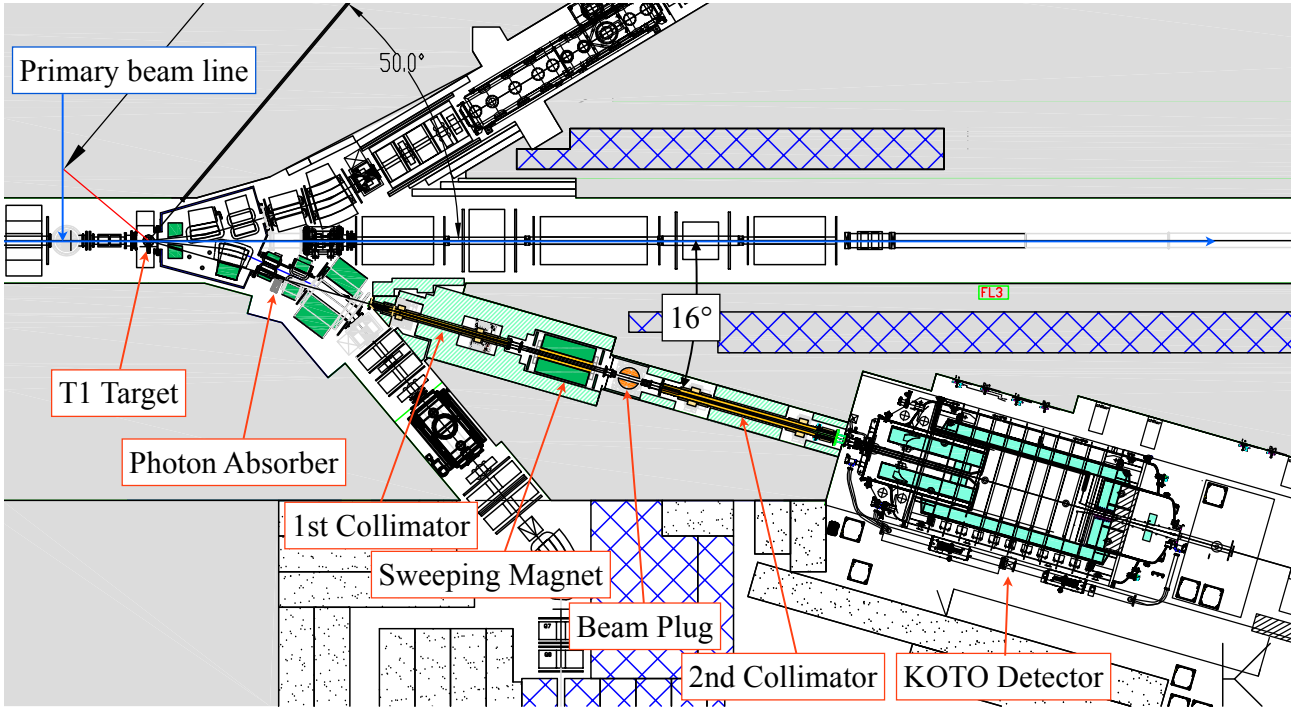
Figure 2.6: Layout of the KL beam line. This figure is taken from [23].
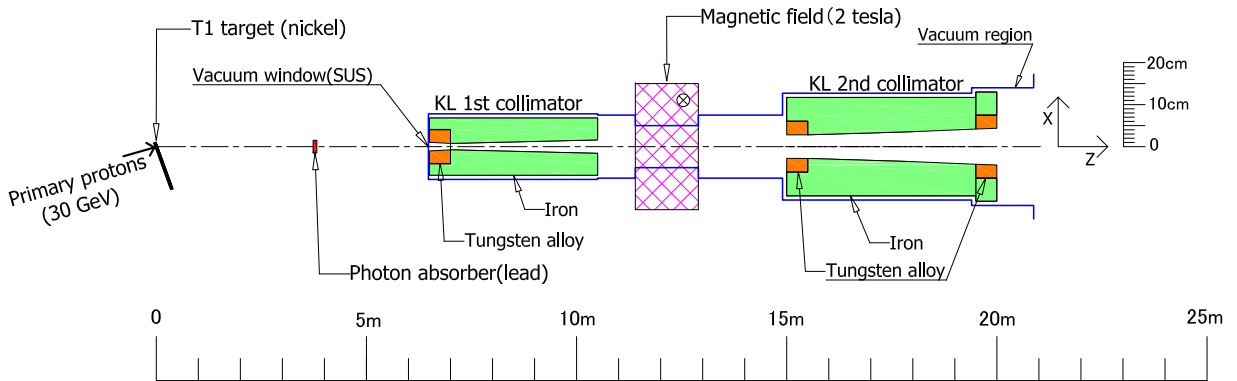
Figure 2.7: Components in the KL beam line [24].
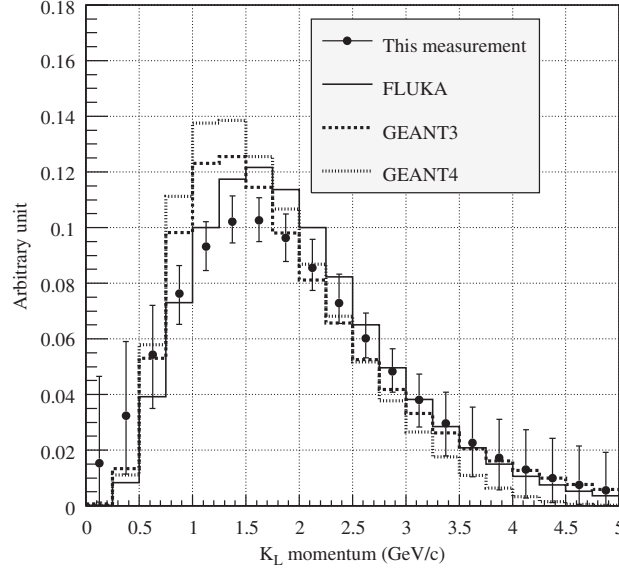
Figure 2.8: The momentum spectrum of K_L in the KL beam line. The dots shows the result from the measurement and the histograms show the expectations from various simulations. This figure is taken from [25].

Absorber". Charged particles from the T1 target are swept out by a dipole magnet placed between the two collimators with the magnetic field of 1.2 T.

A beam plug is a pair of rotatable D-shape brass blocks placed in the middle of the beam line. In the normal state, called "Open" state, beam can go through between two brass block. By rotating the beam plug by 90°, to "Closed" state, most of the beam particle can be stopped at the beam plug.

The beam solid angle is 7.8 μsr, and the width of the beam is 10 cm at the exit of the beam line (21 m from the T1 target). The K_L flux in the beam was measured in the past beam tests [25] for two types of production target materials, nickel and platinum. With 2×10^{14} protons delivered to the T1 target, the numbers of K_Ls passing through the exit of the KL beam line were 1.94×10^7 for the Ni target and 4.19×10^7 for the Pt target.

The momentum spectrum was also measured in the past beam tests. Figure 2.8 shows the measured and expected momentum spectra of K_L; they are both peaked at 1.5 GeV/c.

2.3 Detectors

Figure 2.9 shows the side view of the KOTO detector. The K_Ls in the KL beam line enter the KOTO detector. The kaons and pions that decayed in the region 3∼5 m downstream of the beam exit were used for the analysis. We call this region "decay region". Two photons from π^0 in $K_L \rightarrow \pi^0 \nu \overline{\nu}$ were detected by an electromagnetic calorimeter made of Cesium Iodide crystals (CsI calorimeter) placed downstream of the decay region. The decay region was surrounded by hermetic detector subsystems, called "Veto detectors", to detect extra particles from other K_L decay modes. The detector subsystems to detect charged particles and photons, are called "Charged Veto" and "Photon Veto" detectors, respectively.
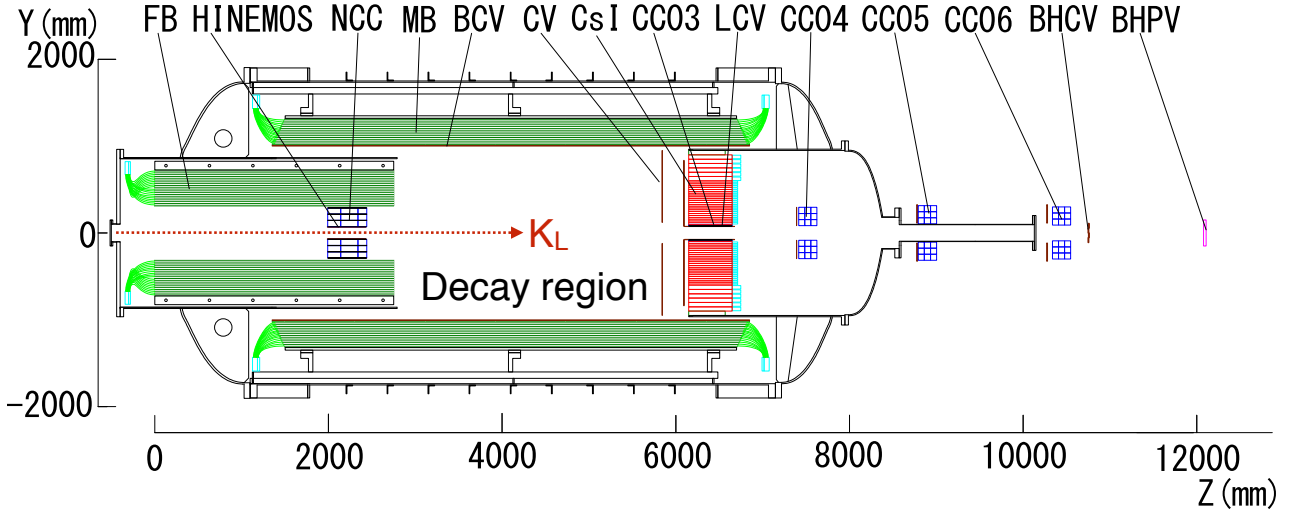
Figure 2.9: Side view of the KOTO detector. CsI calorimeter detects two photons from π^0 in $K_L \to \pi^0 \nu \bar{\nu}$. Many detector subsystems surrounding the decay region are used to detect extra particles from other K_L decay modes. Only one out of 25 BHPV modules is shown in this figure.

2.3.1 Coordinate definition

We define the coordinate for the detector system as follows.

- Origin of the coordinate: On the KL beam axis, the upstream surface of Front Barrel, 21 m downstream of the production target.

- Z: Parallel to the KL beam axis, pointing downstream.

- Y: Points vertically up.

- X: Points in the direction for the coordinate system to be right-handed.

2.3.2 The CsI calorimeter

An electromagnetic calorimeter made of Cesium Iodide crystals (CsI calorimeter) is the main detector of the KOTO experiment. The CsI calorimeter was placed downstream of the decay region with its upstream surface located at $Z = 6148$ mm.

Figure 2.10 shows a front view and Fig. 2.11 shows a photograph of the CsI calorimeter. The CsI calorimeter consisted of 2716 un-doped Cesium Iodide (CsI) crystals stacked inside a cylinder with a diameter of 1.9 m. The length of the CsI crystals was 50 cm which was equivalent to 27 radiation lengths (X_0). The inner square region with a width of 1.2 m consisted of 2240 crystals whose cross sections were 2.5 cm × 2.5 cm ("small crystals"), and the outer region consisted of 476 crystals whose cross sections were 5 cm × 5 cm ("large crystals"). A square of 20 cm × 20 cm beam hole was made at the center of the CsI calorimeter to prevent K_Ls not decayed in the decay region and other particles coming from the beam line from hitting the CsI calorimeter. The beam hole was maintained by a beam pipe made of Carbon-fiber-reinforced-plastic (CFRP).

Figure 2.10: A front view of the CsI calorimeter for the KOTO experiment. This figure is quoted from [26].

Figure 2.11: A photograph of the CsI calorimeter for the KOTO experiment.

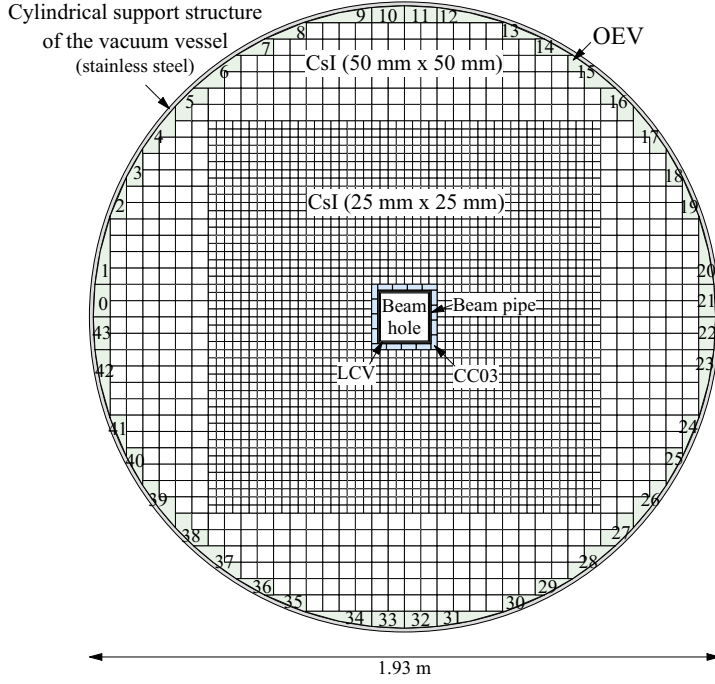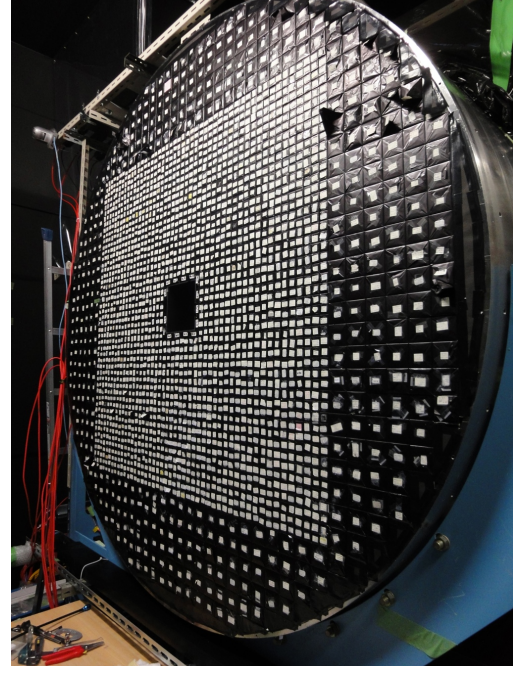The CsI crystals for the CsI calorimeter were originally used at the FermiLab KTeV experiment [27]. There were two types of crystals. The 20% of crystals were made from a single crystal fabricated by HORIBA company (Fig. 2.12), while 80% of crystals were made by glueing two 25-cm-long single crystals (Fig. 2.13) [28]. As shown in Fig. 2.14, each CsI crystal was wrapped with a 13-μm-thick mylar. To achieve a uniform light response along the crystal length, the half of the crystal farther from the PMT was wrapped with aluminized mylar and the other half was wrapped with black mylar. The length of reflective region and effective reflectivity were tuned [1] for each crystal to keep the uniformity of scintillation response within 5% [28, 29, 30].

Two types of Photo Multiplier Tubes (PMTs) were used to read the scintillation light from the two sizes of the CsI crystals. Hamamatsu R5364 3/4 inch PMTs were used for the small crystals and Hamamatsu R5330 1.5 inch PMTs are used for the large crystals. Those PMTs were originally used at the KTeV experiment and re-used in the KOTO experiment. The combination of PMTs and crystals were tuned so that the variation of the product of the light yield of CsI crystals and the gain of PMTs, is kept under 3% [31].

A UV transmitting filter (Schott UG-11), with a peak transmission of around 80% at the wavelength of 300 nm, and a near-zero transmission band in the wavelength range between 400 nm and 650 nm, was attached in front of each PMT to suppress the "slow-component" of the scintillation of CsI crystals.

A 4.6-cm-thick transparent silicone disk, called "Silicone cookie", was placed between each CsI crystal and PMT to connect them optically without glueing. To suppress the heat generated by the PMT bases, we developed a new High Voltage (HV) system with a Cockcroft-Walton

---

[1]The effective reflectivity was tuned by partially masking the aluminized mylar with stripes which are ink applied with a pen[29]
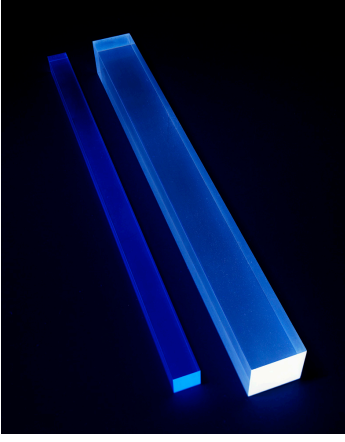
Figure 2.12: A 50-cm-long CsI single crystal. (Picture: Fermilab Visual Media Services)
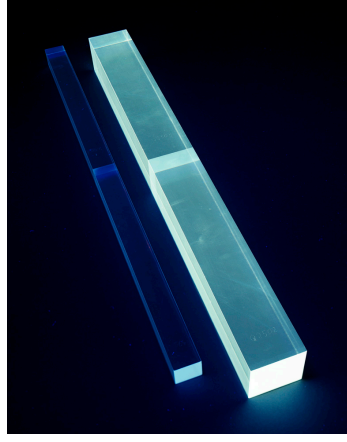
Figure 2.13: A 50-cm-long CsI crystal made by glueing two 25-cm-long CsI single crystals. (Picture: Fermilab Visual Media Services)

Figure 2.14: A CsI crystal being wrapped with an aluminized mylar. (Picture: Fermilab Visual Media Services)

(CW) circuit [32].

To compensate for the low-gain ($\mathcal{O}(10^3)$) of PMTs, three types of preamplifiers with different gains were developed and installed right after the output of PMTs. The types of preamplifiers were chosen according to the gain of PMTs. The preamplifier converted the PMT output signal to a differential signal to reduce the effect from environmental electromagnetic noise. The preamplifier output signal was transferred by a commercial Category-6 Ethernet cable.

2.3.3 Charged Veto (CV)

To detect the charged particles incident on the CsI calorimeter, the Charged Veto (CV) was placed in front of the CsI calorimeter. The CV consisted of two layers of plastic scintillators fixed on the CFRP plate [33]. Figure 2.15 shows a schematic view of the front layer of the CV. Each layer of the CV has a quadrant symmetry. Each quadrant consisted of twelve (eleven) scintillator strips in the front (rear) layer. Each scintillator was 70.7 mm wide and 3 mm thick. The length of scintillators varied depending on the position of the strips. The scintillation light from each strip was read out by seven wavelength-shifting (WLS) fibers glued on the strips. Multi Pixel Photon Counters were attached to the both ends of the WLS fibers. Figure 2.16 shows a photograph of the CV installed in the detector complex.

2.3.4 Barrel Photon Veto

Barrel-shaped photon detectors called the Front Barrel (FB) and the Main Barrel (MB) were placed around the decay region. The FB detects the photons from K_L decayed upstream of the decay volume, and MB detects the photon from those decayed inside the decay region.

The FB and MB were originally developed for and used in the KEK E391a experiment [34]. The FB and MB were lead/scintillator sandwich-type photon detectors. Figure 2.17 shows
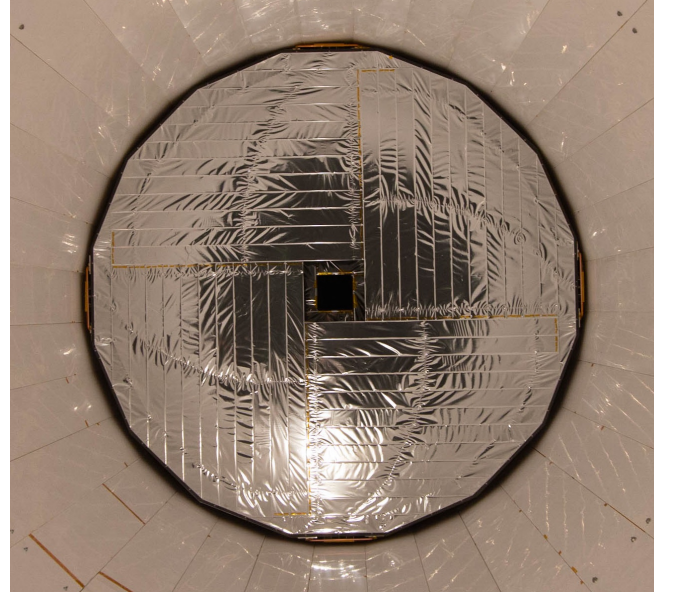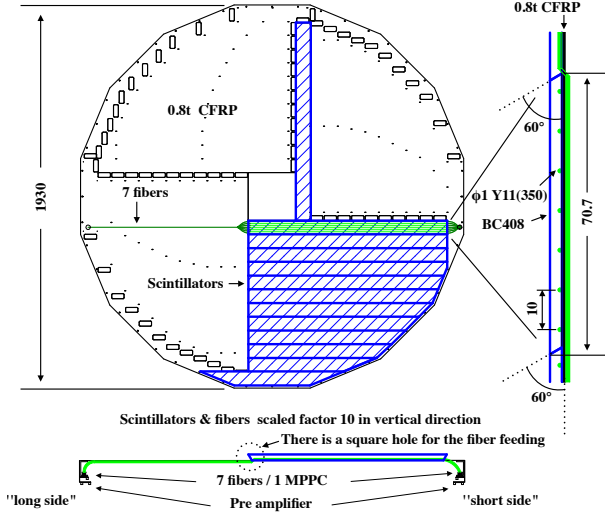
Figure 2.15: A schematic view of the front layer of CV. This figure is taken from [33].

Figure 2.16: A photograph of CV installed in the detector complex.

cross-sections of the module of the FB and MB. The FB consisted of 59 layers of 5-mm-thick plastic scintillators and 1.5-mm-thick lead plates stacked alternately. The MB consisted of 45 layers of 5-mm-thick plastic scintillators and lead plates stacked alternately. For MB, 1-mm-thick lead plates were used for inner 15 layers and 2-mm-thick lead plates were used for outer 32 layers. A 10-mm-thick plastic scintillator was attached in front of the first layer of the MB to detect charged particles. These layers of scintillators and lead plates were fixed to a backbone structure with steel bolts.

The scintillation light from the scintillator was read out by the WLS fibers glued on the scintillators. For MB, PMTs were attached to the both upstream and downstream ends of the WLS fibers. With the readout from both ends of the fibers, the hit position on the MB modules were measured by comparing the timing or energy deposits measured at both ends. For FB, PMTs were only connected to the upstream end of the WLS fibers.

2.3.5 Neutron Collar Counter (NCC)

A small calorimeter made of un-doped CsI crystals called the Neutron Collar Counter (NCC) [35] was placed inside the FB. The NCC detects the photons from the K_L decay to veto them. The NCC was also made to measure the flux and the energy spectrum of the neutrons coming outside the beam (halo neutron). Figure 2.19 shows a schematic view of the NCC. The NCC has a design with three segments along longitudinal and transversal directions to discriminate between photons and neutrons. Scintillation light from the crystals was read out by the WLS fibers glued on the acrylic plate attached to each crystal. The charged veto detector called HINEMOS was placed inside the NCC to cover four inner surfaces of the NCC.

2.3.6 Collar Counters

Detectors made of un-doped CsI crystals were placed around the beam to detect photons and charge particles from K_L decay escaping through the beam hole in the CsI calorimeter. These

18
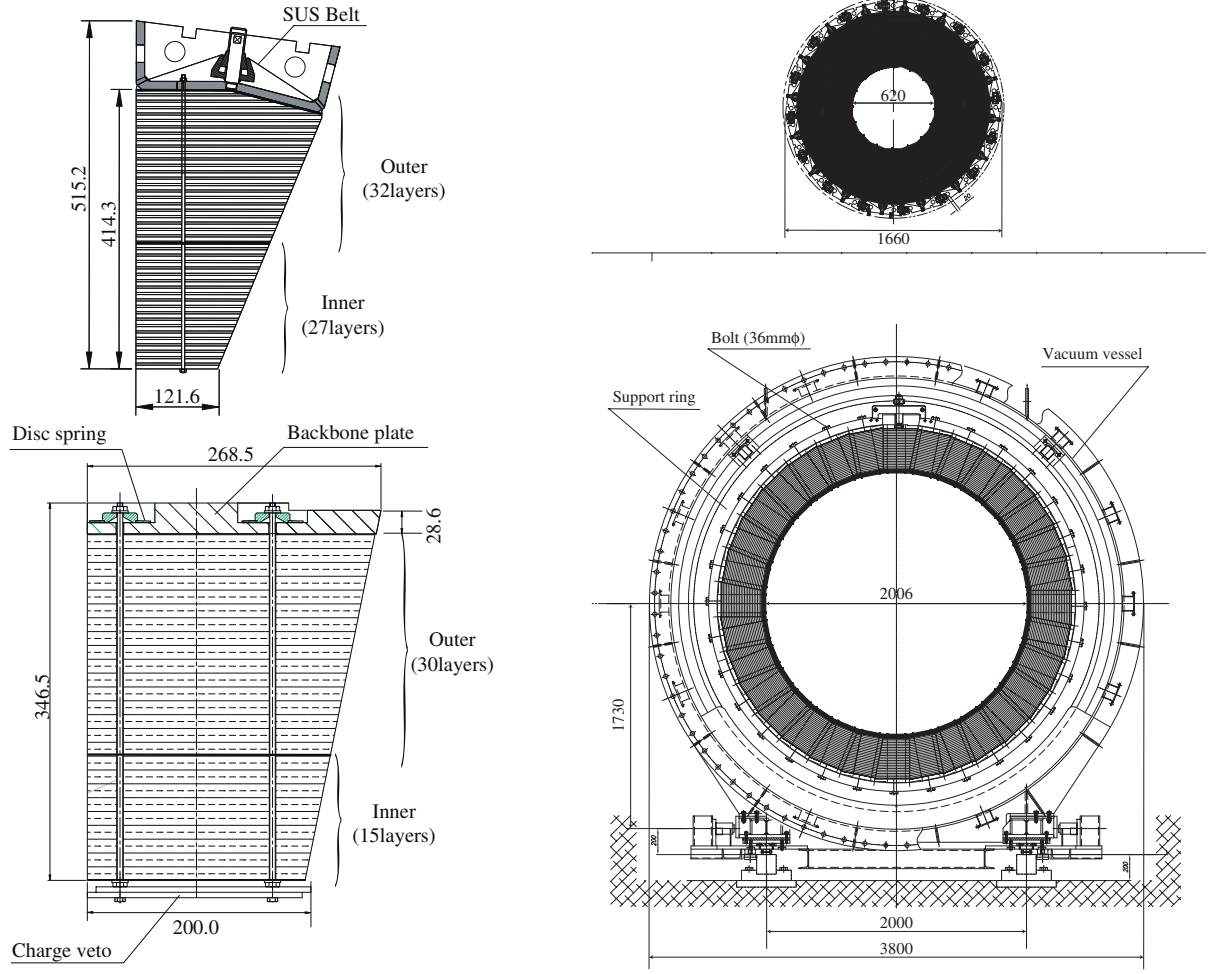
Figure 2.17: Cross-sections of a module of FB (top) and MB (bottom) detectors [34].

Figure 2.18: Cross-sections of FB (top) and MB (bottom) detectors [34].
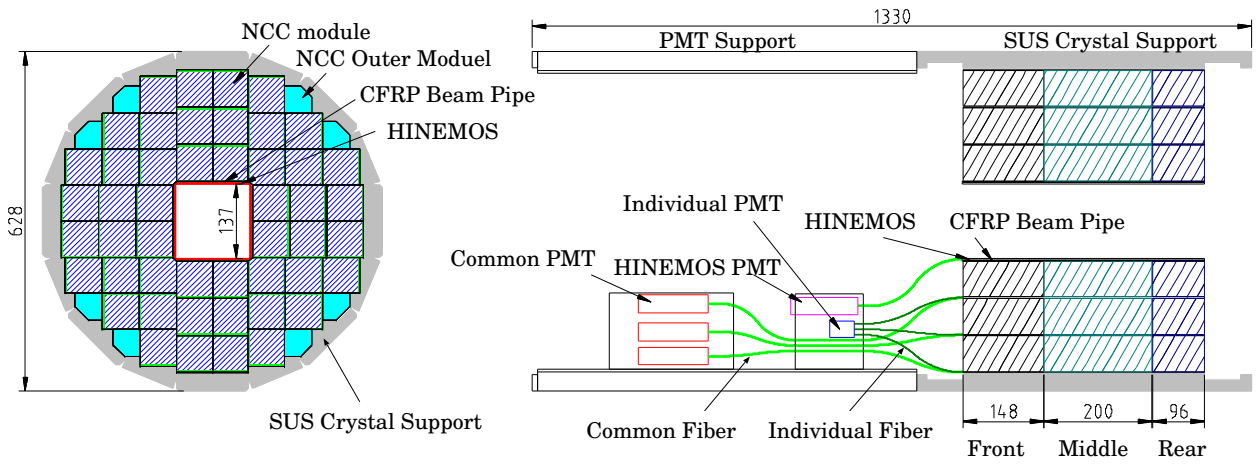
Figure 2.19: A schematic view of the NCC detector. The NCC has a segmented design to separate photons and neutrons. This figure is taken from [35].

detectors are called Collar Counter and named as CC03, CC04, CC05, and CC06.

As shown in Fig. 2.10, the CC03 was placed inside the CsI calorimeter to detect photons hitting the inner region of the CsI calorimeter close to the beam pipe. The CC03 consisted of 16 CsI crystals, and each crystal had two PMTs for readout. The charged veto detector called Liner Charged Veto (LCV) covered four inner surfaces of the CC03. The LCV was made of plastic scintillators readout by WLS fibers.

Other Collar Counters, CC04, CC05, and CC06 were placed downstream of the CsI calorimeter to detect photons and charged particles escaping through the beam hole of the CsI calorimeter. The schematic views of CC04, CC05, and CC06 are shown in Figs. 2.20, 2.21, and 2.22, respectively.

2.3.7 Outer Edge Veto

Outer Edge Veto (OEV) [26] is a photon veto detector subsystem surrounding the CsI calorimeter, as shown in Fig. 2.10. The OEV consisted of 44 modules made of the layers of lead plates and plastic scintillators. Figure 2.23 shows a schematic view of one OEV module. The layers of lead plates and plastic scintillators were stacked and packed inside a frame made of stainless steel. The scintillation light from the scintillator was read out through WLS fibers glued on the scintillators.

2.3.8 Beam Pipe Charged Veto

The Beam Pipe Charged Veto (BPCV) [36] was placed around the beam pipe between the CC05 and the CC06 to detect the charged particles escaping between them. The BPCV was installed before the data taking in 2015. Figure 2.24 shows a schematic view of the BPCV. The BPCV consists of four plastic scintillator plates surrounding the beam pipe. The scintillation light from the scintillator was read out through WLS fibers glued on the scintillators.

2.3.9 Beam Hole Charged and Photon Veto

There were some detectors placed inside the beam to detect the particles escaping along the beam.

2.3.9.1 Beam Hole Charged Veto

The Beam Hole Charged Veto (BHCV) was placed downstream of the CC06. The BHCV used in 2013 was made of plastic scintillators as shown in Fig. 2.25.

In 2015, three layers of Multi Wire Proportional Chambers (MWPC) were added as a "newBHCV". Figure 2.26 shows a layer of MWPCs used as a module of the newBHCV. Mixture of n-Pentane and CF_4 gases was used as an operation gas. Gold-plated tungsten wires were used as anode wires. Graphite-painted polyimide sheet was used as cathode planes.

2.3.9.2 Beam Hole Photon Veto

The Beam Hole Photon Veto (BHPV) was placed at the most downstream of the KOTO detector subsystems. The BHPV consisted of arrays of 25 aerogel Čerenkov counters. Figure 2.27 shows a schematic view of a single BHPV module. Each BHPV module consisted of a lead plate as a photon converter, an aerogel block as a Čerenkov radiator, light-collecting mirrors, and PMTs.
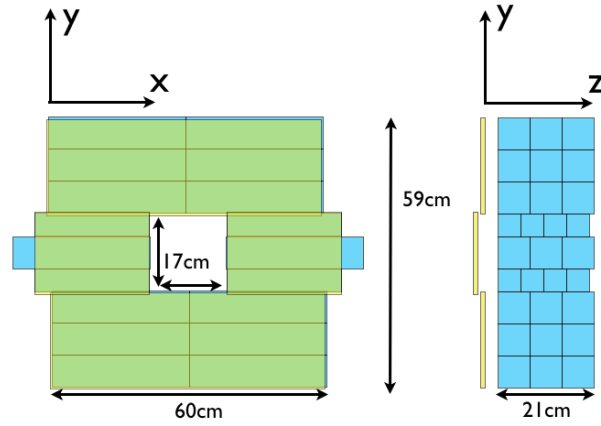
Figure 2.20: A schematic view of the CC04 detector.
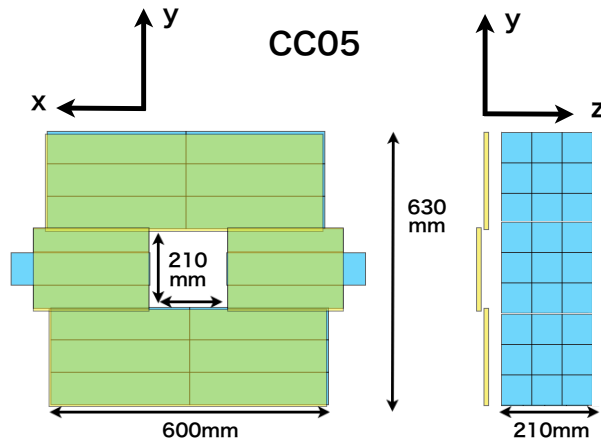
Figure 2.21: A schematic view of the CC05 detector.
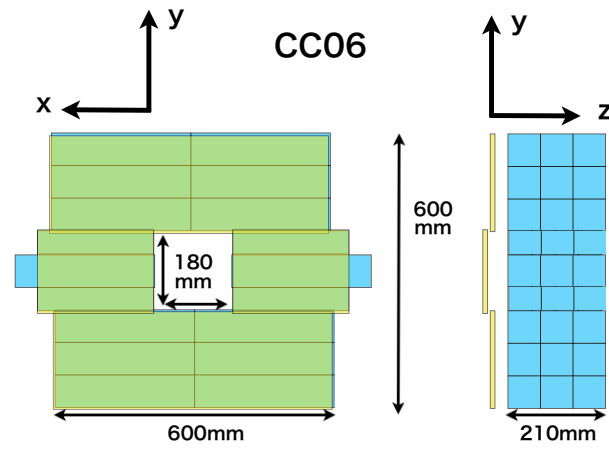
Figure 2.22: A schematic view of the CC06 detector.

Figure 2.23: A schematic view of an OEV detector module. This figure is taken from [26].

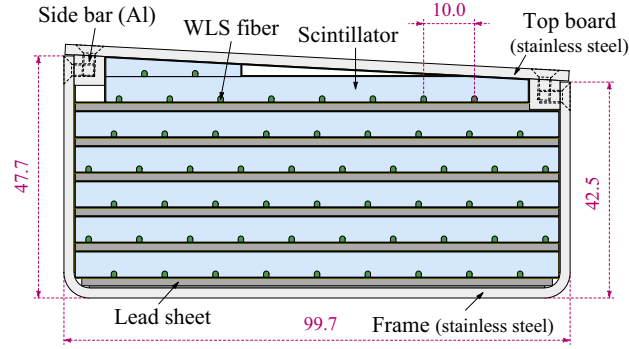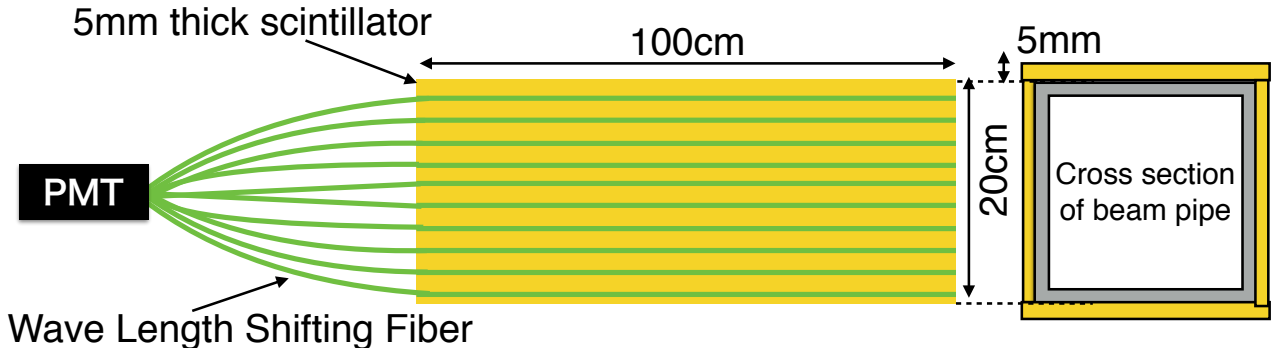
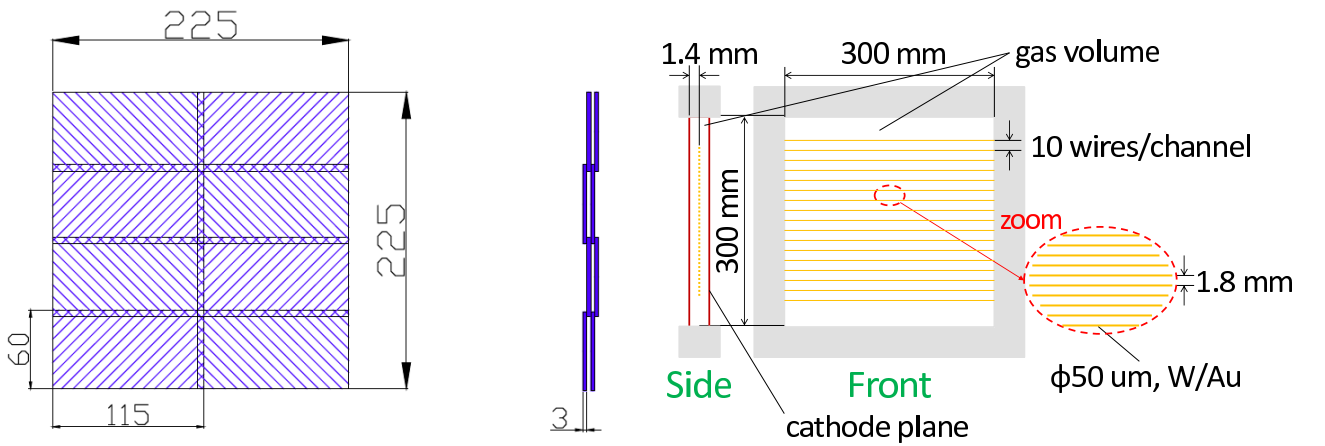Figure 2.24: A schematic view of the BPCV detector. This figure is taken from [36].

Figure 2.25: A schematic view of the BHCV detector used in 2013. BHCV consists of eight plastic scintillators.

Figure 2.26: A schematic view of a MWPC added as the new BHCV detector. This figure is taken from [37].

22

Figure 2.28 shows the layout and configuration of the BHPV detector with full 25 modules. The thickness of the lead converter and aerogel radiator for each module were optimized to achieve a high photon detection efficiency with low sensitivity to the neutrons. Only twelve modules were installed in 2013. Four more modules were additionally installed in 2015.
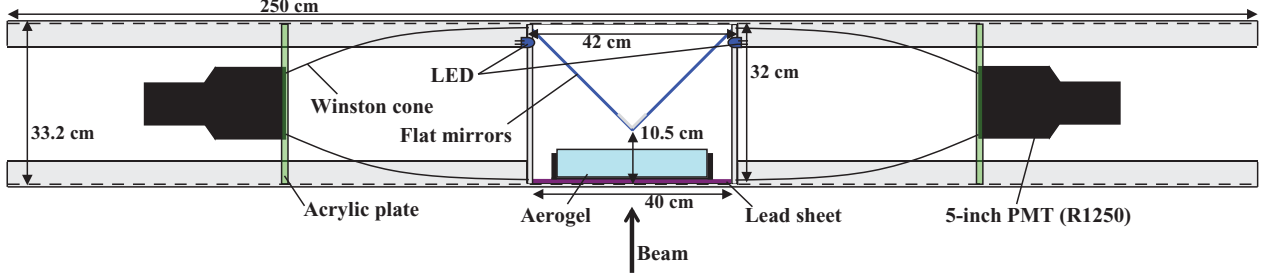
Figure 2.27: A schematic view of a single module of the BHPV detector. This figure is taken from [38].

Parameters for each module		
Module No.:	1-10	11-25
Thickness of lead sheets:	1.5 mm	3 mm
Thickness of aerogel:	2.9 cm	5.8 cm
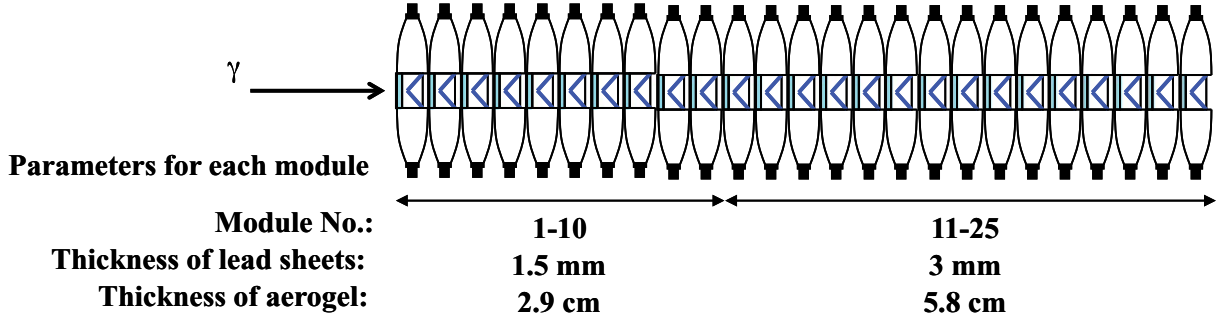
Figure 2.28: A schematic view of the BHPV detector. This figure is taken from [38].

2.3.9.3 Beam Hole Guard Counter

The Beam Hole Guard Counter (BHGC) is a photon veto detector subsystem placed behind the BHPV detector to detect the photons going through the edge region of BHPV. Figure 2.29 shows a schematic view and a layout of the BHGC. The BHGC consisted of four acrylic Čerenkov counters. Each counter was 120 mm wide and 500 mm long. A lead sheet was used as a photon converter and the acrylic plate was used as a Čerenkov radiator.

2.4 Gain monitoring system

To monitor the gain of PMTs and MPPCs, the light from LED or laser was distributed to the detectors. The CsI calorimeter, OEV, CC03 and CC04 used the laser system [31] to monitor their gains. Other veto detector subsystems used the LED to monitor their gains.

Figure 2.29: Left: A schematic view of the BHGC detector. Right: A layout of the BHGC detector with the BHPV detectors. The Black arrow indicates an example of a photon track to be handled by the Guard Counter. This figure is taken from [39].

2.5 Vacuum system

Most of the detectors must be located inside the vacuum to prevent decay particles from interacting with materials before detection. To achieve this, most of the detectors were 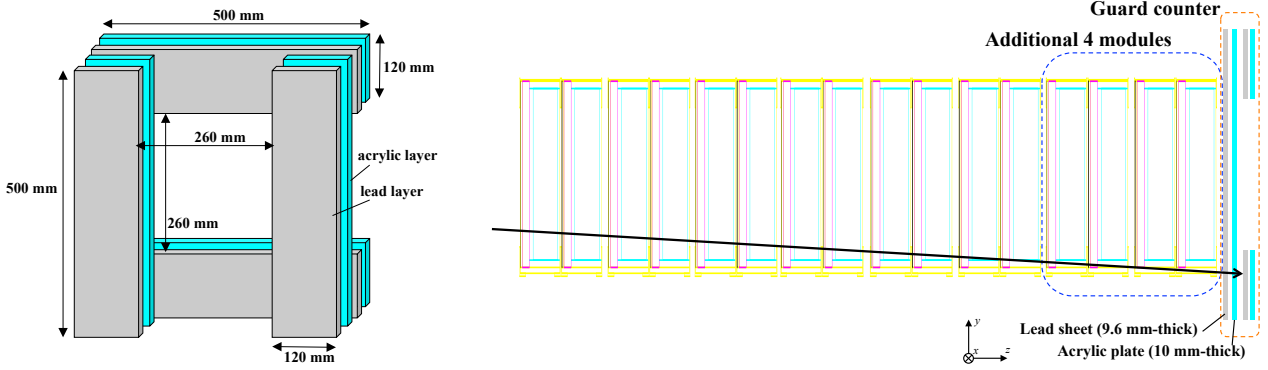placed inside a vacuum vessel. The output signals and HVs of the detectors inside the vacuum vessel were conducted through vacuum feedthroughs.

A vacuum level of 10^{-5} Pa was required for the decay region to suppress the background from the interaction between the neutrons in the beam and the residual gas. To achieve this high-vacuum level, thin membranes separated the decay region from the detector region which was expected to have outgassing from materials.

A vacuum system of KOTO experiment is shown in Fig. 2.30. During the data taking in 2013 and 2015, the decay region was evacuated to around 5×10^{-5} Pa while the detector region was evacuated to the vacuum level of 1 Pa.

2.6 Trigger and Data Acquisition System

The data acquisition system was required to have a 14-bit dynamic range for the energy measurement, a sub-nanosecond timing resolution, and capability to resolve overlapping events. A data acquisition system without dead time was also required to cope with the high counting rates expected for the detector. To satisfy these requirements, we designed new readout and trigger electronics systems based on a waveform digitization and a pipeline readout [40].

A total of about 4000 channels of output signals from the KOTO detector subsystems were digitized with 14-bit 125-MHz ADC modules and 12-bit 500-MHz ADC modules, and were stored in pipeline buffers inside Field Programmable Gate Arrays (FPGAs) on the ADC modules until a trigger decision was made. The digitized waveform information of each channel could be delayed in units of 8 ns so that signals of 4000 channels were time-aligned without long delay cables.

Three levels of the trigger systems used the waveform information to make a trigger decision of increased sophistication at each level. We will refer to these three levels of triggers as Lv1, Lv2, and Lv3 triggers.
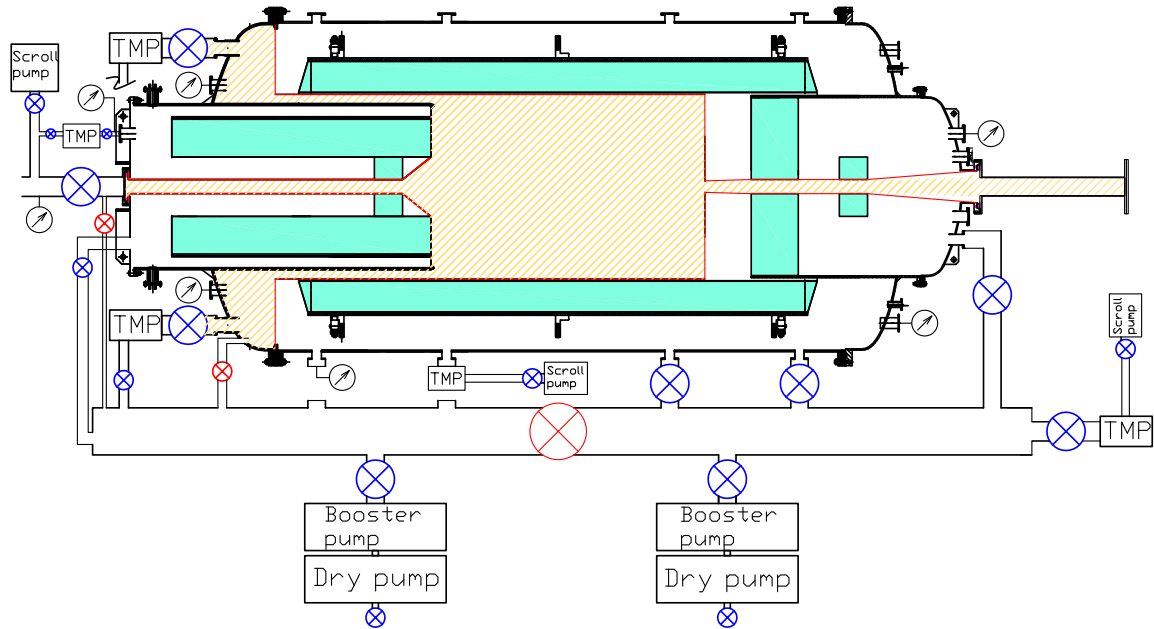
Figure 2.30: A schematic view of the vacuum system. Membranes separated the decay region in high vacuum (hatched region) and detectors region in low vacuum (hollow region). Red and blue ⊗ marks represent closed and opened valves, respectively.
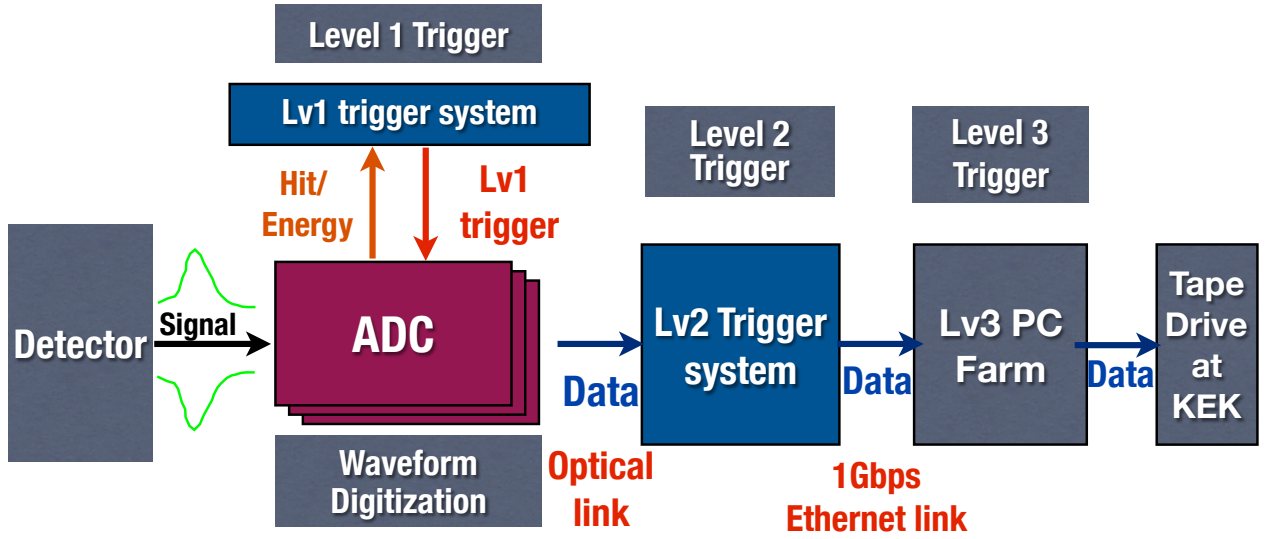
Figure 2.31: Schematic view of the KOTO data acquisition system.

Figure 2.31 shows a schematic view of the KOTO data acquisition system, and Fig. 2.32 shows the layout of the KOTO data acquisition system. In the Hadron Hall, the ADC system was placed near the detector, and the Lv1/Lv2 Trigger systems were placed outside of the concrete shield. A PC farm for the Lv3 Trigger was placed in the KOTO counting room located outside the Hadron Hall.

To reduce the effect from noise and widening of pulses during the transmission via cables, analog output signals from detectors except for CsI and CV were converted from a single-ended to a differential signal by converter modules placed near the vacuum feedthrough for the detector. CsI and CV had differential signals as analog output signals from detectors. Commercial Category-6a Ethernet cables were used as the analog signal cables. In each Ethernet cable, two shielded twisted pairs were used to transfer analog signals from two detector channels. The length of the signal cables for each detector subsystems was determined according to the location. The timing difference among detector subsystems due to different cable lengths was adjusted by delays inside the FPGA in the ADC modules.

The ADC system consisted of 16 6U VME64x crates, and each crate held 16 ADC modules. The system worked synchronously based on the trigger and clock signals sent from the Trigger system. These control signals were generated at the Lv1 Trigger system and sent to the Fanout system, placed inside the KOTO experiment area, via Category-6a cables. The fanout system distributed control signals to the ADC modules via Category-6a cables.

The trigger system consisted of two 9U VME 64x crates which stored the trigger modules for Lv1 and Lv2 trigger systems. Trigger and waveform information from the ADC system were sent to the Lv1 and Lv2 trigger systems via optical fibers. Two individual fibers were used to transfer data to the Lv1 and Lv2 trigger systems. Waveform information of events accepted by the Lv2 trigger was transferred to the Lv3 PC farm via a 1-Gbit Ethernet link with optical fibers. Waveform information of events accepted by the Lv3 trigger was transferred from the Lv3 PC farm to the KEK Computer Research Center in Tsukuba via the SINET4 network.
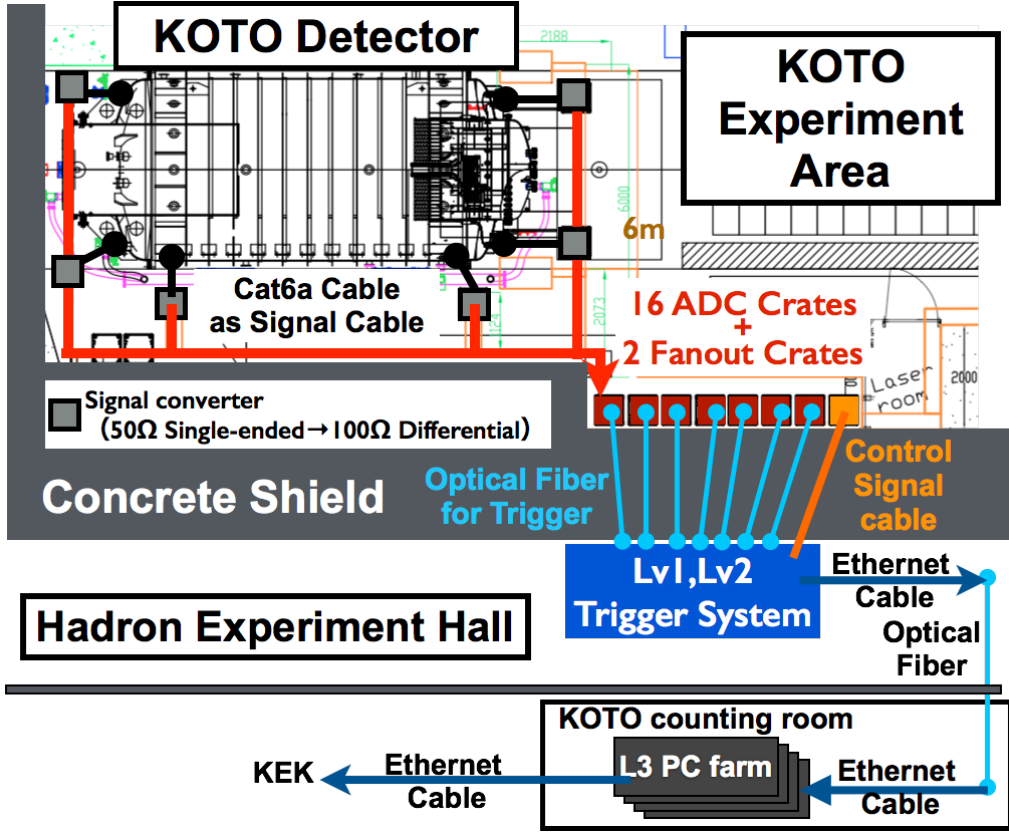
26

Figure 2.32: Layout of the KOTO data acquisition system at J-PARC.

2.6.1 ADC module

We designed a new 14-bit 125-MHz ADC module [41] and a new 12-bit 500-MHz ADC module [42] for the front-end electronics of KOTO to record the waveform from each detector channel. The ADC module is a 6U VME module. The detector subsystems located inside the beam, such as BHCV and BHPV, used 500-MHz ADC modules to cope with expected high counting rates, while most of detector subsystems used 125-MHz ADC modules.

2.6.1.1 14-bit 125-MHz ADC module

Figure 2.33 shows a schematic view of the 125-MHz ADC module. The ADC module can receive 16 differential analog signals via RJ45 connectors.

To record the waveform from about 4000 channels at a reasonable cost, we chose 14-bit 125-MHz ADC chip[2] for ADC modules. Figure 2.34 shows the signal from a CsI crystal with a photomultiplier tube, recorded by an oscilloscope. The leading edge of the photomultiplier signal was too fast for an 8 ns sampling. To increase the number of sampling points in the leading edge, we introduced a 10-pole Bessel filter before the ADC chip. The filter converted differential signals to single-ended signals, and widened the pulses in time to a Gaussian-shape with a FWHM of about 64 ns. Figure 2.35 shows the pulse shape recorded by the 125 MHz ADC module with the filter. With this technique, a timing resolution around 1 ns was achieved even with an 8 ns sampling [43, 44].
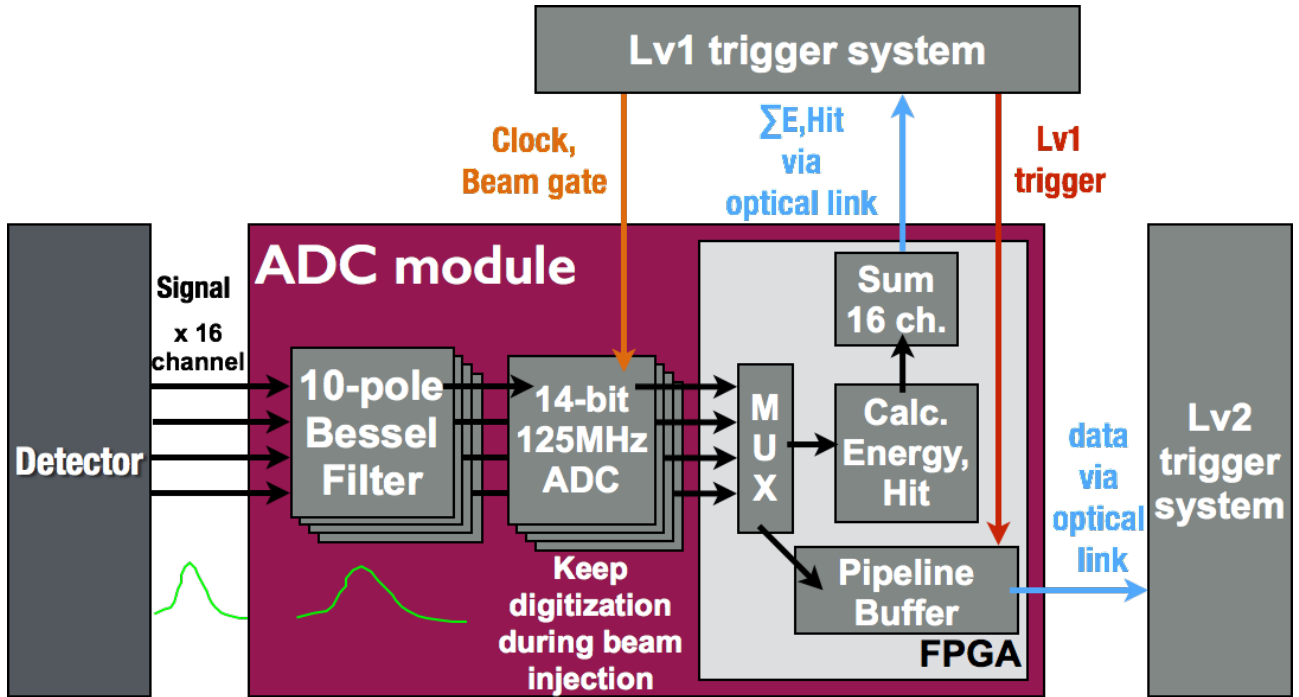
---

[2]Analog Devices AD9254

Figure 2.33: 14-bit 125-MHz ADC module with a 10 pole Bessel Filter.
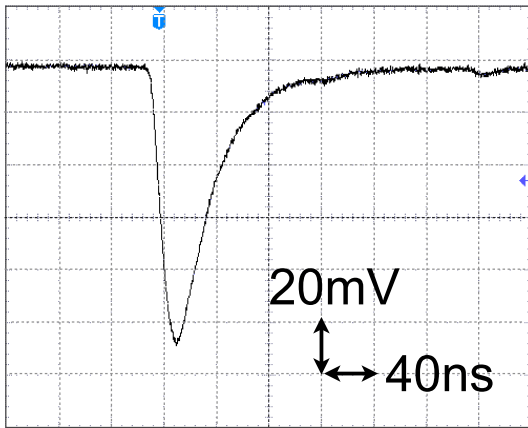

Figure 2.34: Signal from a CsI crystal with a photomultiplier tube recorded by an oscilloscope
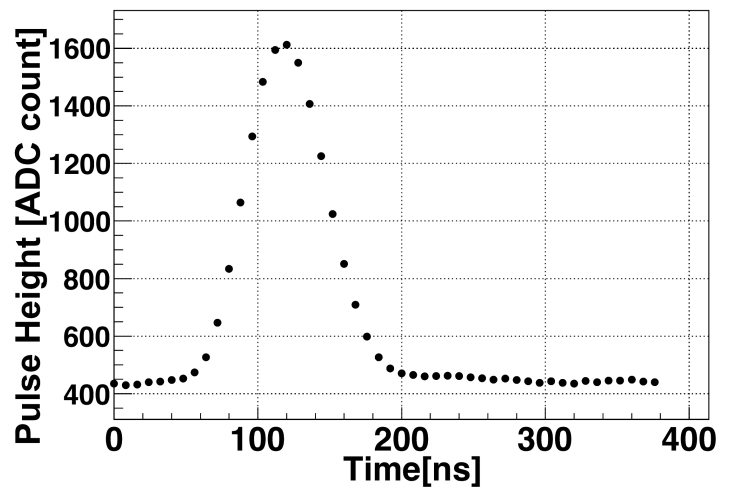

Figure 2.35: Recorded pulse shape by a 125MHz ADC with a 10 pole Bessel filter

28

All ADC modules digitized inputs synchronously based on 125 MHz clock generated by the Trigger system, and kept digitization during beam spills. After the digitization, the waveform information was sent to the FPGA[3] on the ADC module. The waveform information of each channel was delayed inside the FPGA in order to align the timing of channels in units of 8 ns. To avoid dead time, the digitized waveform data was stored in a 4-μs-long pipeline inside the FPGA while waiting for the Lv1 trigger decision. The trigger information such as the sum of energies from the 16 channels after pedestal subtraction [45] or the hit pattern of the 16 channels were calculated inside the FPGA every 8 ns.

The data output from each ADC module was sent to the trigger system via 2.5-Gbps optical-links. Each ADC module had two optical-link transceivers to send data to the Lv1 and Lv2 trigger systems individually. The trigger information was sent to the Lv1 trigger system every 8 ns. If the Lv1 trigger system decided to take the event, the waveform information with a fixed number of samplings in the timing window was saved as the event information and sent to the Lv2 trigger system after it exited the pipeline. In the runs in 2013 and 2015, we saved 64 samples. The ADC module also calculated the energy in each channel by integrating the waveform for a whole timing window of the event. This energy information was used to calculate $\sum_i E_i$, $\sum_i E_i x_i$, and $\sum_i E_i y_i$, where E_i, x_i, and y_i are the energy, x, and y positions of the CsI crystal assigned for i-th ADC channel, respectively. These sums were attached to the waveform information and sent to the Lv2 trigger system.

2.6.1.2 12-bit 500-MHz ADC module

The 12-bit 500-MHz ADC modules without shaping filter were used for BHCV, BHPV, and BHGC located inside the beam.

The 500-MHz ADC modules received 4 single-ended signal via LEMO connectors. Each input signal was digitized by 12-bit 500-MHz ADC chip[4]. The 500-MHz sampling clock was generated from 125-MHz system clock distributed by the trigger system, by Zero Delay PLL Clock Generator [5].

After the digitization, the waveform information was sent to the FPGA on the ADC module. The firmware of the 500-MHz ADC modules treated the 500-MHz sampling information from one channel as 125-MHz sampling information from four channels, allowing the 500-MHz ADC module to be integrated easily with 125-MHz ADC modules.

2.6.2 Trigger system

The KOTO trigger system consisted of three levels. The first two levels were implemented in custom designed hardware modules. The third level trigger was implemented in a computer farm.

The first two levels used the same type of hardware, which consisted of a 9U VME crate with a special P3 backplane and custom-designed 9U VME trigger modules.

The P3 backplane was the fourth backplane in addition to the three standard P0, P1, and P2 VME back planes. The custom designed P3 backplane connected adjacent trigger modules via a 24-bit-wide bus. Thirteen slots in a VME 9U crate had connections to the P3 back plane. We refer to this 24-bit connection as the "daisy-chain" and refer the slots with the connection

---

[3]Altera StratixII EP2S60F1020
[4]Texas Instruments ADS54RF63
[5]ICS8735-21

to the P3 back plane as the "daisy-chain slots". With the daisy-chain in this P3 backplane, we calculated the total sum of the variables in the trigger system. The detail of the P3 backplane and the daisy-chain will be described in Section. 3.

The trigger module was a 9U VME module. Each trigger module had two FPGAs[6], two 2-Gbit DDR2 SDRAMs, a Gigabit Ethernet port, a connection to P3 backplane, and optical links to receive information from up to 16 ADC modules. The Lv1 and Lv2 trigger modules used different firmwares.

In addition to the Lv1 and Lv2 trigger modules, the Lv1 and Lv2 trigger systems had trigger master modules, called MAster Control and TRigger Supervisor (MACTRIS), to make trigger decisions based on the information from the trigger modules. The MACTRIS was a 9U VME module with a FPGA[7], a connection to P3 backplane, LEMO connectors to receive the signals such as the beam extraction timing signal from accelerator, and two RJ45 connectors to exchange logic signals as differential LVDS signals. One of the two RJ45 connectors was used to distribute the control signals to ADC modules via Fanout system, and the other RJ45 connector was used to exchange the trigger signals with other electronics such as the laser and LED systems. The Lv1 Trigger system and Lv2 Trigger system used the MACTRIS with different firmware to use it as its own Trigger Master module.

2.6.2.1 Lv1 trigger system

The Lv1 trigger system was designed to make the Lv1 trigger with the rate of 100 kHz from the hits on the detector subsystems with the rate of up to 1 MHz. The Lv1 trigger decision was made every 8 ns, by requiring the total energy in the CsI calorimeter to be above a given threshold and no activities in the Veto detector subsystems.
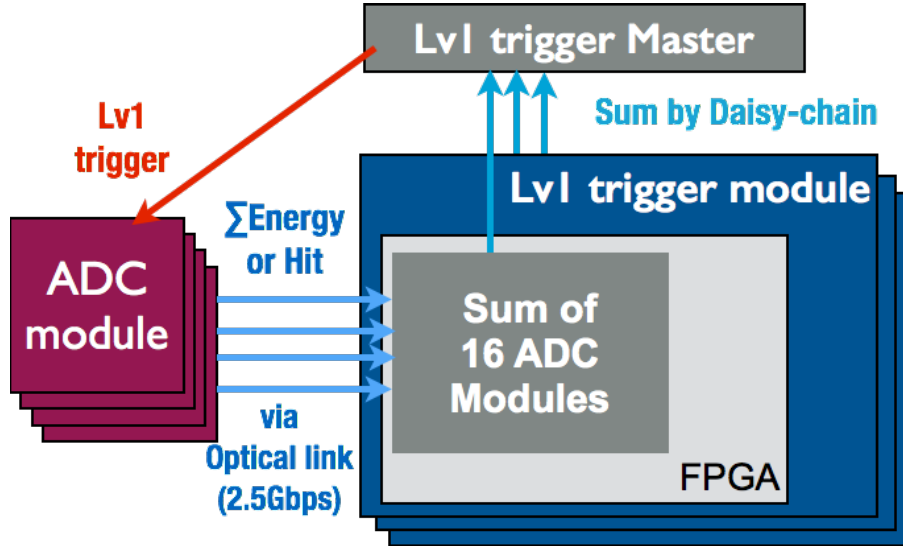

Figure 2.36: Lv1 trigger system with the optical link and daisy-chain.

Figure 2.36 shows a schematic view of the Lv1 trigger system. The Lv1 trigger system consisted of a Lv1 trigger master module and Lv1 trigger modules.

---

[6]Xilinx Virtex5 XC5VFX70 and Virtex4 XC4VFX12
[7]Xilinx Virtex5 XC5VFX30T

Each Lv1 trigger module received information from sixteen ADC modules via optical fibers and calculated the sum of energy deposits in the CsI calorimeter or generated the information of activities in the veto detector subsystems.

The Lv1 trigger master module received the total energy in the CsI calorimeter together with a summary of the informations of activities in all the veto detector subsystems, and made Lv1 trigger decisions. The detail of the Lv1 trigger will be described in Section. 3.

The decision was broadcasted to each ADC module which, in turn, saved the waveform information as it exited the pipeline and sent it to the Lv2 trigger module for a further trigger decision.

The latency to make the Lv1 trigger decision was about 1 μs, and it was shorter than 4 μs, the time that the pipeline held. The latency in the Lv1 stage did not make any dead time for the trigger system.

2.6.2.2 Lv2 trigger system

The Lv2 trigger system was designed to receive the events accepted by Lv1 trigger with the rate of 100 kHz and to make the Lv2 trigger up to about 10kHz. The Lv2 trigger decision was made based on the recorded waveform information for the event. The "Center of Energy (COE) radius" and of the number of photons in the CsI calorimeter were calculated at this stage. The COE radius is the distance between the beam axis and the energy-weighted-average position of all the showers which is represented by:

$$\text{COE radius} = \frac{\sqrt{\left(\sum_i E_i x_i\right)^2 + \left(\sum_i E_i y_i\right)^2}}{\sum_i E_i}, \tag{2.1}$$

where E_i, x_i, y_i are the energy, x, and y positions of i-th crystal in the CsI calorimeter, respectively.

The COE radius was used to select the events with a large transverse momentum P_T.

Figure 2.37 shows a schematic view of the Lv2 trigger system. The Lv2 trigger system received data packets of digitized waveforms from sixteen ADC modules via optical fibers. The data packets were stored on a buffer while waiting for the Lv2 trigger decision. When this buffer became full, the Lv1 trigger decision was suspended. This in turn caused dead time for the whole trigger system.

The COE radius for the full calorimeter was calculated via the daisy-chain bus similarly to the Lv1 trigger system. Each data packet of an event from an ADC module contained $\sum_i E_i$, $\sum_i E_i x_i$, and $\sum_i E_i y_i$ for 16 channels in the ADC module. Each Lv2 trigger module calculated these three energy sums for 16 ADC modules (256 channels). These three energy sum information for all the channels were calculated by summing these energy sums from all the Lv2 trigger modules. To calculate the sum over the Lv2 trigger modules, the daisy-chain bus was used.

The COE radius for the full calorimeter was calculated based on Eq. (2.1). A Lv2 trigger decision was made if the COE radius exceeded a given threshold. Data for events passing the Lv2 decision were stored on one of two 2-Gbit DDR2 SDRAMs while data on the other SDRAM were transferred to a computer farm via a 1-Gbps Ethernet.

The latency to make the Lv2 trigger decision with the COE calculation was about 8.5 μs if 64 samples were read out for each event. The latency included the time to read three sums and 64 samples of waveform information.
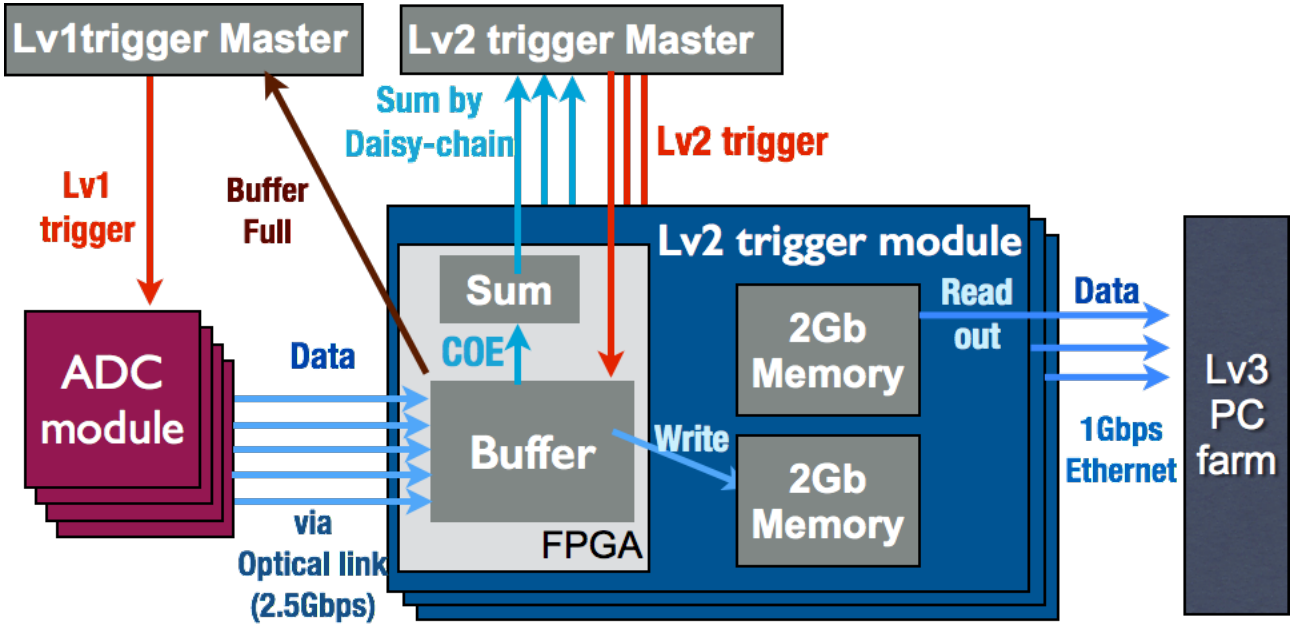
Figure 2.37: Lv2 trigger system which received data from ADC modules via the optical links and sent the data to the Lv3 PC farm via the 1 Gbps ethernet.

2.6.2.3 Lv3 Trigger system

The Lv3 trigger system was designed to handle the data of events accepted by the Lv2 trigger with the rate of 10 kHz and to make the Lv3 trigger with the rate of about 1 kHz. The Lv3 trigger decision was made by a computer farm. The computer farm collected the data packets from the Lv2 trigger modules and built events.
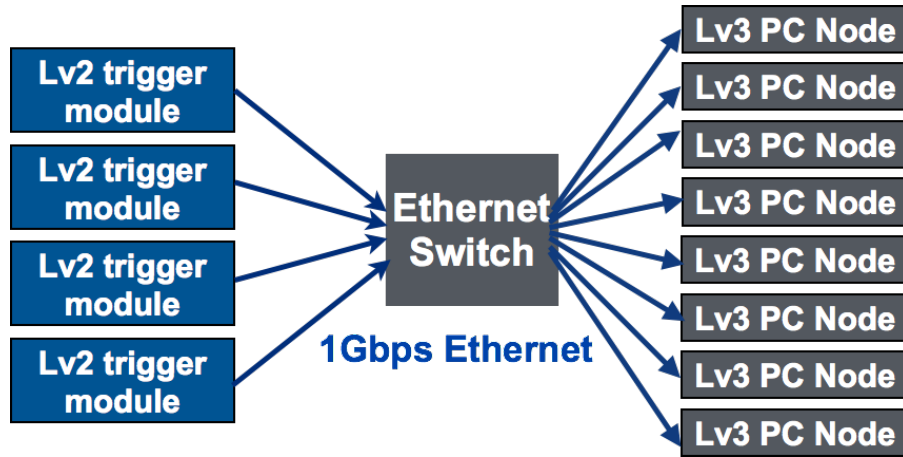

Figure 2.38: Event building by the Ethernet switch.

Figure 2.38 shows how the events were built at the Lv3 trigger system through an Ethernet Switch. The Lv2 trigger modules sent the data packets to a different Lv3 PC node according to its event number. The selected node thus received the full information for a given event.

The Lv3 trigger decision was made by using fully reconstructed events. At present, no data selection cuts has been implemented, and only the data compression was implemented. A lossless bit-packing algorithm was used for the data compression. The waveform informations

32

were encoded to a 14 bit word for the minimum value of the recorded waveform and the words with less number of bits to record the difference from the minimum value. Its compression ratio was 0.25.

The events which passed all the trigger decisions were first stored in the Lv3 PC farm and later sent to KEK via SINET4 network.

2.7 Data taking

2.7.1 DAQ operation in the beam time

Figure 2.39 shows the operation cycle of the KOTO DAQ system. The DAQ system synchronized with the beam extraction cycle. In the the 30-GeV protons were extracted from the MR over 2 s and hit the T1 target. The beam was extracted every 6 s in the runs before the summer of 2015 and 5.52 s after then. The beam extraction timing was given by a signal provided from the MR group and the Hadron beam line group. This beam extraction timing was used to generate a 4.3-s-long "LIVE" signal. The DAQ system collected data only during this LIVE signal. The first 2 s of the duration of LIVE signal with beam extraction was called "On-spill" and used to collect data related to beam. The later 2.3-s duration without beam extraction was called "Off-Spill" and was used to collect data with cosmic-ray muons, laser, and LED events for calibration.
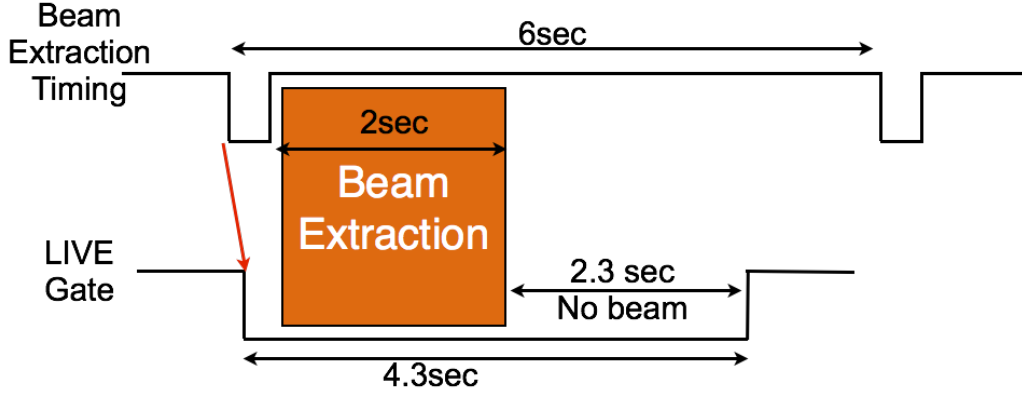
Figure 2.39: The operation cycle of the KOTO DAQ system.

2.7.2 Trigger condition

To conduct the data taking during beam time, several types of triggers were developed. In addition to the physics trigger for $K_L \to \pi^0 \nu \overline{\nu}$, there were the triggers for normalization, calibration, and other purposes. To collect physics-triggered events and other types events simultaneously while keeping the trigger rate within the bandwidth of the trigger system, prescaling feature was introduced. Different prescaling factor was applied to each type of trigger.

2.7.2.1 Physics trigger

To record the events from $K_L \to \pi^0 \nu \bar{\nu}$ decays, we required large P_T for two-photon system incident on the CsI calorimeter, and no activities in the other detector subsystems. To achieve these requirements with the hardware-based trigger system, online veto was used in the Lv1 trigger and the cut on COE-radius was used in the Lv2 trigger for the phsyics trigger. The requirements on the Lv1 and Lv2 trigger systems are shown in Table 2.2.

At first, the CsI trigger was generated based on the total energy of the CsI calorimeter. During the physics data taking in 2013 with the beam power of 23.8 kW, the number of triggers satisfying the total energy condition was 258k triggers/spill, which corresponds to 129 kHz for the 2 s of beam extraction. Total energy deposits in MB, CV, NCC and CC03 were used in online veto for the physics trigger. After imposing these Veto cuts, the number of triggers was reduced to 27k events/spill (14 kHz).

After imposing COE cuts at the Lv2 Trigger stage, the number of triggers was reduced to 5k events/spill (2.5 kHz).

Table 2.2: A list of requirements in the Lv1 and Lv2 trigger systems.

Lv1 Trigger system	
Main Trigger	
CsI	>550MeV
Online Veto	
NCC	<60MeV
MB	<50MeV
CV	<0.8MeV
CC03	<60MeV
Lv2 Trigger	
COE radius	>120mm

2.7.2.2 Normalization trigger

To collect the $K_L \to 3\pi^0$, $K_L \to 2\pi^0$, and $K_L \to \gamma\gamma$ decay events for normalization used in the analysis, the normalization trigger was made by removing COE-radius cut from the physics trigger.

2.7.2.3 Minimum Bias trigger

To take the data with minimum bias, a trigger based only on the total energy of CsI calorimeter without any online veto was made. This trigger is called "Minimum Bias Trigger"

2.7.2.4 $K_L \to 3\pi^0$ trigger

The six photons from $K_L \to 3\pi^0$ hitting the the CsI calorimeter were used for the calibration of the CsI calorimeter. To enhance the fraction of events with six photon clusters on the CsI calorimeter, a hardware cluster-counting logic was used. As shown in Fig. 2.40, the CsI calorimeter was divided into twelve regions. The number of regions with its energy deposit exceeding a certain threshold was counted as the number of hit regions, N_{region}. For the

$K_L \to 3\pi^0$ trigger, we required $N_{region} > 4$. The detail of the hardware cluster-counting trigger is described in Section 3.4.
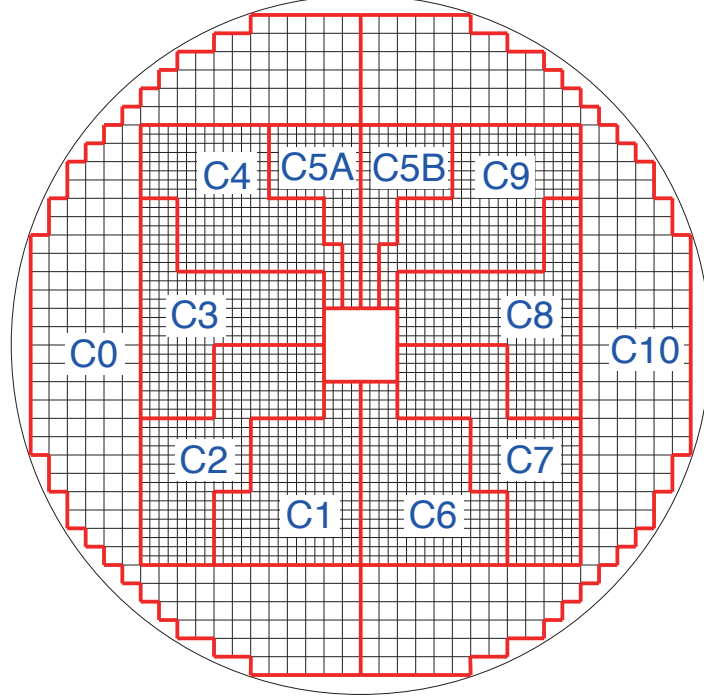

Figure 2.40: Schematic view of the CsI Crystals with 12 regions for the Cluster Counting Trigger. Each region has its own Lv1 CsI Trigger module. The number in each region following the letter "C" represents the ID of ADC crate assigned to the region. The region covered by the ADC crate No.5 was divided into two regions to split all the CsI calorimeter channels into two parts.

2.7.2.5   Gain Monitoring trigger

The trigger signal from the gain monitoring system was used to take the events with flashing LED and laser. The flashing rates of LED and laser triggers were 10 Hz and 5 Hz, respectively. The data taken with these triggers were used for monitoring the gain of PMTs and MPPCs, and also used for monitoring and adjustment of timing offsets between detector modules.

2.7.2.6   Cosmic-ray trigger

For the calibration of the detector, the triggers to take events with cosmic-ray muons were developed for NCC, CsI calorimeter, and OEV. The total energy information was used for NCC and CsI. The number of modules with large energy deposits was used for OEV. The cosmic-ray triggers were enabled only during the off-spill time.

2.7.2.7   Random trigger and Accidental trigger

A 10-Hz clock trigger was used as the random trigger to check the noise and the counting rates of detector channels.

To check the effects from the accidental hits on the detector, a trigger from the detector looking at the T1 target, called " Target Monitor", was used to collect the events with accidental hits related to the beam. Figure 2.41 shows the location of the Target Monitor. The target Monitor is a telescope-type counter made of two layers of plastic scintillators located in the 50° direction respect to the primary beam line.
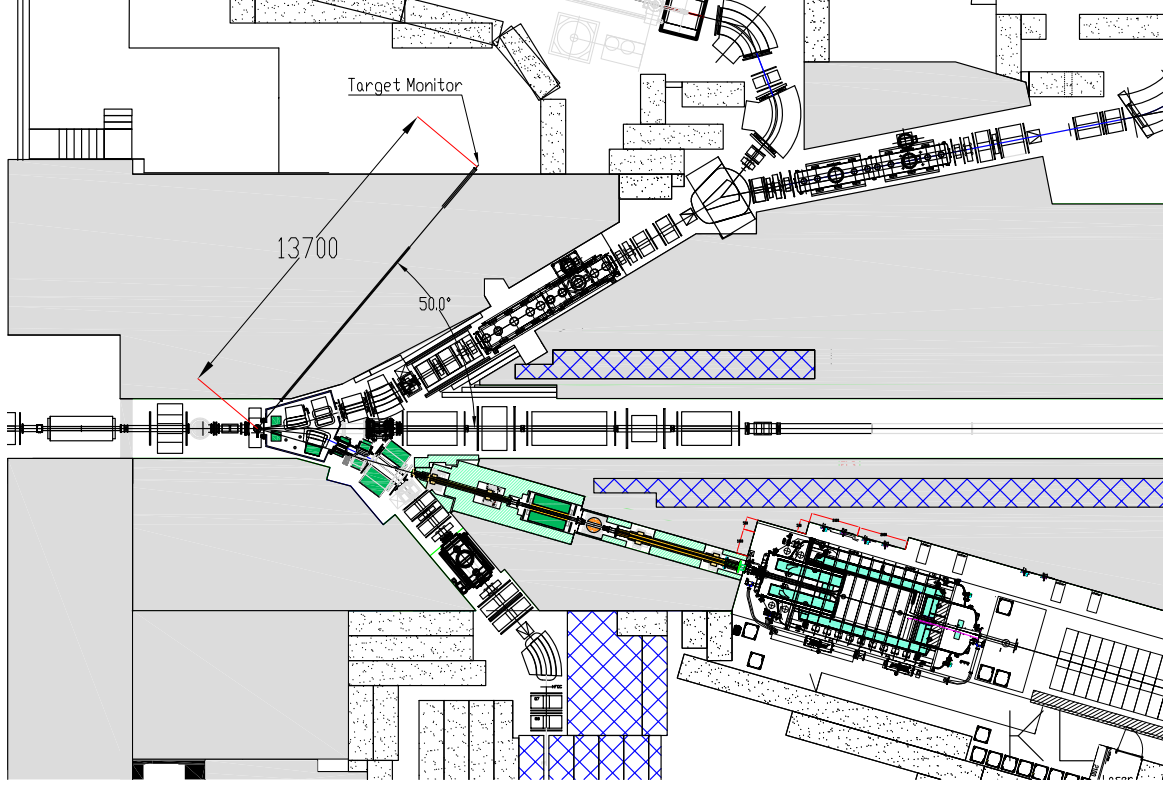
Figure 2.41: Target Monitor looking at the T1 target.

2.7.3 Run Condition

2.7.3.1 Physics run

In the physics run in 2013, data was taken with physics triggers. Other triggers for normalization and calibration were used simultaneously after prescaling. The list of trigger types used during the physics run in 2013 and the typical trigger rates are shown in Table 2.3.

The total number of Lv1 trigger per spill was 28k triggers/spill while only 23k triggers/spill were accepted and recorded. This 17% loss was coming from the dead time in the Lv2 trigger system.

2.7.3.2 Beam muon run

By closing the beam plug, most of the secondary particles from the T1 target were stopped in the beam plug and only high energy muons could enter the detectors. Those muons penetrating the detector subsystems could be used for calibration as minimum ionizing particles. To collect the events with penetrating muons, the coincidence of the collar counters such as NCC, CC04,

Table 2.3: A list of trigger rate per spill for each type of trigger in the Lv1 and Lv2 trigger systems. Note that sum of each trigger type is not matched with the actual total trigger rate because some triggers can be issued at the same time.

Type	Raw Trigger	Prescaling Factor	Lv1 Trigger		Lv2 Trigger
			Requested	Accepted	Accepted
Detector Trigger					
Physics	27,000	1	27,000	22,000	5,000
Normalization	27,000	30	900	700	700
Minimum Bias	258k	300	900	700	700
$K_L \to 3\pi^0$	4000	10	400	300	300
Cosmic	250	1	250	200	200
External Trigger					
Laser/LED	70	1	70	60	60
10-Hz Clock	50	1	50	40	40
Target Monitor	128k	1200	100	80	80
Total			28,000	23,000	7,500

CC05, and CC06 were used. The triggers made by BHCV and BHPV were also used to collect the muons penetrating them.

2.7.3.3   Al target run

KOTO detector system had Aluminum plates which could be inserted in the beam region as a production target for several purposes. The aluminum plates were kept out from the beam during normal data taking.

Figure 2.42 shows the illustrations of the aluminum plates inserted in the beam for special data taking. Two aluminum plates were placed at different positions for different purposes.

A 5-mm thick aluminum plate was inserted in the beam at the downstream of the FB to generate $\pi^0 \to 2\gamma$ for the calibration of the CsI calorimeter. Because the z-position of the Aluminum production target is known, we can reconstruct the invariant mass of two photons with a known decay vertex position. This Aluminum plate is called "Decay Volume Upstream Al target" and the data taking with this target is referred to as "Decay Volume Upstream Al target run".

A 10-mm thick aluminum plate was inserted in the beam at the upstream of the FB to enhance the neutrons hitting the CsI calorimeter for the study of the background caused by them. Because most of photons and charged particles were stopped or detected by FB and NCC, only the events with scattered neutrons hitting the CsI calorimeter were collected. This aluminum plate is called "Z0 Al target" and the data taking with this target is referred to as "Z0 Al Target run".

2.7.3.4   cosmic-ray muon run

To calibrate detector subsystems with cosmic-ray muons as a minimum ionizing particles, cosmic-ray muon runs were taken before and after the beam time. The triggers made from CsI calorimeter, NCC, MB, CC04, CC05, CC06, and OEV were used for data taking.
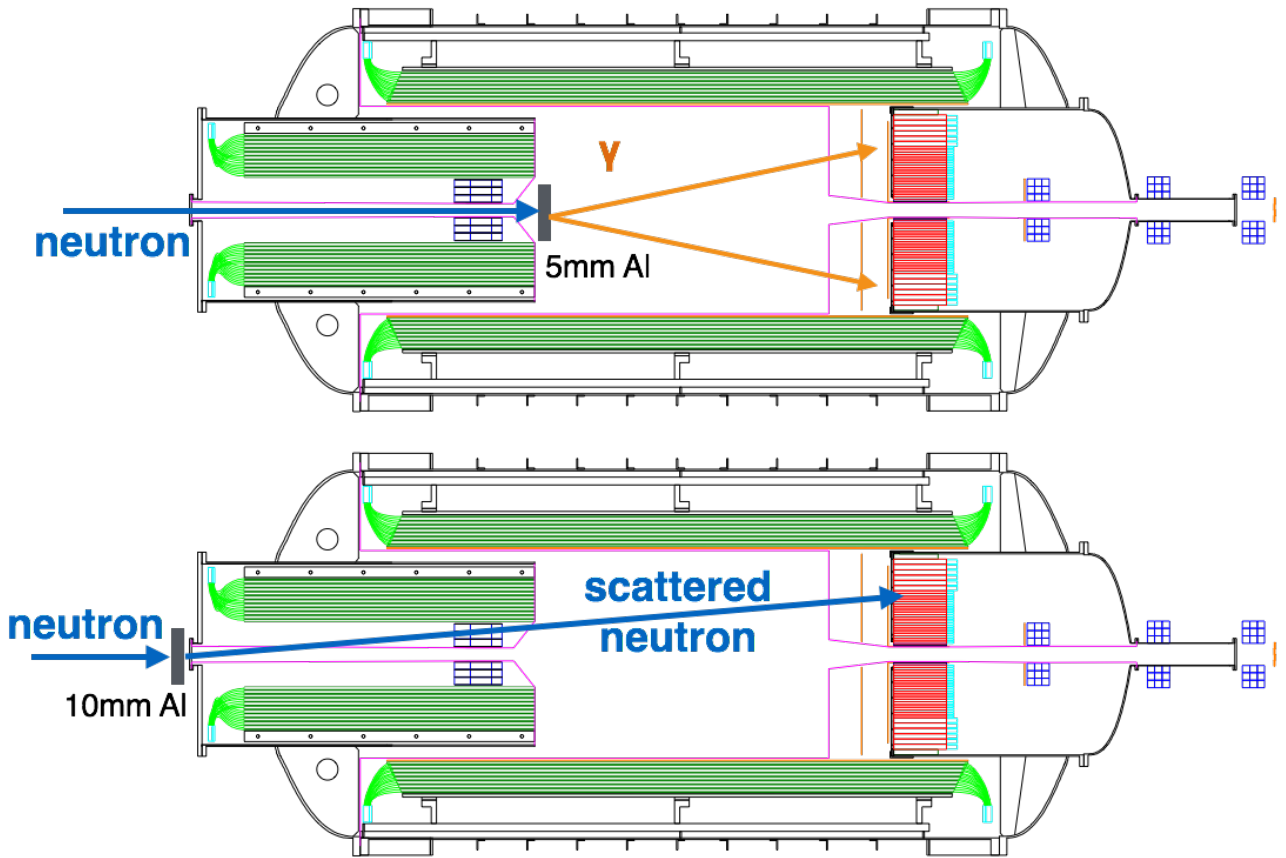
Figure 2.42: Illustration of the aluminum plates inserted into the beam. Top: A 5-mm thick aluminum plate was inserted in the beam at the downstream of the FB to generate $\pi^0 \to 2\gamma$ for the calibration. Bottom: A 10-mm-thick aluminum plate was inserted in the beam at the upstream of the FB to collect the neutrons hitting the CsI calorimeter for the study of background caused by them.

2.7.4 Beam Operation

The data taking periods are distinguished by the operation cycle of the J-PARC MR, which is expressed as "Run". KOTO experiment conduct the physics data taking during the operation cycle Run 49 in 2013, Run 62~65 in 2015.

KOTO experiment completed the construction of detector system including the downstream detector located outside of the vacuum vessel in April, 2013. During the operating cycle Run 49, protons were delivered to the HD-hall between April 28 and May 2, and between May 13 and May 23, 2013. The slow-extraction of protons to HD-hall was originally planned until the end of July. However the beam delivery was stopped at May 23, 2013 due to a radioactive material leak accident [46, 47]. During Run 49, the KOTO experiment conducted the first physics data taking for 100 hours between May 19 and May 23. The intensity of extracted proton beam was 23.8 kW which corresponds to 3.0×10^{13} protons on T1-Target (P.O.T) in each spill.

After the renovation works at the HD-hall, the delivery of protons to HD-hall was resumed on the April 24th, 2015. The KOTO experiment conducted the physics data taking during Run 62~65 in 2015.

Table 2.4 shows the list of physics data taking in the operation cycles Run 49, Run 62~65.

In this thesis, the data taken in the operation cycles Run 49, Run 62, and Run 63 were used.

Table 2.4:   A list of physics data taking periods in the operation cycle Run 49, Run 62~65.

Operation Cycle	Beam Power	duration	Total hours	Number of Protons On T1-Target	
				delivered	recorded
Run 49	23.8 kW	May 19, 2013 ~ May 23, 2013	100	1.42×10^{18}	1.188×10^{18}
Run 62	23.8 kW ,26 kW	April 24, 2015 ~ May 7, 2015	159	3.05×10^{18}	2.36×10^{18}
Run 63	26 kW, 29 kW, 33 kW	June 5, 2015 ~ June 26, 2015	215	4.97×10^{18}	3.69×10^{18}
Run 64	31.7 kW, 32.7 kW, 38.0 kW, 39.0 kW	October 15, 2015 ~ November 12, 2015	254	6.60×10^{18}	5.42×10^{18}
Run 65	38.6 kW, 41.5 kW	November 14, 2015 ~ December 18, 2015	548	1.60×10^{19}	1.33×10^{19}

Chapter 3

Improvements on Trigger system

In this chapter, I will describe the improvements on KOTO data acquisition system which I have developed and which were required for the physics runs.

The studies and developments described in this chapter were done by the collaboration with Dr. M. Tecchio of University of Michigan.

3.1 Requirement on Lv1 Trigger system to conduct physics data taking

The Lv1 trigger system was originally developed as the trigger system for the CsI calorimeter. The requirements for Lv1 trigger system to conduct physics data taking were the followings:

1. Implementation of cut using Veto detector subsystems to keep the Lv1 trigger rate under 15 kHz.

   As shown in Fig. 2.31, the KOTO trigger system consisted of three levels. With the configuration of hardwares in 2013, we had to keep the total Lv1 trigger rate under 15 kHz to keep the total Lv2 trigger rate under 4 kHz. This limitation came from the size of the memory in the Lv2 trigger modules to store the waveform data of the events. [1] The trigger rate of the CsI calorimeter trigger was about 100 kHz with the beam power of 20 kW. The integration of Veto detector subsystems and implementation of cuts using them were thus required to reduce the Lv1 trigger rate.

2. Implement a special trigger to collect $K_L \to 2\pi^0$ and $K_L \to 3\pi^0$ decay events.

   The $K_L \to 2\pi^0$ and $K_L \to 3\pi^0$ decay events were used to calibrate the CsI calorimeter and other detectors. However, most of these events were rejected by "COE radius cut" at the Lv2 trigger stage. Also, the trigger based on the Total Energy of CsI was not efficient enough to select these events. More sophisticated trigger to accumulate the $K_L \to 2\pi^0$ and $K_L \to 3\pi^0$ decay events was thus required.

3. Simultaneous data taking with multiple types of trigger conditions.

---

[1] The event data size in each Lv2 Trigger module was 30kB/Lv2 Trigger module/event in Run 49, Run 62, and Run63. With this event data size, the memory can hold the data of event for up to 8-k events which pass Lv2 Trigger cut and this corresponds to around 4-kHz Lv2 generated triggers for 2-s beam extraction.

As described in Section 2.7.2, the trigger system was required to take data with multiple types of trigger conditions at the same time for calibration, normalization, and for studying trigger biases.

4. Make flexible trigger logic to accommodate the demands at the experimental site.

The combination of detectors used in the trigger decision can be different between the physics runs and other special runs such as Beam-muon run and cosmic-muon run. There may be unexpected special runs with different trigger conditions. To accommodate such demands to change the combination of detector in trigger decision at the experimental site, the trigger logic was required to be flexible and modifiable.

3.2 Original design of Lv1 Trigger system

In this section, I will describe the original design of Lv1 trigger system based on the total energy of the CsI calorimeter. The modification to this system to conduct physics data taking will be described in following sections.

3.2.1 P3 backplane with daisy-chain

As described in Section 2.6.2, the Lv1 trigger system consisted of a 9U VME crate with a special P3 backplane and custom-designed 9U VME trigger modules.

Figure 3.1 shows a schematic view of a special P3 backplane. Thirteen slots in the VME9U crate had connection to the P3 backplane. The Lv1 trigger master module sat at the center of the backplane and twelve Lv1 trigger modules for the CsI calorimeter were divided into left bank and right bank of the backplane. The P3 backplane had two types of links between Lv1 trigger modules: 24-bit interconnection between adjacent modules and Peer-to-Peer serial connection between Lv1 trigger module and Lv1 trigger master module. With this 24-bit interconnection, the trigger module could receive information from a neighboring module, and pass information to the next module. We refer to this connection as the "daisy-chain" and refer the slots with the connection to the P3 back plane as the "daisy-chain slots". With this daisy-chain, we could calculate the total sum of energy by summing its energy to the energy received from a neighboring module, and passing the sums to the next module. The summing was performed from the left and right-most end modules to the trigger master module located at the center of the crate. Because the daisy-chain connection was done between adjacent modules, the daisy-chains in the left and right banks of the P3 backplane were independent.

In addition to summing via the daisy-chain bus, each Lv1 trigger module could send signal directly to Lv1 trigger master via Peer-to-Peer serial links.

3.2.2 Trigger system to calculate the total energy of CsI calorimeter.

Figures 3.2 and 3.3 show how the Lv1 trigger system and modules calculated the total energy in the CsI calorimeter.

At first, each ADC module calculated the sum of energies over its all sixteen input channels every 8 ns and sent it as 16 bit information to the Lv1 trigger module via optical link. During the calculation of the sum of energies, the pedestal was subtracted from the sum of energies [45].
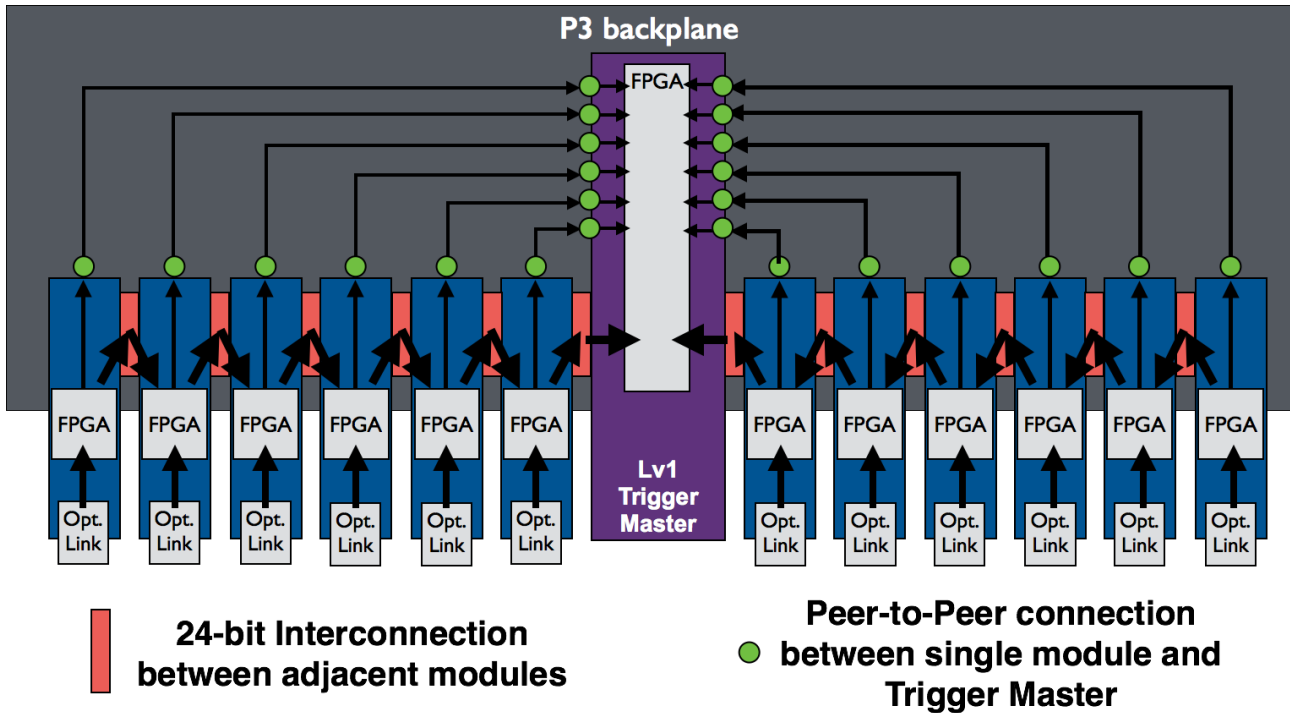
Figure 3.1: Special P3 backplane with daisy-chain bus and peer-to-peer links.

Each Lv1 trigger module received information from sixteen ADC modules via optical fibers and calculated the sum of the energies in the 256 channels of the CsI calorimeter. The energy information of the CsI calorimeter was summed up inside each Lv1 trigger module first and subsequently summed over all the Lv1 trigger modules via the daisy-chain in the P3 backplane. The Lv1 trigger module received information from the module in the outer neighboring slot, and summed it with its own information, and sent it to the module in the inner neighboring slot using the daisy-chain bus. With this scheme, the Lv1 trigger master module received the total energy in the CsI calorimeter.

3.2.3 Peak Finding Logic

To suppress the pulse height dependence of the trigger timing, a peak finding logic was used to make triggers from the total energy deposit in the CsI calorimeter. Figures 3.4 and 3.5 show how the logic worked to find the peak. Peak finding was done by comparing the current value and the value in the previous clock. Peak finding logic was enabled during the time when the total energy deposit in the CsI calorimeter exceeded a given threshold.

3.2.4 Performance

Performance in online information

Figures 3.6 and 3.7 show the pulse height of the waveform of the sum of all CsI calorimeter channels at trigger timing recorded in the trigger system. The threshold for the pulse height was set to 4889 ADC counts. Clear edge can be seen in the pulse height recorded in the trigger system.

Figure 3.8 shows the ADC waveform of sum of all CsI calorimeter channels. Because the waveform of sum of all CsI calorimeter channels fluctuated event by event, the pedestal must
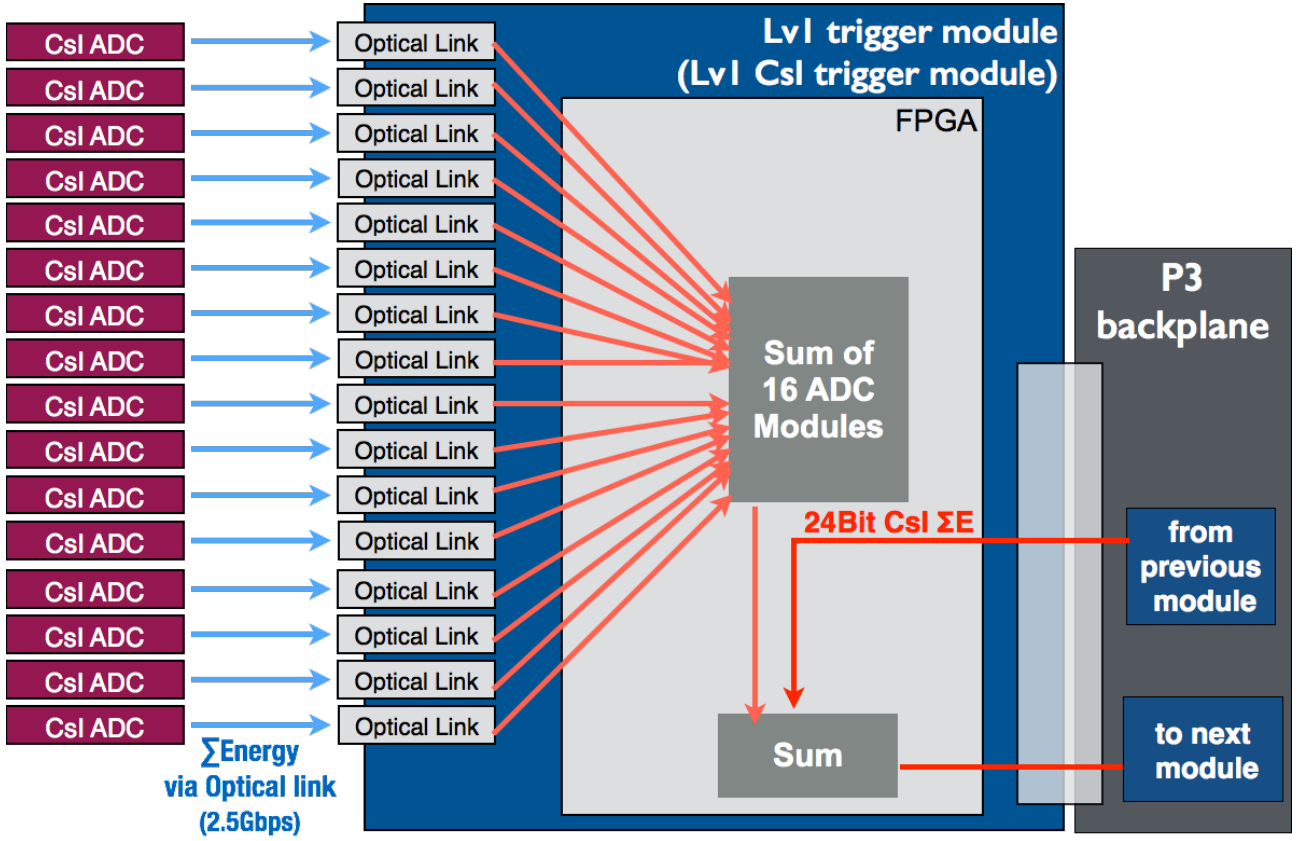
Figure 3.2: Original design of the Lv1 Trigger module to make CsI trigger.

be subtracted from the waveform to evaluate the performance to make trigger decision. In the trigger system, pedestal in each channel was tracked by ADC modules and subtracted from the energy sum information. Because the information about the pedestal used in the energy sum calculation was not recorded, the average of first 10 samples was used as the pedestal value and subtracted from the waveform to evaluate performance. Figure 3.9 shows the difference between the average of first 10 samples and the average of 64 samples for summed waveform of all the CsI calorimeter channels in the events taken by clock trigger. The standard deviation of the distribution was 90 ADC counts. This suggests that the pedestal of the waveform of sum of all CsI calorimeter channels can fluctuate within 90 ADC counts from the global pedestal. Because the logic implemented in the ADC module to track the pedestal was made to track the change of global pedestal, this pedestal fluctuation can affect not only the pedestal used in making this figures but also the pedestal calculated by ADC module to calculate the energy sum.

Figure 3.10 shows the waveform of sum of all the CsI calorimeter channels after the average of first 10 samples was subtracted as pedestal. Most of events had the pulse height higher than pedestal. The smeared edge of the pulse height at the trigger timing can be explained by the fluctuation of pedestal used in making this figures and pedestal calculated by ADC module to calculate the energy sum.

Because the trigger timing is determined by the peak timing of the varying energy information, the peak timing of the waveform of sum of all the CsI calorimeter channels should be distributed at the same timing inside the event window. Figure 3.11 shows the peak timing. Because most of events had peak timing at the 31st clock inside the event window, the trigger
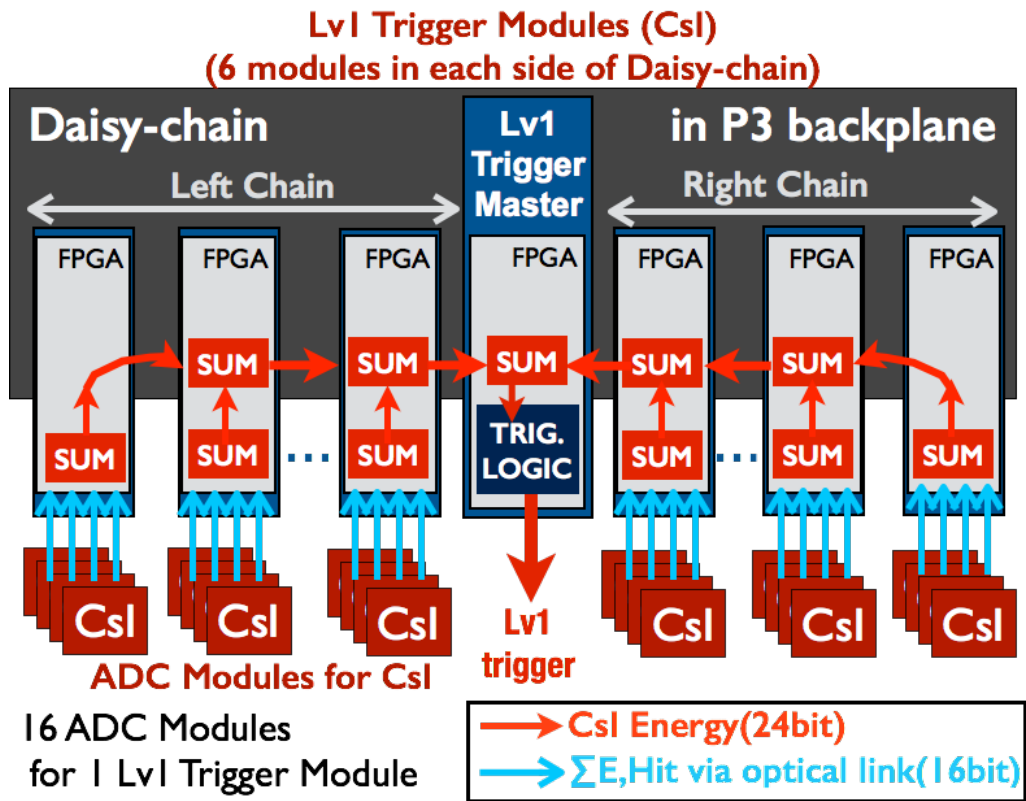
Figure 3.3: Original design of the Lv1 Trigger system to make CsI trigger.
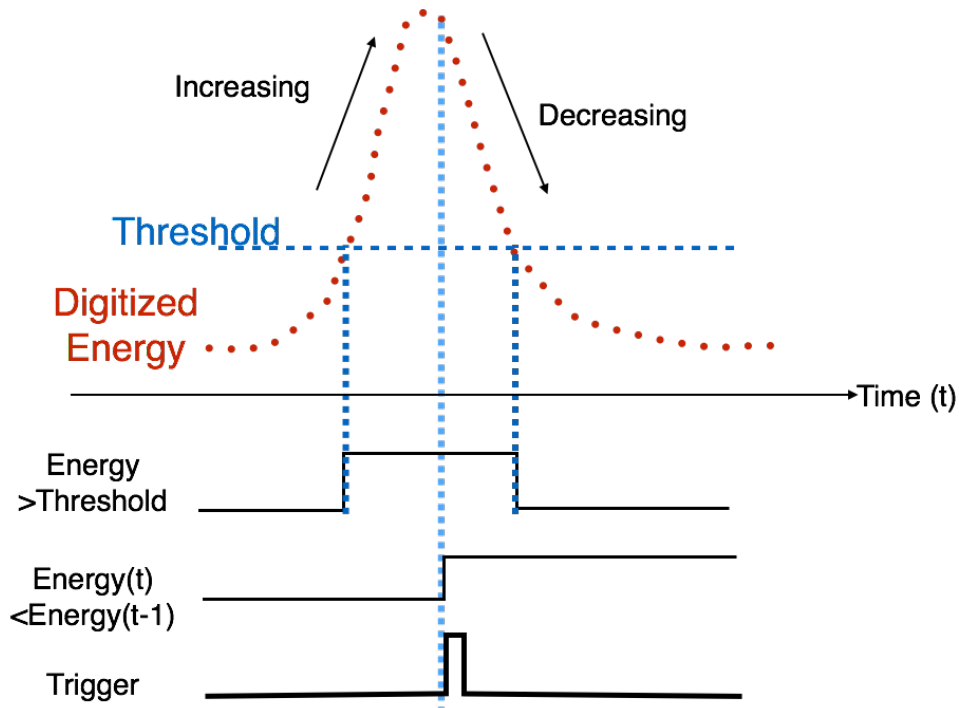
Figure 3.4: Logic to find a peak from varying energy information.
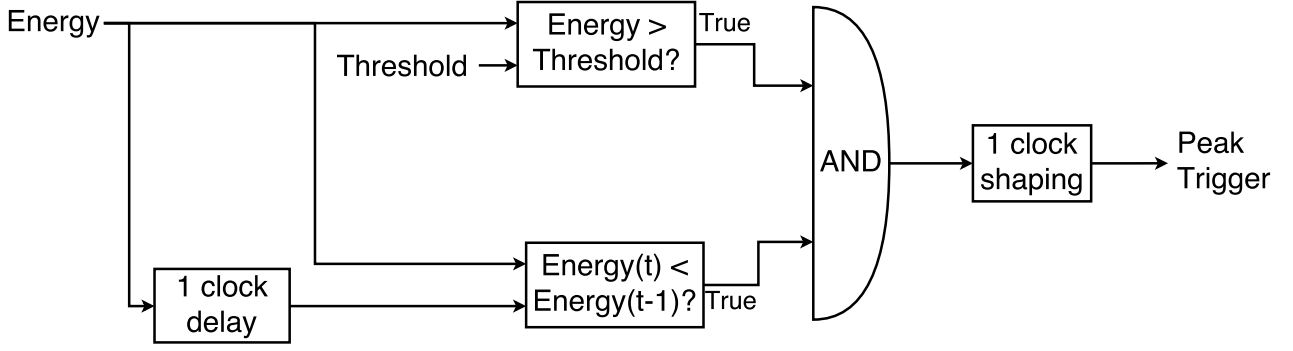
Figure 3.5: Implemented logic to find the peak from varying energy information.

timing was considered to be located at the 31st clock. There were events with peak timing $1 \sim 2$ clocks far from trigger timing. This timing fluctuation can be explained if there was timing jitter between trigger modules or two daisy-chain banks within spills.
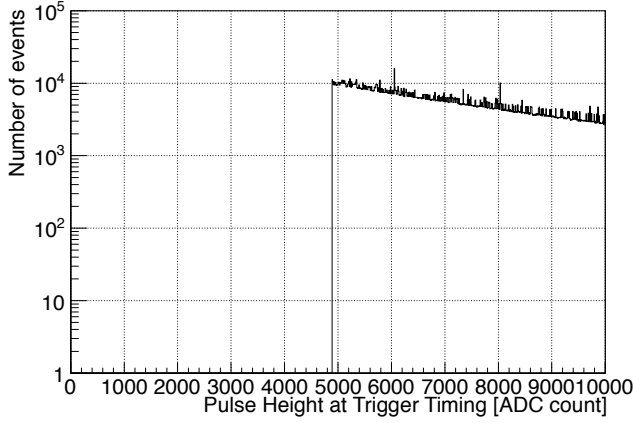
Figure 3.6: Pulse height of CsI summed waveform at trigger timing recorded in the trigger system
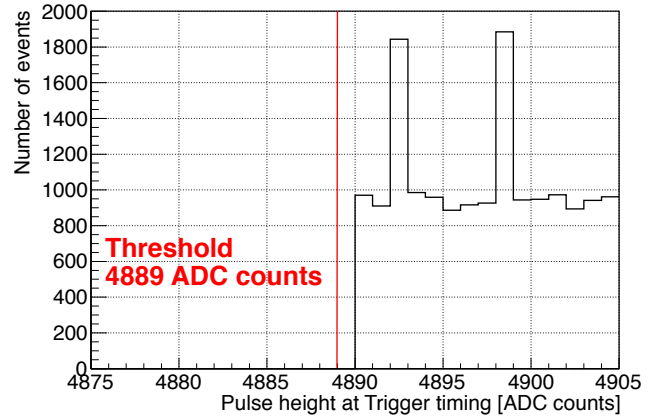
Figure 3.7: Pulse height of CsI summed waveform at trigger timing recorded in the trigger system

Performance for offline analysis

Figure 3.12 shows the total energy distribution of the CsI calorimeter in the offline analysis. The online threshold was calculated and set to record the events with the total energy of CsI calorimeter higher than 550 MeV. The edge can be seen in offline CsI total energy distribution around the online trigger threshold. The smeared edge can be explained by the gain difference among channels and the pedestal fluctuation in online and offline calculation for energy in each channel.

3.3   Online Cut with Veto detector at Lv1 Trigger system

3.3.1   Problems to solve

To integrate all the detector subsystems into Lv1 trigger system, there were two problems to solve.
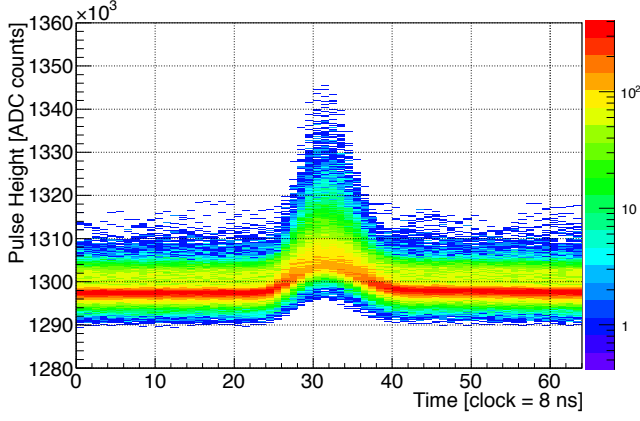
Figure 3.8: The waveform of sum of all CsI calorimeter channels.
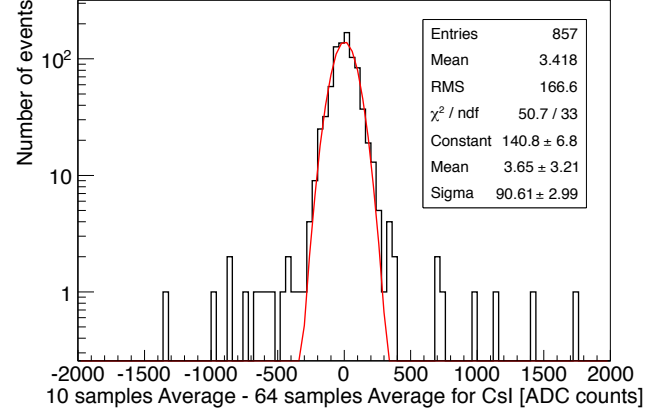
Figure 3.9: The difference between the average of first 10 samples and average of 64 samples for summed waveform of CsI calorimeter channels in the events taken by clock trigger.
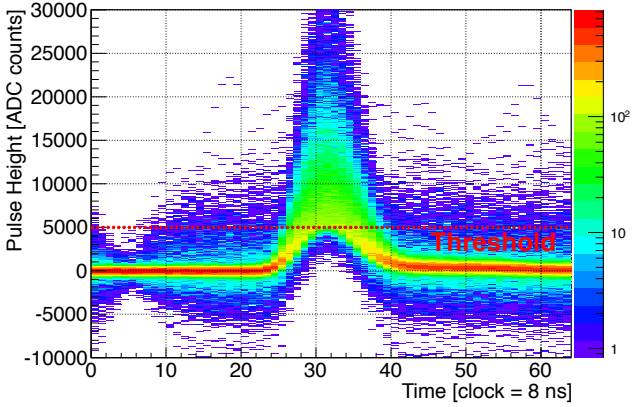
Figure 3.10: The waveform of sum of all CsI calorimeter channels. The average of first 10 samples was used as the pedestal value and subtracted from the waveform.
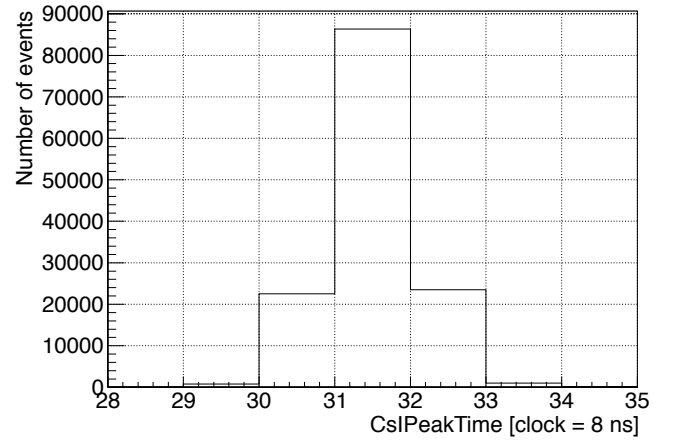
Figure 3.11: The peak timing of summed waveform of CsI calorimeter channels.

46
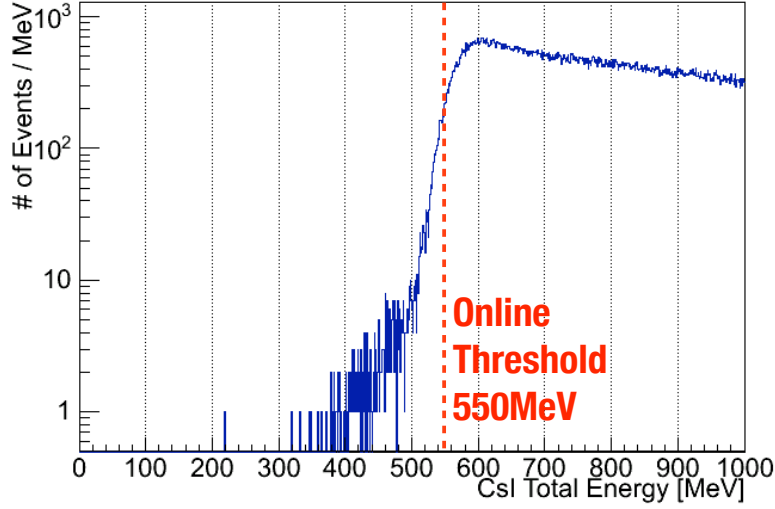
Figure 3.12: CsI calorimeter total energy distribution

1. Different detectors had different types of information to be used for making triggers.

   The methods to determine hits on the detector were different between detector subsystems. Most of the detector subsystems such as CV and CC03 used the sum of energies of all the modules. Some detector subsystems such as OEV and BHPV used the number of modules with large energy deposits. The bit width of the P3 backplane was not wide enough to transfer all these detail trigger informations to the Lv1 Trigger Master Module. Unlike the CsI calorimeter, the trigger decision for each detector thus could not be made at the Lv1 Trigger Master module.

2. The limited path to send the information to the Lv1 Trigger Master module.

   The special connections via P3 backplane and the other signal lines for control signal were the only ways to send signal from Lv1 Trigger modules to the Lv1 Trigger Master module. There were twelve major detector subsystems in KOTO to be implemented in the trigger system: FB, NCC, MB, CV, OEV, LCV, CC03, CC04, CC05, CC06, BHCV, and BHPV. We had to transfer the trigger information from these detectors to the Lv1 Trigger Master module through the limited path.

3.3.2 Solution

To solve these problems, we developed the Lv1 trigger system as shown in Fig. 3.13. In this system, the trigger decision for each detector subsystem was made at their own trigger module and was passed to the Lv1 Trigger Master module via the optical-link and the P3 daisy-chain bus. The solutions for the problems described in Section 3.3.1 were the followings.

1. Make trigger decisions for each detector subsystem at their own trigger module and send it to Lv1 Trigger system.

   To make trigger decision for each detector subsystem, we assigned a dedicated Lv1 trigger module for each detector subsystem. We refer to these Lv1 Trigger modules as Lv1 Veto Trigger modules, and refer to the modules for the CsI calorimeter as the Lv1 CsI Trigger modules. The detector subsystems with a large number of channels such as NCC and CV
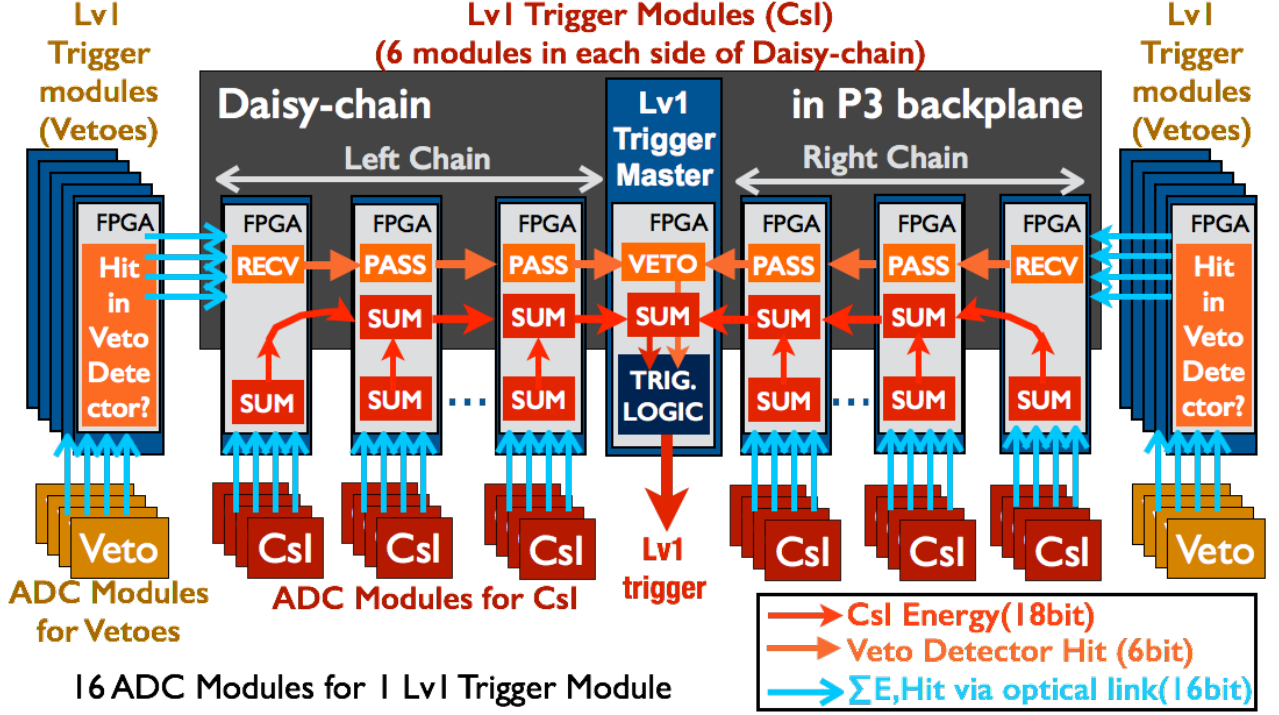
Figure 3.13: Lv1 trigger system with the optical link and daisy-chain.

used one Lv1 Veto trigger module for one detector subsystem. The detector subsystems with smaller numbers of channels shared the same Lv1 Veto Trigger module. For example, CC03, CC04, CC05, CC06 shared the same Lv1 Veto Trigger module.

Figure 3.14 shows how the Lv1 Veto Trigger module worked. The Lv1 Veto Trigger module received the trigger information such as the sum of energies or the hit pattern from the ADC modules via optical links. The Lv1 Veto Trigger module made trigger decisions for detector subsystems based on these information. Peak finding method was used for making trigger decisions from the total energy. In case of using the total number of hit modules, the timing when the total number of hit modules exceeded the threshold was used as the trigger timing.

To transfer the trigger information of the detector subsystem to Lv1 Trigger Master module, trigger information was encoded into 16-bit information and sent from Lv1 Veto Trigger module to Lv1 CsI Trigger module through via the optical fiber. One out of sixteen optical transceiver modules on the Lv1 Veto Trigger module was used not to receive the information from ADC Module but to send the information from Lv1 Veto Trigger module to Lv1 CsI Trigger module.

2. Use daisy-chain bus also to transfer the trigger decision of each detector subsystem.

The 24-bit-width daisy-chain bus in P3 backplane was the only path to send the trigger information from Lv1 Trigger modules to the Lv1 Trigger Master module. In the original design for making the trigger decision of the CsI calorimeter, all 24 lines were used to send and sum up the total energy of the CsI calorimeter. Because the pedestal subtraction mechanism was implemented in the ADC firmware, 18 bits were wide enough to cover the energy range measured for the CsI calorimeter. Remaining 6-bit lines were used for transferring the trigger source of each detector subsystem.
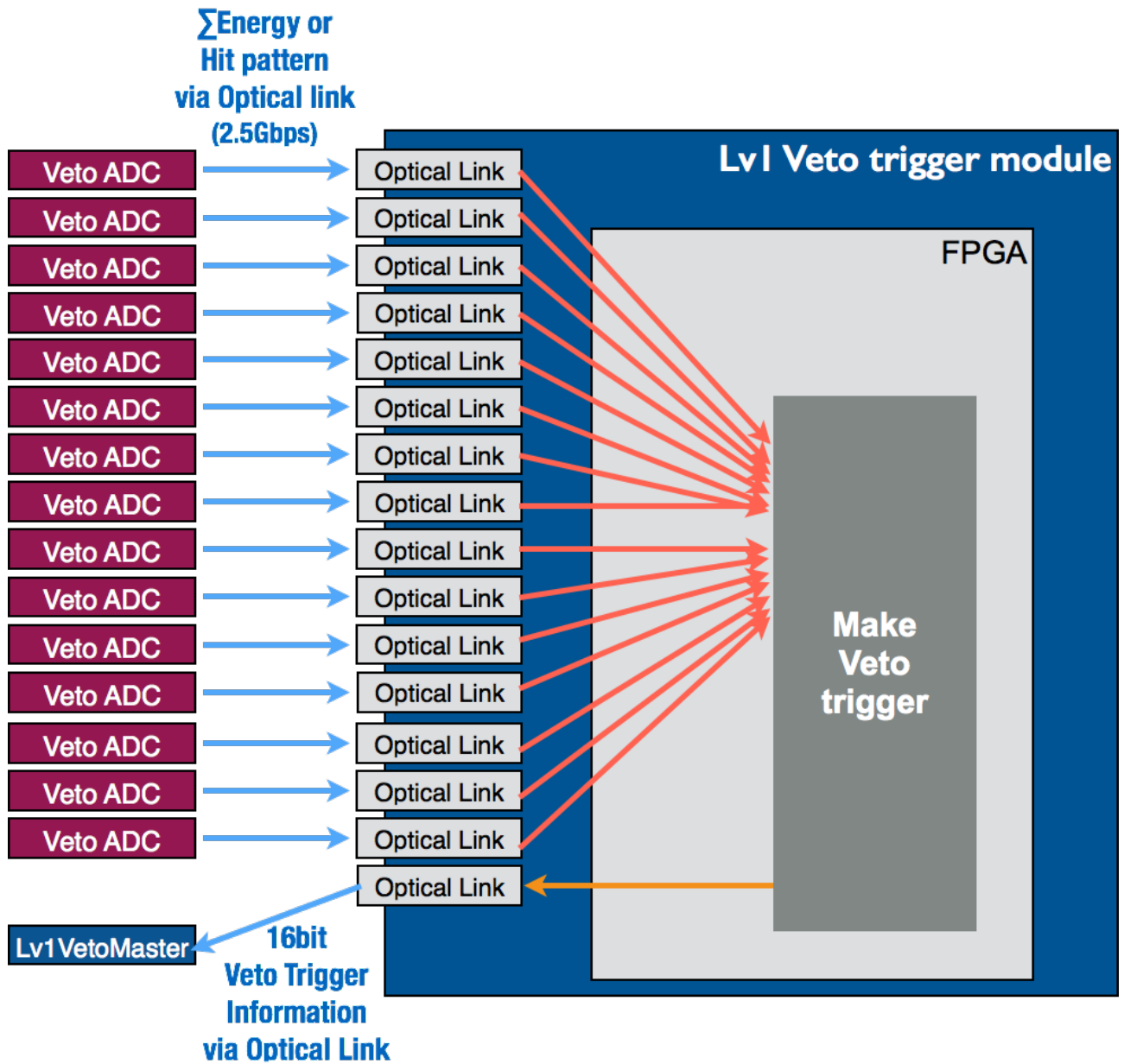
Figure 3.14: Lv1 Veto trigger module
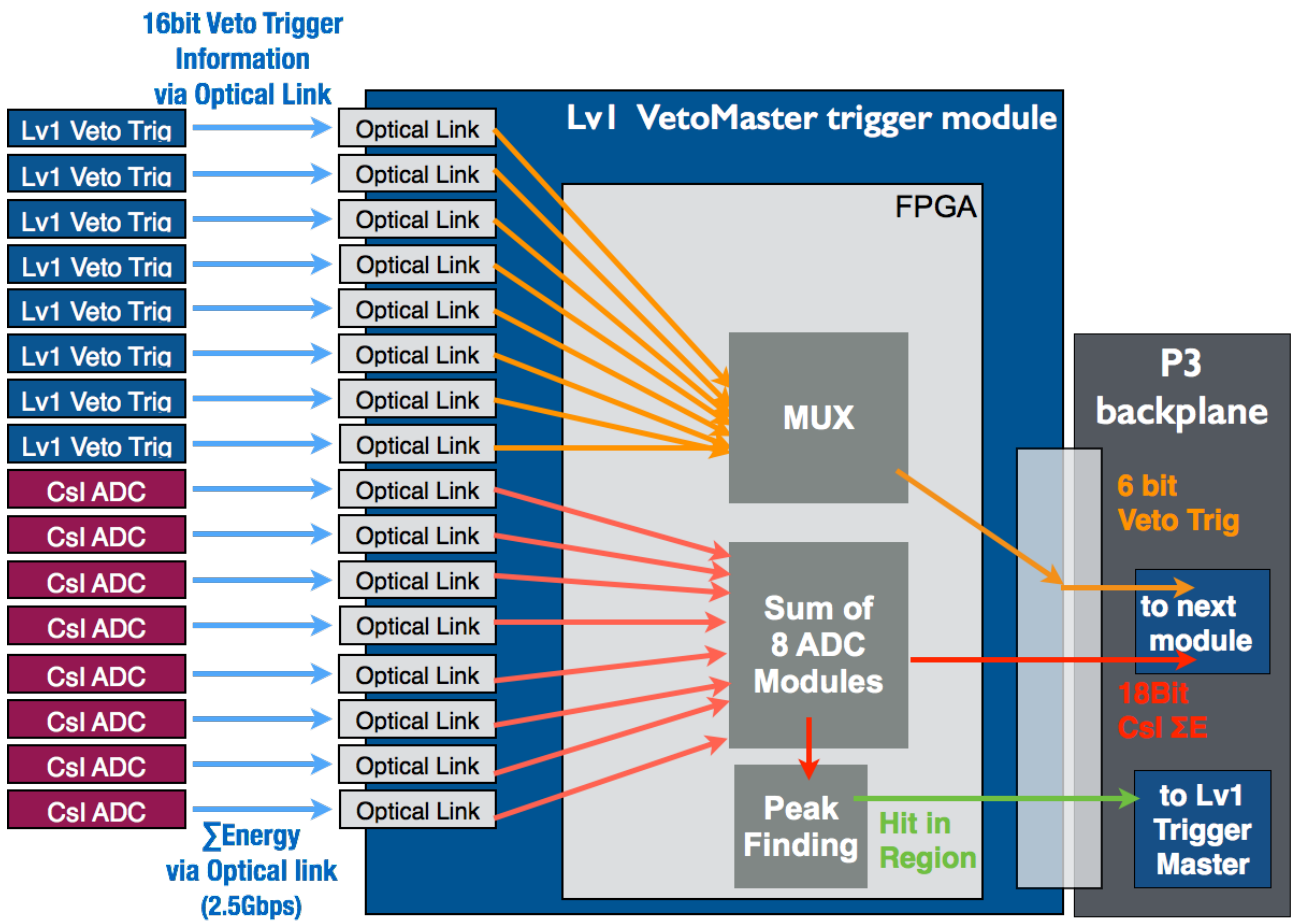
Figure 3.15: Lv1 Veto Master trigger module which receive trigger information both from CsI ADC modules and Lv1 Veto Trigger modules.

To transfer the trigger information from the Lv1 Veto Trigger modules, the two outer most Lv1 CsI Trigger modules received the informations from Lv1 Veto Trigger Modules. We refer to these two modules as "Lv1 Veto Master Trigger module". Figure 3.15 shows how the Lv1 Veto Master Trigger module worked. The Lv1 Veto Master Trigger modules encoded the received information into 6-bit information so that each detector subsystem used 1-bit line and passed it to the daisy-chain with the total energy of CsI calorimeter from its own CsI ADC modules. Because the daisy-chain in the left bank and right bank were independent, we could send the trigger information from up to twelve veto detector subsystems into the daisy-chain. Figure 3.16 shows how the other Lv1 CsI Trigger modules worked to transfer the total energy information of the CsI Calorimeter and the veto detector trigger information. Lv1 CsI Trigger module received and sent the 18-bit CsI total energy information after summing its own energy information. Lv1 CsI Trigger module also received and sent 6-bit veto detector subsystem's trigger information without any treatment. At the end of the daisy-chain, the Lv1 Trigger Master module received the total energy information of the CsI calorimeter and the trigger information from twelve veto detector subsystems. Figure 3.17 shows how the Lv1 Trigger Master module worked. Lv1 Trigger Master took the coincidence or anti-coincidence of CsI trigger and the triggers from other veto detector subsystems to make the Lv1 Trigger decision.
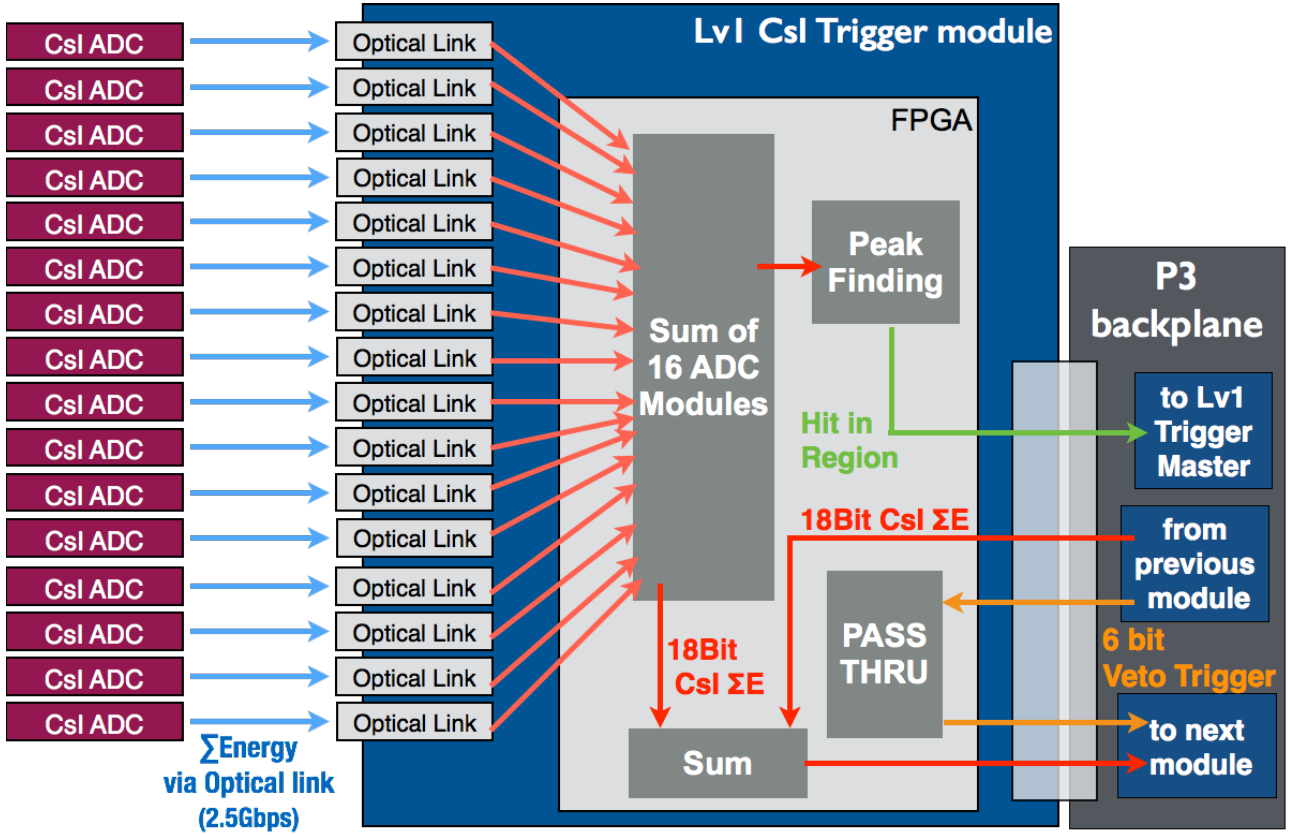
Figure 3.16: Lv1 CsI Trigger module which transferred total energy of the CsI calorimeter and veto detector's trigger information.
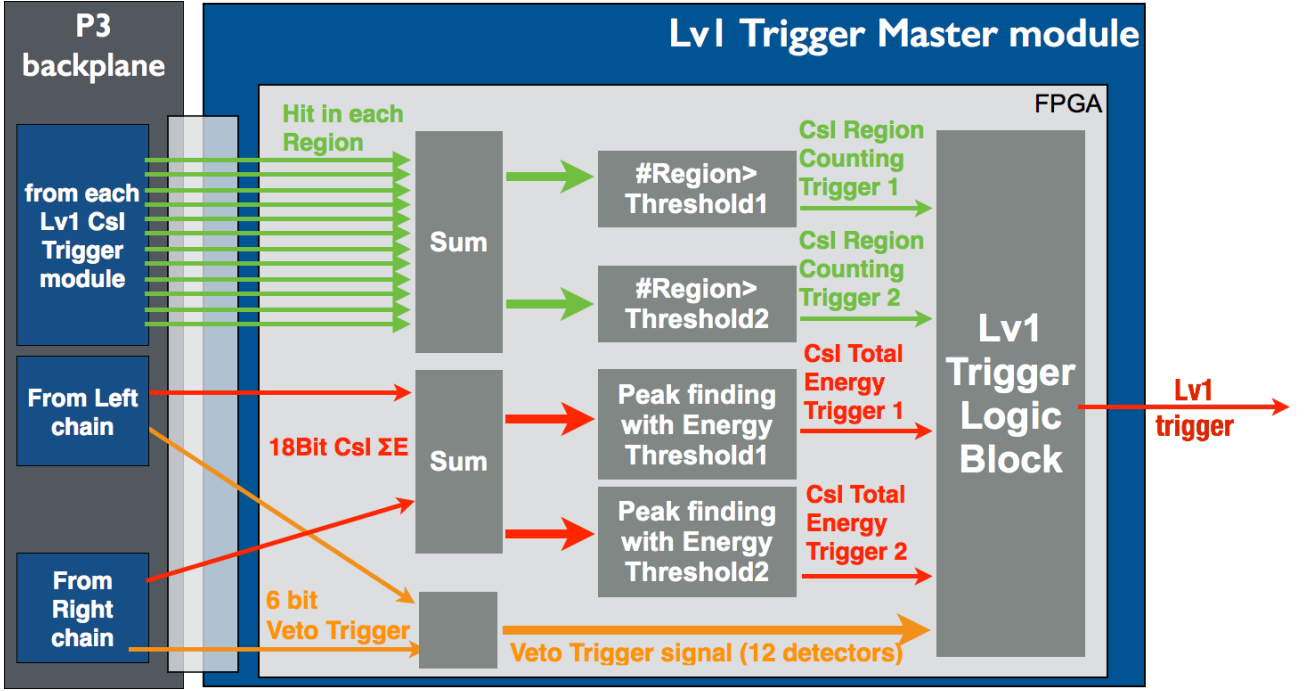
Figure 3.17: Lv1 trigger master module which made Lv1 trigger decision.

3.3.3 Performance

3.3.3.1 Performance in the reduction of the trigger rate.

As described in Section 2.7.2.1, the trigger rate of CsI Trigger was 258k triggers/spill, which corresponds to 129 kHz for 2 s beam extraction. After applying online trigger cut by the total energy of MB, CV, NCC and CC03, the Lv1 trigger rate was reduced to around 27k events/spill, or 14 kHz. The COE-radius cut at Lv2 Trigger stage reduced the Lv2 trigger rate by a factor of 5. With these reductions, the number of Lv2 triggers in each spill was reduced to less than 8000 events, which is the maximum number of events which could be stored in the memory on the Lv2 module.

3.3.3.2 Performance in recorded data

The performance of the veto trigger was evaluated with the recorded waveform of the events taken with Minimum bias trigger which only use the energy information of the CsI calorimeter.

The statuses of triggers of veto detectors in each event were recorded by the Lv1 Trigger Master module as 16-bit information for 16 detector subsystems. We refer this 16-bit information to "DetectorTriggerBit". If there was triggers of veto detectors at the trigger timing, the bits in DetectorTriggerBit for the detectors with trigger were set to 1. By checking the status of DetectorTriggerBit in the events taken with the Minimum bias trigger, the effect of veto cuts at Lv1 trigger stage can be checked.

Performance in online information

Figure 3.18 shows the correlation between the height and timing of the sum of waveforms over all channels in each detector. The summed waveforms of each detector were calculated from the data of events with requiring DetectorTriggerBit of each detector to be 0. Because the

Lv1 Trigger system used the peak timing of the summed waveforms from the detectors to make detector's trigger, there should be no events with the peak height larger than the threshold on the timing of the CsI trigger. As shown in Fig. 3.18, in each detector, there is a clear gap above the threshold at the CsI trigger timing.

There were some events which had larger peak height than threshold at trigger timing for CV and MB. This can be explained by the pedestal fluctuation in these detectors. Figures 3.19, 3.20, 3.21, and 3.22 show the difference between the average of first 10 samples and average of 64 samples for summed waveform of the channels of CV, NCC, MB, and CC03, respectively, in the events taken by clock trigger. The pedestal of CV and MB had large fluctuations than NCC and CC03.

There were also some events which had larger peak height than the threshold around the trigger timing. The timing jitter between Lv1 CsI Trigger modules or two daisy-chain bank are the possible sources of these events. Because the trigger signal of veto detectors were propagated through the daisy-chain, such timing jitter can change the timing of them and prevent the events from rejection.
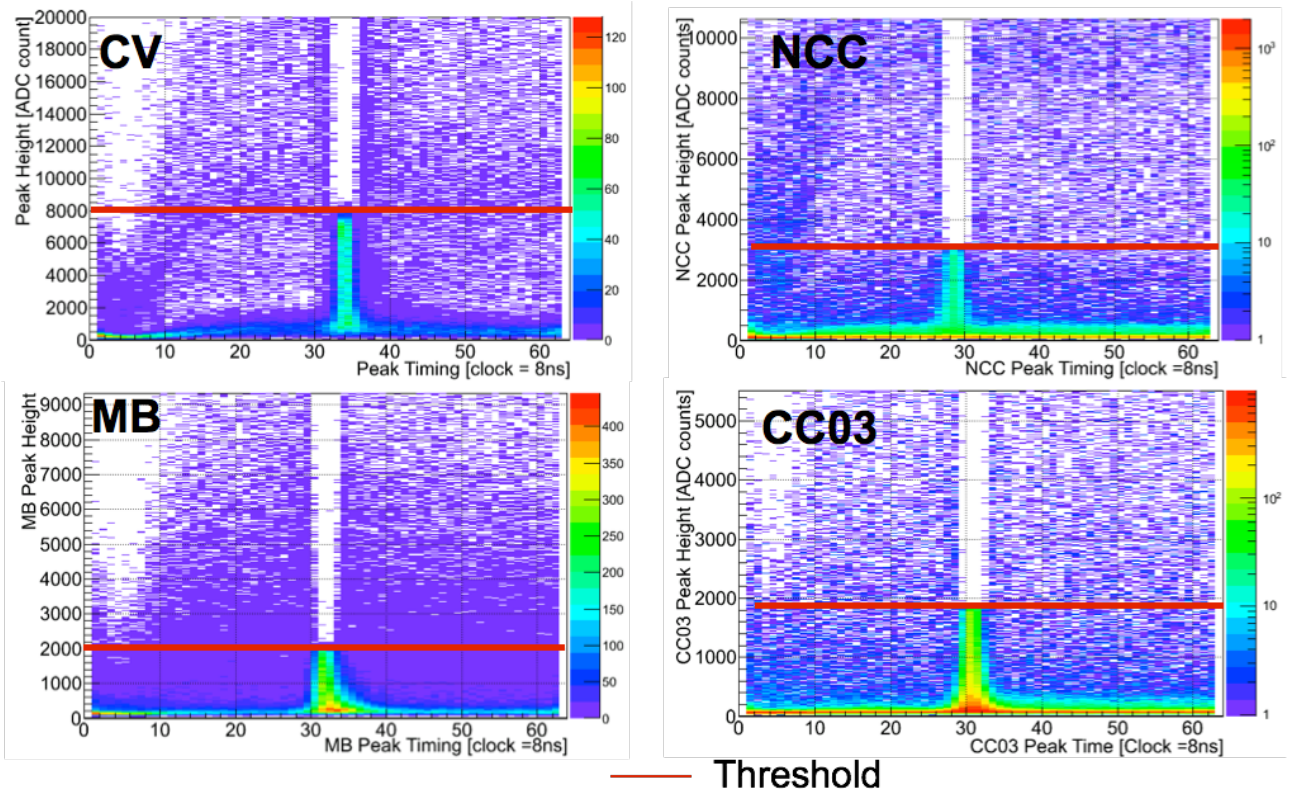
Figure 3.18: The correlation between the peak height and peak timing of the sum of waveforms over all channels in each detector for events with with requiring DetectorTriggerBit of each detector to be 0, for CV (top left), NCC (top right), MB (bottom left), and CC03 (bottom right).

Performance for offline analysis

The sum of energies over all channels of the detector subsystems was calculated in the offline analysis and compared with the targeted threshold. Figure 3.23 shows the energy in the four
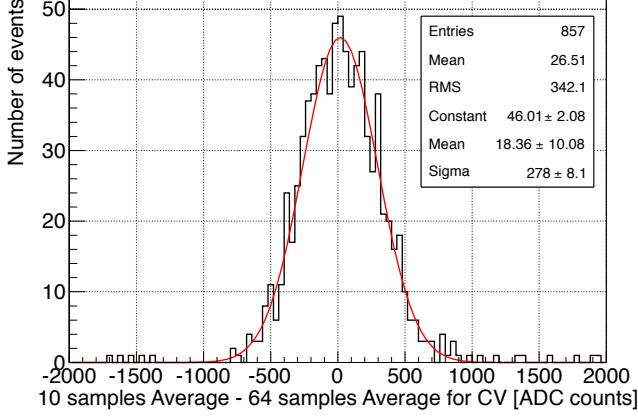
Figure 3.19: The difference between the average of first 10 samples and average of 64 samples for summed waveform of CV channels in the events taken by clock trigger.
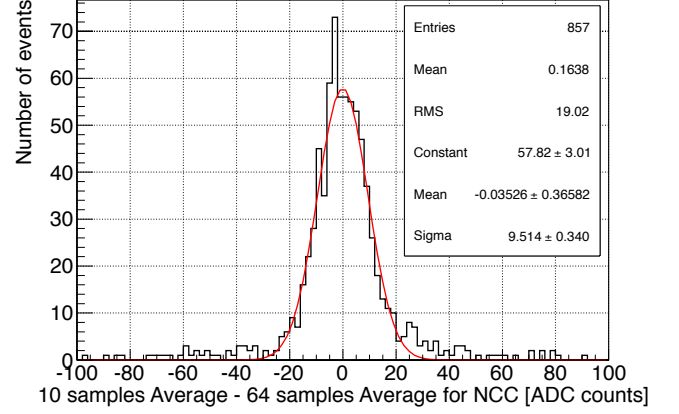
Figure 3.20: The difference between the average of first 10 samples and average of 64 samples for summed waveform of NCC channels in the events taken by clock trigger.
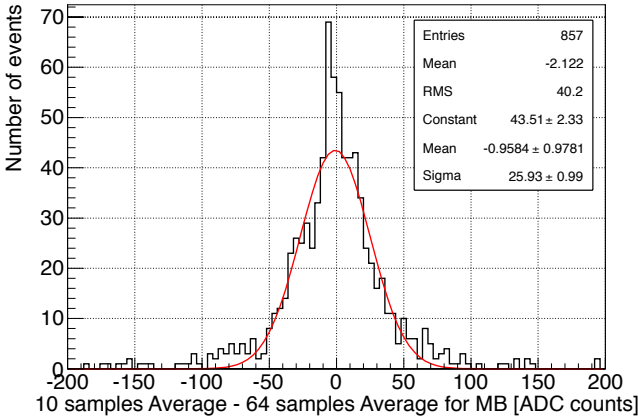
Figure 3.21: The difference between the average of first 10 samples and average of 64 samples for summed waveform of MB channels in the events taken by clock trigger.
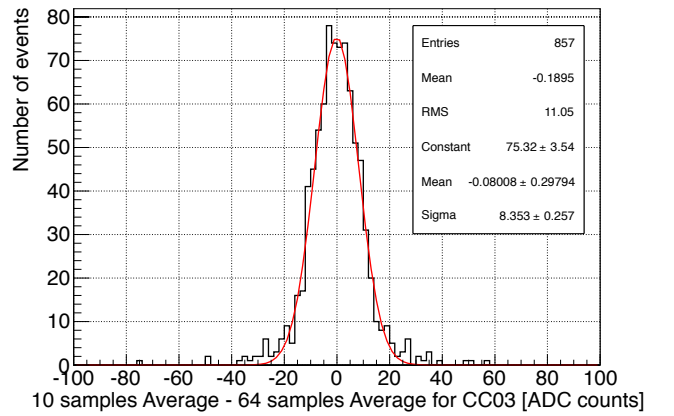
Figure 3.22: The difference between the average of first 10 samples and average of 64 samples for summed waveform of CC03 calorimeter channels in the events taken by clock trigger.

veto subsystems before and after requiring no trigger for each veto subsystem. There is a clear edge around the energy threshold required on the Lv1 trigger decision.

The smeared edge for MB can be explained by the difference of method to calculate the energy in the MB modules which will be described in Section 4.3.2.3.
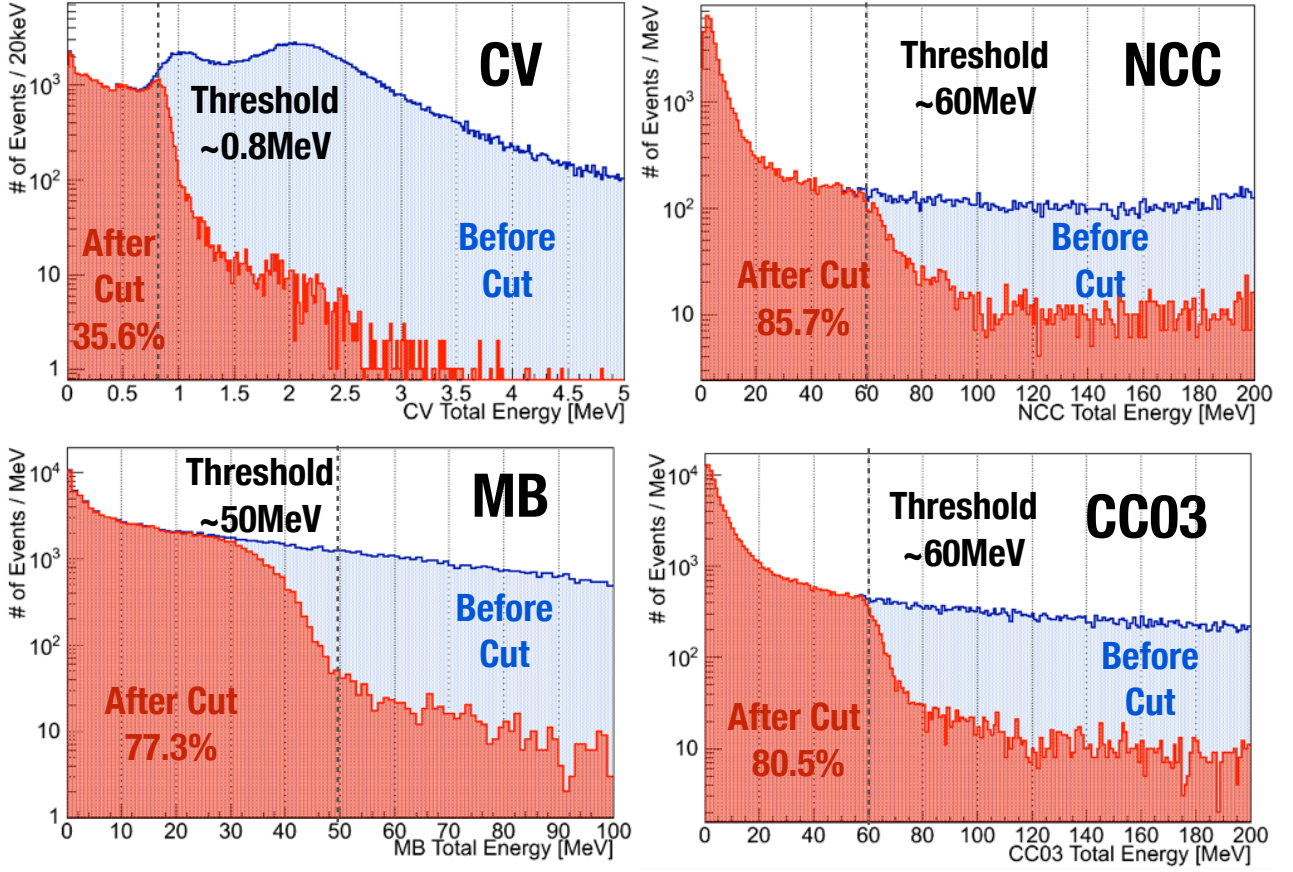
Figure 3.23: Visible Energy distribution in offline analysis for CV (top left), NCC (top right), MB (bottom left), and CC03 (bottom right). The dotted lines represent the trigger thresholds. The number of "After Cut" in each histogram shows the fraction of events with with requiring DetectorTriggerBit of each detector to be 0.

3.4 Region Counting Trigger

3.4.1 Problem to solve

In the original design, the trigger for the CsI calorimeter was generated based on the total energy in the CsI calorimeter.

Figure 3.24 shows the distribution of the number of clusters on the CsI calorimeter for the events taken with the total energy trigger. With the total energy trigger, most of events had a small number of clusters on the CsI calorimeter and the trigger was not efficient to accumulate $K_L \to 3\pi^0$ decay events required for calibration. To enhance the events from $K_L \to 3\pi^0$ decay mode, the trigger system was required to count the number of clusters on the CsI calorimeter.

Figure 3.24: Number of clusters with energy larger than 120 MeV on the CsI calorimeter in the offline analysis of events taken with the CsI Total Energy Trigger.

3.4.2 Solution

To implement the hardware cluster counting mechanism while keeping the original total energy trigger logic, we used the total energy information of each Lv1 CsI Trigger module. As shown in Fig. 2.40, the CsI calorimeter was divided into twelve regions for Lv1 CsI Trigger modules. Because each Lv1 CsI Trigger module had the total energy in its region, we could roughly count the number of clusters on the CsI calorimeter by counting the number of regions, or the number of Lv1 CsI Trigger modules with large energy deposits. To calculate the total number of hit regions, the hit information in each region had to be sent to the Lv1 Trigger Master modules. Because there were no more spare lines in the daisy-chain bus in the P3 backplane, we used Peer-to-Peer serial links between each Lv1 trigger module and the Lv1 Trigger Master module.

As shown in Figs. 3.15 and 3.16, Lv1 CsI Trigger module determined the hit in its region by applying the peak finding method to the total energy in its region. As shown in Fig. 3.17, the Lv1 Trigger Master Module calculated the number of hit regions from the hit informations collected from each Lv1 CsI Trigger module. Lv1 Trigger Master Module generated a trigger if the number of hit regions exceeded a given threshold value. This trigger is called "CsI Region Counting Trigger".

3.4.3 Performance

The performance of the CsI Region Counting Trigger was evaluated with the events taken with Minimum Bias Trigger. Because the status of CsI Region Counting Trigger was also included in DetectorTriggerBit, the performance of the CsI Region Counting Trigger can be evaluated by checking the status of DetectorTriggerBit of the CsI Region Counting Trigger.

The region with hit was required to have energy larger than 120 MeV and the number of hit regions was require to be >4 in the CsI Region Counting Trigger.

Figure 3.25 shows the number of the hit regions for events taken with the CsI Total Energy Trigger before and after requiring DetectorTriggerBit of CsI Region Counting Trigger to be 1. Most of events had 5 or more regions with Energy larger than 120 MeV. Figure 3.26 shows the fraction of events which passed the CsI Region Counting Trigger as a function of the number of the hit regions for events taken with the CsI Total Energy Trigger. There is a clear edge in the number of hit regions between 4 and 5.
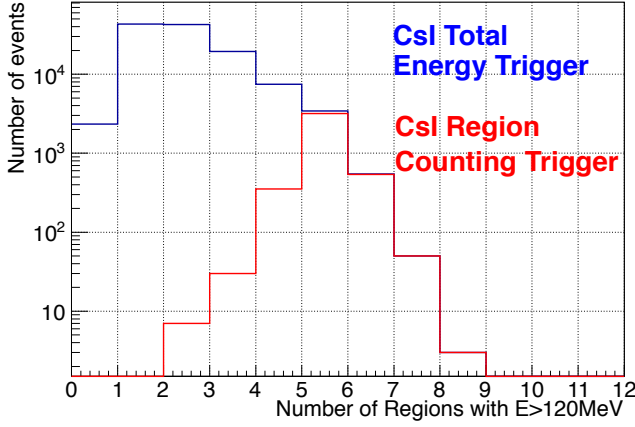
Figure 3.25: Number of the region with energy larger than 120 MeV for events taken with the CsI Total Energy Trigger. Blue and Red histograms show the events before and after requiring DetectorTriggerBit of CsI Region Counting Trigger (which required the number of hit regions >4) to be 1.
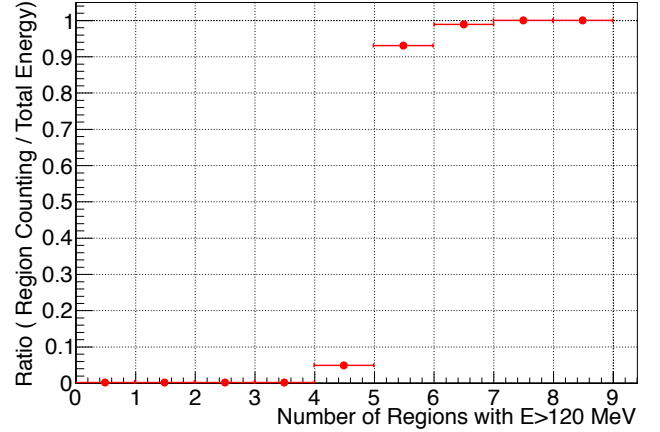
Figure 3.26: Fraction of events which passed the CsI Region Counting Trigger, which required the number of hit regions > 4, as a function of the number of the region with energy larger than 120 MeV for events taken with the CsI Total Energy Trigger.

Figure 3.27 shows the number of clusters with energy larger than 120 MeV in the offline analysis of events taken with the CsI Total Energy Trigger before and after requiring DetectorTriggerBit of CsI Region Counting Trigger to be 1. Most of events had 4 or more clusters. Figure 3.28 shows the fraction of events which passed the CsI Region Counting Trigger as a function of the number of clusters with energy larger than 120 MeV on the CsI calorimeter in the offline analysis. The fraction of events with a smaller number of clusters on the CsI calorimeter was suppressed while keeping a higher efficiency for the events with 6 clusters on the CsI calorimeter.

3.5 Flexible Trigger logic

We developed a new logic of Lv1 Trigger system which allows simultaneous data taking with different trigger conditions with flexible combination of detectors.

Figure 3.29 shows the logic to generate Lv1 Trigger from the trigger information from various detectors.

A special trigger logic, called "Yasu Trigger Logic", receives four types of CsI triggers, two for total energy trigger and two for region counting triggers with different thresholds, and the trigger information from the twelve veto detector subsystems were fed into after timing alignment and shaping to a fixed width. The amount of delay for timing alignment and the width for gate signal were individually adjusted for each trigger signal from detectors. The Yasu Trigger Logic generated triggers based on the trigger information from the detector subsystems. The combination of detector subsystems which Yasu Trigger Logic used in the trigger decision was defined by configuration register accessible from VME. Trigger information from the detector subsystems were fed into eight copies of Yasu Trigger Logic with different configurations, and the OR of triggers generated by these Yasu Trigger Logic were used as the source of Lv1 Trigger. The Lv1 Trigger requested by the Lv1 Trigger system was accepted if the Lv2 trigger system
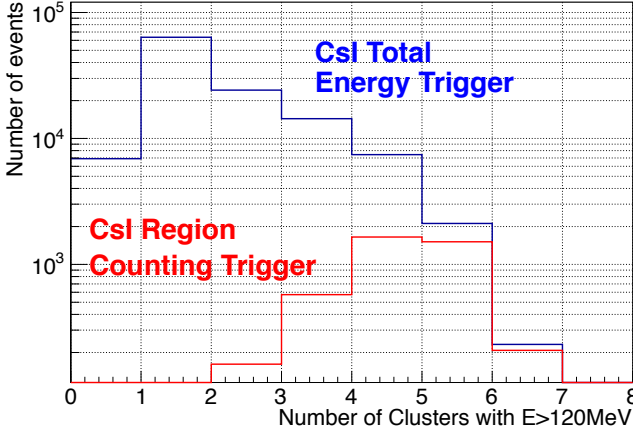
Figure 3.27: Number of clusters with energy larger than 120 MeV in the offline analysis of events taken with the CsI Total Energy Trigger. Blue and Red histograms show the events with CsI Total Energy trigger before and after after requiring DetectorTriggerBit of CsI Region Counting Trigger (which required the number of hit regions >4) to be 1 .
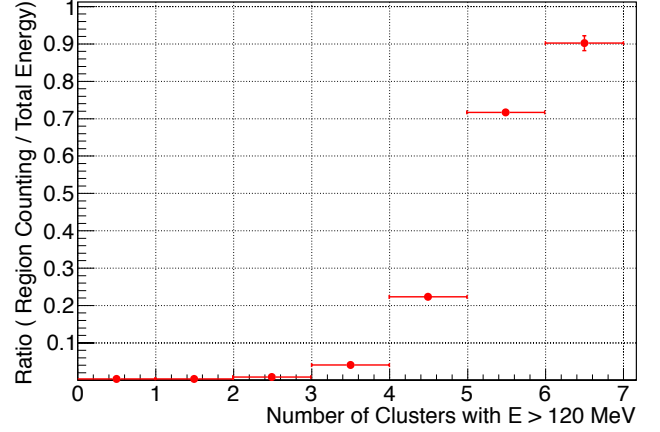
Figure 3.28: Fraction of events which passed the CsI Region Counting Trigger, which required the number of hit regions > 4, as a function of the number of clusters with energy larger than 120 MeV in the offline analysis for events taken with the CsI Total Energy Trigger.

was not busy. The accepted Lv1 trigger was distributed to ADC modules after shaping into logic gate signal with a fixed width. The width of Lv1 trigger signal was changed based on whether the cuts were required at Lv2 trigger stage or not. ADC modules learned whether the Lv2 cut decision was required or not by the length of Lv1 trigger signal, and they encoded it into the header of data stream. Lv2 trigger modules determined whether to cut events or not based on this header.
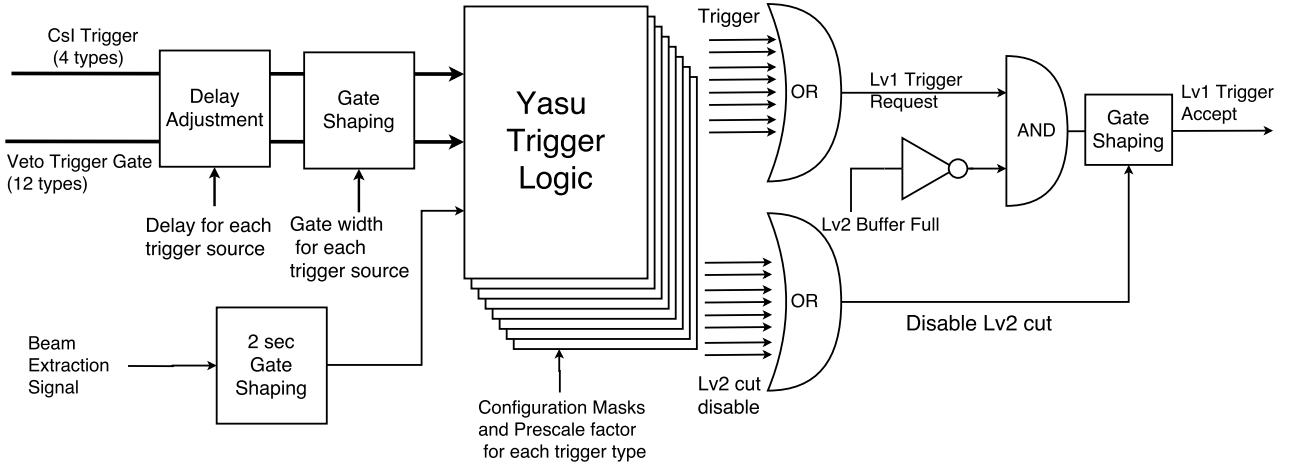
Figure 3.29: Lv1 trigger logic to make multiple types of triggers.

Figure 3.30 shows the logic design inside the Yasu Trigger Logic. Inputs to the logic were four types of CsI calorimeter's triggers, trigger from twelve veto detector subsystems, beam spill gate, and the configuration registers accessible from VME . The combination of detector subsystems was controlled by an 18-bit configuration mask. Table 3.1 shows how the trigger

configuration was defined by various settings of the configuration mask. The sixteen least significant bits (LSB) of the mask were assigned to the detector subsystems: 4 LSB for CsI calorimeter, and the remaining 12-bits for twelve veto detector subsystems. The remaining two most significant bits of the mask were used to control the type of the logic. The sixteenth bit of the mask was used to control whether to take the events or veto to the events if veto detector subsystems had hits. The seventeenth bit of the mask was used to control whether to take AND or OR of all the enabled veto detector subsystems. The trigger decision in the logic block could be disabled during the beam extraction period by an "Off spill" mask. The trigger could be prescaled to reduce its rate. The prescale factor could be set from 1 to 65534 via a VME register. The trigger decision of the Lv2 trigger stage could be ignored by a bit in the configuration mask.

To identify the trigger type used to take each events, the status of 8 types of trigger source from Yasu Trigger Logic in each event was recorded by Lv1 Trigger Master module as 11-bit information including the status of beam extraction and the statuses of two external trigger sources. We refer this 11-bit information to "TriggerTypeBit". TriggerTypeBit was separately recorded for the status before and after prescaling. With this TriggerTypeBit, we can select the event taken with the specific type of trigger.
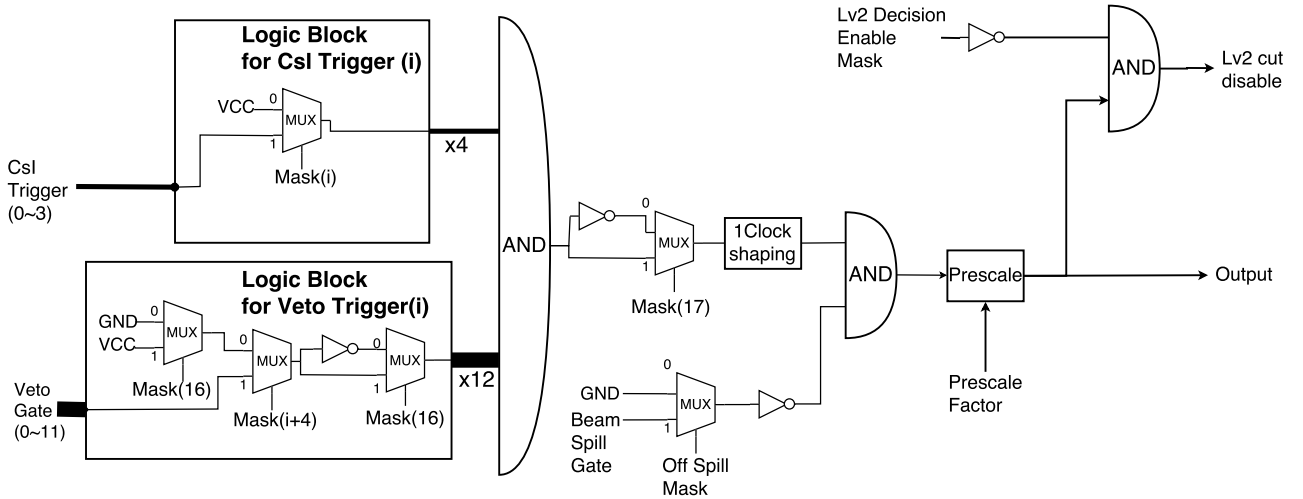
Figure 3.30: "Yasu Trigger Logic":Logic block to provide flexible combination of detector's trigger. Mask(i) represents the i-th bit of the trigger configuration mask.

Table 3.1: The trigger configuration is set by various settings of the configuration mask.

OR/AND 17th bit	Trigger/Cut 16th bit	Veto Detectors 15th bit ∼ 4th bit	CsI 3rd bit ∼ 0th bit	Trigger configuration
0	0	0	any	AND of enabled CsI triggers
0	0	any	any	(AND of CsI) & (NOR of vetos)
0	1	any	any	(AND of CsI) & (AND of vetos)
0	1	any	0	(AND of all enabled veto detectors)
1	0	any	0	(OR of all enabled veto detectors)

RunInfo

Run16925 Run Start:2013-05-23 03:32:05

RunNote:StandardTrig_May19

Now: 2013-05-23 04:33:54

SpillInfo

Spill599 2013-05-23 04:33:38 ~ 04:33:42

SpillFromAcc:615 nBadL2Spill:1 LiveRatio:0.97

SYIM,TMon
SYIM:3164 TMon/SYIM:40
TMon:127233

scalers

L1,L2Trigger Accept/Rejects

TotalL2Accept: 4.5e+06

L2Accept: 7508	L2A/L1A:0.33
L1Accept: 22786	L1AcceptRatio:1
L1Req_L2LIVE: 22786	L2LiveRatio:0.81
L1Request: 28094	
L1_OR: 28094	
Internal: 28049	
External1(Calib): 108	
External2(TMon): 107	

#Trigger for each Trigger Type

Trigger Description	Prescale Factor	Raw	Prescaled	Raw/Prescaled
Trig0:[CsI(TotalEt) ! (CV | NCC | MB | CC03) w/COECut]	1	27072	27072	1.0
Trig1:[CsI(TotalEt) ! (CV | NCC | MB | CC03)]	30	27072	902	30.0
Trig2:[CsI(TotalEt)]	300	258142	861	299.8
Trig3:[CsI(TotalEt & RegionCount1) ! (CV | NCC | MB | CC03)]	10	4028	403	10.0
Trig4:[(NCC) OnlyOffSpill]	1	51	51	1.0
Trig5:[(OEV) OnlyOffSpill]	1	57	57	1.0
Trig6:[CsI(TotalEt) OnlyOffSpill]	1	154	154	1.0
Trig7:[ ]	1	0	0	0.0

Detector scalers

CsI TotalEt	CsI RegionCount	CV	FB	NCC	MB	OEV	Calib	CC03	CC04	CC05	CC06	BHCV	BHPV
258142	12200	385946	667829	317867	359369	12389	0	130459	209467	343003	655723	8477097	4043555

L3 nodes

Node:	0-0	0-1	0-2	0-3	0-4	0-5	0-6	0-7	0-8	0-9	0-10	0-11	0-13	0-14	0-15	0-16	0-17	0-18	1-0	1-1	1-2	1-4	1-5	1-7	1-8	1-9	1-10	1-12	1-14
Data size: (~1GB/30Spill)	21.5 GB	21.5 GB	21.5 GB	21.5 GB	21.5 GB	21.5 GB	21.5 GB	21.5 GB	21.5 GB	21.5 GB	21.5 GB	21.5 GB	21.4 GB	21.5 GB	21.5 GB	21.5 GB	21.5 GB	20.8 GB	20.8 GB	21.5 GB	21.1 GB	20.5 GB	21.5 GB	21.0 GB	21.5 GB	21.4 GB	21.2 GB	20.6 GB	21.2 GB

Figure 3.31: Snapshot of the monitor of the DAQ program in 2013 May.

3.5.1 Performance

As shown in Table 2.3, during the physics run in 2013 May, we took data with different trigger conditions at the same time, by using the trigger logic which I developed. Figure 3.31 shows a snapshot of the monitor of the DAQ program.

Figure 3.32 shows the numbers of triggers in each beam spill. The number of triggers requested and accepted at the Lv1 and Lv2 trigger stages were stable during the physics run. The number of accepted Lv1 triggers was 17% smaller than the number of generated Lv1 triggers; this was due to the dead time incurred by the trigger system as a result of the limited buffering available inside the Lv2 trigger module.

The stability in each trigger condition was also studied. The numbers of $K_L \to 3\pi^0$ decays recorded by Minimum bias trigger and Normalization trigger was used to study the performance and stability of these triggers.

The number of recorded $K_L \to 3\pi^0$ decays was estimated from the number of reconstructed $K_L \to 3\pi^0$ decay in the recorded events after looser cut for $K_L \to 3\pi^0$ analysis which will be described in Chapter 4 and Section 5.2.1.2. The estimation was done with considering the DAQ efficiency and prescale factor as:

$$\text{Number of recorded } K_L \to 3\pi^0 \text{ decay} = \frac{\text{Number of Reconstructed } K_L \to 3\pi^0}{\text{DAQ efficiency} \times \text{Prescale factor}}. \quad (3.1)$$

Figure 3.33 shows the number of $K_L \to 3\pi^0$ decays recorded by Minimum bias trigger in each data taking run during Run 49. The number of $K_L \to 3\pi^0$ decay was normalized by the number of proton on the T1 target (P.O.T.) in each data taking run. The normalized number of $K_L \to 3\pi^0$ decays recorded by the Minimum bias trigger was stable for all data taking runs during Run 49. The average rate of recorded $K_L \to 3\pi^0$ decays was 4333 ± 15.08 $K_L \to 3\pi^0 / 2 \times 10^{14}$
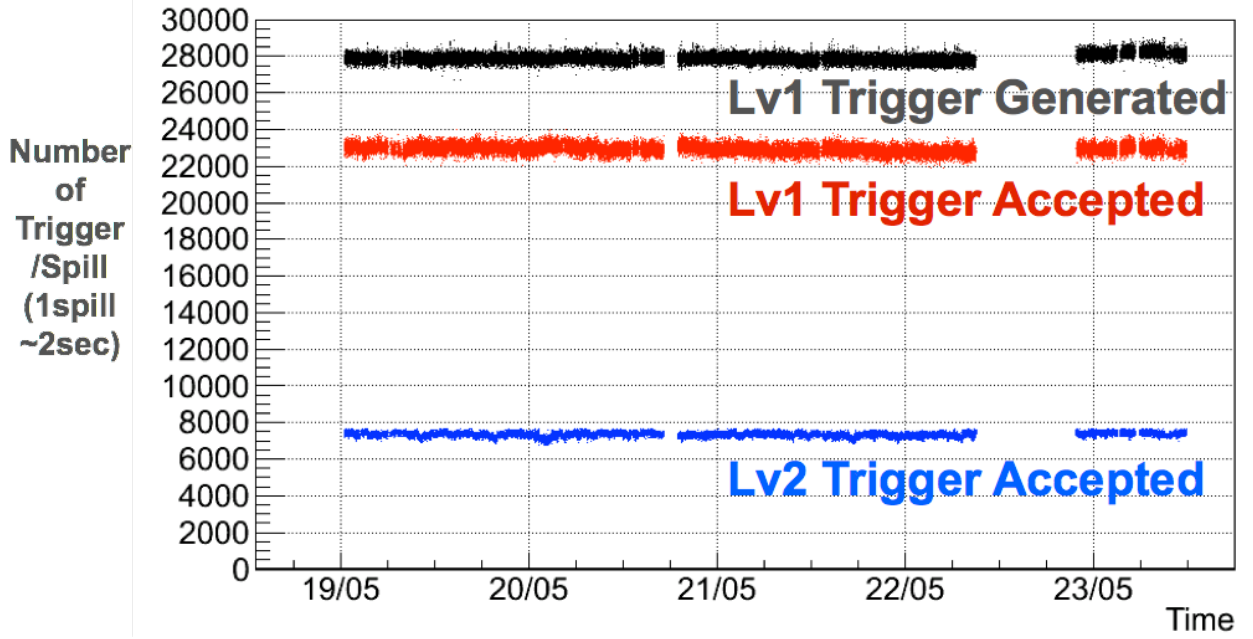
Figure 3.32: Number of triggers in each spill during the physics run in 2013 May.

P.O.T. The acceptance of KOTO detector system for $K_L \to 3\pi^0$ decay after looser cut was estimated to be $5.34 \times 10^{-4} \pm 2.31 \times 10^{-6}$ by MC simulation with 1.0×10^8 $K_L \to 3\pi^0$ decay events. The K_L flux was estimated from the rate of recorded $K_L \to 3\pi^0$ decay, the acceptance, and the branching fraction. The estimated K_L flux was $(4.22 \pm 0.02) \times 10^7/2 \times 10^{14}$ P.O.T.. Because this result is consistent with the previous measurement [23], proper operation of the prescaling feature in the trigger system was confirmed.

Figure 3.34 shows the number of $K_L \to 3\pi^0$ decays normalized by P.O.T. recorded by Normalization trigger in each data taking run during Run 49. The normalized number of $K_L \to 3\pi^0$ decays was stable for all data taking runs during Run 49. The number of recorded $K_L \to 3\pi^0$ decay recorded by Normalization trigger was 17% smaller than that of Minimum bias trigger. This loss was consistent with the loss of events recorded by Minimum bias trigger after applying online veto cut in the offline analysis.

Figure 3.34 shows the ratio of the number of recorded $K_L \to 3\pi^0$ decay between the events recorded by Minimum bias trigger and Normalization trigger in each data taking run during Run 49. The ratio of the number of recorded $K_L \to 3\pi^0$ decay between two trigger condition was stable for all data taking runs during Run 49. This means that the performance of online veto cuts at the Lv1 Trigger system was stable during Run 49.

3.6 Conclusion

The performance of Lv1 Trigger system was evaluated with online and offline information. Even though there were some events which did not fulfill the requirement, the operation performance of Lv1 Trigger system was well understood by using the recorded information.

I confirmed that the data acquisition system worked stably and achieved the required performance during the physics data taking in 2013 and 2015.
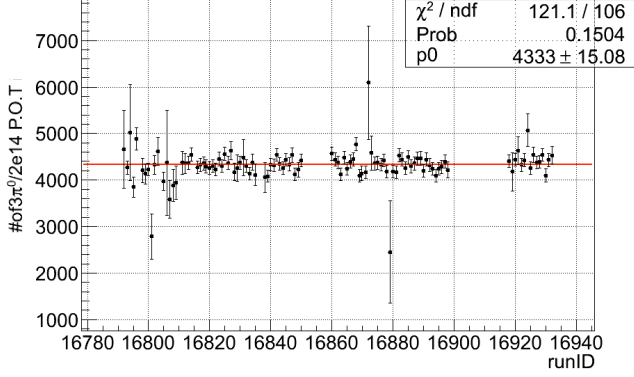
Figure 3.33: Number of $K_L \rightarrow 3\pi^0$ decays recorded by Minimum bias trigger in each data taking run during Run 49. The number in each data taking run was normalized by the number of proton on the T1 target (P.O.T.).
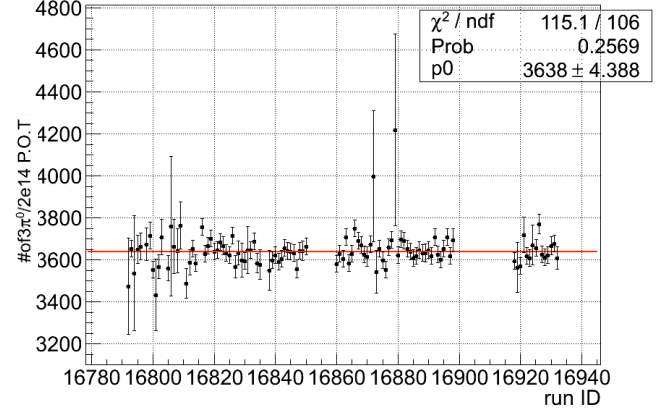
Figure 3.34: Number of $K_L \rightarrow 3\pi^0$ decays recorded by Normalization trigger in each data taking run during Run 49. The number in each data taking run was normalized by the number of proton on the T1 target (P.O.T.).
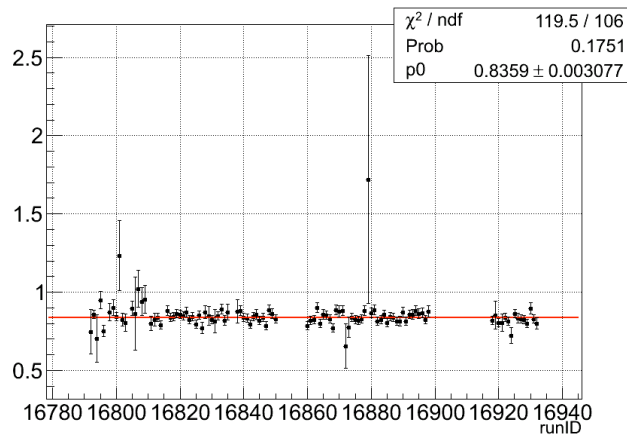
Figure 3.35:   Ratio of the number of recorded $K_L \rightarrow 3\pi^0$ decay between the events recorded by Minimum bias trigger and Normalization trigger in each data taking run during Run 49.

Chapter 4

$K_L \to \pi^0 \nu \overline{\nu}$ analysis and its Backgrounds

We took data for the $K_L \to \pi^0 \nu \overline{\nu}$ analysis in May 2013 with the data acquisition system which I had developed and which is described in Chapter 3.

The purpose of this thesis is to develop a new method to suppress the background caused by neutrons, which was found in the $K_L \to \pi^0 \nu \overline{\nu}$ analysis for the data taken in May 2013.

In this chapter, I will describe the procedure of $K_L \to \pi^0 \nu \overline{\nu}$ analysis because I used the same procedure in Chapter 5 to study the background caused by neutrons. The detail of background found in the analysis will be also described.

4.1   Outline of this chapter

In this chapter, the procedure and its result of $K_L \to \pi^0 \nu \overline{\nu}$ analysis are briefly described. At first, the data used in the $K_L \to \pi^0 \nu \overline{\nu}$ analysis is described in Section 4.2. The method to reconstruct the event information from data is described in Section 4.3. The event selection used in the $K_L \to \pi^0 \nu \overline{\nu}$ analysis is described in Section 4.4. The source and estimated number of the background events are described in Section 4.5. Finally, the result of $K_L \to \pi^0 \nu \overline{\nu}$ analysis is described in Section 4.6. The works described in Section 4.5 and Section 4.6 are mainly done by Dr. K. Shiomi [48] and Dr. Y. Maeda [39].

4.2   Data selection

The data taken between 19 May and 23 May, 2013, which corresponds to a period of 100 hours, was used for the $K_L \to \pi^0 \nu \overline{\nu}$ analysis. The number of protons delivered to the HD-hall during this period was 1.42×10^{18}. The effective number of protons used in the analysis was 1.19×10^{18} after taking the DAQ dead time into account.

Of many trigger types taken at the same time during the data taking period, the events taken with the physics trigger were used for $K_L \to \pi^0 \nu \overline{\nu}$ analysis. The events taken with the Normalization trigger and the Minimum biased trigger were used to estimate the flux of K_L and the biases due to the online cuts.

4.3 Event Reconstruction

4.3.1 Extracting Energy and Timing information from waveform

As described in Section 2.6.1, the digitized waveforms of each channel were recorded in the event data. We have to extract the energy and timing information from the waveform to reconstruct the events.

Because two types of ADC modules with different sampling frequencies were used for the detector subsystems, different methods to extract the energy and timing information were developed.

4.3.1.1 Method for detector using 125-MHz ADC module

In the 2013 physics data taking, the 125-MHz ADC modules collected the waveforms for 64 samples for every event, which correspond to 512 ns for the event window.

For the waveform recorded with the 125-MHz ADC module we assumed that there is a single pulse inside the window and defined its energy and timing information. The pulse closest to the trigger timing, which is called "nominal timing", was chosen if multiple pulses were recorded in the waveform.

Pedestal

To extract the time and energy, the baseline of the waveform, called "pedestal", was first defined. The average and the standard deviation of the first and the last five samples were calculated and the average value with a smaller standard deviation was used as the pedestal of the channel. After defining the pedestal, the pedestal value was subtracted from each sample.

Energy

The integration for the whole waveform after pedestal subtraction was used to calculate energy. The calibration constant to convert the integrated ADC counts to the energy was acquired by the data taken with the $K_L \rightarrow 3\pi^0$ trigger or the data taken in the special runs for the calibration such as the cosmic ray muon runs, beam-muon runs, and Al-target runs.

Timing

To extract the timing information from the recorded waveform, two different methods were developed. A constant fraction method was used for the CsI calorimeters and the parabola fitting method was used for other detector subsystems.

Constant fraction method

The constant fraction method is the method to use the point at which the height of the waveform exceeds the half of the peak height.

The left of Fig. 4.1 shows how the constant fraction timing method was used to get the timing information. At first, the sample with maximum pulse height was identified. The time when the rising edge of the waveform crossed the half-maximum was then calculated by interpolating between the two samples closest to the half maximum.

A timing resolution better than 1 ns was achieved with this method [43]. However, timing might be miscalculated if there were overlapping pulses. The constant fraction method was

used only for the CsI calorimeter because it had less chance to have overlapping pulses due to a small cross section for each crystal smaller than its Molière radius.
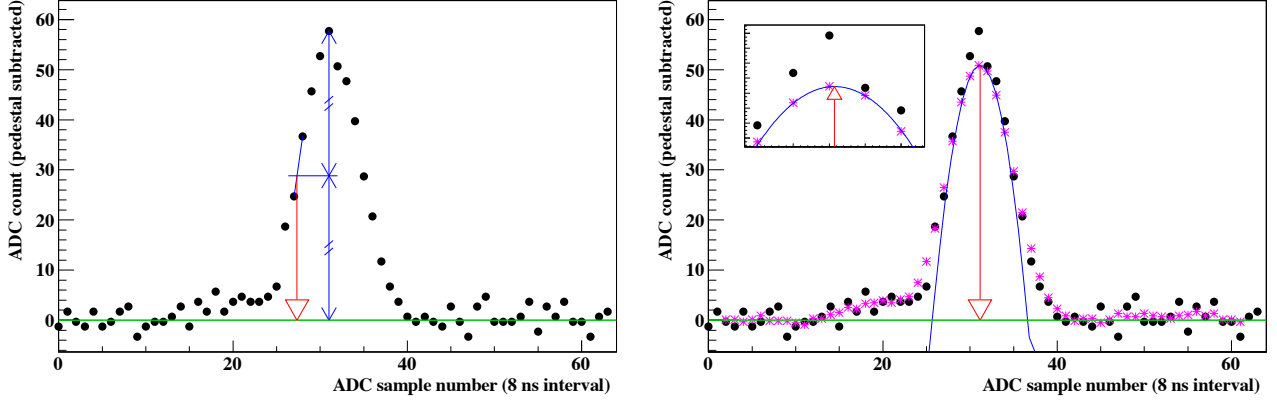
Figure 4.1: Definition of the constant fraction timing (left) and parabola fit timing (right). Black dots represent the data points. Green line represents the baseline called "pedestal". The purple points represent the waveform after smoothing and the blue curve represents the result of the fitting with the parabola function. The red arrows represent the timing defined by the methods. These figures are taken from [39].

Parabola fitting method

The parabola fitting method is the method to define the peak timing of the waveform by assuming that the pulse shape is the parabolic. We can get the peak position by fitting the waveform with a parabolic function because the pulse shape has Gaussian shape due to the 10-pole Bessel filter. The right of Fig. 4.1 shows how the parabolic fitting method was used to get the timing information. To reduce the effect of the fluctuation due to noise, the waveform was smoothed by taking the moving-average of consecutive 5 samples before fitting. After smoothing, the local maxima were searched for and the local maximum closest to the nominal timing was chosen as the location to search for the peak. Three points around the chosen local maximum were used to calculate the peak position of the pulse using the parabolic function:

$$y(t) = A(t - B)^2 + C, \tag{4.1}$$

where y is the pulse height at the time t after smoothing, and A, B, and C are the parameters calculated analytically. The detail of the parabolic fitting method can be found in [39].

As shown in Fig. 4.2, the parabola fitting method can get proper timing information even if the constant fraction method miscalculates the timing.

4.3.1.2   Method for detector using 500-MHz ADC module

In 2013, the downstream detector subsystems such as BHCV and BHPV used 500-MHz ADC modules. The 500-MHz ADC modules collected 256 samples of the waveforms for every event, which correspond to 512 ns.

Because many pulses were expected to be recorded in the event window, we first identified the pulses recorded inside the event window and defined the timing and energy for each pulse.
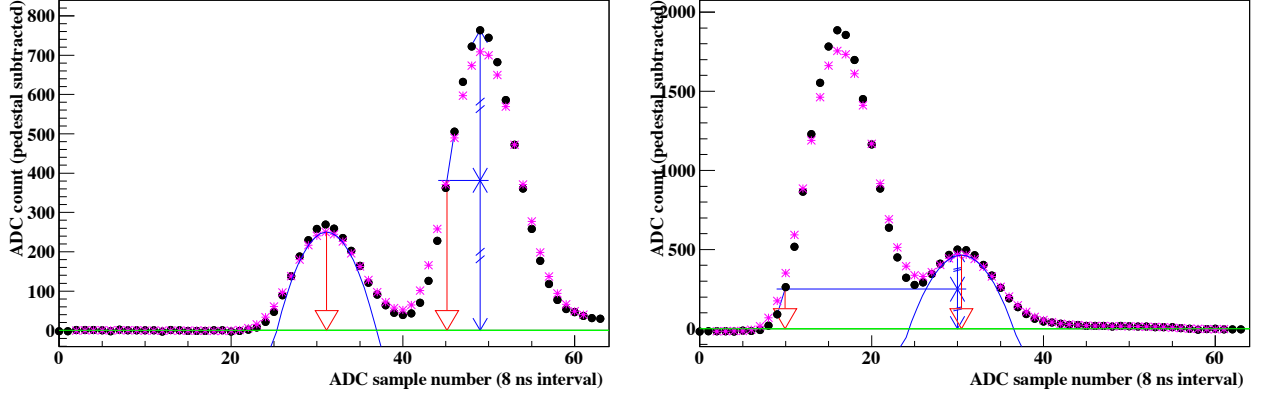
Figure 4.2: The timing for overlapped pulses determined by the constant fraction method and parabola fitting method. The pulse located around the 30th sample is the expected pulse related to the trigger and there is a larger pulse around that pulse. The parabola fitting method can define proper timing while the constant fraction method miscalculates the timing. These figures are taken from[39].
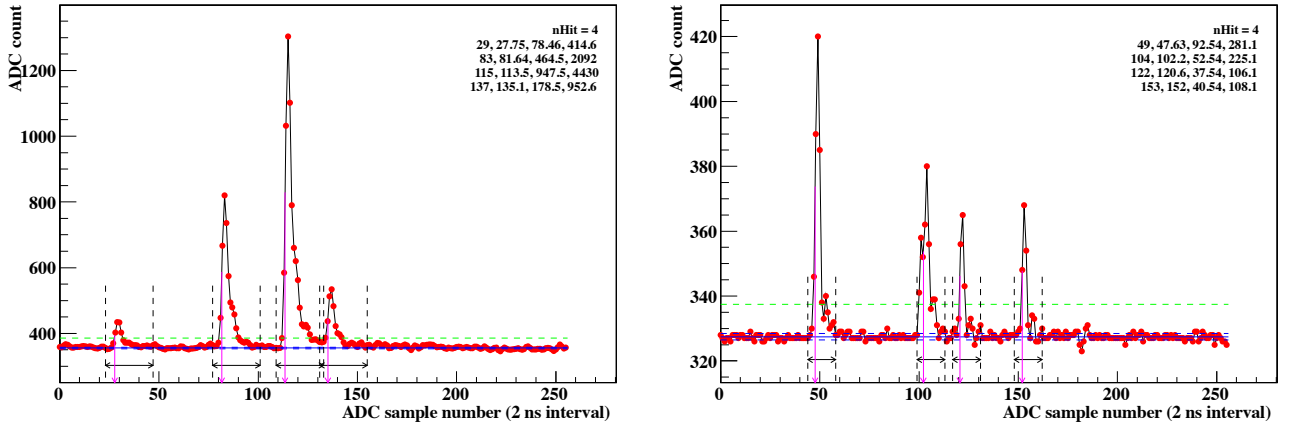
Figure 4.3: Examples of energy and timing extraction from waveforms with 500-MHz sampling. The left (right) figure is for BHCV (BHPV). Red points represent the data points. Blue line represents the pedestal. The region with black arrow is the range for integration to get energy for each pulse. The purple arrows represent the timing of each identified pulse. These figures are taken from [39].

Pedestal

The most frequent value for 256 samples was used as the pedestal of the data for 500MHz ADC modules. This was done by fitting a histogram of ADC values for 256 samples with the gaussian function. After defining the pedestal, the pedestal value was subtracted from each sample.

Pulse identification

The pulse identification was done by searching for local maxima exceeding a given threshold. A certain number of samples around each local maximum was defined as the region to calculate the energy and timing for each pulse. The range of the region for each pulse was 15 samples for the BHPV and 25 samples for the BHCV.

Energy and Timing

The energy of the pulses were calculated by integrating of ADC counts over the region assigned for each pulse. The calibration constant to convert the integrated ADC counts to the energy was acquired by the beam muon data.

Because signals were digitized by 500-MHz ADC without a 10-pole Bessel filter, the pulse shape was different from Gaussian shape, and the parabola fitting method was not suitable. The timing of the pulses were calculated by applying the constant fraction timing method for the selected region of each pulse.

4.3.2 Reconstruction of energy and timing information for the detector modules.

The energy and timing information of the detector modules were calculated from these information of the detector channels.

4.3.2.1 Single-side readout detector

For the detector with the modules with the single-side readout, the energy and timing informations of the channels were used as the information for the module.

4.3.2.2 Detector with dual-side readout

For the detectors with dual-side readout except for the MB and BCV, the sum of the energy of the both ends of the module was used as the energy of the module, and the mean timing of the both ends of the modules was used as the timing of the module.

4.3.2.3 MB and BCV

Because the MB and BCV used the WLS fiber to read the scintillation light out from the scintillator, and the length of the modules were about 5 m, the attenuation of light and the light propagation time inside the WLS fiber were considered.

Timing

Defining the z position of the readout of the modules of MB or BCV as z_{up} and z_{down} for upstream and downstream ends, respectively, a particle hitting the detector at position z_{hit} generates scintillation light arriving at the both ends at:

$$t_{up} = (z_{hit} - z_{up})/v_{prop}, \tag{4.2}$$

$$t_{down} = (z_{down} - z_{hit})/v_{prop}, \tag{4.3}$$

where t_{up} and t_{down} represent the arrival time at upstream and downstream ends, respectively, and v_{prop} represents the propagation velocity of the light in the WLS fiber.

The timing of the modules, t_{mod}, is defined as the average of the timings at the both ends:

$$
\begin{aligned}
t_{mod} &= (t_{up} + t_{down})/2 \\
&= \frac{z_{down} - z_{up}}{v_{prop}}.
\end{aligned}
\tag{4.4}
$$

With this definition, t_{mod} is independent from the hit position.

On the other hand, the hit position z_{hit} can be calculated from Eqs. (4.2) and (4.3) as:

$$z_{hit} = \frac{v_{prop}}{2}(t_{up} - t_{down}) + \frac{z_{up} + z_{down}}{2}. \tag{4.5}$$

The distance between z_{hit} and the z position of the center of the module, $z_{center} = \frac{z_{up}+z_{down}}{2}$, was used as the hit z position of the modules:

$$
\begin{aligned}
z_{mod} &= z_{hit} - z_{center} \tag{4.6} \\
&= \frac{v_{prop}}{2}(t_{up} - t_{down}). \tag{4.7}
\end{aligned}
$$

Energy

Figure 4.4 shows the dependence of ADC output on the z position for cosmic ray muons penetrating the MB and BCV.

By fitting this curve, the position dependence of output at each end can be defined as

$$e_{up} = E_{up} \exp\left(\frac{-z_{mod}}{\Lambda + \alpha z_{mod}}\right), \tag{4.8}$$

$$e_{down} = E_{down} \exp\left(\frac{z_{mod}}{\Lambda - \alpha z_{mod}}\right), \tag{4.9}$$

where $e_{up}(e_{down})$ and $E_{up}(E_{down})$ are the visible output and original energy deposit for the upstream (downstream) end, respectively, and Λ and α are the parameters obtained by fitting, which are shown in Table 4.1.

The energy of the module, E_{mod}, is defined from the Eqs. (4.8) and (4.9) as:

$$
\begin{aligned}
E_{mod} &= E_{up} + E_{down} \\
&= \frac{e_{up}}{\exp\left(\frac{-z_{mod}}{\Lambda+\alpha z_{mod}}\right)} + \frac{e_{down}}{\exp\left(\frac{z_{mod}}{\Lambda-\alpha z_{mod}}\right)}.
\end{aligned}
\tag{4.10}
$$

Parameters	Values
v_{prop}	168.1 mm/ns
Λ	4920.5 mm
α	0.495
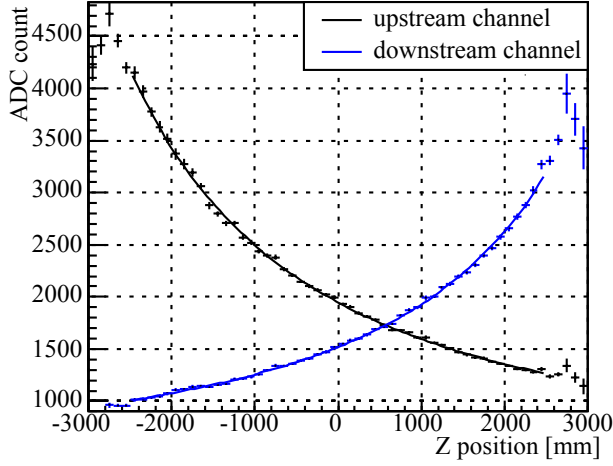
Figure 4.4: Attenuation curve of a MB module taken by cosmic muon events. Horizontal axis represents the distance between the hit position of the cosmic ray muon and the center of the MB module. This plot is taken from [23].

Table 4.1: Parameters used in extraction of the timing and energy information in MB and BCV detector [23].

4.3.3   Photon Cluster Reconstruction

An electro-magnetic shower is created when a photon hits the CsI calorimeter. The shower spread over several crystals because the cross-section of the small crystal of the CsI calorimeter was 2.5 cm and smaller than Molière radius of CsI crystals (3.57 cm[14]).

To reconstruct the energy, timing, and the position of the shower made by photons, we have to define groups of crystals which cover the activity from the shower. We refer the group of crystals as "cluster". At first, the clusters were identified, and the clusters which passed the selection cuts became candidates for the photon clusters.

4.3.3.1   Clustering

Cluster definition

The procedure to define the cluster is called "clustering". At first, the crystals with energy deposits larger than 3 MeV were listed as "seeds" of the cluster. The seed with the maximum energy deposit was chosen as the core seed of the cluster, and the seeds located within 71 mm around the core seed were grouped together to form a cluster. The remaining seeds located within 71 mm from any seeds in the focused cluster were grouped together into the focused cluster. This procedure was iterated until no seeds remained within 71 mm from any seeds in the focused cluster. After defining the first cluster, the same procedure to define the cluster was applied to the remaining seeds until all seeds were assigned into clusters.

Definition of timing, energy, and position information.

69

After defining the clusters, the timing, energy, and position of the clusters were defined as:

$$E_{cluster} = \sum_{i=0}^{n} e_i, \tag{4.11}$$

$$x_{cluster} = \frac{\sum_{i=0}^{n} e_i x_i}{\sum_{i=0}^{n} e_i}, \tag{4.12}$$

$$y_{cluster} = \frac{\sum_{i=0}^{n} e_i y_i}{\sum_{i=0}^{n} e_i}, \text{ and} \tag{4.13}$$

$$t_{cluster} = \frac{\sum_{i=0}^{n} t_i/\sigma_t^2}{\sum_{i=0}^{n} 1/\sigma_t^2}, \tag{4.14}$$

where $E_{cluster}$, $x_{cluster}$, $y_{cluster}$, and $t_{cluster}$ are the energy, x position, y position, and timing of the cluster, respectively. The n represents the number of crystals belonging to the cluster, and e_i, x_i, y_i, and t_i are the energy, x position, y position, and timing of the i-th crystal in the cluster, respectively. The σ_t represents the timing resolution of CsI crystal measured in a past beam-test [44], which was defined as:

$$\sigma_t[ns] = \frac{5}{e_i[MeV]} \oplus \frac{3.63}{\sqrt{e_i[MeV]}} \oplus 0.13, \tag{4.15}$$

where $\oplus$ represents addition in quadrature. The energy of cluster will be corrected after the reconstruction of the decay vertex.

Accidental hit rejection

Because the clustering procedure groups all nearby crystals, the crystals with accidental hit could be included in the cluster. We used the timing difference between the crystal and the cluster to remove the cluster with accidental hits [23]. Figure 4.5 shows the timing difference vs. crystal energy distribution. Two red lines in the plot represent the $\pm 5\sigma$ of timing difference as a function of the crystal energy. These line was made from interpolation of $\pm 5\sigma$ of timing difference in each energy bin. The normalized timing difference for the i-th crystal in the cluster was calculated as:

$$R_i^{time} = \frac{|t_i - t_{cluster}|}{5\sigma(e_i)}, \tag{4.16}$$

where $\sigma(e_i)$ represents the standard deviation of distribution of timing difference for the energy deposit in the i-th crystal, e_i. The crystal with the maximum R_i^{time} with $R_i^{time} > 1$ was removed from the cluster. After removing one crystal, the clustering process was re-iterated with remaining crystals, and the timing of cluster $t_{cluster}$ was recalculated using Eq. (4.14). The R_i^{time} was recalculated based on the updated timing of the cluster, and used to remove accidental hit crystals. This procedure was iterated until all remaining crystals satisfied $R_i^{time} \leq 1$.

4.3.3.2 Photon cluster selection

The clusters with more than one crystal and with total energy larger than 20 MeV are called "photon clusters". Only photon clusters were used for the reconstruction of π^0, and other remaining clusters were not used for reconstruction. Remaining seed crystals were called "isolated hit crystals". Remaining clusters and isolated hit crystals were regarded as extra activities in the CsI calorimeter and used for the event selection.
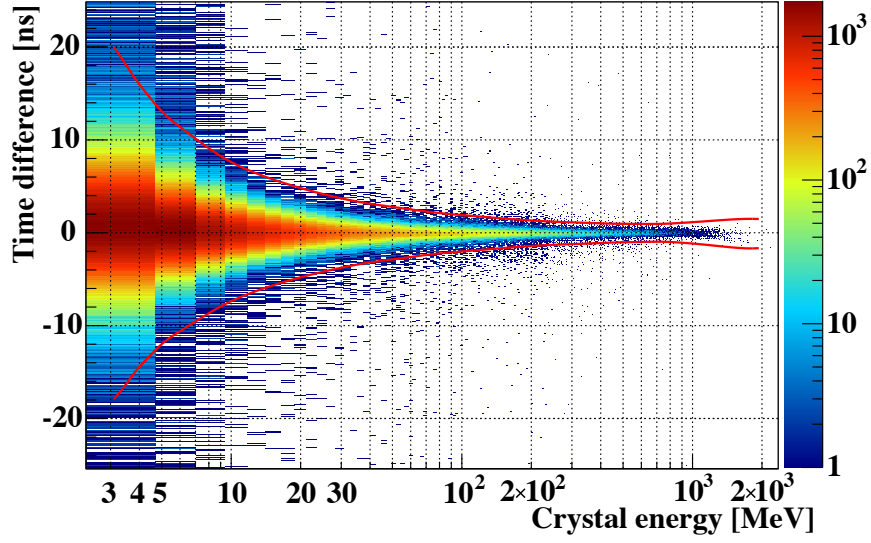
Figure 4.5: The timing difference between cluster and the crystals in the cluster vs. the crystal energy. Horizontal axis represents the energy in each crystal. Colors in the plot represent the number of events in the arbitrary unit. The red line represents the $\pm 5\sigma$ of timing difference in each energy bin. This figure is taken from [23].

4.3.4 π^0 Reconstruction

4.3.4.1 Decay vertex Reconstruction

The π^0s were reconstructed from pairs of photon clusters by assuming that the two photon system has the invariant mass of π^0, $M_{\pi^0}^{PDG} = 134.9766$ MeV/c^2[14], and assuming that the decay vertex is on the beam axis; take $(x, y, z) = (0, 0, Z_{vtx}^{\pi^0})$.

Decay vertex position reconstruction

Figure 4.6 shows a schematic view of the reconstruction of decay vertex of π^0. In case of the two photon system of (γ_1, γ_2) with $(E, x, y, z) = (E_1, x_1, y_1, Z_{CsI}), (E_2, x_2, y_2, Z_{CsI})$, following equations hold from geometrical conditions:

$$
\begin{align}
r_{12}^2 &= d_1^2 + d_2^2 - d_1 d_2 \cos \theta_{12}, \tag{4.17}\\
r_{12}^2 &= (x_1 - x_2)^2 + (y_1 - y_2)^2, \tag{4.18}\\
d_1 &= \sqrt{(\Delta Z)^2 + r_1^2}, \tag{4.19}\\
d_2 &= \sqrt{(\Delta Z)^2 + r_2^2}, \tag{4.20}\\
r_1 &= \sqrt{x_1^2 + y_1^2}, \tag{4.21}\\
r_2 &= \sqrt{x_2^2 + y_2^2}, \text{ and} \tag{4.22}\\
\Delta Z &= Z_{CsI} - Z_{vtx}^{\pi^0}, \tag{4.23}
\end{align}
$$

where r_{12} represents the distance between the two photon clusters, d_i represents the distance between the i-th photon cluster and the decay vertex, r_i represents the distance between the

71
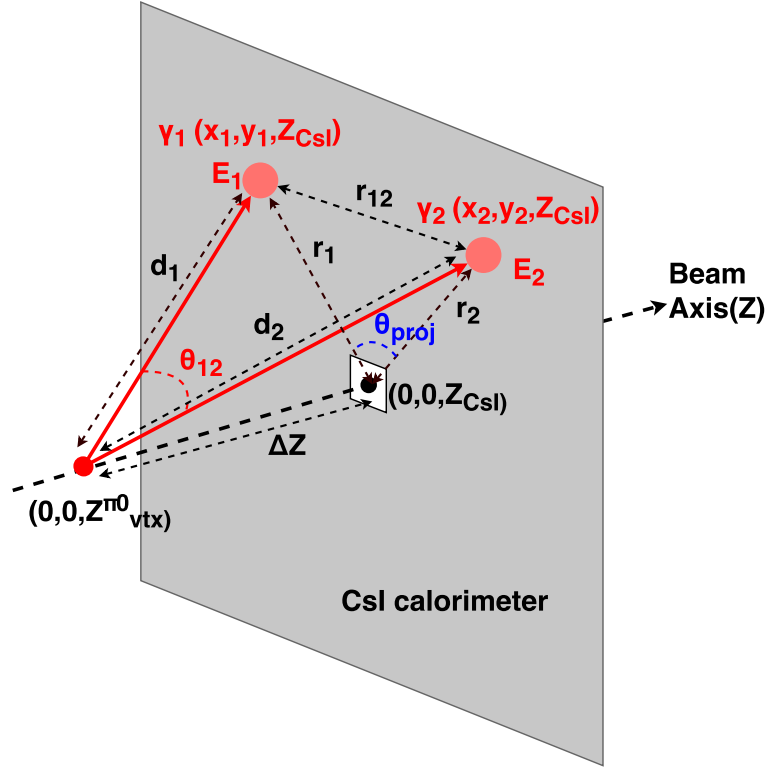
Figure 4.6: Schematic view of π^0 Reconstruction

i-th photon cluster and the center of the surface of the CsI calorimeter, θ_{12} represents the angle between the directions of the two photon clusters, and ΔZ represents the distance between the decay vertex and the center of the surface of the CsI calorimeter which is located on $(x, y, z) = (0, 0, Z_{CsI})$. From the conservation of the four-momentum in the two photon system, following equation holds:

$$M_{\pi^0}^2 = 2E_1 E_2 (1 - \cos \theta_{12}) \tag{4.24}$$

From Eqs. (4.17) and (4.24), the z position of the decay vertex, $Z_{vtx}^{\pi^0}$, can be calculated. The solution of these equations with $Z < Z_{CsI}$ was chosen as $Z_{vtx}^{\pi^0}$.

Decay timing reconstruction

After defining the position of decay vertex, the timing of the π^0 decay was calculated. Because the timing of the decay is the timing when the photons were generated at the decay vertex, the time of the decay can be calculated by subtracting the photons's time of flight from the arrival time at the surface of the CsI calorimeter. The timing of the decay, T_{vtx}, is defined as:

$$T_{vtx} = \frac{\sum_{i=0}^{n} T_i / \sigma_T^2}{\sum_{i=0}^{n} 1 / \sigma_T^2}, \tag{4.25}$$

$$T_i = t_{cluster}^i - d_i / c, \tag{4.26}$$

where c represents the speed of light, $t_{cluster}^i$ represents the arrival time of the i-th photon at the surface of the CsI calorimeter, T_i represents the timing of photon generation at the decay

vertex, and σ_T represents the timing resolution of photon cluster, which is defined as:

$$\sigma_T = \frac{3.18}{\sqrt{E^i_{cluster}[MeV]}} \oplus 0.19 \text{ [ns]}, \tag{4.27}$$

where $E^i_{cluster}$ represents the energy of the i-th photon cluster.

Transverse Momentum reconstruction

The transverse momentum of the two-photon system or reconstructed π^0, $P_T^{\pi^0}$, is defined as:

$$P_T^{\pi^0} = \left| \sum_{i=1,2} E^i_{cluster} \frac{\vec{r_i}}{\sqrt{r_i^2 + \Delta Z^2}} \right|, \tag{4.28}$$

where $\vec{r_i}$ represents the two-dimensional vector for the hit position of for the i-th photon cluster on the surface of the CsI calorimeter, which is defined as $\vec{r_i} = (x_i, y_i)$ and $r_i = |\vec{r_i}|$.

4.3.4.2 Energy and position correction for photon clusters

After reconstructing the decay vertex of the π^0, the energy and the hit position of the photons from the π^0 were corrected based on the incident angle of the photons from the vertex. The procedure of the decay vertex reconstruction was iterated after correcting the energy and positions of the cluster.

Energy correction

We calculated the energy of photon cluster by summing the energy of the seeds crystals. Because we used crystals with energy deposit larger than 3 MeV to make clusters, the energies in other crystals smaller than 3 MeV were not included in the cluster energy, and thus the energy of photon cluster was different from real energy of incident photon. This effect was studied with MC simulation and corrected for based on the incident angle and the measured energy, as described in [49].

Position correction

The x and y positions of cluster, (x_{clus}, y_{clus}), were defined as the energy-weighted mean position with Eqs. (4.12) and (4.13). If photons hit on the CsI calorimeter with finite incident angle, they were different from the actual hit position on the surface of the CsI calorimeter, (x_{inc}, y_{inc}).

Figure 4.7 shows the relationship between the calculated position and actual hit position of the photons. The energy-weighted position corresponds to the position of the shower maximum. The actual hit position, (x_{inc}, y_{inc}), was calculated as:

$$x_{inc} = x_{cluster} - L \sin\theta \cos\phi, \tag{4.29}$$
$$y_{inc} = y_{cluster} - L \sin\theta \sin\phi, \tag{4.30}$$

where θ represents the incident angle, ϕ represents the azimuthal angle, and the L represents the length between the incident position and the shower maximum. The L was estimated with MC simulation and parametrized as:

$$L = X_0 \left(p_0 + p_1 \ln \left(E_{inc}[GeV] \right) \right), \tag{4.31}$$
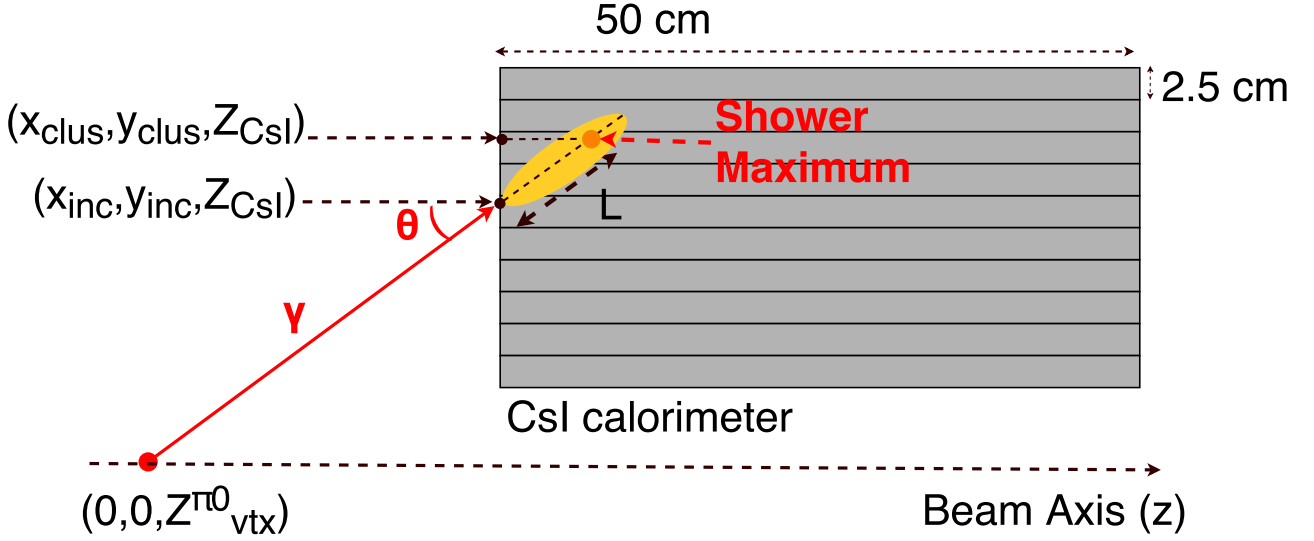
Figure 4.7: Schematic view of the correction of the hit position of photon

where $X_0 = 18.5$mm[14] represents the radiation length of the CsI crystal, p_0 and p_1 represent the length of shower normalized by the radiation length. From MC simulation, these parameters were estimated as $p_0 = 6.490$ and $p_1 = 0.993$.

4.3.5 K_L Reconstruction

The decay modes of the K_L such as $K_L \to 3\pi^0$, $K_L \to 2\pi^0$, and $K_L \to 2\gamma$ were used in the calibration, normalization, and estimation of the background events. In such cases, the K_L was reconstructed from the reconstructed π^0 and γ.

Reconstruction of the $K_L \to 2\gamma$ decay

In case of $K_L \to 2\gamma$ decay mode, K_L can be reconstructed with the same way as the case for π^0 reconstruction, by replacing M_{π^0} with the mass of K_L, M_{K_L}.

Reconstruction of the $K_L \to 3\pi^0$, $K_L \to 2\pi^0$ decay

In the case of the $K_L \to 3\pi^0$ and $K_L \to 2\pi^0$ decays, K_L is reconstructed from the reconstructed π^0. The true decay vertex of K_L and π^0 might not be located on the beam axis. At first, K_L and π^0 were reconstructed by assuming their decay vertex to be on the beam axis and the positions of their decay vertexes were re-calculated after the reconstruction of K_L, as described below.

Reconstruction of the decay vertex of the K_L

K_L was reconstructed by assuming its decay vertex to be on the beam axis. The z position of its decay vertex, Z_{K_L}, was defined as the weighted mean of the z positions of the reconstructed decay vertexes of π^0s:

$$Z_{K_L} = \sum_i^N \frac{Z_{\pi^0}^i / (\sigma_Z^i)^2}{1/(\sigma_Z^i)^2}, \quad (4.32)$$

74

where $Z_{\pi^0}^i$ represents the z position of the decay vertex of the i-th π^0, σ_Z^i represents the position resolution for the decay z vertex position of the i-th π^0. The N represents the number of π^0s used in the reconstruction: 3 for $K_L \to 3\pi^0$ and 2 for $K_L \to 2\pi^0$. For $K_L \to 3\pi^0 (K_L \to 2\pi^0)$, K_L was reconstructed from three (two) π^0s and they were reconstructed from six (four) photon clusters. The number of possible combinations to choose pairs of the photons from six (four) photon clusters is 15 (3). To select the best combination of pairs from these combinations, we define the variance of π^0's vertex as follows:

$$\chi_Z^2 = \sum_i^N \frac{(Z_{\pi^0}^i - Z_{K_L})^2}{\sigma_Z^2}. \tag{4.33}$$

The combination with the smallest χ_Z^2 was regarded as the best combination. The Z_{K_L} with such combination was called $Z_{vtx}^{K_L}$ and used for event selection.

Correction for the decay vertex

After reconstruction of the decay vertex of the K_L, x and y positions of its decay vertex, $(x, y) = (X_{vtx}^{K_L}, Y_{vtx}^{K_L})$, were recalculated by interpolating between the T1 target and the position of the center of energy on the surface of the CsI calorimeter, $(x, y) = (X_{COE}, Y_{COE})$.

By assuming the T1 target as a point source, (X_{vtx}, Y_{vtx}) can be defined as follows:

$$X_{vtx}^{K_L} = X_{COE} \frac{Z_{vtx}^{K_L} - Z_{Target}}{Z_{CsI} - Z_{Target}}, \tag{4.34}$$

$$Y_{vtx}^{K_L} = Y_{COE} \frac{Z_{vtx}^{K_L} - Z_{Target}}{Z_{CsI} - Z_{Target}}, \tag{4.35}$$

$$X_{COE} = \frac{\sum_i^n E_{cluster}^i x_{cluster}^i}{\sum_i^n E_{cluster}^i}, \tag{4.36}$$

$$Y_{COE} = \frac{\sum_i^n E_{cluster}^i y_{cluster}^i}{\sum_i^n E_{cluster}^i}, \tag{4.37}$$

where n represents the number of photon clusters used in the reconstruction, Z_{target} represents the z position of the T1 target.

After defining the $X_{vtx}^{K_L}$ and $Y_{vtx}^{K_L}$, the decay vertexes of π^0 and K_L were re-calculated with the corrected x and y information for decay vertex of K_L.

4.4 Event selection for $K_L \to \pi^0 \nu \overline{\nu}$ analysis

We have developed methods to select the $K_L \to \pi^0 \nu \overline{\nu}$ events. The methods are categorized into the cut on number of photon clusters, veto cuts, photon cluster quality cuts, trigger bias cuts, kinematic cuts, and neural-net cuts, as described below.

4.4.1 Number of photon cluster on the CsI calorimeter

The events with two photon clusters on the CsI calorimeter were used for $K_L \to \pi^0 \nu \overline{\nu}$ analysis.

4.4.2 Signal region and blind region masked for analysis

As shown in Figure 4.8, two regions were defined in the $P_T^{\pi^0} - Z_{vtx}^{\pi^0}$ plane for $K_L \to \pi^0 \nu \overline{\nu}$ analysis.
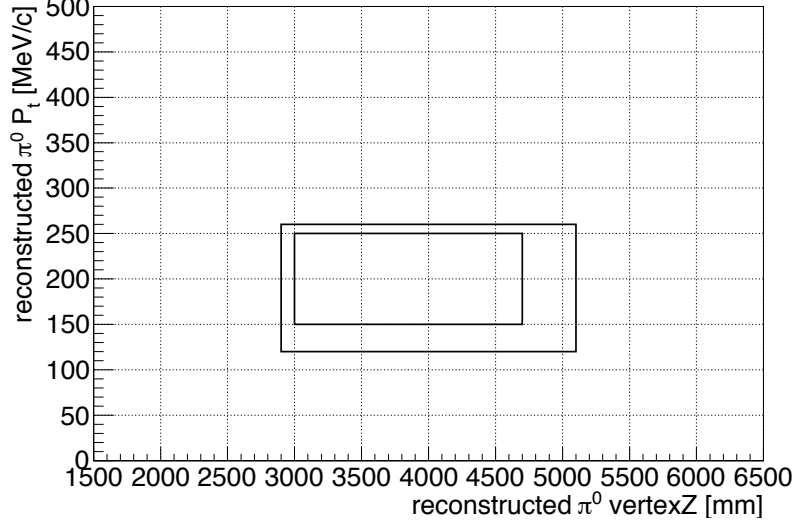
Figure 4.8: The signal region and blind region defined in the $P_T^{\pi^0} - Z_{vtx}^{\pi^0}$ plane. The region inside inner and Outer boxes are the signal region and blind region, respectively.

Signal region

To reject the events from $K_L \to 2\gamma$, $2\pi^0$, and $3\pi^0$ decays, the events with a small $P_T^{\pi^0}$ were rejected. To reject the π^0 and η generated at the detector surrounding the decay region, the $Z_{vtx}^{\pi^0}$ of reconstructed π^0 was required to be far from the NCC, FB, and CV.

The region for such selections is called "signal region" and defined as:

- $150[\text{MeV/c}] < P_T^{\pi^0} < 250[\text{MeV/c}]$

- $3000[\text{mm}] < Z_{vtx}^{\pi^0} < 4700[\text{mm}]$

The events located inside the signal box after imposing all the event selection cuts were regarded as candidate $K_L \to \pi^0 \nu \overline{\nu}$ events.

Blind region

To prevent the human bias that could affect the optimization of the event selection or the estimation of the number of background events, the events inside and around the signal box were excluded from the analysis during these processes. The region for exclusion is called "blind region" and defined as:

- $120[\text{MeV/c}] < P_T^{\pi^0} < 260[\text{MeV/c}]$

- $2900[\text{mm}] < Z_{vtx}^{\pi^0} < 5100[\text{mm}]$

76

After finalizing the optimization of cuts and the estimation of the number of backgrounds, the events inside the blind region were examined.

4.4.3 Veto cuts

Veto cuts are the cuts to reject the events with extra activities in the detector subsystems. To prevent losses caused by accidental hits on the detector subsystems, the timing and energy of the modules of the detector subsystems were re-defined based on the timing and position of the decay vertex. If a detector module has a hit consistent with a particle coming from the vertex, the event was rejected.

4.4.3.1 CsI Veto Cuts

As described in Section 4.3.3.2, only the photon clusters were used in the reconstruction of π^0 and K_L. Other clusters and isolated hit crystals were used for rejecting the events with extra activities in the CsI calorimeter.

Extra cluster veto cut

Extra clusters on the CsI calorimeter can be caused by extra photons from $K_L \to 3\pi^0$ and $K_L \to 2\pi^0$ decay modes or accidental hits of photons from the beam. To reject events with extra photons from $K_L \to 3\pi^0$ and $K_L \to 2\pi^0$ decays, the timings of the extra photons at the K_L vertex were calculated and compared with the time of decay. The events which had any extra clusters within ± 10 ns of the decay timing were rejected.

Isolated hit crystals veto cut.

There were two sources of the isolated hit crystals. Accidental hits not related to the decay of K_L or π^0 could be the source of the isolated hit crystals. However, electromagnetic showers caused by photon hits could also be the source of the isolated hit crystals. To distinguish whether the isolated hit crystal was caused by the accidental hit or the photon hit, the characteristics of the isolated hit crystals around the photon cluster was studied with MC simulation. Figure 4.9 shows the correlation between the energy deposit in the isolated crystal and the distance from the closest photon cluster. The energy threshold E_{th} for isolated hit crystal to reject accidental hits is shown in the red line in Fig. 4.9 and defined as:

$$E_{th} = \begin{cases} 10 \text{ [MeV]} & \text{for } d \leq 200 \text{ mm,} \\ (13.5 - 0.0175d) \text{ [MeV]} & \text{for } 200 < d \leq 600 \text{ mm,} \\ 3 \text{ [MeV]} & \text{for } d > 600 \text{ mm.} \end{cases} \tag{4.38}$$

The events with any isolated crystal with energy deposit larger than threshold value and with hit timing within ± 10 ns of the timing of the closest cluster were rejected.

4.4.3.2 Other Detector Veto Cuts

To reject events with extra particles from the K_L decay hitting the veto detector subsystems, the timing of the extra particle extrapolated back to the decay vertex was calculated. This timing was defined as the timing of modules for veto cut, called "veto timing" t_{mod}^{veto}, and were compared with the timing of the decay vertex. The modules with the veto timing within the certain range from the T_{vtx}, called "veto window", were regarded as the modules hit by particles
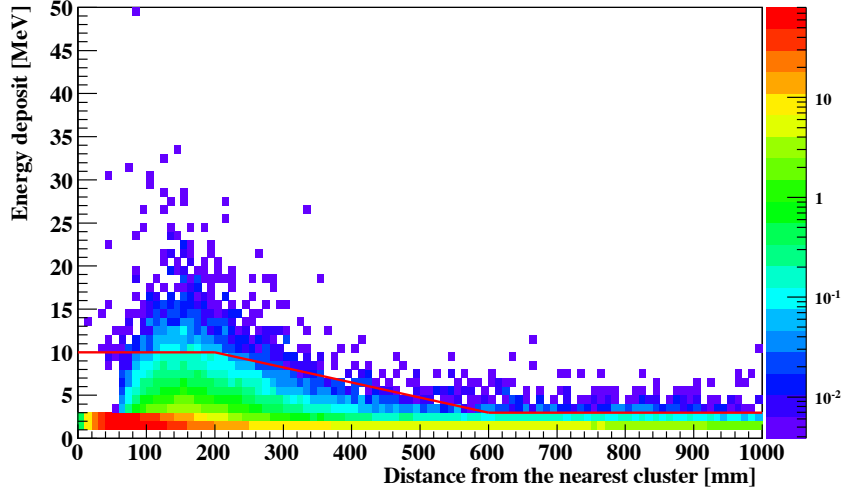
Figure 4.9: The correlation between the energy deposit in the isolated hit crystal and distance from the closest photon cluster. The result from MC simulation for $K_L \to \pi^0 \nu \overline{\nu}$ is shown. Hit crystal with energies and distances above the red line are rejected. This figure is taken from [39].

from K_L decay. The timing and energy of the module with the maximum energy was used for veto cuts. For BHPV, different method was developed and defined for veto cut.

Timing definition

The veto timing of veto detector modules was defined as the timing when possible particle which hit the modules was generated at the decay vertex. The veto timing for detector modules t_{mod}^{veto} were defined as:

$$t_{mod}^{veto} = t_{mod} - L_{module}/c, \tag{4.39}$$

where t_{mod} represents the timing of the module, c represents the speed of light, and L_{module} represents the distance between the hit position on the module of the detector subsystems and the decay vertex.

The definition of L_{module} is different depending on type the detector because the definition of hit position in the detector modules are different. For the MB and BCV, the detectors which can reconstruct the hit z position, L_{module} was calculated as:

$$
\begin{aligned}
L_{module} &= \sqrt{r_{module}^2 + (z_{hit} - Z_{vtx}^{\pi^0})^2} \\
&= \sqrt{r_{module}^2 + (z_{mod} + z_{center} - Z_{vtx}^{\pi^0})^2},
\end{aligned} \tag{4.40}
$$

where r_{module} represents the inner radius of the MB or BCV modules. For CV, L_{module} was defined as:

$$L_{module}^i = \sqrt{x_i^2 + y_i^2 + (z_i - Z_{vtx}^{\pi^0})^2}, \tag{4.41}$$

where L_{module}^i represents the L for the i-th module of CV, x_i and y_i represent the x and y positions of the center of the i-th module of CV, and z_i represents the z position of the i-th module of CV. For the detectors located downstream of the CsI calorimeter, such as the CC03,

78

CC04, CC05, CC06, and BHCV, L_{mod} was defined as just the difference in z positions:

$$L_{module} = |z_{det} - Z^{\pi^0}_{vtx}|, \tag{4.42}$$

where z_{det} represents the z position of the detectors.

For the detectors located upstream of the CsI calorimeter such as FB and NCC, ΔZ defined in Eq. (4.23), was used instead of L_{module} to suppress the bias due to the miscalculation of $Z^{\pi^0}_{vtx}$, and t^{veto}_{mod} was defined as:

$$t^{veto}_{mod} = t_{mod} - \Delta Z/c, \tag{4.43}$$

which is effectively the timing difference between the timing of module and averaged timing of the photon clusters.

BHPV

The development of the electromagnetic shower induced by the photon is observed as coincident hits in consecutive BHPV modules. To identify the activities from the photons, we have to define a group of coincident hits in the consecutive BHPV modules which cover the electromagnetic shower. The number of consecutive BHPV modules with coincident hits ($N_{coincident}$) was used in veto cut as follows.

Hit definition for veto cut

Among the hits identified in the 256-samples of waveform of BHPV channels, the pulses with the energy deposits larger than 2.5 photoelectrons were regarded as the hits in the module and used in further selections.

Timing correction

The timings of hits in the modules were corrected to be aligned with the timing of the first BHPV module by taking the photon's time of flight into account and defined as:

$$T^j_i = t^j_i - \Delta z_{0i}/c, \tag{4.44}$$

where t^j_i and T^j_i represent the timings of the j-th hit in the i-th BHPV module before and after correction, respectively. The Δz_{0i} represents the distance between the first BHPV module and the i-th BHPV module.

Definition of coincident hits

After the timing correction, the modules with hits in either end of readout were scanned from upstream to downstream to identify consecutive modules with coincident hits. At first, the earliest hit in the either end of the most upstream module was chosen as the core hit of the group. The hits within ± 10 ns of the timing of core hit were searched for in the other end of the module and in the channels of the consecutive modules, and grouped together as coincident hits.

This procedure was iterated until no hits were found in the consecutive modules. After defining the first group of coincident hits, the same procedure to define a group was applied to the remaining hits in the modules until all hits were assigned into groups.

Definition of timing for veto cut
The timing of the group of the coincident hits is called "coincident time", defined as:

$$T_{\text{coincident}} = \frac{\sum_i^N T_i}{N}, \tag{4.45}$$

where N represents the number of hits in the group, and T_i is the timing of the i-th hit in the group. The timing of the group of the coincident hits for veto cut is defined as:

$$T_{\text{coincident}}^{\text{veto}} = T_{\text{coincident}} - (T_{vtx} + \frac{Z_{BHPV0} - Z_{vtx}^{\pi^0}}{c}), \tag{4.46}$$

where Z_{BHPV0} represents the z position of the first BHPV module.

4.4.4 Photon Cluster Quality Cuts

The photon cluster quality cut is the cut to reject the clusters with poor information or clusters made by charged-particle hits or hadronic interactions. The cuts were applied to the sizes, positions, and the energies of photon clusters.

Fiducial Cuts
To reject the photons with a shower leak, the photons that hit near the inner or outer edges of the CsI calorimeter were rejected. To reject the photons hitting close to the beam hole and CC03, the hit x and y positions of photons were required to have $|x|$ and $|y|$ larger than 150 mm. To reject photons hitting the outer edge of the CsI calorimeter, the distance between photon cluster and the beam-axis, $\sqrt{x^2 + y^2}$, was required to be smaller than 850 mm.

Cluster size
To reject clusters with small energies or the clusters made by minimum ionizing particles, the number of crystals in the cluster is required to be larger than 4.
To reject clusters made by hadronic interactions such as neutron hits, clusters with small size were rejected. The size of cluster was called "Cluster RMS ($RMS_{cluster}$)" and defined as

$$RMS_{cluster} = \sqrt{\sum_i \frac{e_i R_i^2}{\sum_j e_j}}, \tag{4.47}$$

$$R_i = \sqrt{(x_i - x_{cluster})^2 + (y_i - y_{cluster})^2}, \tag{4.48}$$

where R_i represents the distance between the i-th crystal with $(x, y) = (x_i, y_i)$ and the center of energy of the cluster $(x_{cluster}, y_{cluster})$ defined in Eqs. (4.12) and (4.13). The $RMS_{cluster}$ was required to be larger than 10 mm.

Photon Energy
To reject photons with small energies, which have poor information and which may be made by hadronic interactions, the energy of each photon was required to be between 100 MeV and 2000 MeV.

Cluster distance from closest dead channel
There were some dead channels in the CsI calorimeter both in 2013 and 2015 runs. To prevent miscalculations of the energies and positions of the photon clusters, the photon clusters were required to be at least 53 mm far away from the dead channels.

$E\theta$ cut

The product of the energy and the incident angle of each photon was required to be less than 2500 MeV·degree to reject photons associated to a π^0 reconstructed with wrong pairing.

Shape χ^2

To reject non-photon clusters, the transversal shape of the photon cluster, *i.e.* the distribution of crystal energies, was compared with the typical shape of a single photon cluster derived from MC simulation. To evaluate the consistency of an observed cluster with an assumption of the photon cluster, χ^2_{Shape} is defined as

$$\chi^2_{\mathrm{Shape}} \quad = \quad \frac{1}{N} \sum_i^N \left(\frac{e_i/E_{inc} - \mu}{\sigma} \right)^2, \tag{4.49}$$

where N represents the number of crystals in the cluster which were used for the summation, e_i represents the energy in the i-th crystal in the cluster, E_{inc} represents the energy of incident photon. The μ and σ are the mean and RMS values for e_i/E_{inc} derived from the MC simulation, respectively. The χ^2_{Shape} was calculated for each cluster, and the maximum χ^2_{Shape} among two photon-clusters was used for the selection for π^0. The detail of the study about the cluster shape and the definition of χ^2_{Shape} can be found in [49].

4.4.5 Trigger Bias Cut

Total energy of two photons

As shown in Table 2.2, the data was taken by requiring the total energy of CsI calorimeter to be larger than 550 MeV. As shown in Fig. 3.12, the effective threshold at the online trigger stage was smeared by the difference of timings and gains between channels. To remove such bias due to the online trigger, the total energy of the two photons was required to be larger than 650 MeV.

COE radius cut

As discussed in Section 2.6.2.2, the COE radius was required to be larger than 165 mm in the Lv2 Trigger decision. Figure 4.10 shows the COE radius distribution of the CsI calorimeter in the offline analysis with and without Lv2 Trigger decision imposed. Here the offline COE radius is defined as:

$$COE_{\mathrm{offline}} = \frac{\sqrt{(E_1 x_1 + E_2 x_2)^2 + (E_1 y_1 + E_2 y_2)^2}}{E_1 + E_2}, \tag{4.50}$$

where E_i, x_i, y_i are the energy, x, and y positions of the i-th photon cluster. The effective threshold for COE radius at online trigger stages was smeared by the difference of timing and gains between channels. To remove such bias due to online trigger, the COE radius in offline analysis was required to be larger than 200 mm.

4.4.6 Kinematic Cuts

The kinematic cuts are the cuts to reject events with two photon clusters made by background. The kinematic cuts use the information of the two photon clusters and the reconstructed π^0.
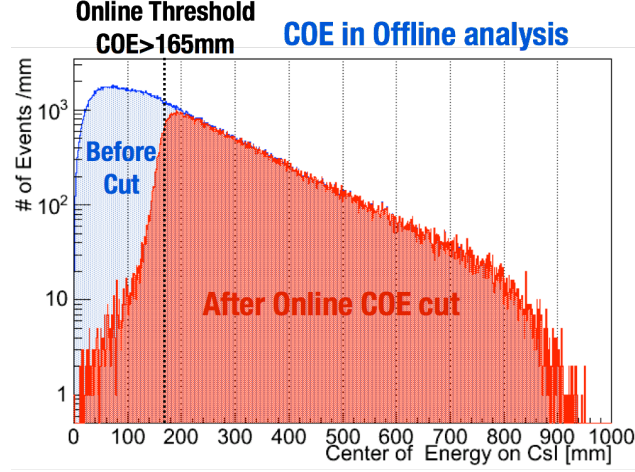
Figure 4.10: COE radius distribution

4.4.6.1 Cut for two photons

Hit position distance

To ensure that the two photon clusters were separated far enough to prevent mis-identification of one photon cluster as two clusters, the distance between the two photon clusters was required to be larger than 300 mm.

Energy ratio of two photons

The energy balance between the two photons was required to reject π^0 reconstructed with a wrong pair of photons. The energy ratio between the two photons, E_L/E_H, was required to be larger than 0.2, where E_L and E_H represent the energy of low-energy and high-energy photons, respectively.

Timing difference between two photons

The timing difference between the two photons, $|T_2 - T_1|$, was required to be less than 2 ns to ensure that they came from the same vertex, where T_i is the timing when the i-th photon was generated at the vertex, defined in Eq. (4.26).

4.4.6.2 Cut for π^0

π^0 kinematic cut

The correlation between $P_T^{\pi^0}$, $Z_{vtx}^{\pi^0}$, the longitudinal momentum ($P_Z^{\pi^0}$), and the energy of reconstructed π^0 (E_{π^0}) were studied with the MC simulation to reject $\eta \to \gamma\gamma$ generated by neutrons hitting the CV. Figure 4.11 shows the correlations between $P_T^{\pi^0}/P_Z^{\pi^0}$ vs. $Z_{vtx}^{\pi^0}$ E_{π^0} vs. $Z_{vtx}^{\pi^0}$, which were made from the MC simulation of $K_L \to \pi^0 \nu \bar{\nu}$. The allowed region for π^0 was defined as shown in Fig. 4.11.

Projected opening angle cut

The opening angle between the two photon directions projected on the x-y plane was used to suppress the two photons emitted back-to-back from $K_L \to 2\gamma$ decay. As shown in Fig. 4.6, this projected opening angle, θ_{proj}, was calculated from the position of the two photon clusters. The θ_{proj} was required to be smaller than 150°.
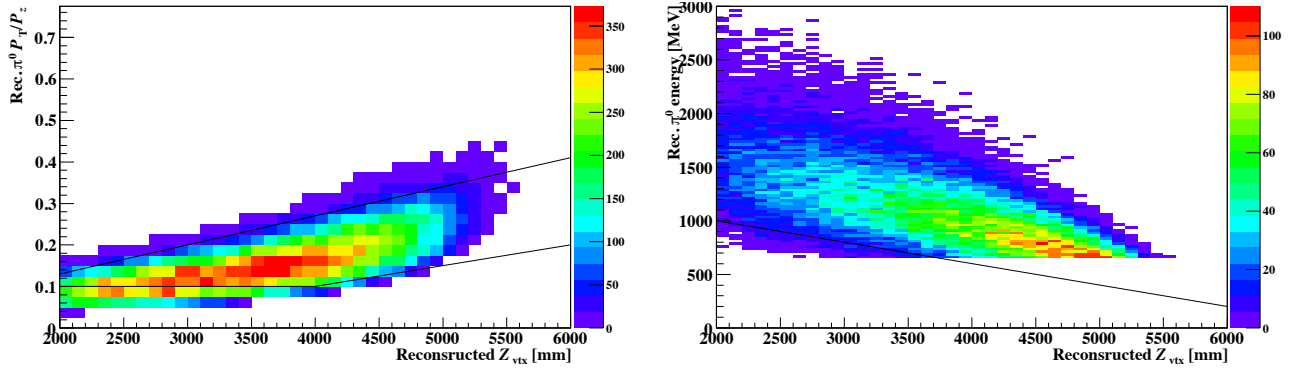
Figure 4.11: The correlation between $P_T^{\pi^0}/P_Z^{\pi^0}$ or E_{π^0} and $Z_{vtx}^{\pi^0}$ in MC simulation of $K_L \to \pi^0 \nu \overline{\nu}$. The black line shows the border of the allowed region. These figures are taken from [39].

4.4.7 Neural Net Cuts

To reject the background induced by neutrons hitting the CsI calorimeter, two cuts based on the output of the neural net were developed. One cut uses the difference in the distributions of reconstructed kinematics between MC simulation and neutron-rich events, and is called "Kinematics Neural net cut (NN_{kine})". The other cut uses the difference in transversal shapes of the clusters between MC simulation and neutron-rich events and is called "Cluster Shape Neural net cut (NN_{shape})". These neural net cuts were trained with the MC simulation for $K_L \to \pi^0 \nu \overline{\nu}$ events, and neutron-rich events taken in 2013 with the Aluminum target inserted in the beam. The detail of the neural net cuts can be found in [39].

4.4.8 Summary of the Cuts

The cuts used in the event selection for $K_L \to \pi^0 \nu \overline{\nu}$ analysis are summarized in Table 4.2 and Table 4.3.

Table 4.2: The list of the veto windows and the energy thresholds imposed on the detector subsystems.

Detector	Energy Threshold[MeV]	Veto Window[ns]
CsI(Isolated hit crystal)	depends on the distance	±10
CsI(Extra clusters)	3	±10
FB,NCC	2	±20
MB	2	±30
BCV	1	±30
CV	0.2	±40
LCV	0.6	±15
OEV	2	±10
CC03,CC04,CC05,CC06(CsI)	3	±15
CC03,CC04,CC05,CC06(Scintillator)	1	±15
BHCV	0.3	±7.5
BHPV	($N_{coincident}$ <3)	±7.5

Table 4.3: The summary of kinematics cuts and other cuts.

Cut	Requirement
Trigger Bias Cuts	
Total energy of two photons	>650 MeV
COE radius	$COE_{offline}$ >200 mm
Photon Cluster Quality Cuts	
Fidutial Cut	$\|x_{cluster}\|$ >150 mm, $\|y_{cluster}\|$ >150 mm, $\sqrt{x_{cluster}^2 + y_{cluster}^2}$ <850 mm
Cluster Size	$N_{crystal} > 4$ crystals, $RMS_{cluster}$ >10 mm
Photon Energy	100 MeV< E_γ <2000 MeV
Distance from dead channel	>53 mm from the closest dead channel
$E\theta$	<2500 MeV
Maximum χ_{shape}^2 for two photon clusters	<4.6
Kinematics Cuts	
Cluster distance	>300 mm
Energy ratio	>0.2
Photon timing difference	<2 ns
π^0 kinematics cut	Figure 4.11
Projected Opening angle cut	$\theta_{proj} < 150°$
Neural Net Cuts	
Kinematics Neural net cut	NN_{kine} >0.67
Cluster shape Neural net cut	NN_{shape} >0.8

4.4.9 Result after event selection

Figure 4.12 shows the $Z_{vtx}^{\pi^0} - P_T^{\pi^0}$ distribution for the events remained after all the event selection cuts imposed.

4.5 Background sources and its estimation

There are two types of the background sources: Kaon decay events and neutron-induced events. The number of background events from the Kaon decay events was estimated with the MC simulation of the Kaon decay modes. The number of background events related to neutron hits on the detector was estimated with both the neutron-rich events taken in special run in 2013 with Aluminum target inserted, and the MC simulation of halo neutrons around the beam. The number of background events in the signal box was estimated with the MC simulation and data events in the side-band region around the blind-region shown in Fig. 4.12.

The sources of the background events and the estimation of the contribution of them are briefly summarized in this section. The estimation of the number of the background events was done by Dr. K. Shiomi [48] and Dr. Y. Maeda [39], and details of these estimation can be found in the references [39, 48]. In this section, the possible source and the number of the background events in each region, shown in Fig. 4.12, are described.
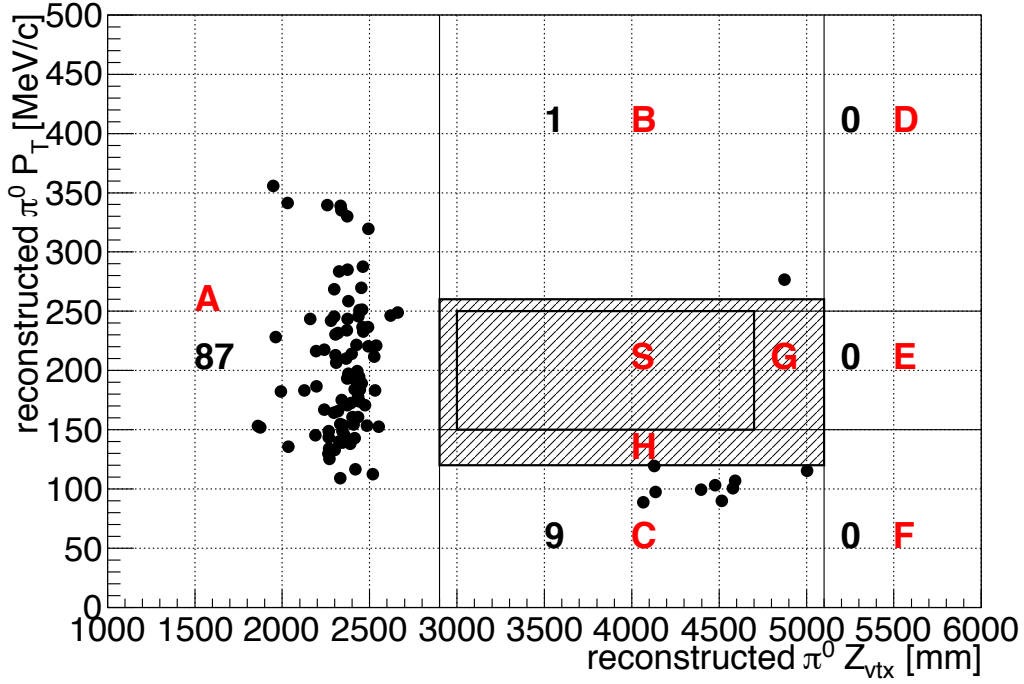
Figure 4.12: $Z_{vtx}^{\pi^0} - P_T^{\pi^0}$ distribution after all event selection imposed. The number of events in each region and the label of each region are also shown.

4.5.1 Neutron background

4.5.1.1 Region A: Upstream neutron background (NCC background)

In region A, many background events are located around $2000[\text{mm}] < Z_{vtx}^{\pi^0} < 2600[\text{mm}]$. This z position corresponds to the location of the NCC. If the halo neutrons around the beam hit the NCC, they can produce π^0. Two photons from the π^0 can hit the CsI calorimeter and pass all the event selection cuts. The background from this process was the main source of the background in the KEK E391a experiment. Even though the signal region was set far from NCC, the background from this process can enter the signal region due to the z position resolution for the reconstructed decay vertex. We refer to the background from this process as "NCC background". The number of NCC background events in the signal region was estimated to be 0.06 ± 0.06 based on the MC simulation for halo-neutrons [48].

4.5.1.2 Region B: Downstream neutron background (Hadronic interaction events)

Figure 4.13 shows the $Z_{vtx}^{\pi^0} - P_T^{\pi^0}$ distribution after imposing all the event selection cuts except for the cuts related to the cluster shape such as NN_{shape} and χ^2_{shape}. Because many events appeared in region B and E after removing the cluster shape related cuts, the background events in these regions were considered to have clusters made by hadronic interactions.

Single neutron hitting the CsI calorimeter can produce two clusters if the first cluster made by incident neutron produces another neutron which makes the second cluster. This process can be a source of background events if we cannot distinguish betwen electromagnetic showers and that from hadronic showers. We refer to the background from this process as "Hadronic interaction events".

To estimate the number of the hadronic interaction events, the events taken in the special

run with Decay Volume Upstream Al target in the beam was used as the controlled samples which contain the neutrons scattered at the aluminum target. Because there was a discrepancy in the energy distribution between events from the Physics run and from the Decay Volume Upstream Al target run, the events from Decay Volume Upstream Al target run were weighted so that their distributions agree with that of the physics data. Figure 4.14 shows $Z_{vtx}^{\pi^0} - P_T^{\pi^0}$ distribution for the events of Decay Volume Upstream Al target run after weighting events and imposing all event selection cuts except for the cluster shape related cuts. The number of the hadronic interaction events was estimated by applying the reduction factor of shape-related cut to the number of events of controlled samples in the signal region. The reduction factor of shape-related cuts was estimated by comparing the number of events in the region B, D, and E, with and without the shape-related cuts. The number of events in the controlled samples in the signal region was scaled so that number of events in the region E be the same as that of physics data without the shape-related cuts and the cut on NN_{kine}. Because π^0s generated at the Decay Volume Upstream Al target can be seen in this plot, the events in the controlled samples in the signal region with $Z_{vtx}^{\pi^0} > 3200$ mm were used for the estimation. The number of hadronic interaction events in the signal region was estimated to be 0.18 ± 0.15 [48].
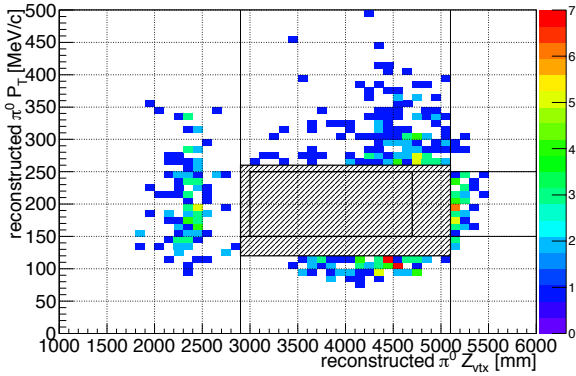
Figure 4.13: $Z_{vtx}^{\pi^0} - P_T^{\pi^0}$ distribution after imposing all the event selection cuts except the cluster shape related cut.
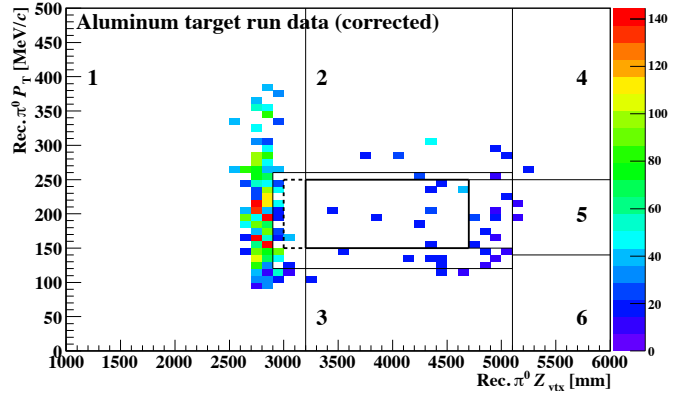
Figure 4.14: $Z_{vtx}^{\pi^0} - P_T^{\pi^0}$ distribution for the events of Decay Volume Upstream Al target run after weighting events and imposing all the event selection cuts except the cluster shape related cut. [39]

4.5.2 Kaon background

4.5.2.1 Region C: $K_L \to \pi^+\pi^-\pi^0$ background

The $K_L \to \pi^+\pi^-\pi^0$ decays can be the source of the background events if only two photons from π^0 are observed in the CsI calorimeter and both π^+ and π^- are missed. This can be caused by the charged particle detection inefficiency of detectors. Because the vacuum pipe made of 5-mm-thick stainless steel was located between the CC05 and CC06 in Run 49 in 2013, $\pi^\pm$ which escaped from the beam hole of the CsI calorimeter and passed the vacuum pipe might not be detected by CC05 and CC06. The contribution of this process due to the vacuum pipe was considered in the estimation of the background events from $K_L \to \pi^+\pi^-\pi^0$. The number of background events in the region C due to this process was estimated to be 7.08 ± 0.52. This process was thus considered as the main source of the background events in region C.

Because the lower limit of the transverse momentum of π^0 for signal region was set higher than the kinematical limit of that for $K_L \to \pi^+ \pi^- \pi^0$, the contribution of this process in the signal region was expected to be small. The number of background events in the signal region from this process was estimated to be 0.0016 ± 0.0016 based on the MC simulation [48].

4.5.2.2 Contribution from other Kaon decay modes

Though the main contribution of the background events around the signal region is explained by the processes described above, there are still contribution from another Kaon decay modes.

$K_L \to 2\pi^0, 3\pi^0$

The $K_L \to 2\pi^0, 3\pi^0$ decays can be the source of the background if only two photons from π^0 are observed in the CsI calorimeter and the other two or four photons are missed. This can be caused by interactions of photons with inactive material around the detector such as the support structure of the detector, or the photon detection inefficiencies of detectors. The numbers of background events in the signal region due to $K_L \to 2\pi^0$ and $K_L \to 3\pi^0$ were estimated to be 0.047 ± 0.033 and 0.047 ± 0.033, respectively [48].

$K_L \to 2\gamma$

The events from $K_L \to 2\gamma$ decay can be easily rejected if K_L decayed on the beam axis because the transverse momentum of the two-photon system is small in these events. However, they can be a source of background if K_L was scattered at the beam window and have a larger transverse momentum. To estimate the background events due to this process, the samples of K_L which were scattered at the beam window and decayed to 2γ were generated and studied. The number of background events in the signal region due to this process was estimated to be 0.030 ± 0.018 [48].

$K_L \to \pi^\pm l^\mp \nu \ (l = e, \mu)$

The $K_L \to \pi^\pm l^\mp \nu \ (l = e, \mu)$ decays can be the source of the background if CV could not detect $\pi^\pm l^\mp \nu \ (l = e, \mu)$ and the cluster made by them cannot be rejected by the selection cuts.

The number of background events in the signal region due to $K_L \to \pi^\pm e^\mp \nu$ was estimated to be less than $0.008(90\% \text{C.L})$ [48]. The contribution of $K_L \to \pi^\pm \mu^\mp \nu$ was estimated to be negligible because it should have a cluster shape different from electromagnetic showers.

Inefficiency due to accidental Hit

Even though the parabola fitting method is more effective than the constant fraction method against accidental hits, it can miscalculate the timing of pulse if accidental hit comes much closer to the pulse from the decayed kaon.

I have studied the pulse identification efficiency of parabola fitting method for the two pulses, which were made by overlaying two waveforms recorded in 2013. Figure 4.15 shows the pulse identification efficiency of parabola fitting method for the two pulses as a function of the timing difference between the two pulses. The parabola fitting method cannot separate the two pulses if one comes after another one within 100 ns.

To estimate the effect of this process, the waveform analysis was done for the MC simulation in the same way as for the real data. The pulse for the hit from decayed kaon was generated based on the energy and timing information of MC simulation. The waveforms of detectors in the data taken with the accidental trigger in Run 49 were used for the waveform for accidental

event. The effect of accidental hit was simulated by overlaying the waveform of accidental event on the simulated pulse. Figure 4.16 shows an example of overlapped pulses in MC simulation which were identified as a single pulse and caused miscalculation of timing. The estimation was done by Dr. Y. Maeda and the detail can be found in [39].

The number of background events due to accidental hits was estimated to be 0.014 ± 0.014 for $K_L \to 3\pi^0$ and 0.0092 ± 0.0053 for $K_L \to 2\pi^0$ [48]. The number for $K_L \to 2\pi^0$ was already included in the estimation for $K_L \to 2\pi^0$ decay described above.
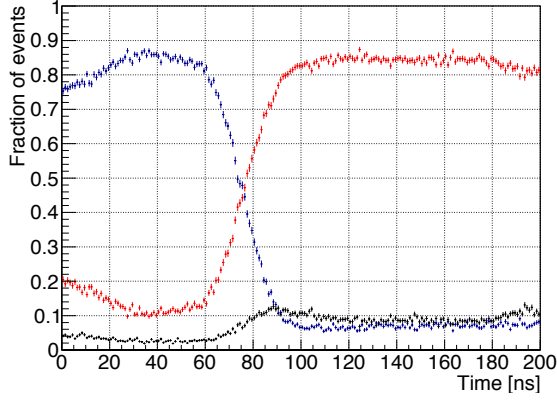
Figure 4.15: The pulse identification efficiency of "parabola fitting method" for the two pulses generated in the waveform as a function of the timing difference between the two pulses. The blue, red, and black points represent the probabilities to identify 0, 1 and 2 pulses in the waveform, respectively.
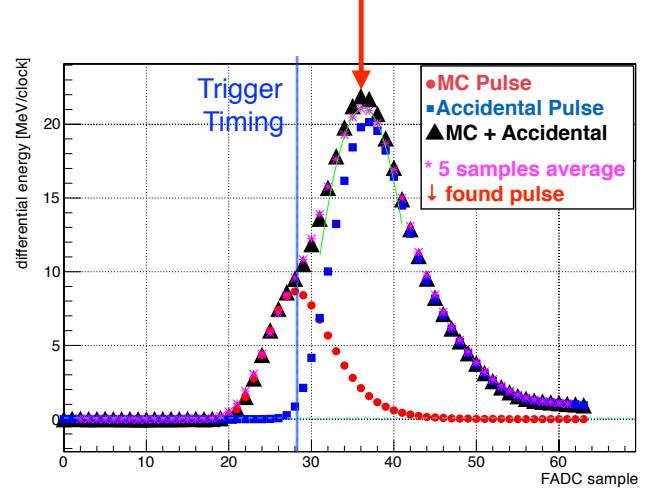
Figure 4.16: An example of overlapped pulses in MC simulation which were identified as a single pulse and cause miscalculation of timing. The red and blue points represent the pulses of hit from Kaon decay and that of the accidental hit, respectively. The black points are the waveform with two pulses summed together. The purple points are the waveform after taking a moving average. The green curve is the parabolic function used in the timing calculation.

4.5.3   Summary of the Background estimation

Table 4.4 shows the estimated number of background events in the signal region from each source of the background events. The contribution from the hadron interaction events was dominant among the sources of the background events.

4.6   Result of the $K_L \to \pi^0 \nu \overline{\nu}$ analysis for Run 49

After finalizing all the selection cuts, we removed the blinding. Figure 4.17 shows the $Z_{vtx}^{\pi^0} - P_T^{\pi^0}$ distribution after all the event selection cuts imposed and the blinding removed. One event was observed in the signal box. The energies and hit positions on photons are (E[MeV],x[mm],y[mm]) $= (519.4, 534.3, -57.4), (357.4, 11.5, -244.3)$. This event is considered to be the hadronic inter-

Table 4.4: The summary of estimated number of background events [48].

Source	Estimated Number of background events
K_L decay background	
$K_L \to 2\pi^0$	0.047±0.033
$K_L \to 2\gamma$	0.030±0.018
$K_L \to \pi^+\pi^-\pi^0$	0.0016±0.0016
$K_L \to 3\pi^0$	0.022±0.004
$K_L \to \pi^\pm e^\mp \nu$	<0.008(90%C.L)
Background due to accidental hits	
$K_L \to 3\pi^0$	0.014±0.014
$K_L \to 2\pi^0$	0.0092±0.0053
	(included in K_L decay background)
$K_L \to \pi^+\pi^-\pi^0$	<0.005(90%C.L)
$K_L \to \pi^\pm e^\mp \nu$	<0.005(90%C.L)
$K_L \to \pi^\pm \mu^\mp \nu$	<0.016(90%C.L)
Neutron background	
NCC background	0.06±0.06
Hadron interaction events	0.18±0.15
Total	0.36±0.16

action event because the hadronic interaction events had the largest contribution (0.18±0.15) in the estimated number of background events.

From the analysis with the data of Normalization events, the single event sensitivity, the branching ratio at which the experiment can observe single event, with the physics data was estimated to be 1.29×10^{-8} [48].
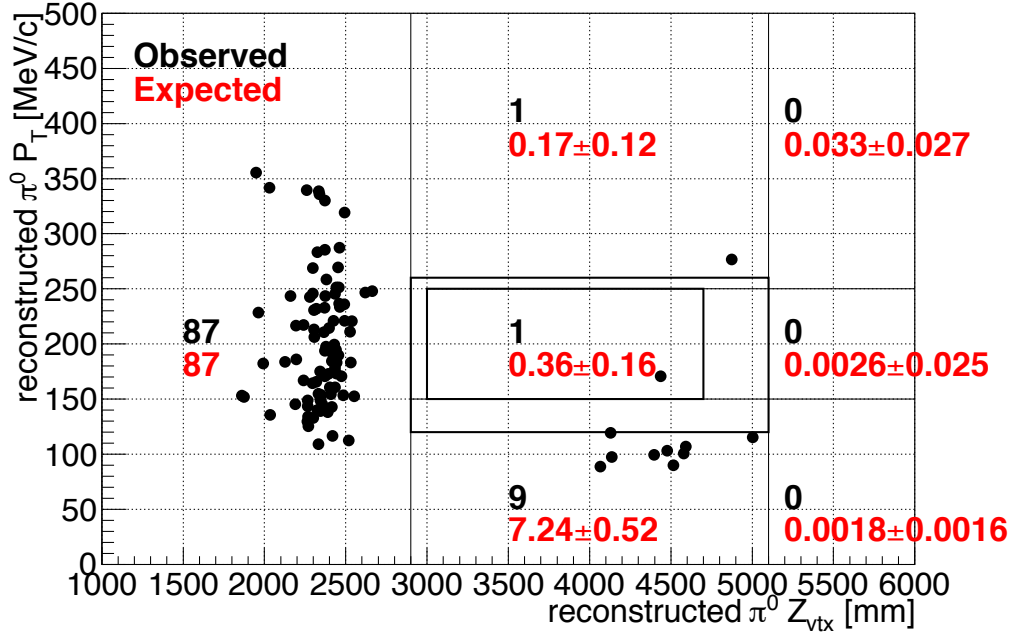
Figure 4.17: $Z_{vtx}^{\pi^0} - P_T^{\pi^0}$ distribution for the events in the data of 2013 physics data taking after all event selection imposed.
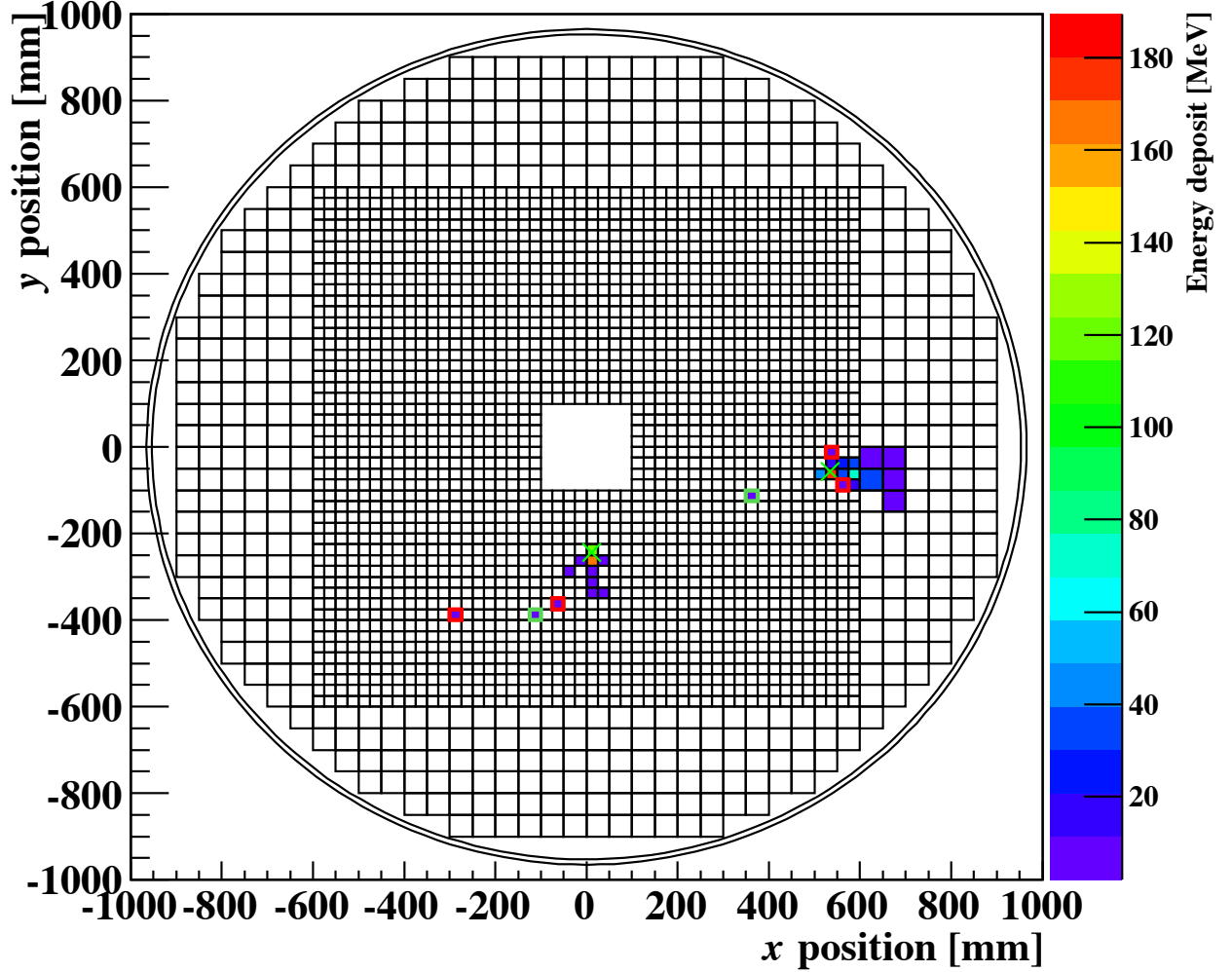
Figure 4.18: Hit pattern in the calorimeter for the observed event. Hits with energy deposit smaller than 2 MeV are ignored. Cross marks indicate reconstructed photon hit positions. The energies and hit positions on photons are (E[MeV],x[mm],y[mm])=(519.4, 534.3, −57.4), (357.4, 11.5, −244.3). Crystals surrounded by red (green) boxes are isolated hit crystals which are (are not) regarded as simultaneous hits. This figure is taken from [39].

Chapter 5

Pulse shape study

In the analysis of $K_L \to \pi^0 \nu \overline{\nu}$ for the data taken in 2013 physics run, one event was observed with the sensitivity 500 times larger than the branching ratio predicted by SM. Because this event is considered to be the event with neutron-induced clusters, we need a new discrimination method to reject neutron-induced cluster in addition to the existing method using cluster shapes.

I have developed a new method utilizing pulse-shapes to discriminate neutron-induced clusters. The motivation for pulse-shape studies is described in Section 5.1. The data and event selection for the data sample of photon-rich events and neutron-rich events are described in Section 5.2. The procedure and result of the pulse-shape studies are described in Section 5.3. The developed method to discriminate incident photons and neutrons using pulse-shape information and its performance are described in Section 5.5. The impact of the developed method for the current $K_L \to \pi^0 \nu \overline{\nu}$ analysis is described in Section 5.6.

5.1 Motivation

5.1.1 Requirement from the current result for $K_L \to \pi^0 \nu \overline{\nu}$ analysis

The contribution of hadronic interaction events in the $K_L \to \pi^0 \nu \overline{\nu}$ analysis was estimated to be 0.18 ± 0.15 events with the single event sensitivity of 1.29×10^{-8}. This means that the signal to background ratio, S/N, with the background only from hadronic interaction events is 1/90. To increase the S/N ratio to larger than 1, further improvements by a factor of 100 to reject neutron-induced clusters is needed.

The improvement by a factor of 30 was expected with an improved cut on the cluster shape and a cut on the shower depth [50], which will be described in Chapter 6. To achieve S/N>1, a new method with an improvement by more than a factor of 3 was required in addition to those cuts.

5.1.2 Requirement from the characteristics of neutron-induced clusters

The characteristics of neutron-induced clusters were studied with MC simulation. Geant4 with QGSP BERT physics package was used for the MC simulation. On the CsI calorimeter, 1-GeV neutrons were injected normal to the upstream surface and events with two neutron-induced clusters made from single incident neutron were used for study. In those events, hadronic

interactions at the primary neutron-induced cluster generated a secondary neutron which then made secondary neutron-induced cluster.
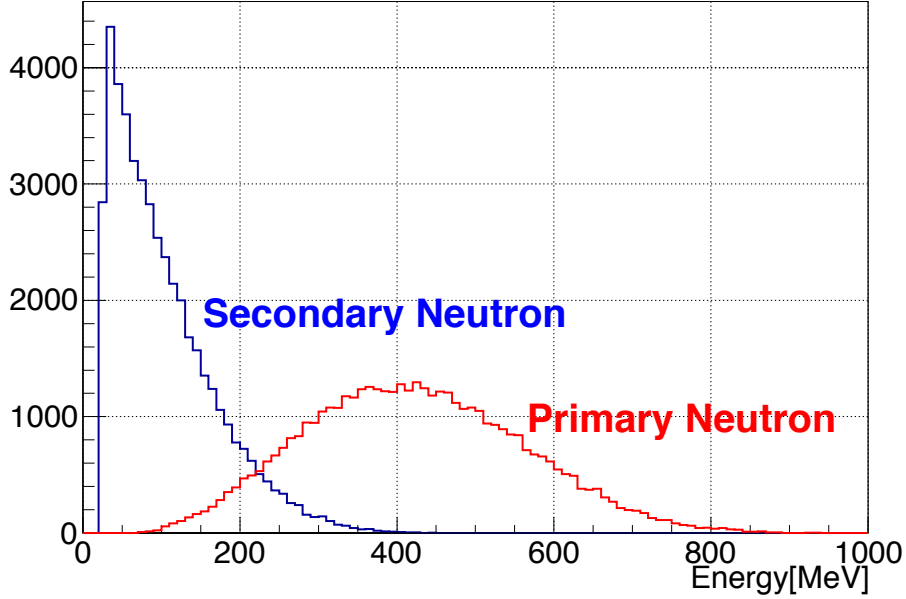
Figure 5.1: Energy distribution for primary and secondary neutron-induced clusters made by a single neutron hit.

Figure 5.1 shows the energy distribution for primary and secondary neutron-induced clusters. The primary neutron-induced clusters have higher energy than the secondary neutron-induced clusters. To reject both neutron-induced clusters, the energy dependence of the new method must be studied.

If the neutron-induced background events seen in the physics data were made by the neutrons in the beam halo region, the primary neutron-induced clusters tend to be located closer to the center of the CsI calorimeter surface. The position of the secondary neutron-induced cluster can be far from the center of CsI calorimeter. To reject both neutron-induced clusters, the hit position dependence of the new method must be also studied.

In addition to those characteristics, the new method will be used with existing cuts on the cluster shape such as χ^2_{shape}, NN_{kine}, NN_{shape}. To achieve further reduction of neutron-induced background in addition to these cuts, the new method should have small correlation with them. The correlation between the new method and these cuts should thus be studied.

5.1.3 Motivation to study pulse-shape discrimination

The pulse shape discrimination (PSD) technique was a candidate for a new method to discriminate photon-induced clusters and neutron-induced clusters. The PSD technique is popular and widely used for organic liquid scintillators [51]. The light output of organic scintillators has two components: a "fast" component with a decay time of few ns to tens of ns, and a "slow" component with a decay time longer than 100 ns. The fraction of the light yield in the slow component depends on the type and energy of particles producing the scintillation. The scintillation light caused by neutrons and protons has a larger slow component than that by photons. Different ratio of slow to fast components changes the pulse shape. The PSD technique uses this difference in pulse-shape to discriminate neutrons from photons. The organic

liquid scintillators have PSD capability for wide range of energy from 1 keV to 100 MeV [51]. In addition to organic scintillators, some inorganic scintillating crystals such as CsI(Tl) and NaI(Tl) have PSD capabilities [51, 52]. For example, CsI(Tl) crystals have PSD capability for neutrons, photons, and various charged particles in the energy range from 1 MeV to 200 MeV [52, 53, 54]. Un-doped CsI crystals also have a PSD capability between photons and neutrons in the energy range up to 45 MeV [55]. If un-doped CsI crystals have the PSD capability for the photons and neutrons with the energy over 100 MeV, the PSD can be a tool for the KOTO experiment to reject the neutron-induced cluster made by high energy neutrons.

5.2 Data and Event selection

To study the difference in pulse shapes between photon-induced clusters and neutron-induced clusters, the waveform data of photon-rich events and neutron-rich events taken in Run 49, Run 62, and Run 63 were used.

5.2.1 Photon-rich events

The events of $K_L \to 3\pi^0$ decay mode were used as data sample of photon-rich events because $K_L \to 3\pi^0$ has a large branching ratio and six photons in the final state.

5.2.1.1 Data selection

The data taken in the same period as for $K_L \to \pi^0 \nu \overline{\nu}$ analysis were used for the analysis. The events taken with the Normalization trigger, Minimum Bias trigger, and $K_L \to 3\pi^0$ trigger were used for the $K_L \to 3\pi^0$ analysis. There were two type of event selection cuts. The events with tighter cut was used to estimate the discrimination efficiency for photon-induced clusters. The events with looser cut was used to study the pulse-shape in $K_L \to 3\pi^0$ events

5.2.1.2 Event selection

In addition to the event selection cuts described in Chapter 4, the cuts on the variables related to the reconstructed K_L and π^0 were used in the analysis. The event selection cuts used in the analysis of the $K_L \to 3\pi^0$ are summarized in Table 5.1.

Veto cuts

Veto cuts shown in Table 4.2 were used in the tighter cut. No veto cuts were applied in the looser cut to increase the statistics.

Total energy in CsI calorimater

To remove the bias due to the online trigger, the total energy of two photons was required to be larger than 650 MeV in the tighter cut.

In the looser cuts, the cut for total energy in the CsI calorimeter was loosened. The total energy deposit in the left or right half of the CsI calorimeter was required to be larger than 350 MeV.

Reconstructed mass of K_L

The mass of reconstructed K_L, M_{K_L}, was required to be within ± 15 MeV/c^2 of the nominal K_L mass ($M_{K_L}^{PDG}$ = 497.614-MeV/c^2 [14]) to remove the π^0s reconstructed with a wrong pair of photons.

Transverse momentum of reconstructed K_L

The transverse momentum of reconstructed K_L was required to be less than 50 MeV/c to ensure that there are no missing particles in the K_L decay.

z position of the decay vertex of reconstructed K_L

The Z_{vtx} of reconstructed K_L, $Z_{vtx}^{K_L}$, was required to be far from the NCC, FB, and CV. For the estimation of discrimination efficiency for photon-induced clusters, $Z_{vtx}^{K_L}$ was required to be 3000 mm $< Z_{vtx}^{K_L} <$ 4700 mm. For the study of pulse-shape in $K_L \to 3\pi^0$ events, the cuts on the $Z_{vtx}^{K_L}$ was loosened to be 2000 mm $< Z_{vtx} <$ 5400 mm.

The deviation in z position of the decay vertex of reconstructed π^0s

To ensure that all the π^0s were coming from the same K_L, the distance between of the decay vertexes of the reconstructed π^0s with the smallest and the largest $Z_{vtx}^{\pi^0}$, $\Delta Z_{vtx}^{\pi^0}$, was required to be less than 400 mm.

Mass of reconstructed π^0

After reconstructing the decay vertex of the K_L, the invariant masses of π^0s decayed from K_L were re-calculated by using the K_L vertex. To ensure that all the π^0s were coming from the same vertex, the masses of π^0s were required to be within 10 MeV/c^2 of the nominal π^0 mass ($M_{\pi^0}^{PDG}$).

5.2.1.3 Statistics after event selection

The numbers of reconstructed $K_L \to 3\pi^0$ after two types of event selections were 210424 with the tighter cut and 2895362 with the looser cut for pulse shape study.

5.2.2 Neutron-rich events

5.2.2.1 Data selection

To collect the events with neutrons hitting the CsI calorimeter, we conducted special data taking by inserting the Z0-Al-target in the beam upstream of the FB. We call this special data taking as "Z0-Al-target run", as described in Section 2.7.3.3. The neutrons in the beam interacted with the Z0-Al-target and produced hadrons such as protons, neutrons, and π^0s. Because the Z0-Al-target was placed upstream of FB, photons from π^0 decays stopped in FB and NCC, and could hit the CsI calorimeter. Only neutrons and protons can hit the CsI calorimeter from the Z0-Al-target. Neutron-rich event were selected by applying the cuts on veto detectors which is described in Table 4.2.

The data taken in the Z0-Al-target run during Run 62 and Run 63 shown in Table 5.2 was used in this study. The total number of protons on T1 target recorded in these data taking was comparable with that of physics data taken in 2013 for the $K_L \to \pi^0 \nu \bar{\nu}$ analysis.

Table 5.1: The summary of event selection cuts for $K_L \rightarrow 3\pi^0$ analysis.

Cut	Requirement	
	Tighter cut	Looser cut
Number of Photon Clusters	6	
Total Energy Cuts		
Total energy of photons	>650 MeV	
Total energy in the half of		>350 MeV
the CsI calorimeter		
Veto cuts	Table 4.2	Not applied.
Photon Cluster Quality Cuts		
Fidutial Cut	$\|x_{cluster}\| > 150$ mm, $\|y_{cluster}\| > 150$ mm,	
	$\sqrt{x_{cluster}^2 + y_{cluster}^2} < 850$ mm	
Photon Energy	$E_\gamma > 50$ MeV	
Cluster distance	>150 mm	
Photon timing difference	<3 ns	
Cuts for Kaon and Pion		
χ_Z^2	<20	
$\|M_{K_L} - M_{K_L}^{PDG}\|$	<15 MeV	
$\|M_{\pi^0} - M_{\pi^0}^{PDG}\|$	<10 MeV	
P_T of reconstructed K_L	<50 MeV/c	
$\Delta Z_{vtx}^{\pi^0}$	<400 mm	
$Z_{vtx}^{K_L}$	3000 mm$< Z_{vtx}^{K_L} <$4700 mm	2000 mm$< Z_{vtx}^{K_L} <$5400 mm

Table 5.2: A list of data taking periods for Z0-Al-Target run

Run Name	Beam Power	Duration	Total hours	Number of Protons on T1 Target	
				delivered	recorded
Run 62	23.8 kW	April 28~29, 2015	15 hours	1.60×10^{17}	1.44×10^{17}
Run 62	26.4 kW	May 5~6, 2015	10 hours	1.72×10^{17}	1.68×10^{17}
Run 63	29.3 kW	June 11~12,	37 hours	6.88×10^{17}	6.68×10^{17}
		June 14~15,			
		and June 16, 2015			
Run 63	33 kW	June 25~26, 2015	22 hours	4.81×10^{17}	4.62×10^{17}
Total			84 hours	1.50×10^{18}	1.44×10^{18}

Table 5.3 shows the trigger rates of the physics triggers with and without the Z0-Al-target. With the Z0-Al-target, the Lv1 trigger rates increased by a factor of 4 compared to the rate without the target, and the fraction of events which passed Lv2 trigger condition increased by a factor of 2.5. Because the physics trigger rate increased by a factor of $4 \times 2.5 = 10$, the physics triggers were prescaled to 1/10. Neutrons scattered at the Z0-Al-target should be the main source of the increase in the trigger rate.

Table 5.3: A list of trigger rates per spill for physics trigger conditions with and without the Z0-Al-target inserted into the beam.

Type	Raw Trigger	Prescaling Factor	Lv1 Trigger Requested	Lv1 Trigger Accepted	Lv2 Trigger Accepted	Lv2 Trigger rejection(%)
With Z0Al target	118,000	10	11,800	11,000	7,000	38%
Without Z0Al target	30,000	1	30,000	24,000	5,000	76%

5.2.2.2 Event selection

The events with two clusters in the CsI calorimeter were used for analyzing the pulse-shape in the neutron-rich sample.

To increase the statistics, only cuts on veto detectors, and a cut on the $Z_{vtx}^{\pi^0} > 3000$mm to remove NCC background events were applied to study pulse shapes.

To evaluate the performance of discriminating between photons and neutrons, the same cuts as the ones used for the $K_L \to \pi^0 \nu \overline{\nu}$ analysis, shown in Table 4.2 and Table 4.3, were used. To evaluate the performance of the developed method alone, the cluster-shape cut using χ_{shape}^2 and all Neural-net cuts were removed, and a cut on $Z_{vtx}^{\pi^0}$ to remove NCC background events described above were added in the analysis. We will call this set of event selection cuts as "loose cuts".

5.2.2.3 Statistics after event selection

The number of reconstructed π^0 in the neutron-rich sample after loose cuts was 5362. The number of events with two clusters after cuts on veto detectors and $Z_{vtx}^{\pi^0}$ for pulse shape study was 363064.

5.2.2.4 Estimation of the contamination of K_L decay events

Because most of K_L decay events were rejected by the loose cuts in the $K_L \to \pi^0 \nu \overline{\nu}$ analysis, the contamination of K_L decay events in the neutron-rich sample after loose cuts should be small. The amount of background events from K_L decay in the neutron-rich sample after loose cut was expected to be 10% of the amount in the $K_L \to \pi^0 \nu \overline{\nu}$ analysis described in Chapter 4, considering the total number of protons used in the analysis and the prescale factor.

Only cuts on veto detectors and $Z_{vtx}^{\pi^0}$ were applied for pulse shape study. NCC background events can be rejected by applying cut on the $Z_{vtx}^{\pi^0}$. Most of K_L decay modes except for the $K_L \to 2\gamma$ mode were rejected by the cut on veto detector. The number of $K_L \to 2\gamma$ decay events in the events selected for pulse shape study was estimated from that in physics data after applying the event selection cuts for $K_L \to 2\gamma$ shown in Table 5.4. Based on the umber of reconstructed $K_L \to 2\gamma$ decay in the physics data (27730), the number of $K_L \to 2\gamma$ decay

events recorded in the data taken in Z0-Al-target run was estimated to be 3361, considering the total number of protons used in the analysis and the prescale factor. This corresponds $0.93 \pm 1.59 \times 10^{-4}$ of events for the pulse shape study. The contamination of K_L decay events was thus negligible also in the data for the pulse shape study.

Table 5.4: The summary of event selection cuts for $K_L \to 2\gamma$ analysis.

Cut	Requirement
Number of Photon Clusters	2
Trigger Bias Cuts	
Total energy of photons	>650 MeV
Veto cuts	Table 4.2
Photon Cluster Quality Cuts	
Fidutial Cut	$|x_{cluster}| >150$ mm, $|y_{cluster}| >150$ mm, $\sqrt{x_{cluster}^2 + y_{cluster}^2} <850$ mm
Photon Energy	$E_\gamma >50$ MeV
Cluster distance	>150 mm
Photon timing difference	<3 ns
Cuts for Kaon	
P_T of reconstructed K_L	<50 MeV/c
$Z_{vtx}^{K_L}$	3000 mm< $Z_{vtx}^{K_L}$ <4700 mm

5.3 Waveform fitting

To compare the pulse shapes in photon-induced clusters and neutron-induced cluster, we need to quantify the characteristics of the pulse shape. To quantify the characteristics of the pulse shape, the waveforms were fitted with a given function.

In this section, the fitting function and procedure of fitting waveforms will be described.

5.3.1 Asymmetric Gaussian

The recorded pulse had the shape similar to the Gaussian function because the signals from the CsI calorimeter channels were digitized and recorded after shaping by a 10-pole Bessel filter. If there is any enhancement in the tail region of the original pulse right after PMT, the pulse shape will be broader and asymmetric. To parametrize the width and asymmetry of the pulse-shape, the waveforms were fitted with the Gaussian-like function called "Asymmetric Gaussian function":

$$A(t; A, t_0, \sigma_0, a) = |A| \exp\left(-\frac{(t-t_0)^2}{2(a(t-t_0)+\sigma_0)^2}\right) + \text{Pedestal}, \qquad (5.1)$$

where $|A|$ represents the pulse height, t_0 represents the timing of the peak, and σ_0 represents the width of pulse shape. The parameter "a" is called "asymmetric parameter" which represents the asymmetry of the pulse shape.

5.3.2 Fitting procedure

The waveforms of all the channels included in the cluster were analyzed. At first, the pulse and the timing of its peak were identified in the waveform by fitting the waveform with a pulse shape template, with the method described in [43, 49]. The pulse shape template for each channel was made from averaged waveforms of $K_L \to 3\pi^0$ events taken in Run 49. After identifying pulses, the waveform was fitted with the Asymmetric Gaussian function. The range to fit the waveform was between 20 clocks before the peak and 6 clocks after the peak. Figure 5.2 shows an example of fitting the waveform of one CsI calorimeter channel with the asymmetric Gaussian function.
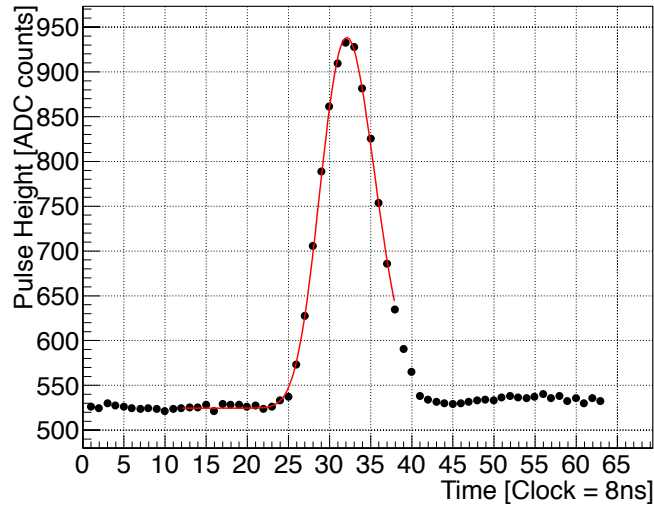
Figure 5.2: An example of fitting waveform with an asymmetric gaussian function.

5.4 Comparison of typical pulse shape

5.4.1 Pulse shape template for photon-rich sample and neutron-rich sample

The typical pulse shapes of photon-rich sample and neutron-rich sample were compared. The mean and standard deviation of two fitting parameters, σ_0 and a, were derived from the fit result for events, and were used to make pulse shape templates. The templates were prepared for each channel and for multiple pulse-height ranges. The template were made separately for photon-rich sample and for the neutron-rich sample. Figures 5.3 and 5.4 show the statistics of the events used to make the template of those samples. Most of crystals had more than 10000 events for the photon-rich samples. For neutron-rich samples, the crystals in the region 500 mm from the center of the CsI calorimeter had around 10000 events for the neutron-rich events and the crystals outside the region had $100 \sim 1000$ events.

Figures 5.5 and 5.6 show the σ_0 and the asymmetric parameter "a" used to make template pulses for one crystal. There are clear discrepancies between photon-rich sample and neutron-
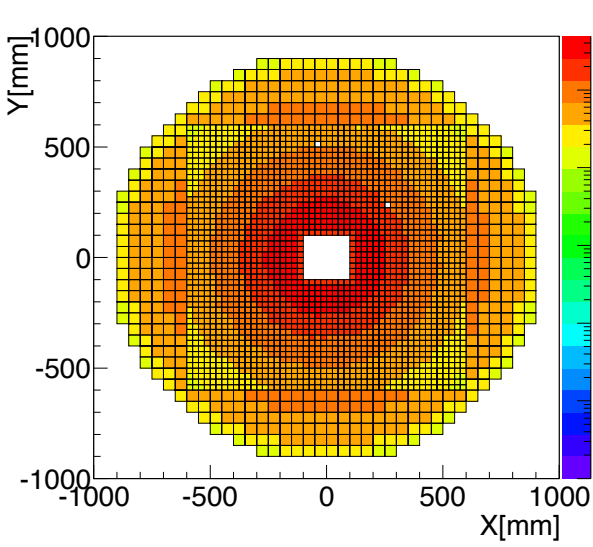
Figure 5.3: The statistics of the events used for making the template of the photon-rich sample.
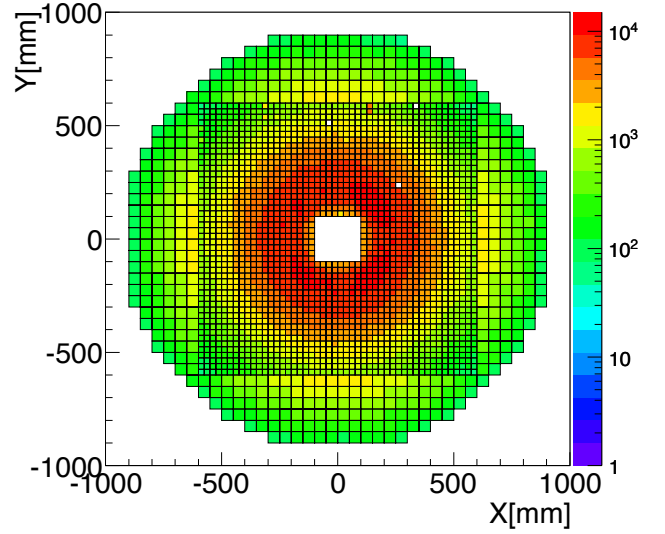
Figure 5.4: The statistics of the events used for making the template of the neutron-rich sample.

rich sample in both σ_0 and a. In particluar, the discrepancies are significant above 500 ADC counts which corresponds to 50 MeV deposit in a single crystal.

Figures 5.7 and 5.8 show the difference in fit parameters between the photon-rich sample and the neutron-rich sample for all the crystals. The discrepancy between the two samples increases with the pulse-height in both σ_0 and a, for most of the crystals.

Figures 5.9 and 5.10 show the significance of the difference in the fit parameters:

$$\frac{\Delta p}{\sigma_{\Delta p}} = \frac{p_n - p_\gamma}{\sqrt{RMS_\gamma^2 + RMS_n^2}}, \tag{5.2}$$

where p_γ (p_n) and RMS_γ (RMS_n) represent the mean and the standard deviation of the fit parameter for the photon-rich (neutron-rich) sample, respectively. The differences of fit parameters are significant if pulse height is higher than 300~500 ADC counts.

5.4.2 Correlation between the difference in the cluster shape and the pulse shape

To check the correlation between the cluster shape and the pulse shape, the pulse shape templates for the events before and after the cluster shape cut ($\chi^2_{shape} < 4.6$) were compared. As shown in Fig. 5.11, after cut on the cluster shape, most of crystals have events less than 500 events for making the template of neutron-rich sample.

Figures 5.12 and 5.13 show the σ_0 and the asymmetric parameter "a" used to make template pulses for one crystal for the photon-rich sample, the neutron-rich sample, and the neutron-rich sample after the cut on the cluster shape. Even after the cut on the cluster shape, both fit parameters had larger value in neutron-rich sample than that in the photon-rich sample.

Figures 5.14 and 5.15 show the significance of the difference in the fit parameters $\Delta p/\sigma_{\Delta p}$ between the photon-rich sample and the neutron-rich sample after requiring $\chi^2_{shape} < 4.6$. Even after the cluster shape cut, the significances of difference in the fit parameters have the same tendency against pulse height.
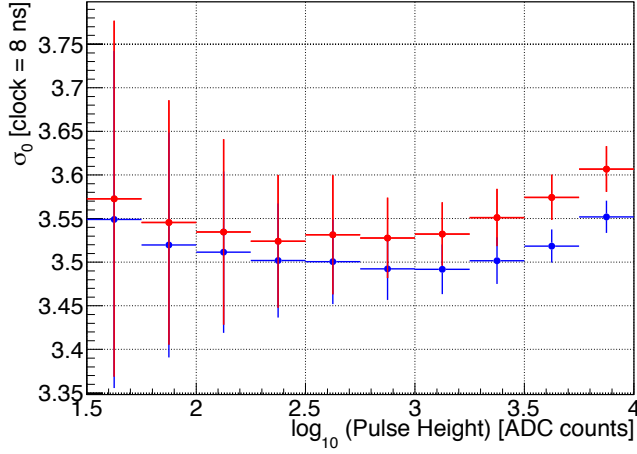
Figure 5.5: The distribution of σ_0 as a function of pulse-height for CsI ID=1406. Red and blue points represent the neutron-rich sample and the photon-rich sample, respectively. The error bars represent the standard deviation of the parameter.
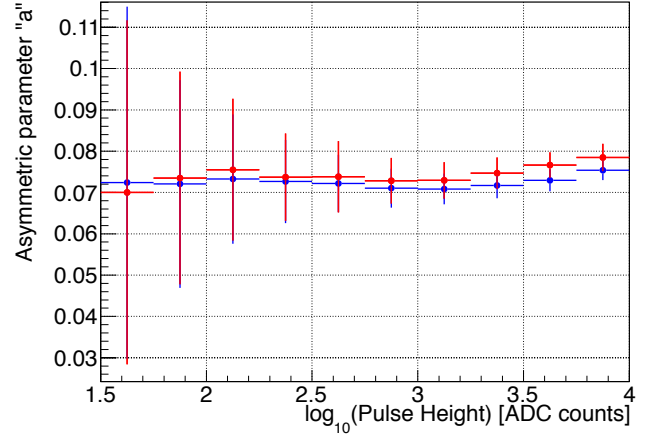
Figure 5.6: The distribution of the asymmetric parameter "a" as a function of pulse-height for CsI ID=1406. Red and blue points represent the neutron-rich sample and the photon-rich sample, respectively. The error bars represent the standard deviation of the parameter.
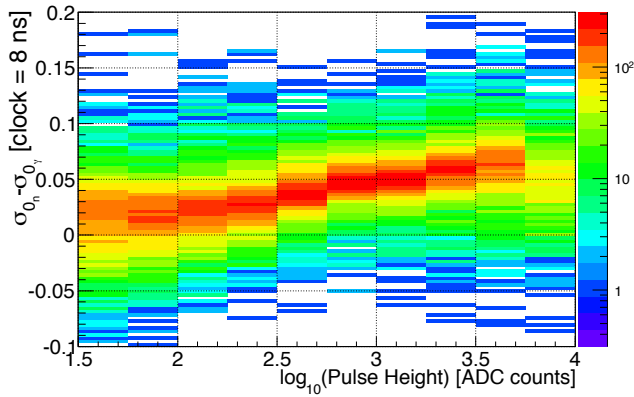
Figure 5.7: The difference in σ_0 between the photon-rich sample and the neutron-rich sample vs. pulse-height distribution for all channels of the CsI calorimeter.
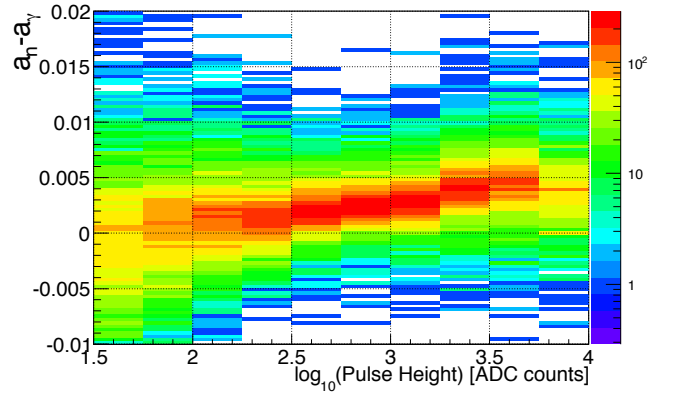
Figure 5.8: The difference in the asymmetric parameter "a" between the photon-rich sample and the neutron-rich sample vs. pulse-height distribution for all channels of the CsI calorimeter.
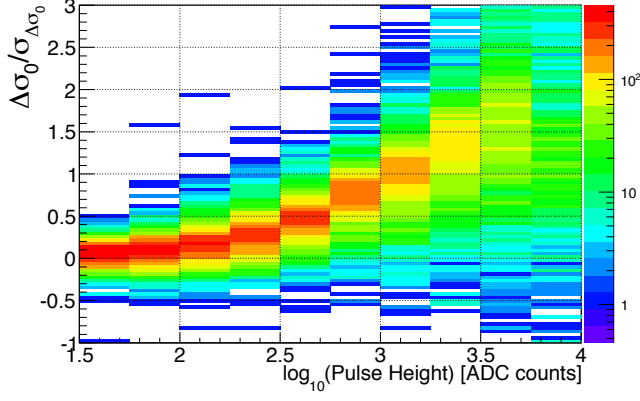
Figure 5.9: The significance of the difference of σ_0 between the photon-rich sample and the neutron-rich sample vs. pulse-height distribution for all channels of the CsI calorimeter.
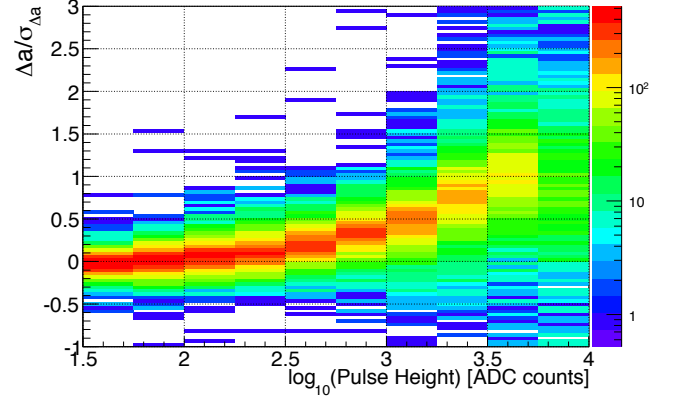
Figure 5.10: The significance of the difference of the asymmetric parameter "a" between the photon-rich sample and the neutron-rich sample vs. pulse-height distribution for all channels of the CsI calorimeter.
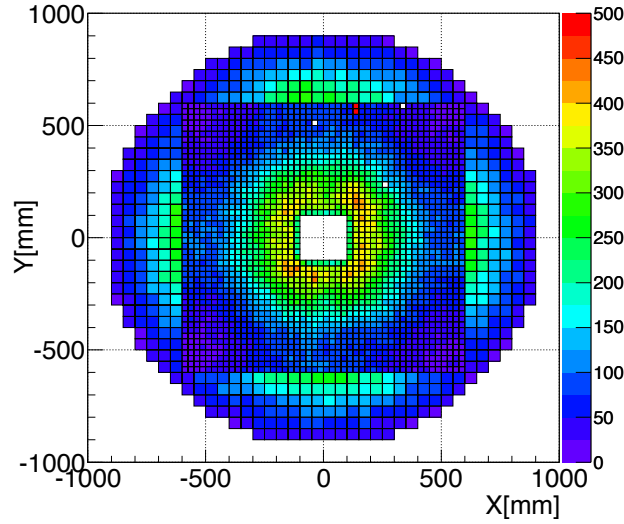
Figure 5.11: The statistics of the events used for making the template of neutron-rich sample after requiring $\chi^2_{shape} < 4.6$.
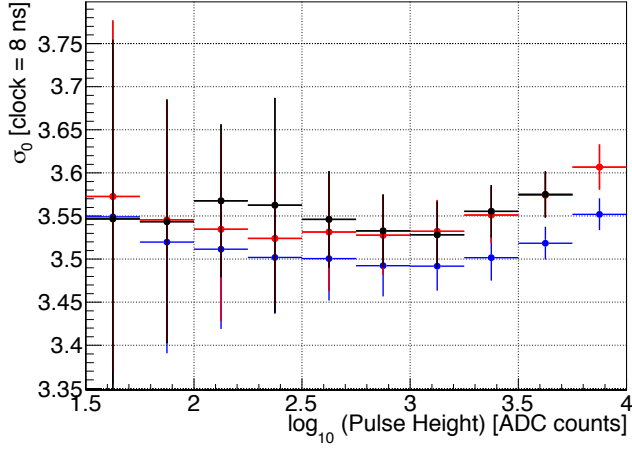
Figure 5.12: The distribution of σ_0 as a function of pulse-height for CsI ID=1406. Red and blue points represent the neutron-rich sample and the photon-rich sample, respectively. Black points represent the neutron-rich sample with requiring $\chi^2_{shape} < 4.6$. The error bars represent the standard deviation of the parameter.
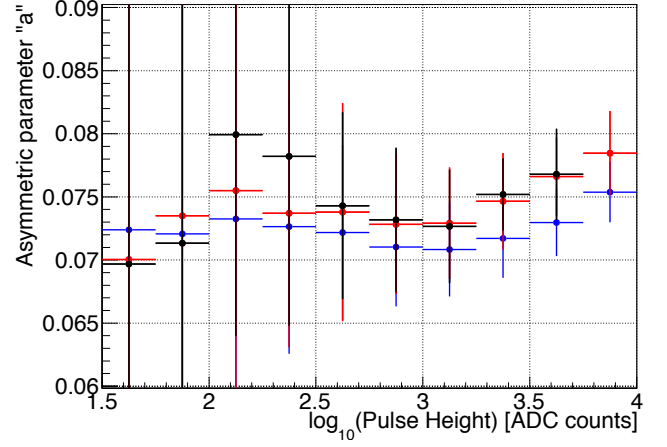
Figure 5.13: The distribution of the asymmetric parameter "a" as a function of pulse-height for CsI ID=800. Red and blue points represent the neutron-rich sample and the photon-rich sample, respectively. Black points represent the neutron-rich sample with requiring $\chi^2_{shape} < 4.6$. The error bars represent the standard deviation of the parameter. The error bars represent the standard deviation of the parameter.
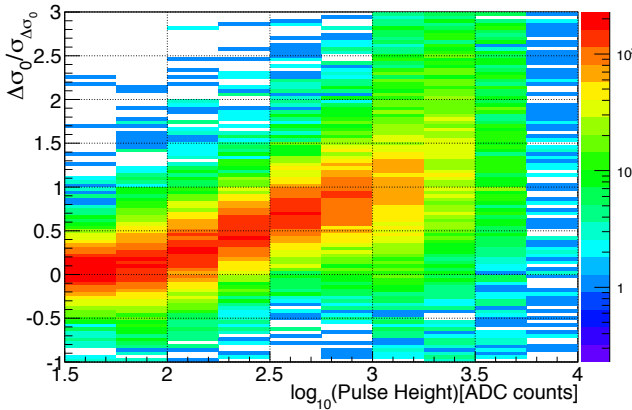
Figure 5.14: The significance of the difference of σ_0 between photon-rich sample and neutron-rich sample after requiring $\chi^2_{shape} < 4.6$ vs. pulse-height distribution for all channels of the CsI calorimeter.
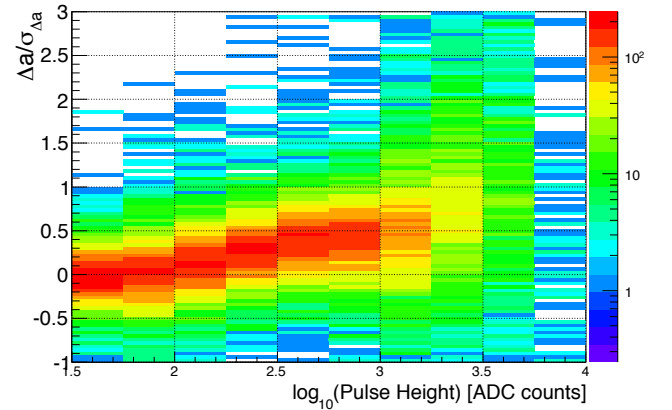
Figure 5.15: The significance of the difference of the asymmetric parameter "a" between photon-rich sample and neutron-rich sample after requiring $\chi^2_{shape} < 4.6$ vs. pulse-height distribution for all channels of the CsI calorimeter.

Figures 5.16 and 5.17 show the significance of the difference in the fit parameters $\Delta p/\sigma_{\Delta p}$ between the neutron-rich sample before and after requiring $\chi^2_{shape} < 4.6$. The differenced of parameters were defined as $\Delta p = p_{\mathrm{with}\chi^2_{shape}\mathrm{cut}} - p_{\mathrm{without}\chi^2_{shape}\mathrm{cut}}$. The significances of differences of fit parameters were within $0.5\ \sigma$. The differences in fit parameters are thus independent with the cluster shape difference.
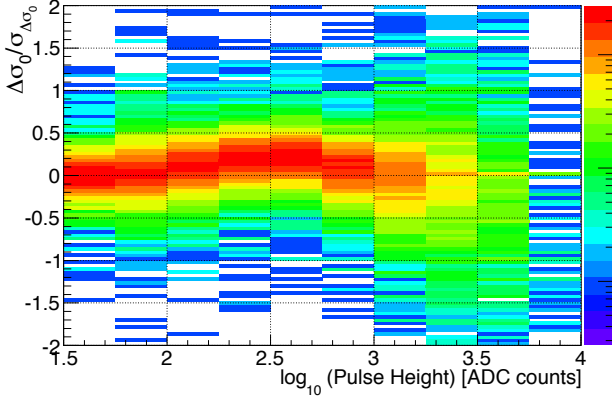
Figure 5.16: The significance of the difference of σ_0 between neutron-rich sample before and after requiring $\chi^2_{shape} < 4.6$ vs. pulse-height distribution for all channels of the CsI calorimeter.
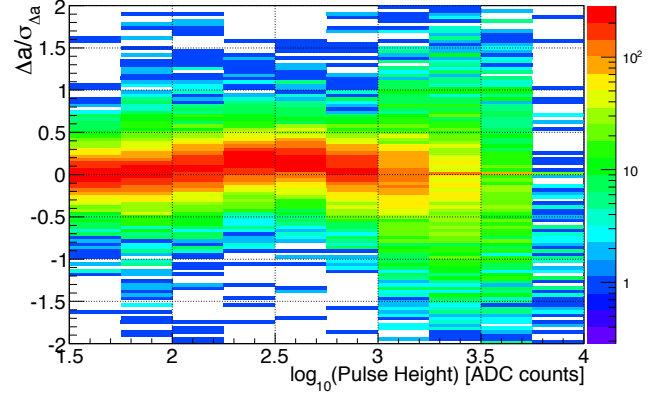
Figure 5.17: The significance of the difference of the asymmetric parameter "a" between neutron-rich sample before and after requiring $\chi^2_{shape} < 4.6$ vs. pulse-height distribution for all channels of the CsI calorimeter.

5.5 Method to discriminate Neutrons and Photons

I have developed a new method to discriminate between photon-induced clusters and neutron-induced clusters utilizing the pulse shape difference we saw in Section 5.4 .

5.5.1 Pulse-shape Likelihood ratio method

To determine the types of clusters between photon-induced clusters and neutron-induced clusters, the likelihood for the assumption of each type were calculated and compared. This method is referred to as "Pulse-shape likelihood method".

5.5.1.1 Likelihood definition

The likelihood for each assumption was defined based on the fit parameters for each crystal, each single cluster, and two-cluster system used for reconstructing π^0. The likelihood for each fitting parameter in each crystal was defined by assuming that its probability density function (PDF) was Gaussian. Figures 5.18 and 5.19 show the fit parameter distribution for CsI=1406 in neutron-rich sample for the events with pulse height between 500 and 1000 ADC counts. These figures show that the distributions of fit parameters can be treated as Gaussian.

The likelihood for each crystal in a cluster, $L^{crystal}$, is defined as:

$$L^{crystal} \quad = \quad \prod_p^{\sigma_0,a} \exp\left(-\frac{(p^{meas.} - p^{exp}(H))^2}{2RMS_{p^{exp}}(H)^2}\right), \tag{5.3}$$
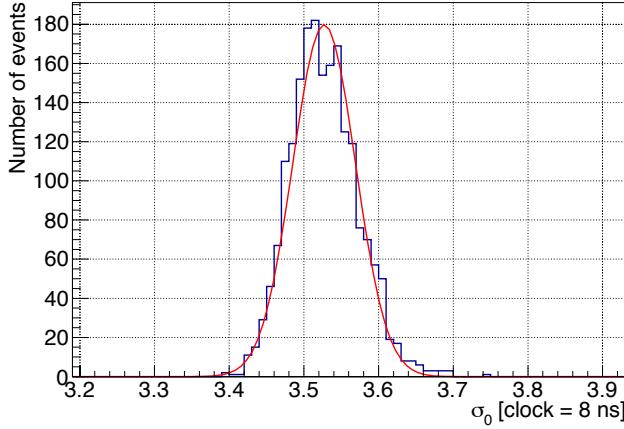
104

Figure 5.18: σ_0 distribution for CsI=1406 in the neutron-rich sample for the events with pulse height between 500 and 1000 ADC counts.
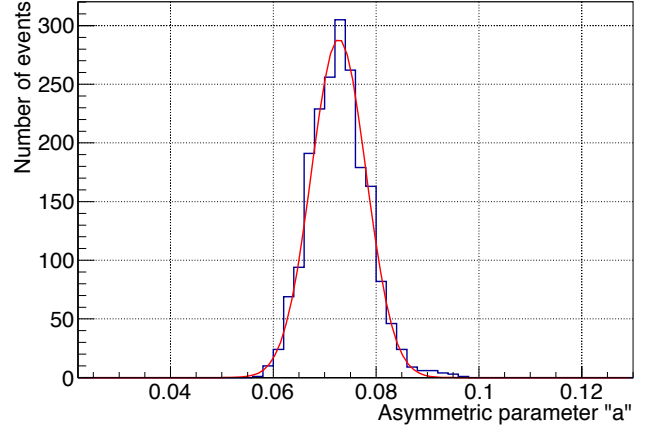
Figure 5.19:   Asymmetric parameter "a" distribution for CsI=1406 in the neutron-rich sample for the events with pulse height between 500 and 1000 ADC counts.

where p represents the fitting parameters σ_0 and a, $p^{meas.}$ represents the parameters measured by fitting the waveform of the events, $p^{exp}(H)$ and $RMS_{p^{exp}}(H)$ represent the expected values and the standard deviation of the fitting parameters at the pulse-height H for the assumed type of cluster.

Here, the Gaussian function without normalization was used as the PDF for fit parameters. Because Gaussian function without normalization has value $\sigma\sqrt{2\pi}$ times larger than that with normalization, the assumption with larger standard deviation has larger probability and likelihood. Templates of neutron-rich sample have larger standard deviation than that of photon-rich samples, as shown in Figs. 5.5 and 5.6. This can enhance the performance to reject neutron-induced clusters.

Only the crystals with energy deposit larger than 50 MeV were used for calculating the likelihood of the clusters because the pulse shape discrepancy between neutron and photon clusters is significant in that energy range. If no crystal had energy deposit larger than 50 MeV, the likelihood of the crystal with the maximum energy deposit was used for the calculation. The likelihood for each cluster is defined as:

$$L^{1cluster} \quad = \quad \prod_j L_j^{crystal},\tag{5.4}$$

where j represents the crystals in the cluster used for the calculation, and $L_j^{crystal}$ represents $L^{crystal}$ for j-th crystal in the crystals used for the calculation.

The likelihood of the two-cluster system used for reconstructing π^0 is defined as:

$$L^{2cluster} \quad = \quad L_1^{1cluster} \times L_2^{1cluster},\tag{5.5}$$

where $L_1^{1cluster}$, $L_2^{1cluster}$ represent the $L^{1cluster}$ for each cluster used for reconstructing π^0.

5.5.1.2 Pulse-shape likelihood ratio

To determine the type of single cluster or two-cluster system, likelihood ratio R_γ is defined for single cluster or two-cluster system as:

$$R_\gamma^{1cluster} = \frac{L_\gamma^{1cluster}}{L_\gamma^{1cluster} + L_n^{1cluster}}, \tag{5.6}$$

$$R_\gamma^{2cluster} = \frac{L_\gamma^{2cluster}}{L_\gamma^{2cluster} + L_n^{2cluster}}, \tag{5.7}$$

where L_γ and L_n represent the pulse-shape likelihood for a photon-cluster assumption and neutron-induced cluster assumption, respectively. A large R_γ means that the single-cluster or two-cluster system are more likely to be induced by photons.

5.5.2 Performance evaluation

The performance of the pulse-shape likelihood-ratio method was evaluated with the photon-rich and the neutron-rich samples. As described in Section 5.1.2, the correlation between the pulse-shape likelihood-ratio method and the energy, position, and the cut variables for the cluster shape cuts is important. These correlations were also evaluated.

5.5.2.1 Cluster discrimination

$R_\gamma^{1cluster}$ is defined for each cluster, and the type of each cluster can be discriminated between a photon-induced cluster and a neutron-induced cluster using $R_\gamma^{1cluster}$. Figure 5.20 shows the $R_\gamma^{1cluster}$ distributions for the clusters in the photon-rich and neutron-rich samples. The clusters in the neutron-rich sample have $R_\gamma^{1cluster}$ close to 0 while the clusters in the photon-rich sample have $R_\gamma^{1cluster}$ close to 1. Figure 5.21 shows the fraction of clusters with $R_\gamma^{1cluster}$ larger than a given threshold value. By requiring $R_\gamma^{1cluster}$ to be higher than 0.1, 67% of the clusters in the neutron-rich samples were rejected while keeping 94% of the photon-clusters.
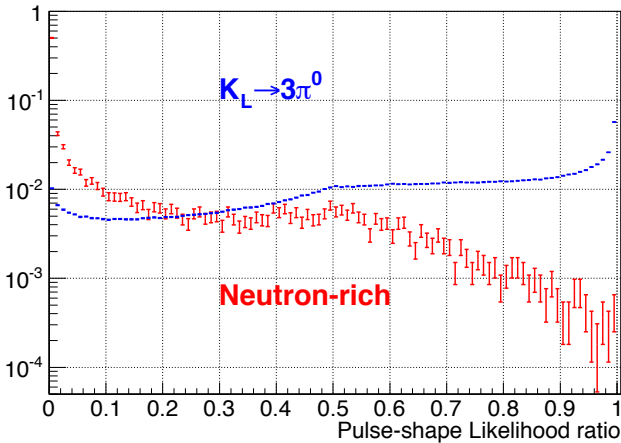
Figure 5.20: $R_\gamma^{1cluster}$ distribution for the photon-rich sample (blue) and the neutron-rich sample (red).
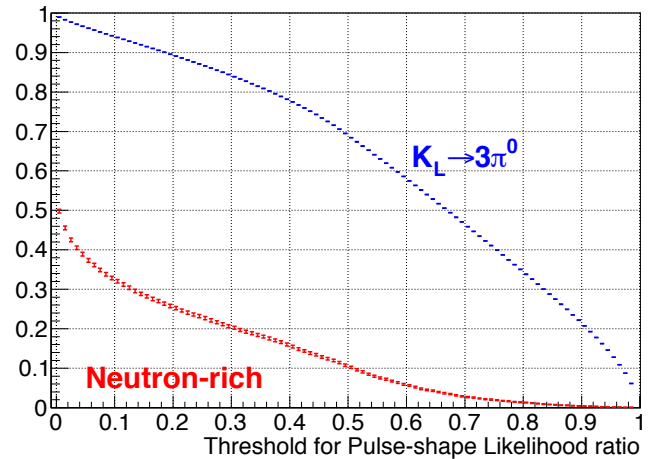
Figure 5.21: Fraction of clusters with $R_\gamma^{1cluster}$ larger than a given threshold shown as a function of threshold value in the photon-rich sample (blue) and the neutron-rich sample (red).

Energy dependence

Figure 5.22 and 5.23 show the correlations between $R_\gamma^{1cluster}$ and the energy deposit of the cluster in the photon-rich and the neutron-rich samples, respectively. The clusters with energy deposit smaller than 400 MeV have $R_\gamma^{1cluster}$ around 0.5. These low energy clusters made the peaks at 0.5 in the $R_\gamma^{1cluster}$ distribution and can degrade the performance to reject neutron-induced clusters in the low energy region.
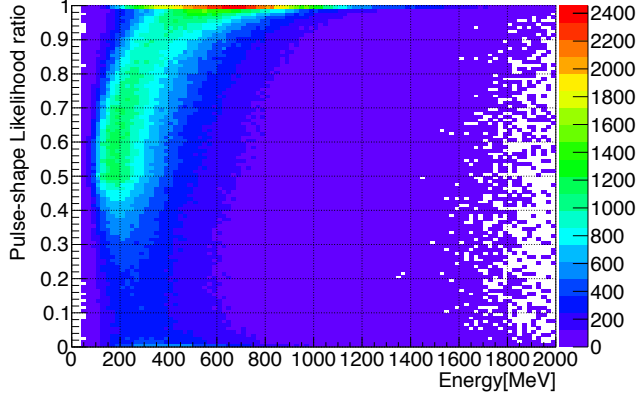
Figure 5.22: Correlation between $R_\gamma^{1cluster}$ and the energy deposit of the cluster in the photon-rich sample.
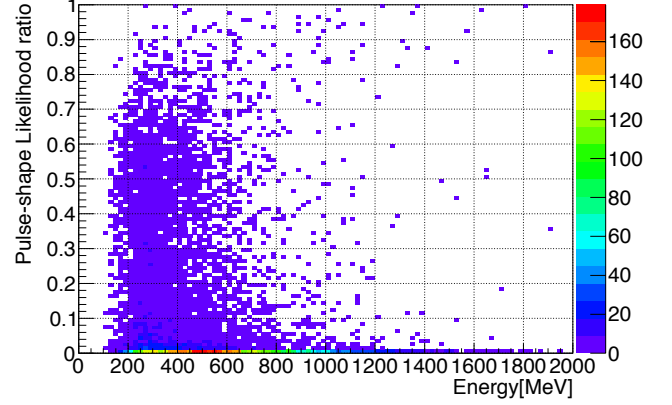
Figure 5.23: Correlation between $R_\gamma^{1cluster}$ and the energy deposit of the cluster in the neutron-rich sample.

Figures 5.24 and 5.25 show the fraction of clusters with $R_\gamma^{1cluster}$ larger than 0.1 as a function of the energy deposit of the cluster in the photon-rich sample and the neutron-rich sample, respectively. These figures show that the performance to reject the neutron-induced clusters has large energy dependence below than 800 MeV.
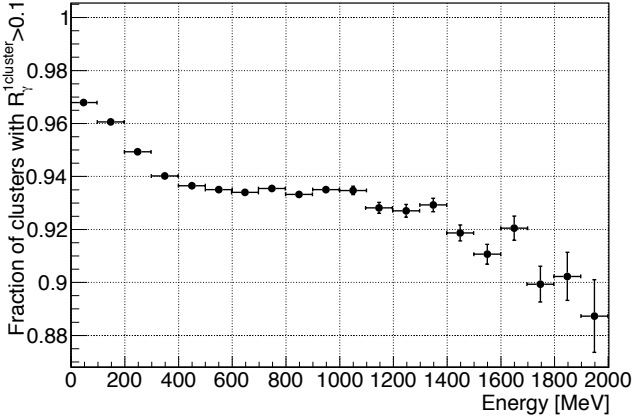
Figure 5.24: Fraction of clusters with $R_\gamma^{1cluster}$ larger than 0.1 as a function of the energy deposit of the cluster in the photon-rich sample.
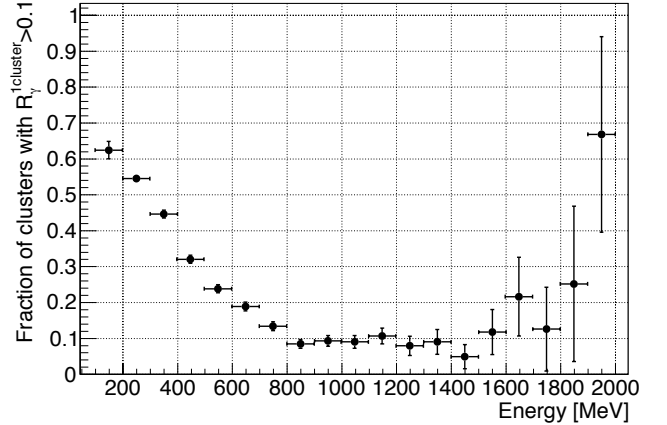
Figure 5.25: Fraction of clusters with $R_\gamma^{1cluster}$ larger than 0.1 as a function of the energy deposit of the cluster in the photon-rich sample.

Hit position dependence

107

Figures 5.26, 5.27 show the correlation between $R_\gamma^{1cluster}$ and the distance between the cluster position and the center of the surface of the CsI calorimeter in the photon-rich and the neutron-rich samples, respectively.
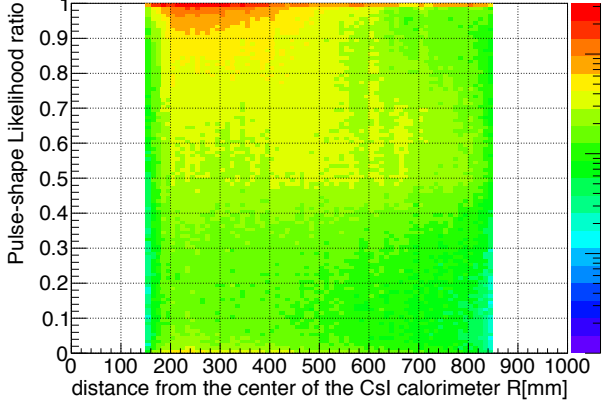
Figure 5.26: Fraction of clusters with $R_\gamma^{1cluster}$ larger than 0.1 as a function of the distance between the cluster position and the center of the surface of the CsI calorimeter for the cluster in the photon-rich sample.
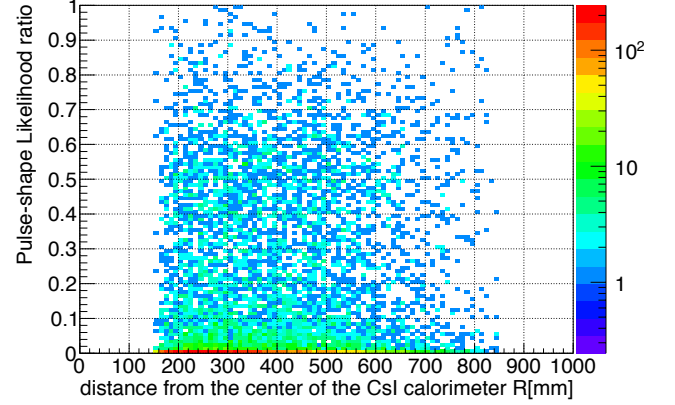
Figure 5.27: Fraction of clusters with $R_\gamma^{1cluster}$ larger than 0.1 as a function of the distance between the cluster position and the center of the surface of the CsI calorimeter for the photon-rich sample.

To isolate the correlation between the cluster position and the performance to reject the neutron-induced cluster from the energy dependence, the correlation for the cluster with energy larger than 400 MeV were studied. Figures 5.28 and 5.29 show the fraction of clusters with $R_\gamma^{1cluster}$ larger than 0.1 as a function of the distance between the cluster position and the center of the CsI calorimeter for the cluster with energy larger than 400 MeV in the photon-rich sample and the neutron-rich sample, respectively. These figures show that the clusters located farther from the center of the CsI calorimeter surface will be determined more likely to be photon-induced cluster. This degrades the performance to reject such neutron-induced cluster.

Correlation with Cluster Shape cut χ^2_{shape}

In the present $K_L \to \pi^0 \nu \bar{\nu}$ analysis, the cluster-shape cut using χ^2_{shape} rejects most of the neutron background. To achieve a further rejection of the neutron background with the new method, smaller correlation between $R_\gamma^{1cluster}$ and χ^2_{shape} is desired.

Figures 5.30, and 5.31 show the correlation between $R_\gamma^{1cluster}$ and cluster-shape cut variable χ^2_{shape} in the photon-rich samples and the neutron-rich samples, respectively. No strong correlation can be seen in any sample.

To isolate the correlation between χ^2_{shape} and the performance to reject the neutron-induced cluster from the energy dependence, the correlation for the cluster with energy larger than 400 MeV were studied. Figures 5.32 and 5.33 show the fraction of clusters with $R_\gamma^{1cluster}$ larger than 0.1 as a function of the cluster-shape cut variable χ^2_{shape} for the clusters with the energy larger than 400 MeV in the photon-rich sample and the neutron-rich sample, respectively. These figures show that the performance to reject the neutron-induced cluster becomes better for the cluster with smaller χ^2_{shape}.
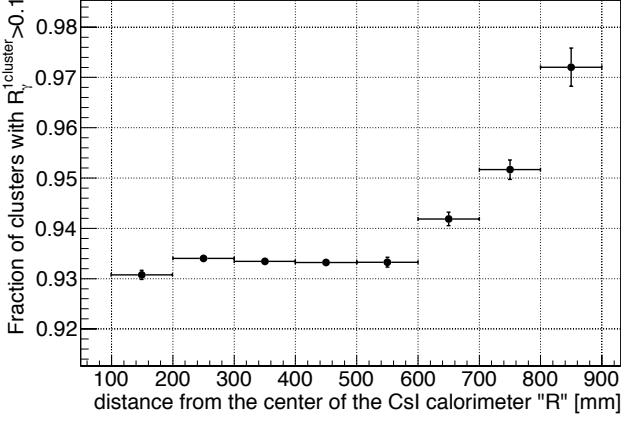
Figure 5.28: Fraction of clusters with $R_\gamma^{1cluster}$ larger than 0.1 as a function of the distance between the cluster position and the center of the surface of the CsI calorimeter for the cluster with energy larger than 400 MeV in the photon-rich sample.
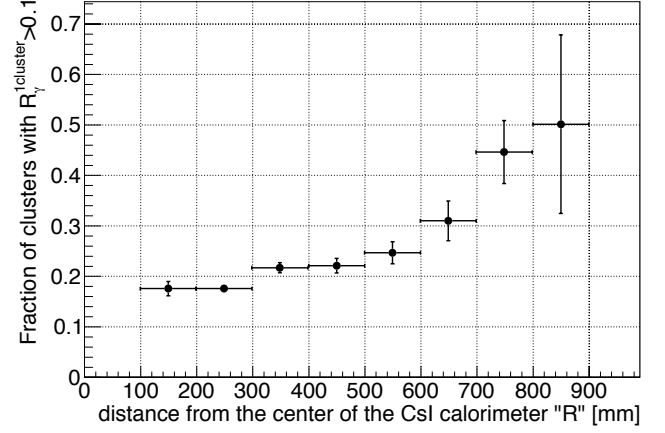
Figure 5.29: Fraction of clusters with $R_\gamma^{1cluster}$ larger than 0.1 as a function of the distance between the cluster position and the center of the surface of the CsI calorimeter for the cluster with energy larger than 400 MeV in the neutron-rich sample.
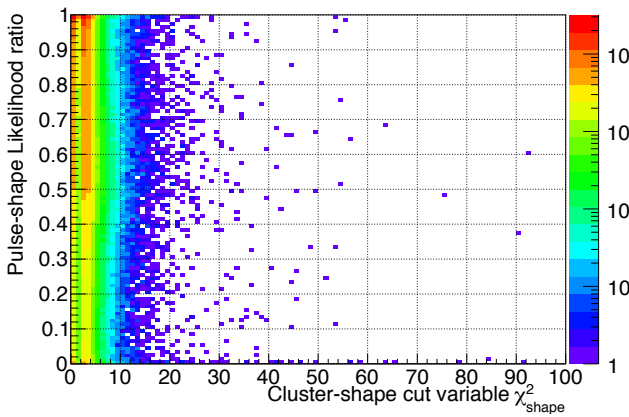
Figure 5.30: Correlation between $R_\gamma^{1cluster}$ and cluster-shape cut variable χ_{shape}^2 in the photon-rich sample.
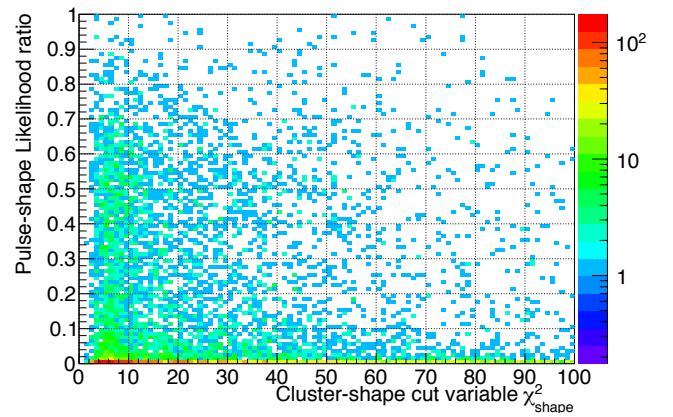
Figure 5.31: Correlation between $R_\gamma^{1cluster}$ and cluster-shape cut variable χ_{shape}^2 in the neutron-rich sample.
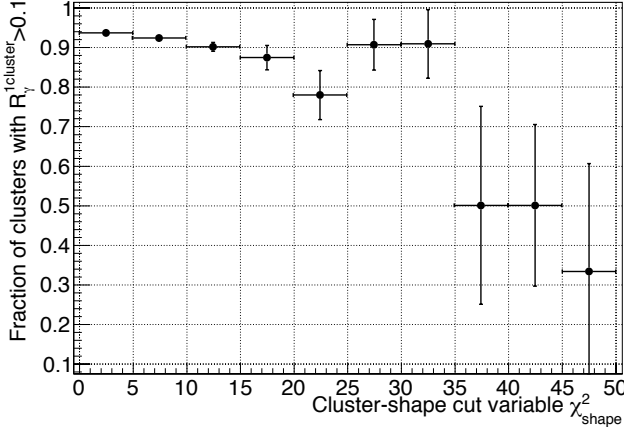
Figure 5.32: Fraction of clusters with $R_\gamma^{1cluster}$ larger than 0.1 as a function of the cluster-shape cut variable χ_{shape}^2 for the clusters with energy larger than 400 MeV in the photon-rich sample.
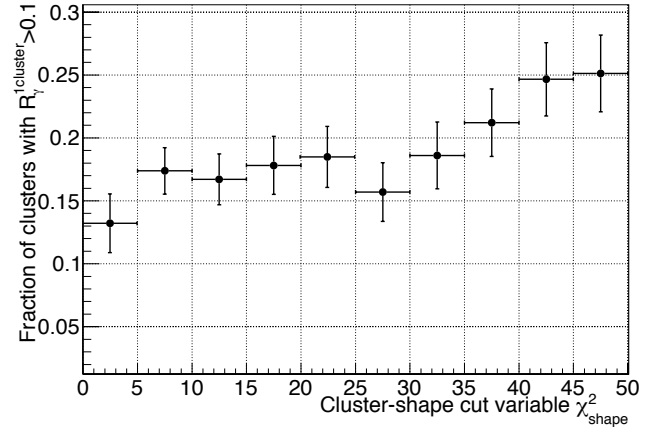
Figure 5.33: Fraction of clusters with $R_\gamma^{1cluster}$ larger than 0.1 as a function of cluster-shape cut variable χ_{shape}^2 for the clusters with energy larger than 400 MeV in the neutron-rich sample.

Dependence on the number of crystals

To investigate the source of the peak at 0.5 for the clusters with energy less than 400 MeV, the dependence of $R_\gamma^{1cluster}$ on the number of crystals used for calculation was studied as shown in Figs. 5.34 and 5.35. Clusters consisting of less than 3 crystals have $R_\gamma^{1cluster}$ around 0.5 in both samples.
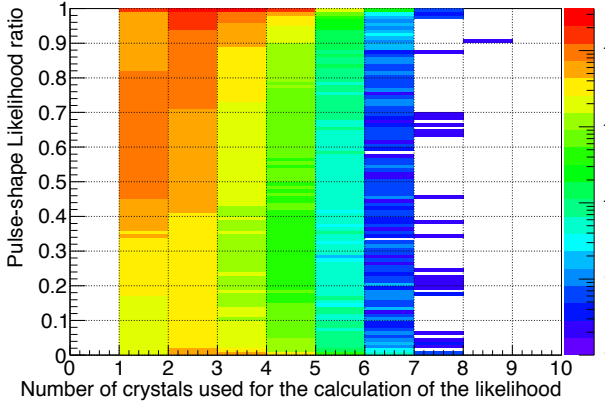
Figure 5.34: Correlation between $R_\gamma^{1cluster}$ and the number of crystals used for its calculation in the photon-rich sample.
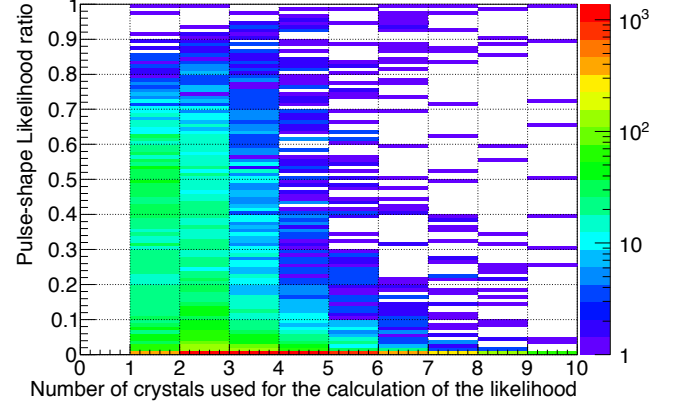
Figure 5.35: Correlation between $R_\gamma^{1cluster}$ and the number of crystals used for its calculation in the neutron-rich sample.

Figures 5.36, 5.37, and 5.38 show the correlation between $R_\gamma^{1cluster}$ and the cluster energy in the photon-rich sample in case of one, two and three or more crystals used in the calculation, respectively. These figures show that clusters with low likelihood ratio in the low energy region correspond to the case with small number of crystal used in the calculation. In particular, Fig. 5.36 shows that the cluster which had one or no crystal with energy deposit larger than 50 MeV made the peak at 0.5 in the likelihood distribution.

The same correspondences can be seen in the case of the neutron-rich sample. Figures 5.39, 5.40, and 5.41 show the correlation between single-cluster pulse-shape likelihood ratio and the
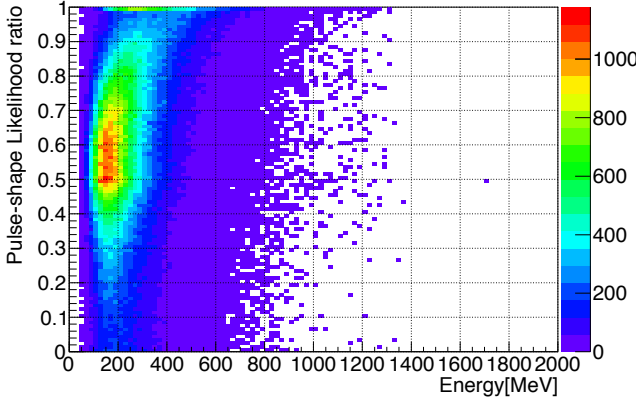
Figure 5.36: Correlation between $R_\gamma^{1cluster}$ and the cluster energy in the case with one crystal used in the calculation in the photon-rich sample.
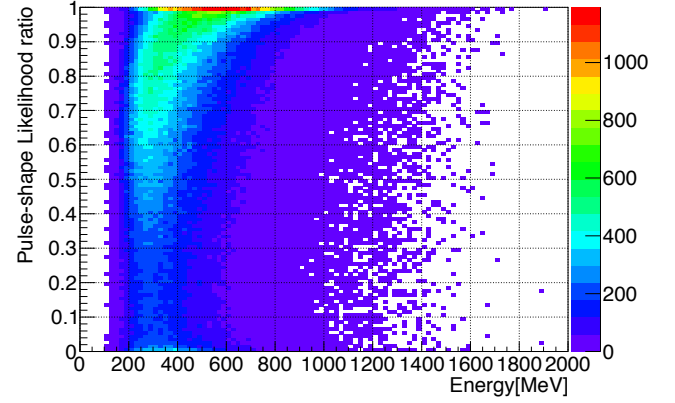
Figure 5.37: Correlation between $R_\gamma^{1cluster}$ and the cluster energy in the case with two crystals used in the calculation in the photon-rich sample.

energy deposit of the cluster in the neutron-rich sample in case of one, two and three or more crystals used in the calculation, respectively. These figures show that clusters in the neutron-rich sample with low likelihood ratio in the low energy region correspond to the case with small number of crystals used in the calculation.
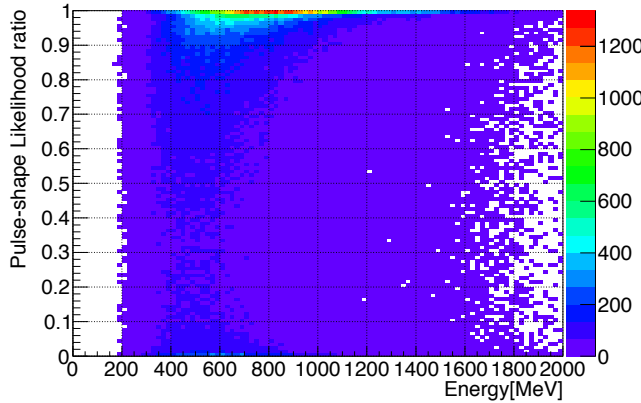
Figure 5.38: Correlation between $R_\gamma^{1cluster}$ and the cluster energy in the case with three or more crystals used in the calculation in the photon-rich sample.
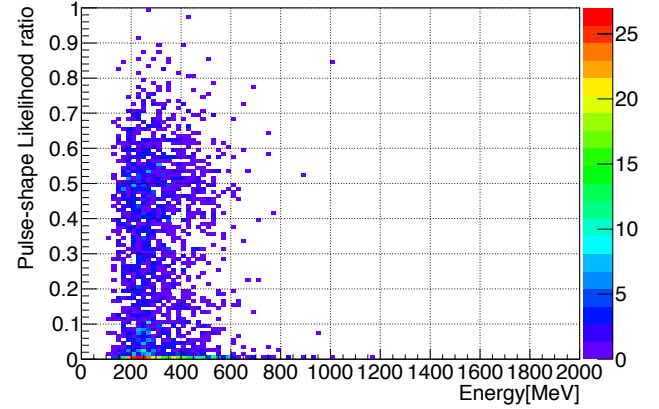
Figure 5.39: Correlation between $R_\gamma^{1cluster}$ and the energy deposit of the cluster in the case with one crystal used in the calculation in the neutron-rich sample.

The crystals with poor performance

As shown in Fig. 5.20, there were some photon-induced clusters which had $R_\gamma^{1cluster}$ less than 0.1 in the photon-rich sample. To investigate the source of this component, the performance to discriminate photon-induced cluster in each crystal was studied. Figure 5.42 shows the fraction of clusters with $R_\gamma^{1cluster}$ less than 0.1 in each crystals for the clusters in the photon-rich sample. There were some crystals which had more photon-induced clusters with $R_\gamma^{1cluster}$ less than 0.1 (18%) compared with other crystals (5%).
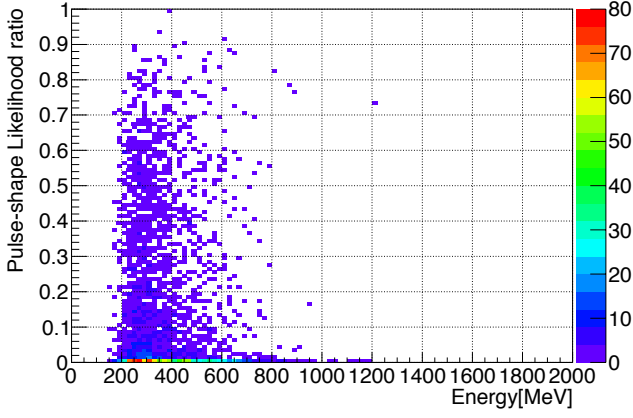
Figure 5.40: Correlation between $R_\gamma^{1cluster}$ and the energy deposit of the cluster in the case with two crystals used in the calculation in the neutron-rich sample.
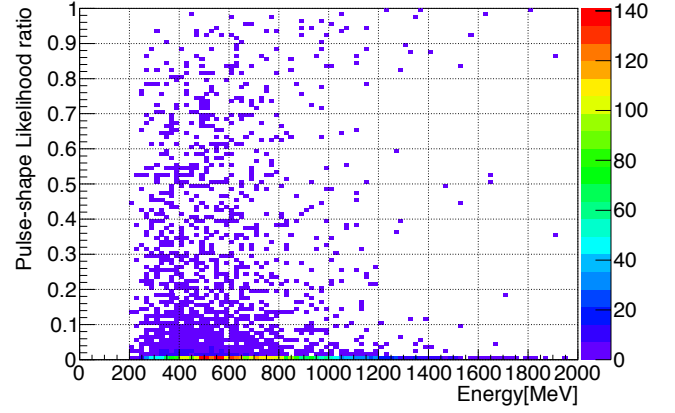
Figure 5.41: Correlation between $R_\gamma^{1cluster}$ and the energy deposit of the cluster in the case with three or more crystals used in the calculation in the neutron-rich sample.
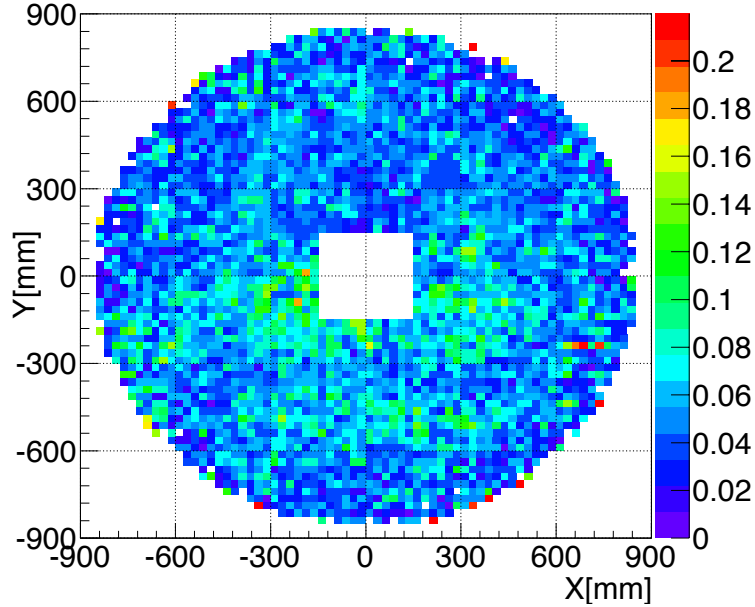
Figure 5.42: Fraction of clusters with $R_\gamma^{1cluster}$ less than 0.1 in each crystals for the clusters in the photon-rich sample.

To investigate the source of poor performance in these crystal, the waveform templates for these crystal were checked. Figures 5.43 and 5.44 show the σ_0 and the asymmetric parameter "a" used to make template pulses for crystal with CsI ID=975, which is located at $(x, y) = (-212.5 \text{ mm}, -87.5 \text{ mm})$, for the photon-rich sample and the neutron-rich sample, respectively. This crystal had standard deviation for the fit parameters twice larger than other crystals in neutron-rich sample for whole range of pulse height. This large standard deviation made this crystal to have poor performance to determine photon-cluster and made the cluster with $R_\gamma^{1cluster}$ less than 0.1 in photon-rich sample.
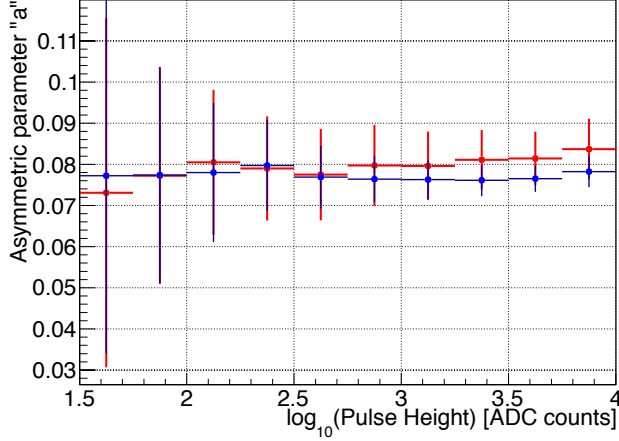
Figure 5.43: The distribution of σ_0 as a function of pulse-height for CsI ID=975. Red and blue points represent neutron-rich sample and photon-rich sample, respectively. The error bars represent the standard deviation of the parameter.
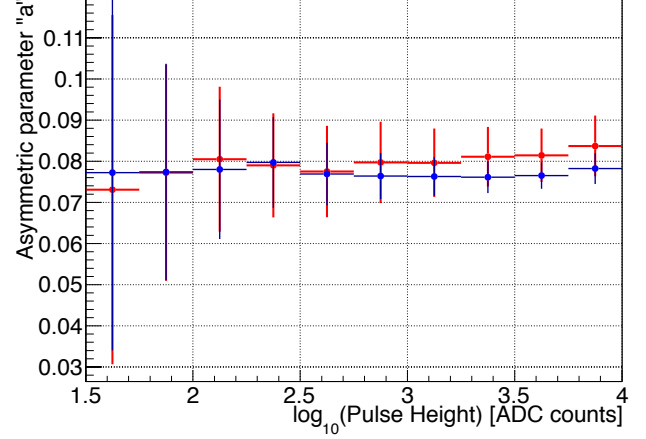
Figure 5.44: The distribution of asymmetric parameter "a" as a function of pulse-height for CsI ID=975. Red and blue points represent neutron-rich sample and photon-rich sample, respectively. The error bars represent the standard deviation of the parameter.

5.5.2.2 Two-cluster system discrimination

The $R_\gamma^{2cluster}$ is defined for the two-cluster system used for the reconstruction of π^0, and the type of two-cluster system can be discriminated between two photon-induced clusters or two neutron-induced clusters using $R_\gamma^{2cluster}$. Figure 5.45 shows the distribution of $R_\gamma^{2cluster}$ for the photon-rich sample and the neutron-rich sample. Compared with the $R_\gamma^{1cluster}$ distribution shown in Fig. 5.20, there is no peak at 0.5 in $R_\gamma^{2cluster}$ distribution for both samples. Figure 5.46 shows the fraction of two-cluster systems whose likelihood ratio is larger than a given threshold as a function of the threshold. By requiring the likelihood ratio to be higher than 0.1, 92% of two-cluster systems in the neutron-rich sample were rejected while keeping 92% of the two-cluster systems in the photon-rich sample.

Energy dependence

Because the performance to reject single neutron-induced cluster had an energy dependence, the energy dependence of the performance to reject neutron-induced two-cluster systems was studied. Figures 5.47 and 5.48 show the fraction of two-cluster systems with $R_\gamma^{2cluster} > 0.1$ as a function of the energy of higher energy cluster and lower energy cluster, respectively, in the
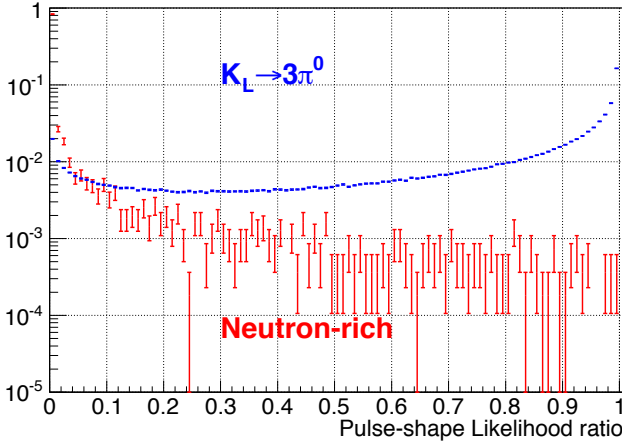
Figure 5.45: $R_\gamma^{2cluster}$ distribution for two-cluster system in the photon-rich sample (blue) and neutron-rich sample (red).
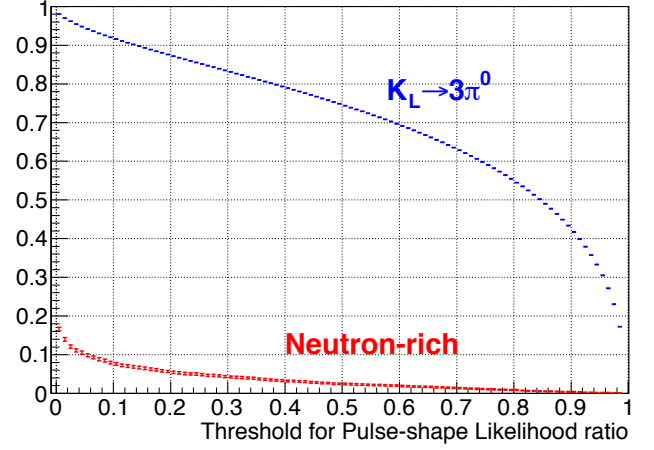
Figure 5.46: Fraction of two-cluster system with the $R_\gamma^{2cluster}$ larger than a given threshold in the photon-rich sample (blue) and neutron-rich sample (red), shown as a function of the threshold value.

photon-rich sample. These figures show that the method has a small energy dependence for both energies and has better performance if both cluster have energies less than 1 GeV.
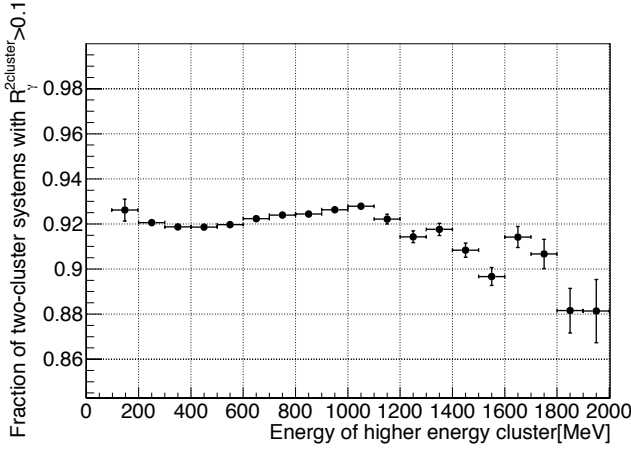
Figure 5.47: Fraction of two-cluster systems with $R_\gamma^{2cluster}$ larger than 0.1 as a function of the energy of higher energy cluster in the photon-rich sample.
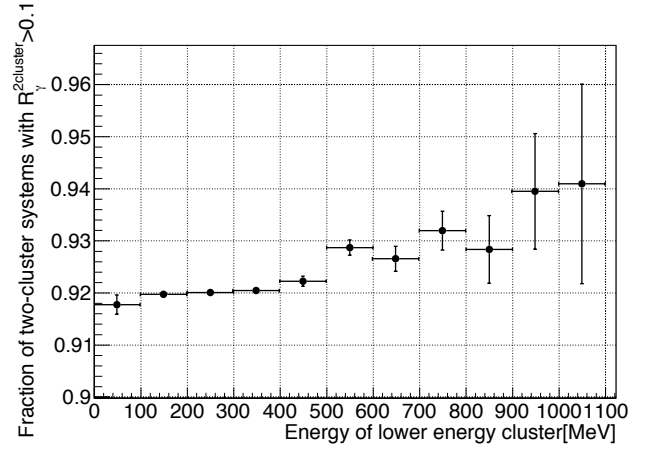
Figure 5.48: Fraction of two-cluster systems with $R_\gamma^{2cluster}$ larger than 0.1 as a function of the energy of lower energy cluster in the photon-rich sample.

Figures 5.49 and 5.50 show the fraction of two-cluster systems with $R_\gamma^{2cluster} > 0.1$ as a function of the energy of higher energy cluster and lower energy cluster, respectively, in the neutron-rich sample. These figures show that the method has an energy dependence for both energies if both clusters had the energy less than 1 GeV.

Correlation with Cluster-shape cut and Neural-net cuts

In the present $K_L \to \pi^0 \nu\overline{\nu}$ analysis, the cluster-shape cuts and neural-net cuts are used to reject the two-cluster systems induced by neutrons. To achieve a further improvement to
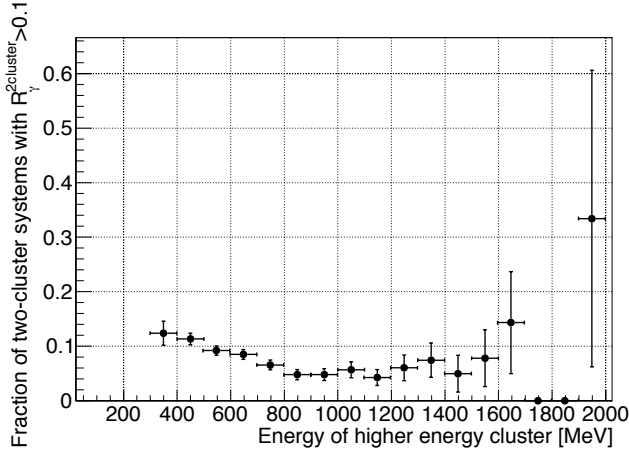
Figure 5.49: Fraction of two-cluster systems with $R_\gamma^{2cluster}$ larger than 0.1 as a function of the energy of higher energy cluster in the neutron-rich sample.
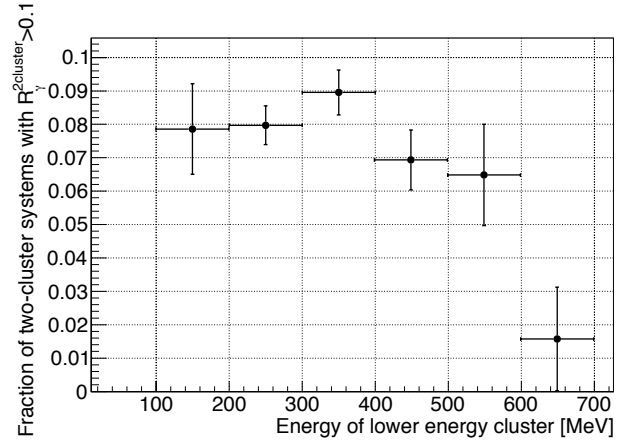
Figure 5.50: Fraction of two-cluster systems with $R_\gamma^{2cluster}$ larger than 0.1 as a function of the energy of lower energy cluster in the neutron-rich sample.

reject the neutron background with new method, a smaller correlation with those cut variables is desired for the $R_\gamma^{2cluster}$.

The correlation between the $R_\gamma^{2cluster}$ and the maximum χ_{shape}^2 of two-cluster systems which was used to reject the neutron background in $K_L \to \pi^0 \nu \overline{\nu}$ analysis, were studied. Figures 5.51 and 5.52 show the correlation between $R_\gamma^{2cluster}$ and the maximum χ_{shape}^2 of the two cluster system in the photon-rich sample and the neutron-rich sample, respectively.
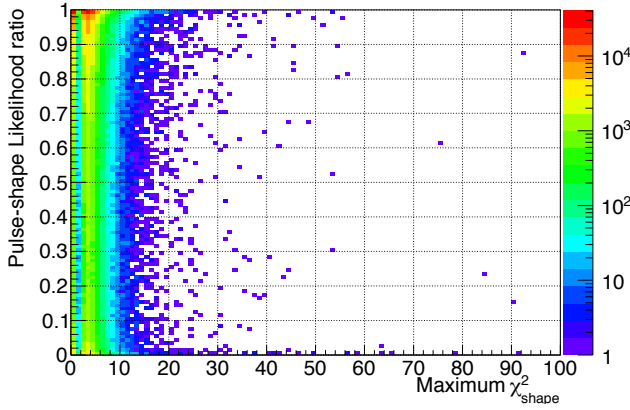
Figure 5.51: Correlation between $R_\gamma^{2cluster}$ and the maximum χ_{shape}^2 of the two-cluster system in the photon-rich sample.
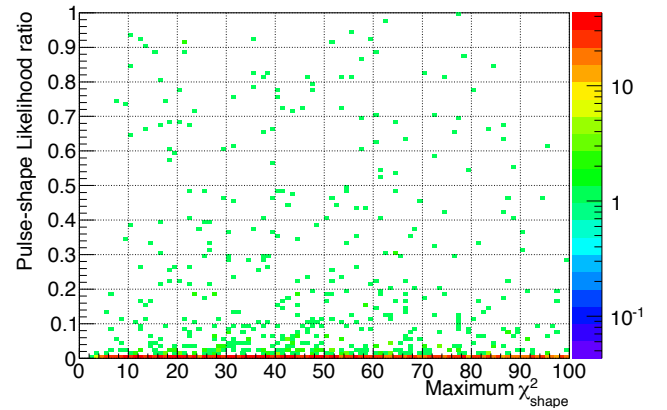
Figure 5.52: Correlation between $R_\gamma^{2cluster}$ and the maximum χ_{shape}^2 of the two-cluster system in in the neutron-rich sample.

Figures 5.53 and 5.54 show the fraction of the two-cluster systems with $R_\gamma^{2cluster} > 0.1$ as a function of the maximum χ_{shape}^2 of the two-cluster system in photon-rich sample and neutron-rich sample. Both figures show that the pulse shape likelihood method can reject the neutron-induced two-cluster system more efficiently for the two-cluster system with smaller maximum χ_{shape}^2.

The correlations between the $R_\gamma^{2cluster}$ and neural-net cut variables were also studied. The correlations were studied only with the neutron-rich sample. Figure 5.55 shows the correlation
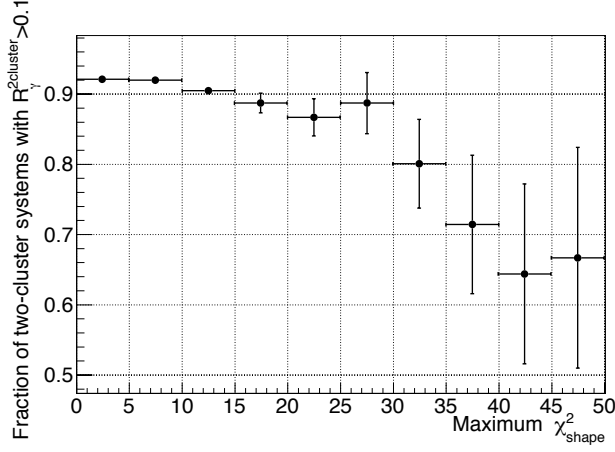
Figure 5.53: Fraction of two-cluster systems with $R_\gamma^{2cluster}$ larger than 0.1 as a function of the maximum χ^2_{shape} of the two-cluster system in the photon-rich sample.
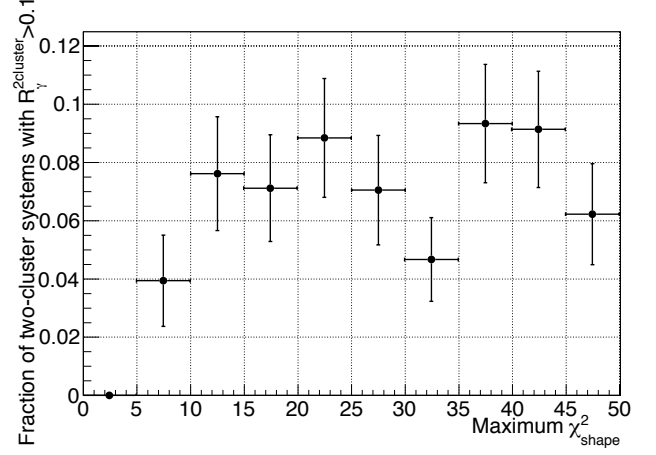
Figure 5.54: Fraction of two-cluster systems with $R_\gamma^{2cluster}$ larger than 0.1 as a function of the the maximum χ^2_{shape} of the two-cluster system in the neutron-rich sample.

between the $R_\gamma^{2cluster}$ and Kinematical Neural-net cut variable NN_{kine} in neutron-rich sample. Figure 5.56 shows the correlation between the $R_\gamma^{2cluster}$ and cluster-shape Neural-net cut variable NN_{shape} in neutron-rich sample. There is no strong correlation between $R_\gamma^{2cluster}$ and either neural-net cut variables.
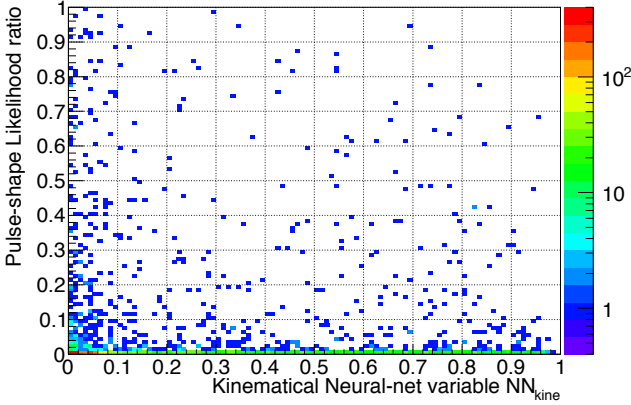
Figure 5.55: Correlation between $R_\gamma^{2cluster}$ and Kinematical Neural-net cut variable NN_{kine} in the neutron-rich samples.
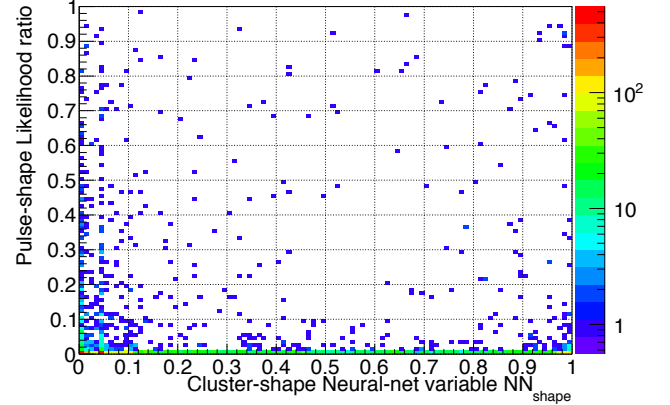
Figure 5.56: Correlation between $R_\gamma^{2cluster}$ and Cluster-Shape Neural-net cut variable NN_{shape} in the neutron-rich samples.

Figures 5.57 and 5.58 show the fraction of the two-cluster systems with $R_\gamma^{2cluster}$ larger than 0.1 as a function of the Kinematical Neural-net variable NN_{kine} and the Cluster-shape Neural-net variable NN_{shape}, respectively, in the neutron-rich sample. No clear correlation could be seen in both figures.

Combination with existing Cluster Shape Cut and Neural-net cuts

The performance of pulse-shape likelihood method imposed after the current event selection cuts were evaluated. In this evaluation, $R_\gamma^{2cluster}$ was used. To evaluate the performance, the
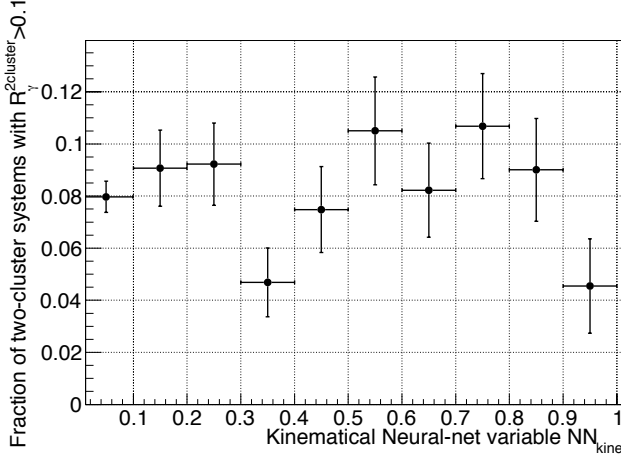
Figure 5.57: Fraction of two-cluster systems with $R_\gamma^{2cluster}$ larger than 0.1 as a function of the Kinematical Neural-net variable NN_{kine} in the neutron-rich sample.
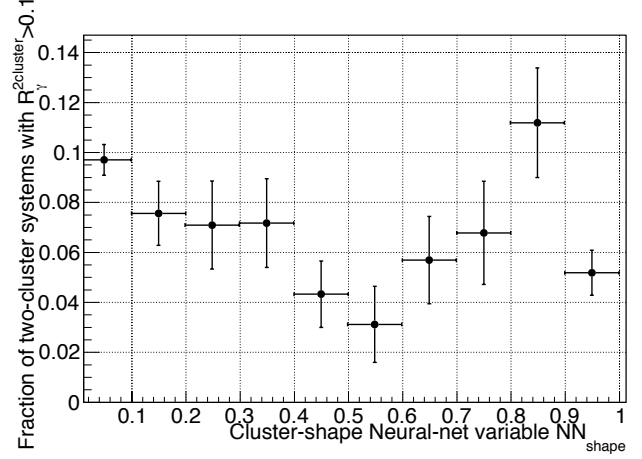
Figure 5.58: Fraction of two-cluster systems with $R_\gamma^{2cluster}$ larger than 0.1 as a function of the Cluster-shape Neural-net variable NN_{shape} in the neutron-rich sample.

neutron-rich sample after imposing the loose cuts were used. The number of events with $Z_{vtx} >$ 2900 mm and $P_t >$ 120 MeV/c were compared for various event selection conditions. The energy on crystal to calculate the likelihood was required to be 50 MeV and the $R_\gamma^{2cluster}$ was required to be larger than 0.1.

Table 5.5: Number of events with $Z_{vtx} >$ 2900 mm and $P_t >$ 120 MeV/c in the neutron-rich sample for each cut condition.

Cut Condition	Before Pulse-Shape Cut	After Pulse-Shape Cut	After/Before(%)
Loose cut	5362	425	7.9±0.37
$+NN_{kine}$ cut	594	53	8.9±1.17
$+NN_{shape}$ cut	778	56	7.2±0.93
$+NN_{kine}$ cut $+NN_{shape}$ cut	62	4	6.5±3.12
$+\chi_{shape}^2$ cut	19	0	0
All cuts for $K_L \to \pi^0 \nu\overline{\nu}$	2	0	0

Table 5.5 shows the number of events in the neutron-rich sample for each cut condition. Pulse-shape likelihood method rejected the background events in the defined region even after applying the current event selection cuts for $K_L \to \pi^0 \nu\overline{\nu}$ analysis.

Because no events remained after combining χ_{shape}^2 cut and χ_{shape}^2 cut, the improvement by Pulse-shape likelihood method was estimated by changing the threshold for χ_{shape}^2 cut.

Figure 5.59 shows the fraction of events with $R_\gamma^{2cluster} > 0.1$ for the events with maximum χ_{shape}^2 smaller than given threshold as a function of the threshold in the neutron-rich sample. Pulse-shape likelihood method rejected more fraction of events with lower threshold for the maximum χ_{shape}^2. The fraction of events with $R_\gamma^{2cluster} > 0.1$ for the events with maximum $\chi_{shape}^2 < 4.6$ was estimated to be $(1.88 \pm 0.90) \times 10^{-2}$ by fitting the change of performance for the region with $5 < \chi_{shape}^2 < 20$ with straight line, taking covariance between fit parameters into account.

Figure 5.60 shows the fraction of neutron-rich events with $R_\gamma^{2cluster} > 0.1$ for the events after both neural-net cuts and the maximum χ_{shape}^2 cut. The fraction is shown as a function of the threshold for the maximum χ_{shape}^2. The fraction of neutron-rich events rejected by pulse-shape likelihood method decreased for smaller threshold for the maximum χ_{shape}^2. The fraction of events with $R_\gamma^{2cluster} > 0.1$ for the events with maximum $\chi_{shape}^2 < 4.6$ after both neural-net cuts was estimated to be $(0.155 \pm 3.63) \times 10^{-2}$ by fitting the change of performance for the region with $5 < \chi_{shape}^2 < 40$ with straight line, taking covariance between fit parameters into account.
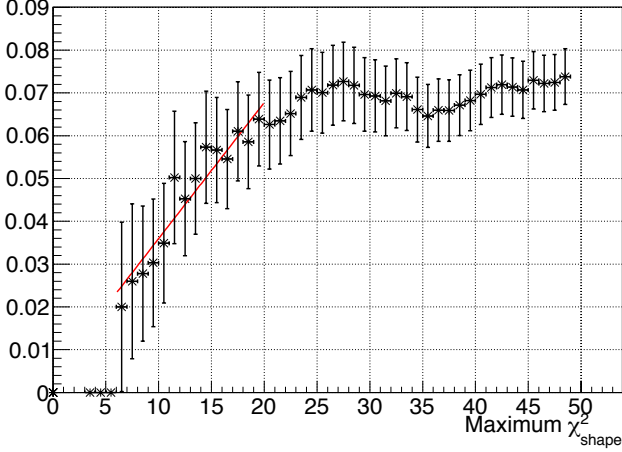
Figure 5.59: Fraction of events with $R_\gamma^{2cluster}$ larger than 0.1 for the events with maximum χ_{shape}^2 smaller than given threshold as a function of the threshold for the maximum χ_{shape}^2 of the two-cluster system in the neutron-rich sample.
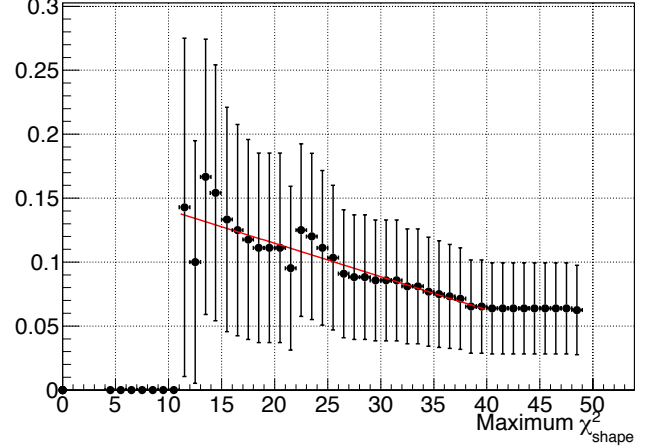
Figure 5.60: Fraction of events with $R_\gamma^{2cluster}$ larger than 0.1 for the events after both neural-net cuts with requireing maximum χ_{shape}^2 smaller than given threshold as a function of the threshold for the maximum χ_{shape}^2 of the two-cluster system in the neutron-rich sample.

5.6 Improvement in $K_L \to \pi^0 \nu \overline{\nu}$ analysis

5.6.1 Performance of the pulse shape likelihood method in the physics data

The developed pulse-shape likelihood method was applied to the physics data to study the improvement of background rejection.

To evaluate the performance, the physics data sample after imposing the loose cuts were used. The number of events with $Z_{vtx} > 2900$ mm and $P_t > 120$ MeV/c were compared for various event selection conditions. The energy on crystals to calculate the likelihood was required to be larger than 50 MeV and the likelihood ratio was required to be larger than 0.1. Table 5.6 shows the number of events in the physics data for each cut condition. Pulse-shape likelihood method rejected the background events in the defined region even after applying all the current event selection cuts for $K_L \to \pi^0 \nu \overline{\nu}$ analysis.

After applying all the event selection cuts for $K_L \to \pi^0 \nu \overline{\nu}$ analysis and the pulse-shape likelihood cut, one event remained in the defined region. This event was located inside the signal region. The $R_\gamma^{2cluster}$ for two-cluster system in this event was 0.838. The $R_\gamma^{1cluster}$(Energy) for each cluster was 0.93 (519 MeV) and 0.26 (357 MeV). The higher-energy cluster seemed to

Table 5.6: Number of events in the physics data with $Z_{vtx} > 2900$ mm and $P_t > 120$ MeV/c for each cut condition.

Cut Condition	Before Pulse-Shape Cut	After Pulse-Shape Cut	After/Before(%)
Loose cut	5150	562	10.9±0.43
$+NN_{kine}$ cut	940	130	13.8±1.13
$+NN_{shape}$ cut	387	59	15.2±1.83
$+NN_{kine}$ cut $+NN_{shape}$ cut	94	19	20.2±4.14
$+\chi^2_{shape}$ cut	7	2	28.6±17.1
All cuts for $K_L \to \pi^0 \nu \overline{\nu}$	2	1	50±35.4

be a photon-induced cluster, in particular because its single-cluster pulse-shape likelihood ratio was close to 1 and its energy was large enough to have good discrimination performance. The lower-energy cluster may be a cluster by a hadronic interaction because it has relatively low pulse-shape likelihood ratio.

5.7   Summary of this chapter

The difference of pulse-shape was confirmed between the photon-rich events and neutron-rich events. The method to discriminate the photons and neutrons based on the pulse-shape difference was developed. The performance of developed method to reject the neutron-induced cluster was evaluated with neutron and photon rich samples. The method achieved 67% rejection for each cluster and the 92% rejection for two-cluster system, with less than 10 % loss for photon-induced cluster and two-cluster systems. The developed method has no clear correlation with existing cuts based on the cluster-shape.

The effect of the method for the physics data taken in 2013 was studied and further reduction from current event selection was confirmed even though it was smaller than the improvement evaluated with neutron-rich sample.

The improvement by Pulse-shape likelihood method after all the present event selection cuts was estimated to be about by a factor of 6 from neutron-rich sample and 2 from physics data. If we combine these two samples, 4 events remained after applying Cluster-shape likelihood cut and 1 event remained after applying both Pulse-shape likelihood method cut and Cluster-shape likelihood cut. This gives us the improvement by a factor of 4.

Chapter 6

Discussion

As described in Chapter 5, the difference in pulse-shape was confirmed between the photon-rich events and neutron-rich events. The possible mechanism to have the pulse shape difference will be described in Section 6.1. The possible source of a position dependence of the pulse shape discrimination method will be described in Section 6.2. The discussion about remained event in the physics data and the possible source of a performance difference between neutron-rich sample and physics data will be described in Section 6.3. The result with the pulse shape likelihoods which use the Gaussian function with normalization as the PDF will be described in Section 6.4. To reach the sensitivity at the level of the branching ratio of $K_L \rightarrow \pi^0 \nu \overline{\nu}$ predicted by the SM, we need further improvements in addition to the developed pulse shape discrimination method and the present event selection cuts. The further improvement for the background reduction will be described in Section 6.5.

6.1   Mechanism to make difference in pulse shape

The pulse shape of output signal from PMT is determined by the following three factors:

- Timing structure of scintillation light emitted from CsI crystals

- Timing structure of scintillation light arriving at PMT after traveling thorough CsI crystals

- Response of PMT against the scintillation light

The difference in pulse shapes between the clusters produced by photons and neutrons should reflect the difference in their interactions with the CsI crystals.

Because the pulse shape difference remains even after cluster shape cuts, there should be the source of the pulse shape difference other than the difference in the transversal development of shower between the electromagnetic shower and the hadronic shower.

One possible mechanism to make a difference in pulse shape is the difference of scintillation process. If the scintillation light from the hadronic interaction is emitted via a process different from the process for electromagnetic interaction, the scintillation light from the hadronic interaction may have a different timing structure for emission.

6.1.1 Mechanism of the luminescence from the CsI crystal

At room temperature, the emission spectra of the scintillating light from the un-doped CsI crystals has two peaks: a narrow peak at 315 nm and a broad peak at 480 nm. The scintillation light around 315 nm has fast components with the decay times of 10 ns and 36 ns. The scintillation light around 480 nm has a slow component with the decay time of $\sim 1 \ \mu$s [27].

The peak position and the fraction of the emission spectra of the slow component vary between crystals. The slow component with wider and various spectra is explained by the luminescence from electrons trapped in the vacancies of I^- due to impurities in the CsI crystals [56, 57].

The fast component is regarded as the luminescence from the radiative decay of the self-trapped excitons (STE) [58, 59]. There are two types of STEs in CsI crystals in terms of configuration of electrons and holes: on-center and off-center configurations. The excited states of the two types of STE have singlet and triplet configuration. The on-center STE has the emission with the peak at 290 nm and the off-center STE has the emission with the peak at 340 nm. The fast component is reported as luminescence mainly from the on-center configuration STE [58]. The decay time of the luminescence from the on-center STE were measured at room temperature [58]. The decay of luminescence from the on-center STE has two decay times. The faster component is assigned to the singlet configuration, and the slower component is assigned to the triplet configurations. The decay time of faster and slower components from the on-site STE were measured to be 15 ns and 120 ns, respectively.

6.1.2 Pulse shape difference due to the ionization density difference

In the KOTO CsI calorimeter, only the fast component with the wavelength shorter than 400 nm can be detected by PMT, because a UV transmitting filter was inserted between the CsI crystal and PMT, as described in Section 2.3.2. The pulse-shape difference observed in the KOTO CsI calorimeter should be related to the nature of the fast component. As discussed above, the fast component of the decay of the luminescence from the CsI crystal has two components and the faster component is related to the singlet configuration of STE, whereas the slower component is related to the triplet configuration. If the fraction of triplet configuration becomes larger, the decay of the luminescence and thus the pulse-shape of the PMT output becomes broader and more asymmetric.

This mechanism was used to explain the pulse shape difference between incident particles in the organic scintillator [60]. Fast charged particles passing through the scintillating materials generate the excitation and the ionization of the molecules of the scintillating materials. The excitation of molecules leads to the singlet state while the recombination of ions and electrons after ionization leads to the triplet state. In the region of high density of excitation and ionization, a singlet state can be converted to a triplet state via the ionization due to the electric field of neighboring ions or interaction between the singlet states. Most of excited molecules result in the triplet state due to this conversion in the region of the high ionization density. Heavier particles with the same kinetic energy have larger dE/dX and thus have higher ionization density than that by lighter particles. Hadronic showers can make the region with high ionization density because they consist of low-energy charged hadrons, while the electromagnetic showers cannot make such region because they are made of relativistic electron and positrons. This ionization density difference due to the mass and charge difference changes the pulse shape of hadronic showers.

If this mechanism is also true for the scintillation in the CsI crystal, the pulse-shape difference seen between the neutron-rich sample and the photon-rich sample can be explained by the difference of population in the triplet state due to the ionization density difference.

6.1.3 Future prospect

To check whether the difference of the population of slower component changes the pulse shape for neutron-induced event, we have to measure the the decay time and the fraction of fast and slow components in the waveform. Because the signal from the CsI calorimeter channels were digitized and recorded after shaping by a 10-pole Bessel filter, we cannot directly measure the decay time and the fraction of the faster and slower components in the waveform. To check the decay time of waveform and the population of slower component in the waveform for neutron-induced cluster, the waveform digitization without the shaping is needed.

6.2 Source of position dependence of the Pulse shape discrimination method

As described in Section 5.5.2, the performance of pulse shape discrimination method depends the distance between the cluster position and the center of the surface of the CsI calorimeter. The position dependence was large in neutron-rich sample and small in photon-rich sample.

In this section, the study on the source of this correlation will be described.

6.2.1 Correlation between the position and the energy of cluster

Figures 6.1 and 6.2 show the correlation between the energy of cluster and the cluster distance from the center of the CsI calorimeter for photon-rich sample and neutron-rich sample, respectively. There is a clear correlation between the energy of cluster and the distance for both samples.
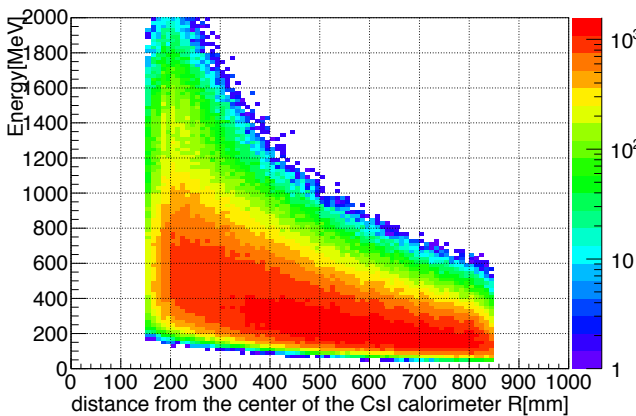
Figure 6.1: Correlation between the energy of cluster and the distance between the position of cluster and the center of the CsI calorimeter surface for photon-rich sample.
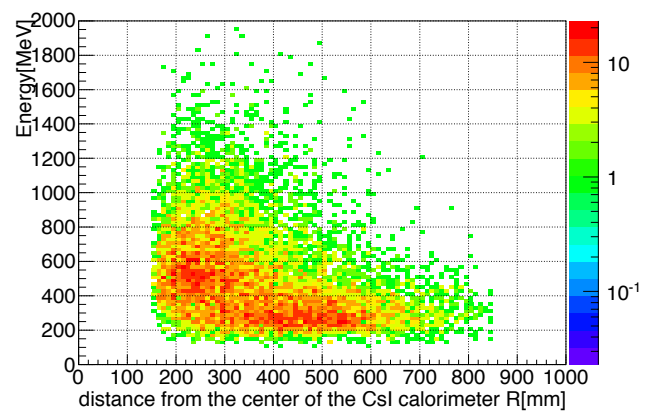
Figure 6.2: Correlation between the energy of cluster and the distance between the position of cluster and the center of the CsI calorimeter surface for neutron-rich sample.

Because the pulse shape discrimination method has an energy dependence, the correlation between the energy of cluster and the distance can be a source of the hit position dependence of the method.

6.2.2 Statistics of events used for template

The difference in the number of events used for making pulse shape template can also be a source of the correlation.

As shown in Figs. 5.3 and 5.4, most of crystals had more than 10000 events for the photon-rich samples while only the crystals in the region 400 mm from the center had around 10000 events for the neutron-rich events. If the crystals with templates made from a large number of event can discriminate photon-induced clusters from neutron-induced clusters more effectively, the small position dependence in photon-rich sample and large dependence in neutron-rich sample can be explained by the difference in the number of events used for making pulse shape templates.

Figures 5.28 and 5.29 show that hit position dependence were small in the region within 400 mm from the center for the clusters with energy larger than 400 MeV. This small dependence in the region within 400 mm from the center can be also explained by the number of events used to make pulse shape templates; the crystals in the region 400 mm from the center had a large number of events for making templates than the other crystals outside the region.

6.2.3 Future Prospect

If we can have more neutron-rich events to make pulse shape template, more crystals will have better performance and position dependence of the method may decrease. Because there is strong correlation between energy and position of cluster, improvement on the position dependence of the method may also improve the energy dependence of the method.

6.3 The remained event in the physics data and the difference of performance between neutron-rich sample and physics data

6.3.1 The remained event in the physics data

As described in Section 5.6, the effect of the pulse shape likelihood method for the physics data taken in 2013 was smaller than the improvement evaluated with the neutron-rich sample. After applying all the event selection cuts and the cuts on $R_\gamma^{2cluster}$, one event remained in the signal region. This suggests that the physics data contains more events which the pulse shape likelihood method cannot reject. To understand the type of such events, I compared the fit parameters of the event remained in the signal region with the template, and estimated the probabilities for each cluster to be a photon-induced cluster and a neutron-induced cluster.

6.3.2 Fit parameters of the remaining event in the physics data

In the the remaining event in the physics data, four crystals were used to calculate the likelihood. In the cluster with (E[MeV],x[mm], y[mm])=(519.4, 534.3, -57.4), crystal of CsI ID=1002

$(x[mm], y[mm])$=(-537.5, -62.5) with energy of 172.3 MeV, and crystal of CsI ID=1000 ($x[mm]$,
$y[mm]$)=(-587.5, -62.5) with energy of 162.4 MeV were used.

Figures 6.3 and 6.4 show the templates and the obtained values in the remaining event for
the fit parameters σ_0 and a for the crystal of CsI ID=1002. Both parameters in the remaining
event are far from values in the neutron template and within the standard deviation of the
photon template.
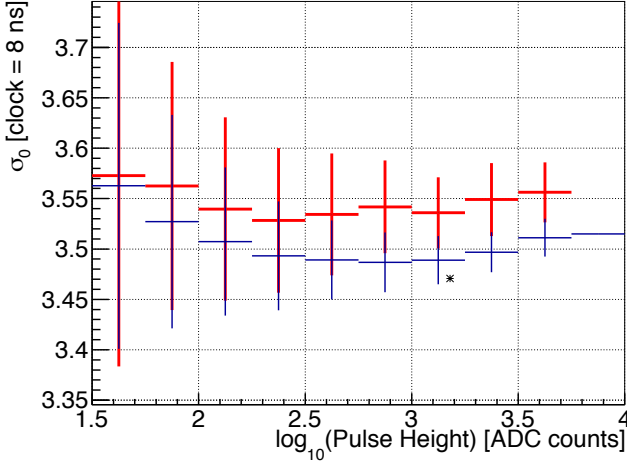
Figure 6.3: The distribution of σ_0 as a function
of pulse-height for the crystal of CsI ID=1002
($x[mm]$, $y[mm]$)=(-537.5, -62.5) with energy of
172.3 MeV. Red and blue points represent the
neutron template and the photon template, re-
spectively. The error bars represent the stan-
dard deviation of the parameter. The * repre-
sents the obtained value in the remaining event
in the physics data.
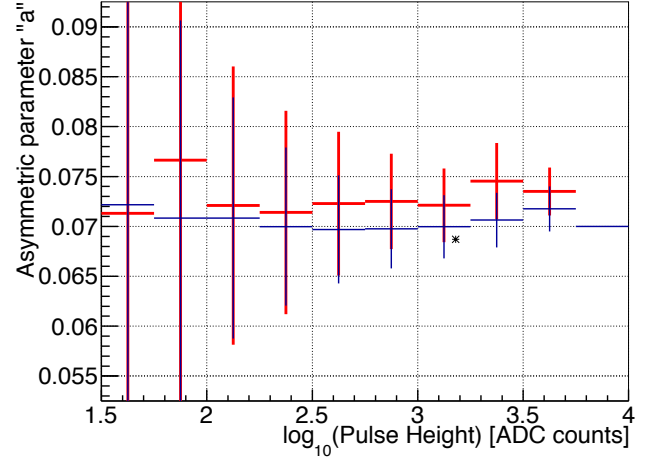
Figure 6.4: The distribution of asymmetric pa-
rameter "a" as a function of pulse-height for
the crystal of CsI ID=1002 ($x[mm]$, $y[mm]$)=(-
537.5, -62.5) with energy of 172.3 MeV. Red
and blue points represent the neutron template
and the photon template, respectively. The er-
ror bars represent the standard deviation of the
parameter. The * represents the obtained value
in the remaining event in the physics data.

Figures 6.5 and 6.6 show the templates and the obtained values of the remaining event for
the fit parameters σ_0 and a for the crystal of CsI ID=1000. The obtained value of σ_0 in the
remaining event is far from the value of the neutron template and closer to the value in the
photon template even though it is located out of the standard deviation of the photon template.
The obtained value of a in the remaining event is closer to the value in the neutron template
even though it is within the standard deviation of both templates.

In the cluster with (E[MeV],$x[mm]$, $y[mm]$)=(357.4, 11.5, -244.3), crystal of CsI ID=647
($x[mm]$, $y[mm]$)=(-12.5, -262.5) with energy of 162.4 MeV, and crystal of CsI ID=695 ($x[mm]$,
$y[mm]$)=(-12.5, -237.5) with energy of 119.9 MeV were used.

Figures 6.7 and 6.8 show the templates and the obtained values in the remaining event
for the fit parameters σ_0 and a for the crystal of CsI ID=647. The obtained values of both
parameters in the remaining event are closer to the values in the photon template even though
they are located within the standard deviation of both templates.

Figures 6.9 and 6.10 show the templates and the obtained values in the remaining event
for the fit parameters σ_0 and a for the crystal of CsI ID=695. The measured values of both
parameters in the remaining event are closer to the values in the neutron template even though
they are located within the standard deviation of both templates.
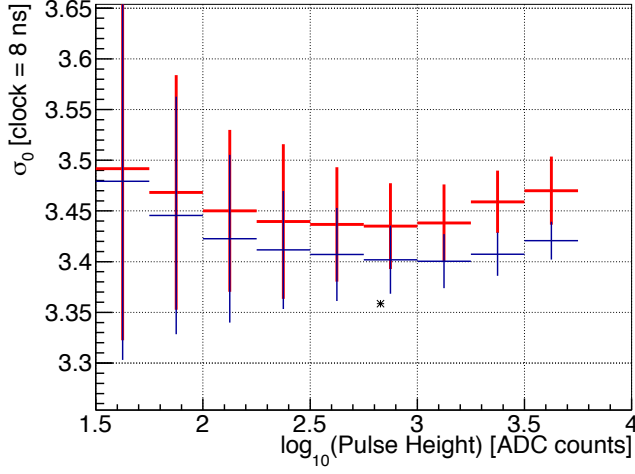
Figure 6.5: The distribution of σ_0 as a function of pulse-height for the crystal of CsI ID=1000 (x[mm], y[mm])=(-587.5, -62.5) with energy of 74.5 MeV. Red and blue points represent the neutron template and the photon template, respectively. The error bars represent the standard deviation of the parameter. The * represents the obtained value in the remaining event in the physics data.
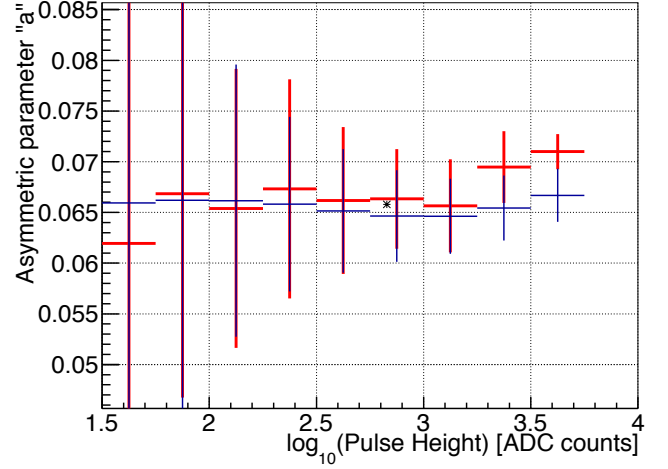
Figure 6.6: The distribution of asymmetric parameter "a" as a function of pulse-height for the crystal of CsI ID=1000 (x[mm], y[mm])=(-587.5, -62.5) with energy of 74.5 MeV. Red and blue points represent neutron-rich sample and photon-rich sample, respectively. The error bars represent the standard deviation of the parameter. The * represents the obtained value in the remaining event in the physics data.
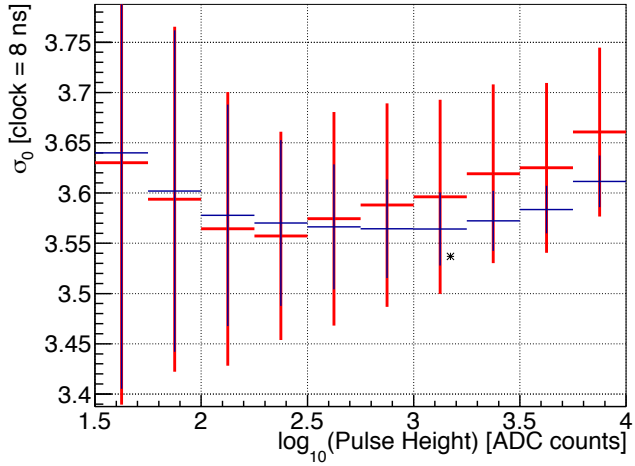
Figure 6.7: The distribution of σ_0 as a function of pulse-height for the crystal of CsI ID=647 (x[mm], y[mm])=(-12.5, -262.5) with energy of 162.4 MeV. Red and blue points represent the neutron template and the photon template, respectively. The error bars represent the standard deviation of the parameter. The * represents the obtained value in the remaining event in the physics data.

Figure 6.8: The distribution of asymmetric parameter "a" as a function of pulse-height for the crystal of CsI ID=647 (x[mm], y[mm])=(-12.5, -262.5) with energy of 162.4 MeV. Red and blue points represent neutron-rich sample and photon-rich sample, respectively. The error bars represent the standard deviation of the parameter. The * represents the obtained value in the remaining event in the physics data.

Figure 6.9: The distribution of σ_0 as a function of pulse-height for the crystal of CsI ID=695 (x[mm], y[mm])=(-12.5, -237.5) with energy of 119.9 MeV. Red and blue points represent neutron-rich sample and photon-rich sample, respectively. The error bars represent the standard deviation of the parameter. The * represents the obtained value in the remaining event in the physics data.

Figure 6.10: The distribution of asymmetric parameter "a" as a function of pulse-height for the crystal of CsI ID=695 (x[mm], y[mm])=(-12.5, -237.5) with energy of 119.9 MeV. Red and blue points represent neutron-rich sample and photon-rich sample, respectively. The error bars represent the standard deviation of the parameter. The * represents the obtained value in the remaining event in the physics data.

6.3.2.1 $\chi^2_{pulseshape}$

To evaluate the consistency of an observed cluster with an assumption of the photon cluster and the neutron-induced cluster, $\chi^2_{pulseshape}$ is defined based on the pulse shape template:

$$\chi^2_{pulseshape,crystal} = \sum_{p}^{\sigma_0, a} \frac{(p^{meas.} - p^{exp}(H))^2}{RMS_{p^{exp}}(H)^2}, \tag{6.1}$$

$$\chi^2_{pulseshape} = \sum_{j}^{N} \chi^2_{pulseshape,crystal}, \tag{6.2}$$

where j represents the crystals in the cluster used for the calculation, and N represents the number of such crystals. In this calculation, the numbers of degrees of freedom (NDF) are 2 for $\chi^2_{pulseshape,crystal}$ and $2N$ for $\chi^2_{pulseshape}$. The $\chi^2_{pulseshape,crystal}$ and $\chi^2_{pulseshape}$ were defined for the photon assumption and the neutron assumption.

Figure 6.11 shows the number of crystals used in the calculation of $\chi^2_{pulseshape}$ for both photon and neutron assumptions. In both samples, most of clusters used 2 crystals for the calculation of $\chi^2_{pulseshape}$.

Figures 6.12 and 6.13 show the $\chi^2_{pulseshape,crystal}/NDF$ distribution with the photon assumption and the neutron assumption, respectively, for the photon-rich sample and the neutron-rich sample. Both figures show that $\chi^2_{pulseshape,crystal}/NDF$ had smaller value with the correct assumption and larger value with a wrong assumption.

Figures 6.14 and 6.15 show the χ^2_{pulse}/NDF distribution with the photon assumption and the neutron assumption, respectively, for the photon-rich sample and the neutron-rich sample.
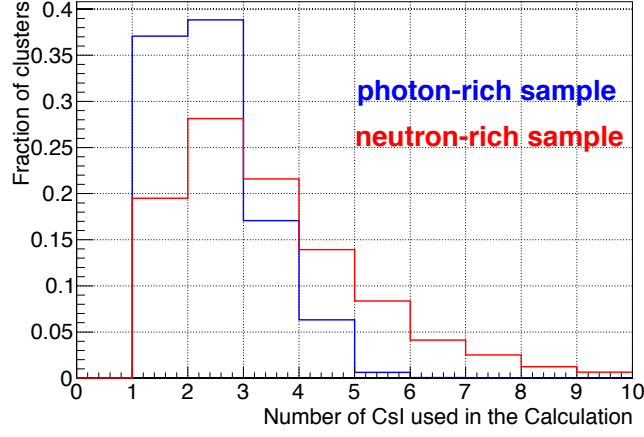
Figure 6.11: Number of crystals used in the calculation of $\chi^2_{pulseshape}$. Blue and Red histograms represent photon-rich and neutron-rich sample, respectively.
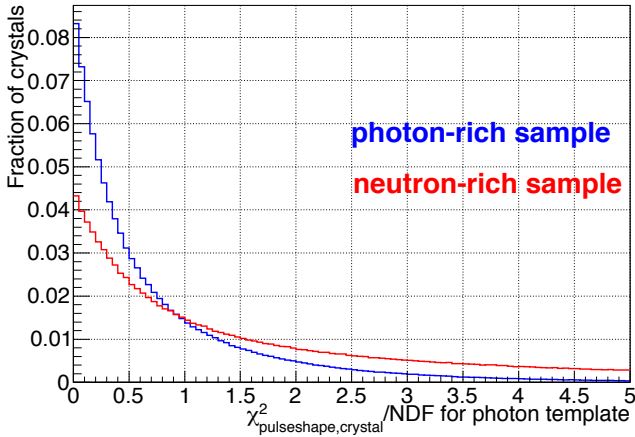
Figure 6.12: $\chi^2_{pulseshape,crystal}/NDF$ distribution with the photon assumption. Blue and Red histograms represent photon-rich and neutron-rich sample, respectively.
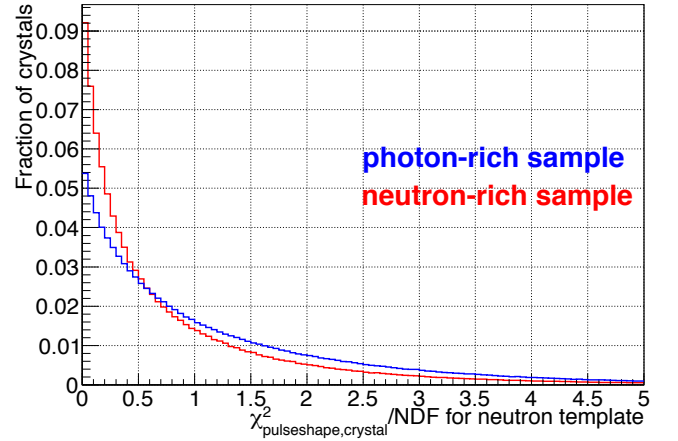
Figure 6.13: $\chi^2_{pulseshape,crystal}/NDF$ distribution with the neutron assumption. Blue and Red histograms represent photon-rich and neutron-rich sample, respectively.

Both figures show that $\chi^2_{pulseshape}/NDF$ had smaller value with correct assumption and larger value with wrong assumption.
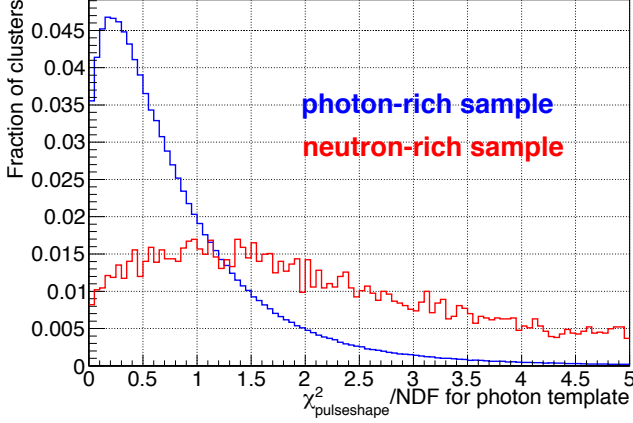
Figure 6.14: $\chi^2_{pulseshape}/NDF$ distribution with the photon assumption. Blue and Red histograms represent photon-rich and neutron-rich sample, respectively.
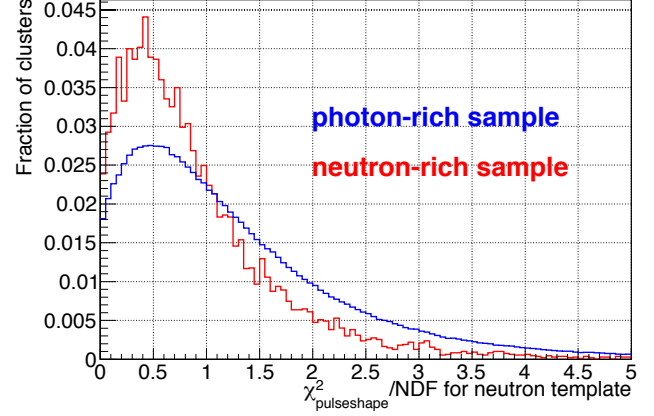
Figure 6.15: $\chi^2_{pulseshape}/NDF$ distribution with the neutron assumption. Blue and Red histograms represent photon-rich and neutron-rich sample, respectively.

6.3.2.2 Interpretation of the type of the remaining event

Type of the interaction in each crystal

As described in Section 6.3.2, four crystals were used to calculate the likelihoods of the remaining event in the physics data. For the cluster with energy of 519.4 MeV, crystal of CsI ID=1002 and crystal of CsI ID=1000 were used. For the cluster with energy of 357.4 MeV, crystal of CsI ID=647 and crystal of CsI ID=695 were used.

To determine the type of interaction in each crystal in the remaining event in the physics data are closer to the photon template or the neutron template, I calculated $\chi^2_{pulseshape,crystal}$ and estimated the probabilities of each crystal with the photon assumption and neutron assumption.

Table 6.1: The obtained value of $\chi^2_{pulseshape,crystal}$ and the probability to have $\chi^2_{pulseshape,crystal}$ larger than obtained value, for crystals in the clusters used in the calculation of likelihoods in the remaining event in the physics data. The values with the photon assumption and with the neutron assumption are shown separately.

Energy of Cluster	CsI ID	Photon assumption		Neutron assumption	
		$\chi^2_{pulseshape,crystal}$	Probability	$\chi^2_{pulseshape,crystal}$	Probability
519 MeV	1002	0.92	63%	4.70	9.5%
	1000	1.58	45%	3.08	21%
357 MeV	647	2.02	36%	0.88	64%
	695	0.91	63%	0.05	97%

Table 6.1 shows the obtained value of $\chi^2_{pulseshape,crystal}$ and the probability to have $\chi^2_{pulseshape,crystal}$ larger than obtained value, for crystals in the clusters used in the calculation of likelihoods in the remaining event in the physics data. The values with the photon assumption and with the neutron assumption are shown separately.

Both crystals in the cluster with energy of 519 MeV had smaller $\chi^2_{pulseshape,crystal}$ and larger probabilities with the photon assumption than with the neutron assumption. Both crystals are thus considered to contain an electromagnetic shower.

For the crystals in the cluster with energy of 357 MeV, the crystal with CsI ID=647 had smaller $\chi^2_{pulseshape,crystal}$ and larger probabilities with the neutron assumption than with the photon assumption even though obtained values are closer to the values in the photon template, as shown in Figs. 6.7 and 6.8. This is due to a larger standard deviation of fit parameters for the neutron template than those for the photon template in this crystal. The crystal with CsI ID=695 had smaller $\chi^2_{pulseshape,crystal}$ and larger probabilities with the neutron assumption. Both crystals are thus considered to be the crystals with an hadronic interaction.

Type of each cluster

I calculated $\chi^2_{pulseshape}$ for the clusters in the remained event in the physics data and estimated the probabilities to be a cluster with electromagnetic shower or that with a hadronic interaction.

The cluster with energy of 519 MeV had $\chi^2_{pulseshape} = 2.50$ for the photon assumption and $\chi^2_{pulseshape} = 7.78$ for neutron assumption with $NDF = 4$. The probabilities to have $\chi^2_{pulseshape}$ larger than the measured value were 64% for the photon assumption and 10% for the neutron assumption. This means that this cluster was not a cluster with a hadronic interaction at the 90% confidence level.

The cluster with energy of 357 MeV had $\chi^2_{pulseshape} = 2.92$ for the photon assumption and $\chi^2_{pulseshape} = 0.92$ for neutron assumption with $NDF = 4$. The probabilities to have $\chi^2_{pulseshape}$ larger than the measured value were 57% for the photon assumption and 92% for the neutron assumption. This means that this cluster was a cluster with a hadronic interaction at the 92% confidence level.

Type of the event

If we assume that cluster with energy of 519 MeV was a photon-induced cluster and cluster with energy of 357 MeV was a neutron-induced cluster, the sum of $\chi^2_{pulseshape}$ of each cluster for such assumption was 3.42 with $NDF = 8$. The probability to have the sum of $\chi^2_{pulseshape}$ larger than such value was 90.5%. This means that the assumption is correct at the 90% confidence level. On the other hand, if we assume that both clusters were photon-induced cluster, the sum of $\chi^2_{pulseshape}$ of each cluster for such assumption was 5.41 with $NDF = 8$. The probability to have the sum of $\chi^2_{pulseshape}$ larger than such value was 71%.

This event is thus considered to have a photon-induced cluster and a cluster with a hadronic interaction.

6.3.3 Contribution of events with with a photon-induced cluster and a neutron-induced cluster

Likelihood ratios by taking events with a photon-induced cluster and a cluster with a hadronic interaction into account

Because the $R^{2cluster}_\gamma$ was made to discriminate the two photon-induced clusters from the two neutron-induced clusters, it may less effective to reject the events with a photon-induced cluster and a cluster with a hadronic interaction. The smaller performance in the physics data than the neutron-rich sample can be explained if the physics data contains more events with a

photon-induced cluster and a cluster with a hadronic interaction, and if the cut on $R_\gamma^{2cluster}$ is less effective to reject such events.

To check the contribution of events with a photon-induced cluster and a cluster with a hadronic interaction in the physics data and the neutron-rich sample, I defined new likelihood ratios by taking the such events into account:

$$L_{n\gamma}^{2cluster} = L_{1,n}^{1cluster} L_{2,\gamma}^{1cluster} + L_{1,\gamma}^{1cluster} L_{2,n}^{1cluster} \tag{6.3}$$

$$R^{\gamma\gamma} = \frac{L_\gamma^{2cluster}}{L_\gamma^{2cluster} + L_{n\gamma}^{2cluster} + L_n^{2cluster}} \tag{6.4}$$

$$R^{n\gamma} = \frac{L_{n\gamma}^{2cluster}}{L_\gamma^{2cluster} + L_{n\gamma}^{2cluster} + L_n^{2cluster}} \tag{6.5}$$

$$R^{nn} = \frac{L_n^{2cluster}}{L_\gamma^{2cluster} + L_{n\gamma}^{2cluster} + L_n^{2cluster}} \tag{6.6}$$

A large $R_{n\gamma}^{2cluster}$ means that the two-cluster system is more likely to have a photon-induced cluster and a cluster with a hadronic interaction.

The pulse shape likelihood ratios for the event remained in the signal region in the physics analysis are $R_{\gamma\gamma}^{2cluster} = 0.25$, $R_{n\gamma}^{2cluster} = 0.70$, and $R_{nn}^{2cluster} = 0.05$.

Figures 6.16, 6.17, and 6.18 show $R_{\gamma\gamma}^{2cluster}$, $R_{nn}^{2cluster}$, and $R_{n\gamma}^{2cluster}$ distributions, respectively, for two-cluster system in the photon-rich sample and neutron-rich sample. Because most of the photon-induced two-cluster systems had $R_{n\gamma}^{2cluster}$ around 0.5, the photon-rich sample no longer had a peak at 1 in $R_{n\gamma}^{2cluster}$ distribution.
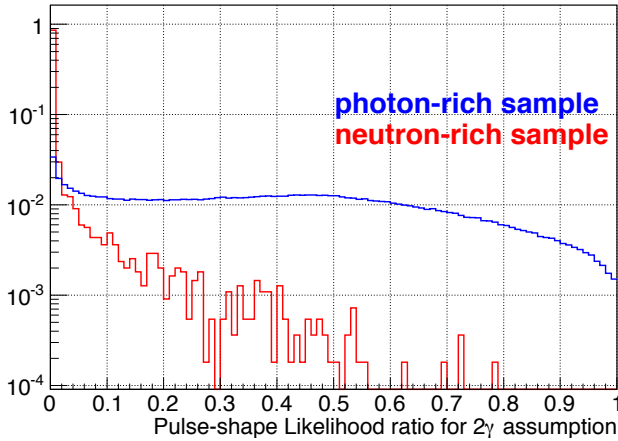
Figure 6.16: $R_{\gamma\gamma}^{2cluster}$ distribution for two-cluster system in the photon-rich sample (blue) and the neutron-rich sample (red).
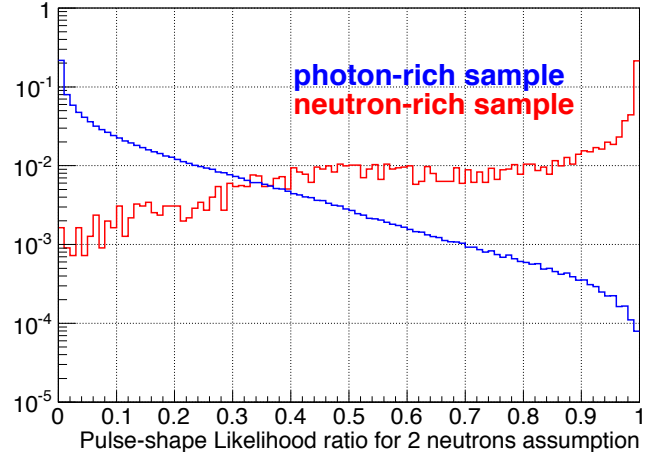
Figure 6.17: $R_{nn}^{2cluster}$ distribution for two-cluster system in the photon-rich sample (blue) and the neutron-rich sample (red).

Figure 6.19 shows $R_{n\gamma}^{2cluster}$ distribution for two-cluster system in the neutron-rich sample and the physics data. The contribution of the events with larger $R_{n\gamma}^{2cluster}$ ($R_{n\gamma}^{2cluster} > 0.6$) was larger in the physics data than in the neutron-rich sample in the region. This means that the physics data after loose cut contains more events with a photon-induced cluster and a cluster with a hadronic interaction than the neutron-rich sample.
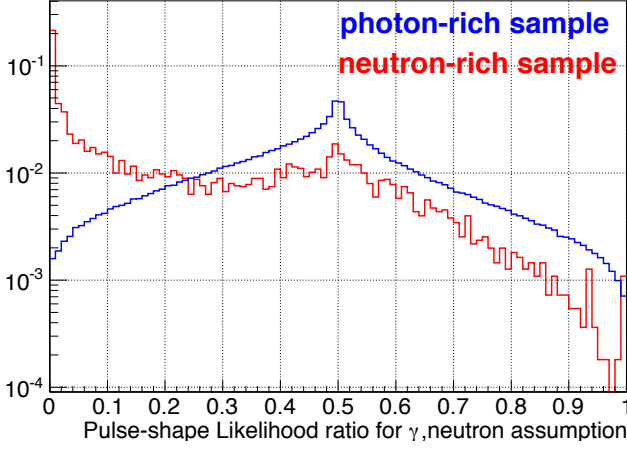
Figure 6.18: $R_{n\gamma}^{2cluster}$ distribution for two-cluster system in the photon-rich sample (blue) and the neutron-rich sample (red).
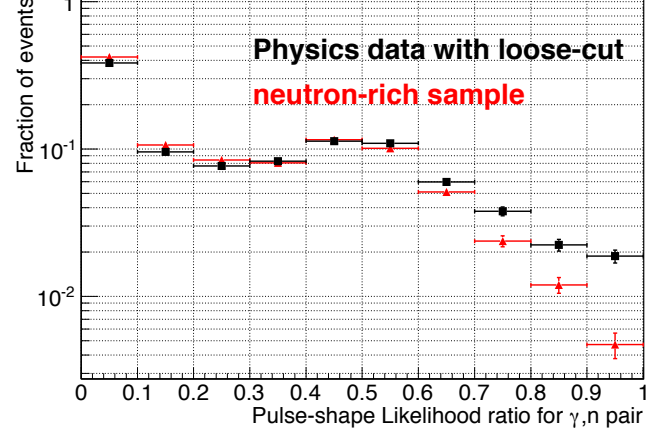
Figure 6.19: $R_{n\gamma}^{2cluster}$ distribution for two-cluster system in the neutron-rich sample (red) and the physics data (black).

$R_{n\gamma}^{2cluster}$ dependence of the cut $R_{\gamma}^{2cluster}$

If the cuts on $R_{\gamma}^{2cluster}$ is less effective for the events with larger $R_{n\gamma}^{2cluster}$, a larger contribution of the events with larger $R_{n\gamma}^{2cluster}$ ($R_{n\gamma}^{2cluster} > 0.6$) in the physics data than in the neutron-rich sample can explain the difference of the performance of the cut on $R_{\gamma}^{2cluster}$ between the physics data and the neutron-rich sample.

To check whether the cut on $R_{\gamma}^{2cluster}$ is less effective for the events with larger $R_{n\gamma}^{2cluster}$, $R_{n\gamma}^{2cluster}$ dependences of the performance of the cut on $R_{\gamma}^{2cluster}$ was studied.

Figure 6.20 shows the fraction of two-cluster systems with $R_{\gamma}^{2cluster}$ larger than 0.1 as a function of the $R_{n\gamma}^{2cluster}$ in the neutron-rich sample and the physics data. The 30% of the events with $R_{n\gamma}^{2cluster} > 0.4$ remained after requiring $R_{\gamma}^{2cluster} > 0.1$ while most of the events with $R_{n\gamma}^{2cluster} < 0.4$ were rejected after the cut on $R_{\gamma}^{2cluster}$.

Because the cut on $R_{\gamma}^{2cluster}$ is less effective for the events with $R_{n\gamma}^{2cluster} > 0.4$, a larger contribution of the events with with $R_{n\gamma}^{2cluster} > 0.6$ in the physics data than in the neutron-rich sample can degrade the performance of the cut on $R_{\gamma}^{2cluster}$ for the events in the physics data than in the neutron-rich sample.

$R_{n\gamma}^{2cluster}$ dependence of other cut to reject neutron-induced clusters

In addition to the cut on $R_{\gamma}^{2cluster}$, $R_{n\gamma}^{2cluster}$ dependences of the performance of other cuts to reject neutron-induced clusters were also studied.

Figures 6.21, 6.22, and 6.22 show the fraction of two-cluster systems which passed the cuts on the maximum χ_{shape}^2, NN_{kine}, and NN_{shape}, respectively, as a function of the $R_{n\gamma}^{2cluster}$ in the neutron-rich sample and the physics data. These event selection cuts have no strong correlation with $R_{n\gamma}^{2cluster}$.

Performance of the combination of the event selection cuts for the events with large $R_{n\gamma}^{2cluster}$

To check the contribution of the different population of the events with large $R_{n\gamma}^{2cluster}$ on the difference of the performance of the cut on $R_{\gamma}^{2cluster}$ between the physics data and the neutron-rich sample, the performance of the pulse shape likelihood method and other event selection cuts to reject the neutron-induced cluster were studied for the events with $R_{n\gamma}^{2cluster} < 0.6$. The
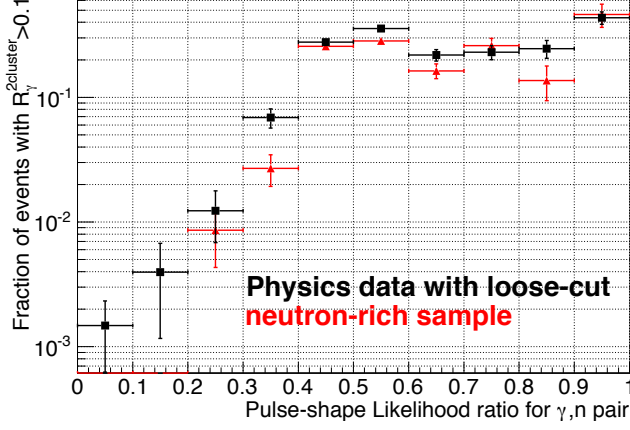
Figure 6.20: Fraction of two-cluster systems with $R_\gamma^{2cluster}$ larger than 0.1 as a function of the $R_{n\gamma}^{2cluster}$ in the neutron-rich sample and the physics data.
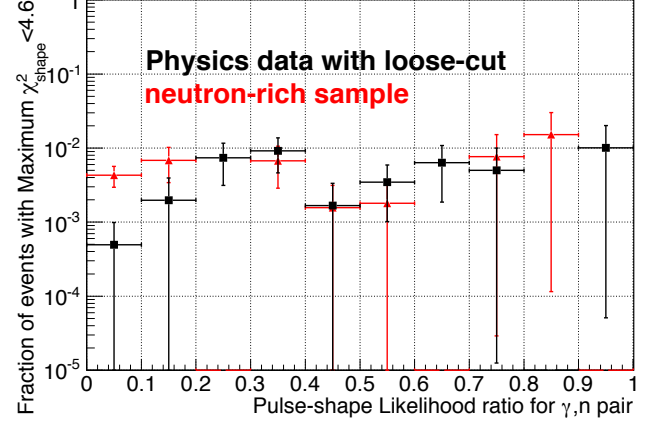
Figure 6.21: Fraction of two-cluster systems with the maximum $\chi_{shape}^2 < 4.6$ as a function of the $R_{n\gamma}^{2cluster}$ in the neutron-rich sample and the physics data.
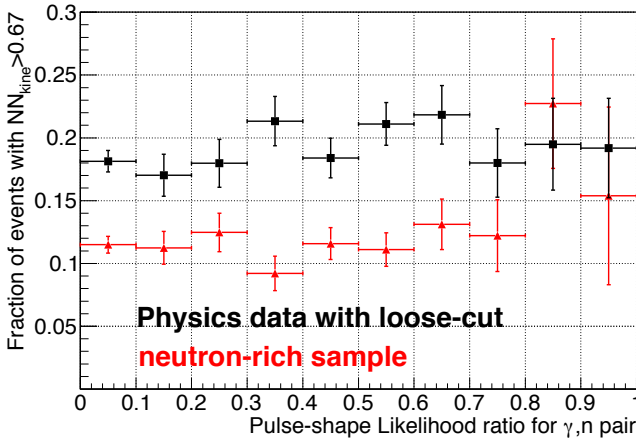
Figure 6.22: Fraction of two-cluster systems which passed the cut on NN_{kine} as a function of the $R_{n\gamma}^{2cluster}$ in the neutron-rich sample and the physics data.
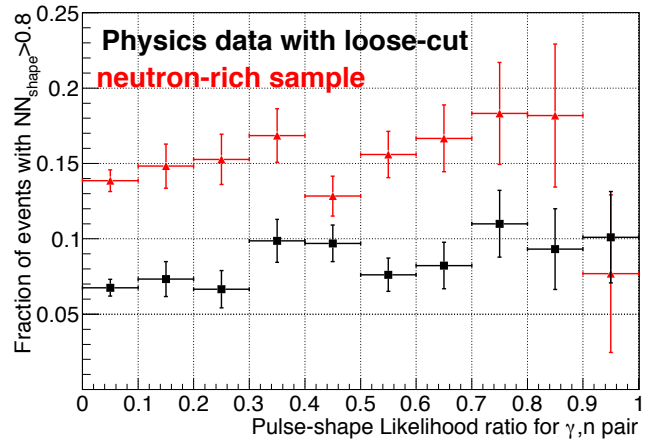
Figure 6.23: Fraction of two-cluster systems which passed the cut on NN_{shape} as a function of the $R_{n\gamma}^{2cluster}$ in the neutron-rich sample and the physics data.

132

energy on crystals to calculate the likelihood was required to be larger than 50 MeV and the $R_\gamma^{2cluster}$ was required to be larger than 0.1.

Table 6.2: The number of events in the neutron-rich sample with Z_{vtx} >2900 mm, P_t >120 MeV/c, and $R_{n\gamma}^{2cluster} < 0.6$ for each cut condition.

Cut Condition	Before Pulse-Shape Cut	After Pulse-Shape Cut	After/Before(%)
Loose cut	4872	325	6.68±0.35
$+NN_{kine}$ cut	527	38	7.21±1.12
$+NN_{shape}$ cut	695	44	6.33±0.92
$+NN_{kine}$ cut $+NN_{shape}$ cut	54	4	7.40±3
$+\chi_{shape}^2$ cut	18	0	0
All cuts for $K_L \rightarrow \pi^0 \nu\overline{\nu}$	2	0	0

Table 6.3: The number of events in the physics data with Z_{vtx} >2900 mm, P_t >120 MeV/c, and $R_{n\gamma}^{2cluster} < 0.6$ for each cut condition.

Cut Condition	Before Pulse-Shape Cut	After Pulse-Shape Cut	After/Before(%)
Loose cut	4432	381	8.60±0.42
$+NN_{kine}$ cut	797	84	10.5±1.09
$+NN_{shape}$ cut	323	38	11.8±1.79
$+NN_{kine}$ cut $+NN_{shape}$ cut	79	12	15.2±4.04
$+\chi_{shape}^2$ cut	5	0	0
All cuts for $K_L \rightarrow \pi^0 \nu\overline{\nu}$	1	0	0

Tables 6.2 and 6.3 show the number of events in the neutron-rich sample and the physics data, respectively, for each cut condition by requiring $R_{n\gamma}^{2cluster} < 0.6$.

By requiring $R_{n\gamma}^{2cluster} < 0.6$, the difference of the performance of the pulse shape likelihood method between the physics data and the neutron-rich sample became small compared with the results without the cut on $R_{n\gamma}^{2cluster}$ which are shown in Tables. 5.5 and 5.6 . The events with large $R_{n\gamma}^{2cluster}$ are thus considered to be one of the sources of different performance of the pulse shape likelihood method in the physics data and the neutron-rich sample.

6.3.4 The properties of the event with large $R_{n\gamma}^{2cluster}$

To investigate the type of the events with large $R_{n\gamma}^{2cluster}$, the parameter distributions for such events were studied.

Figures 6.24 and 6.25 show the energy distribution of higher energy cluster and lower energy cluster, respectively, in the physics data for the case without cut on $R_{n\gamma}^{2cluster}$, with $R_{n\gamma}^{2cluster} > 0.6$, and with $R_{n\gamma}^{2cluster} > 0.9$. The events with $R_{n\gamma}^{2cluster} > 0.9$ have larger energy compared with the case before the cut on $R_{n\gamma}^{2cluster}$.

Figure 6.26 shows Maximum $\chi_{pulseshape}^2$ distribution in the physics data with the loose cuts for the case without cut on $R_{n\gamma}^{2cluster}$, with $R_{n\gamma}^{2cluster} > 0.6$, and with $R_{n\gamma}^{2cluster} > 0.9$. Figures 6.27

Figure 6.24: Energy distribution of higher energy cluster in the physics data. Blue,red and black histograms represent the physics data without cut on $R_{n\gamma}^{2cluster}$, with $R_{n\gamma}^{2cluster} > 0.6$, and with $R_{n\gamma}^{2cluster} > 0.9$, respectively.
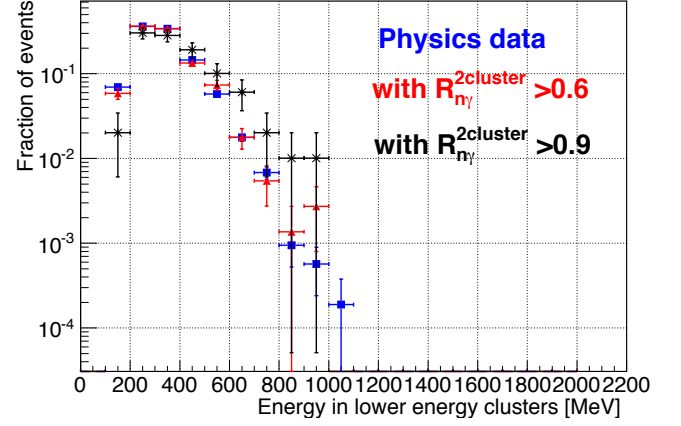
Figure 6.25: Energy distribution of lower energy cluster in the physics data. Blue,red and black histograms represent the physics data without cut on $R_{n\gamma}^{2cluster}$, with $R_{n\gamma}^{2cluster} > 0.6$, and with $R_{n\gamma}^{2cluster} > 0.9$, respectively.

and 6.28 show the distribution of the kinematical Neural-net variable NN_{kine} and cluster shape Neural-net variable NN_{shape} for the events in the physics data with the loose cuts for the case without cut on $R_{n\gamma}^{2cluster}$, with $R_{n\gamma}^{2cluster} > 0.6$, and with $R_{n\gamma}^{2cluster} > 0.9$. No significant difference could be seen in Figs. 6.26, 6.27, and 6.28 between before and after the cut on $R_{n\gamma}^{2cluster}$.
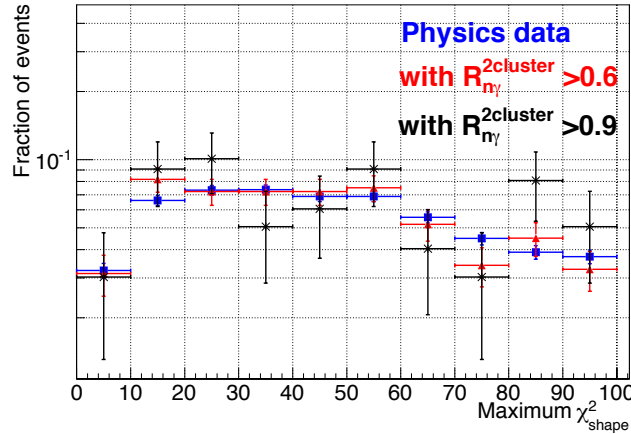
Figure 6.26: Maximum $\chi^2_{pulseshape}$ distribution in the physics data with the loose cuts. Blue,red and black histograms represent the physics data without cut on $R_{n\gamma}^{2cluster}$, with $R_{n\gamma}^{2cluster} > 0.6$, and with $R_{n\gamma}^{2cluster} > 0.9$, respectively.

6.4 Pulse shape likelihood method with normalized PDF

As described in Section 5.5.1, the Gaussian function without normalization was used as the PDF for fit parameters. This can effectively enhance the likelihood of the neutron-induced cluster assumption due to larger standard deviation of fit parameters in the neutron-rich sample compared with the photon-rich sample.
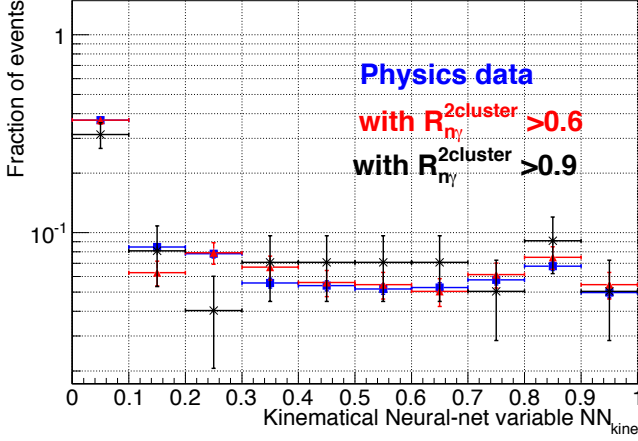
Figure 6.27: Kinematical Neural-net variable NN_{kine} distribution for the events in the physics data with the loose cuts. Blue, red and black histograms represent the physics data without cut on $R_{n\gamma}^{2cluster}$, with $R_{n\gamma}^{2cluster} > 0.6$, and with $R_{n\gamma}^{2cluster} > 0.9$, respectively.
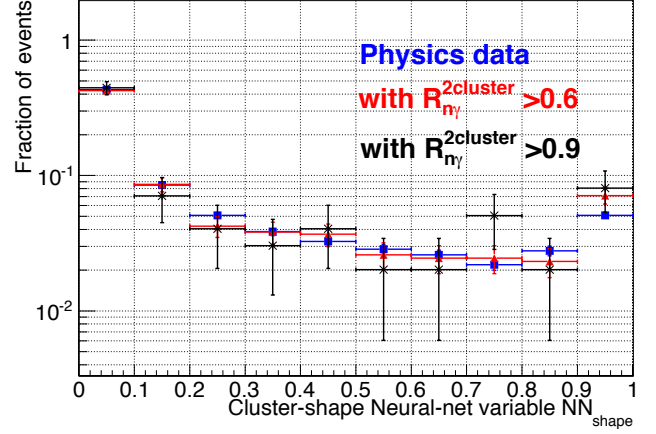
Figure 6.28: Cluster shape Neural-net variable NN_{shape} distribution for the events in the physics data with the loose cuts. Blue, red and black histograms represent the physics data without cut on $R_{n\gamma}^{2cluster}$, with $R_{n\gamma}^{2cluster} > 0.6$, and with $R_{n\gamma}^{2cluster} > 0.9$, respectively.

To evaluate the effect of enhancement due to the use of the Gaussian function without normalization as the PDF, the pulse shape likelihoods which use the Gaussian function with normalization as the PDF were defined:

$$L'^{crystal} = \prod_{p}^{\sigma_0, a} \frac{1}{\sqrt{2\pi} RMS_{p^{exp}}(H)} \exp\left(-\frac{(p^{meas.} - p^{exp}(H))^2}{2 RMS_{p^{exp}}(H)^2}\right), \tag{6.7}$$

$$L'^{1cluster} = \prod_{j} L'^{crystal}_{j}, \tag{6.8}$$

$$L'^{2cluster} = L'^{1cluster}_{1} \times L'^{1cluster}_{2}, \tag{6.9}$$

$$R'^{1cluster}_{\gamma} = \frac{L'^{1cluster}_{\gamma}}{L'^{1cluster}_{\gamma} + L'^{1cluster}_{n}}, \tag{6.10}$$

$$R'^{2cluster}_{\gamma} = \frac{L'^{2cluster}_{\gamma}}{L'^{2cluster}_{\gamma} + L'^{2cluster}_{n}}, \tag{6.11}$$

Figure 6.29 shows the $R'^{1cluster}_{\gamma}$ distributions for the clusters in the photon-rich and neutron-rich samples. Figure 6.30 shows the fraction of clusters with $R'^{1cluster}_{\gamma}$ larger than a given threshold value. By requiring $R'^{1cluster}_{\gamma}$ to be higher than 0.1, 54% of the clusters in the neutron-rich samples were rejected while keeping 98% of the photon-clusters.

Figure 6.31 shows the distribution of $R'^{2cluster}_{\gamma}$ for the photon-rich sample and the neutron-rich sample. Figure 6.32 shows the fraction of two-cluster systems with $R'^{2cluster}_{\gamma}$ larger than a given threshold as a function of the threshold. By requiring the likelihood ratio to be higher than 0.1, 77% of two-cluster systems in the neutron-rich sample were rejected while keeping 98.6% of the two-cluster systems in the photon-rich sample.

The $R'^{2cluster}_{\gamma}$ for two-cluster system in the event remained in the 2013 physics data was 0.99. The $R'^{1cluster}_{\gamma}$(Energy) for each cluster in this event was 0.97 (519 MeV) and 0.86 (357 MeV). The cluster with energy of 357 MeV had $R'^{1cluster}_{\gamma}$ close to 1 even though the fit parameters
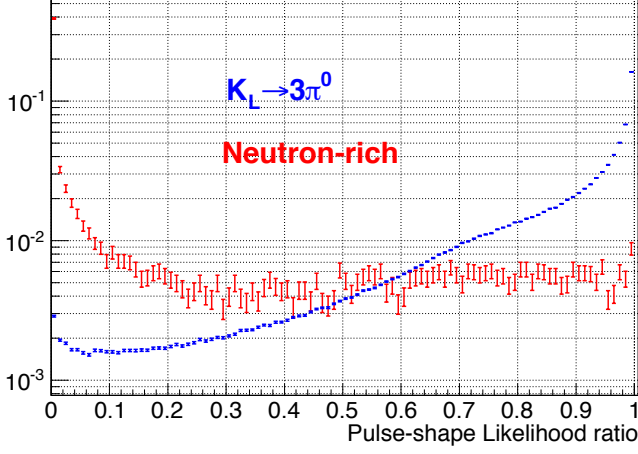
Figure 6.29: $R'^{1cluster}_{\gamma}$ distribution for the photon-rich sample (blue) and the neutron-rich sample (red).
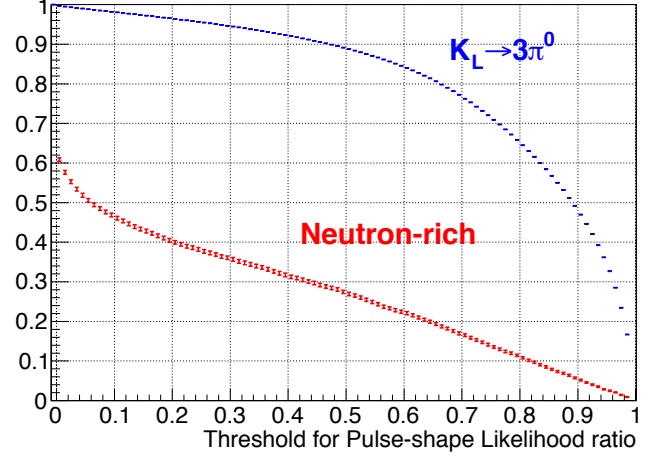
Figure 6.30: Fraction of clusters with $R'^{1cluster}_{\gamma}$ larger than a given threshold shown as a function of threshold value in the photon-rich sample (blue) and the neutron-rich sample (red).
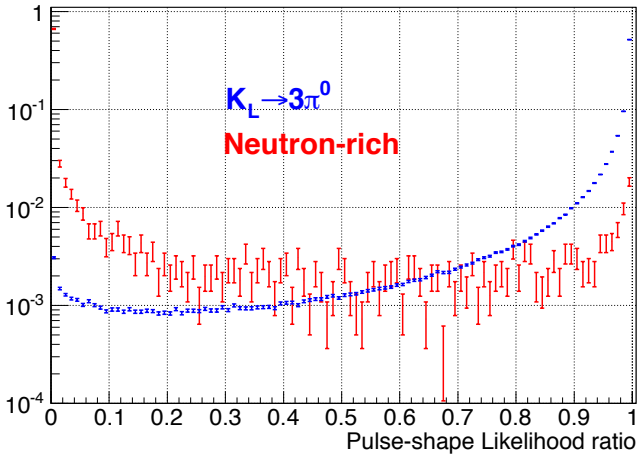
Figure 6.31: $R'^{2cluster}_{\gamma}$ distribution for two-cluster system in the photon-rich sample (blue) and neutron-rich sample (red).
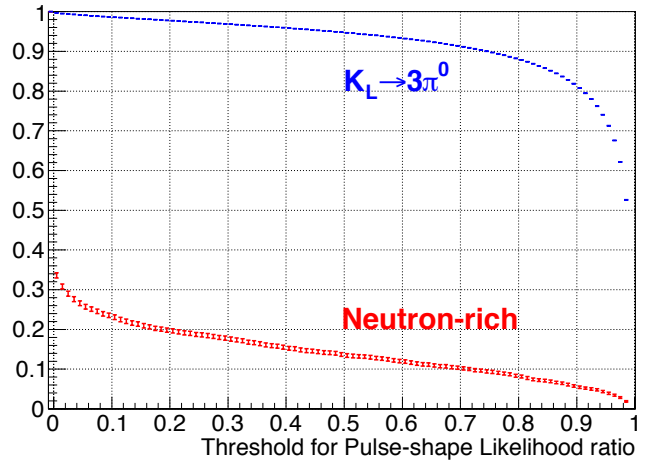
Figure 6.32: Fraction of two-cluster system with the $R'^{2cluster}_{\gamma}$ larger than a given threshold in the photon-rich sample (blue) and neutron-rich sample (red), shown as a function of the threshold value.

of the crystal with CsI ID=695 are closer to the values in the neutron template, as shown in Figs. 6.9 and 6.10. This can be explained by the larger standard deviation of fit parameters for the neutron template than those for the photon template in this crystal.

6.5 Further improvement for the background reduction

As described in Section 4.5, there were two types of background event sources: kaon decay events and hadronic interaction events with neutron-induced clusters. To achieve sensitivity at the level of the branching ratio of $K_L \to \pi^0 \nu \overline{\nu}$ predicted by SM with a better S/N ratio, we need to reduce the number the event from both types of backgrounds, in addition to the developed pulse shape discrimination method and the present event selection cuts.

Several studies were already done for the improvement. The improvements to reject neutron-induced clusters will be described in Section 6.5.1. The improvements to reduce K_L decay background will be described in Section 6.5.2.

6.5.1 Neutron-induced cluster rejection

Two different methods were studied to achieve a better reduction for neutron-induced clusters. Further improvements for the cluster-shape cut were studied by Dr. K.Sato and Dr. E.Iwai. A new method to reject neutron-induced cluster using the shower max position information was also studied. Here I will describe the correlation and expected improvement with these new methods and Pulse shape discrimination method.

6.5.1.1 Improved Cluster-shape cut

In the current event selection, χ^2_{shape} is mainly used to reject clusters with hadronic interactions. χ^2_{shape} was calculated by comparing the fraction of energy deposit in each crystal with the expectation from MC simulation. New method uses the cluster shape projected to the x and y directions instead. The likelihood of the cluster-shape for x and y projections was calculated by assuming photons. This method was originally developed by Dr. E. Iwai to reject the $K_L \to 2\gamma$ from K_L in the beam halo by comparing the likelihood [43, 44], and modified by Dr. K. Sato to discriminate neutron-induced clusters.

Figure 6.33 shows the concept of the cluster-shape likelihood method. Sum of energy deposits in each row and each column of the cluster were calculated for each cluster. Energy distribution for crystal columns and rows were used as the x- and y-projected cluster shape. Projected cluster shapes were compared with the templates of projected cluster shapes of single-photon made by MC simulation in wide range of energy and incident angle.

To reject neutron-induced clusters, we define a normalized sum of logarithms of the likelihood of x-projected and y-projected cluster shapes:

$$\text{ClusterShapeLH} = \frac{\log_{10} LH_x + \log_{10} LH_y}{\text{Number of crystals in the cluster}}, \tag{6.12}$$

where LH_x and LH_y represent the likelihoods of x-projected and y-projected cluster-shape, respectively. Figure 6.34 shows the correlation between ClusterShapeLH and the energy of photon cluster generated in the MC simulation. Because ClusterShapeLH has a dependence on energy and incident angle of photon, the threshold value for ClusterShapeLH was defined separately for each region of the energy and the incident angle. Figure 6.35 shows the threshold
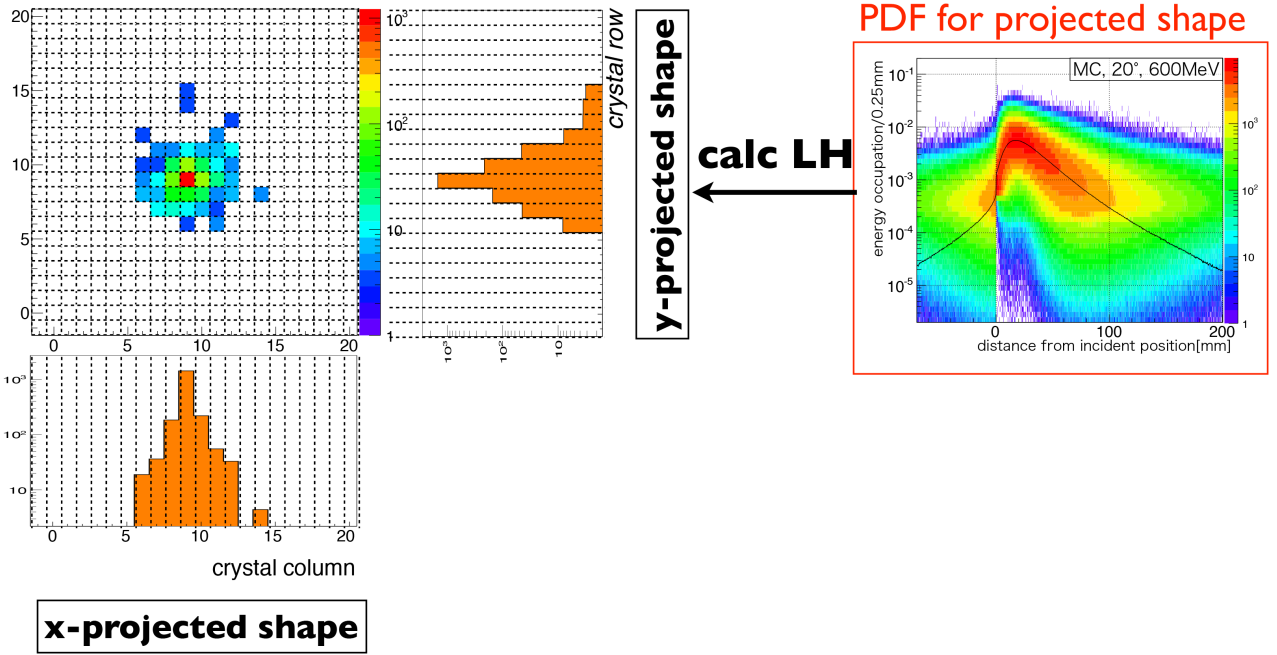
Figure 6.33: The concept of the Cluster-shape Likelihood method. The cluster-shapes projected in x and y directions are compared with the template of the cluster shape. This figure was made by Dr. K. Sato.

for ClusterShapeLH as a function of energy in the case of incident angle $\theta = 0$. The cluster was rejected if its ClusterShapeLH was smaller than the threshold value.

Figure 6.36 shows the correlation between ClusterShapeLH and the energy of photon cluster in $K_L \rightarrow 3\pi^0$ sample taken with beam in Run 49. Most of photons are above the threshold line. The loss of single photons after imposing cut on the ClusterShapeLH was 15.3% without the cut on the χ^2_{shape} and 11.8% with the cut on the χ^2_{shape}. The fraction of $\pi^0 \rightarrow 2\gamma$ remaining after the cut on the ClusterShapeLH was 72% (78%) before (after) the χ^2_{shape} cut .

Figure 6.37 shows the correlation between ClusterShapeLH and the energy of photon cluster in the neutron-rich sample with the loose-cut. Most of clusters are below the threshold line. The cut on the ClusterShapeLH rejects 68% (95%) of clusters in the neutron-rich sample before (after) the cut on the χ^2_{shape}.

With this improved cluster-shape cut, the improvement on the reduction of neutron-induced cluster by a factor of 3 was expected [50], in addition to the present event selection cuts.

The correlation and the expected improvement with the cluster shape likelihood method and the pulse shape discrimination method were studied with the neutron-rich sample and physics data. Table 6.4 shows the number of events in neutron-rich sample with $Z_{vtx} > 2900$ mm and $P_t > 120$ MeV/c for various cut conditions.

Because most of the events in neutron-rich sample were rejected by the cluster shape likelihood method alone, it is hard to estimate the improvement or to check the correlation between the pulse shape likelihood method and cluster shape likelihood method.

After the cluster shape likelihood cut, 5 events in neutron-rich sample remained, and all of them were rejected after applying cut with the pulse-shape likelihood method. The upper limit on the number of remaining events after cuts with the both likelihood method was expected
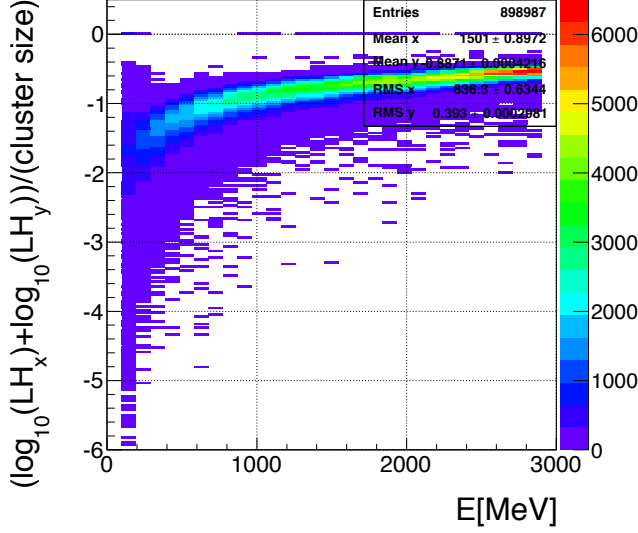
Figure 6.34: The correlation between the ClusterShapeLH and the energy of photon cluster generated in MC simulation. This figure is prepared by Dr. K. Sato.
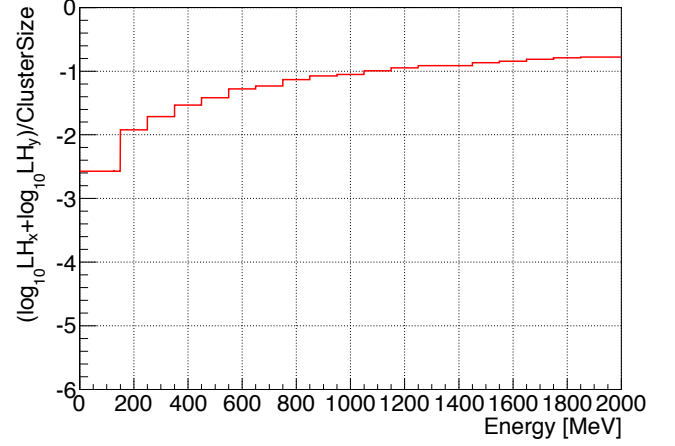
Figure 6.35: The threshold for ClusterShapeLH in the case of incident angle $\theta = 0$.
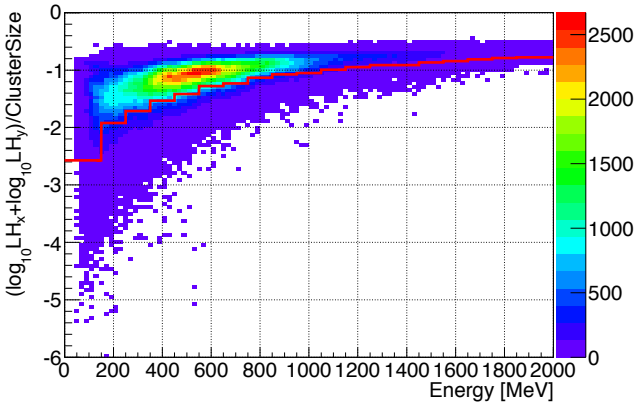
Figure 6.36: The correlation between the ClusterShapeLH and the energy of photon cluster in $K_L \to 3\pi^0$ sample taken with beam in run49. The red line represents the threshold for the case of incident angle $\theta = 0$.
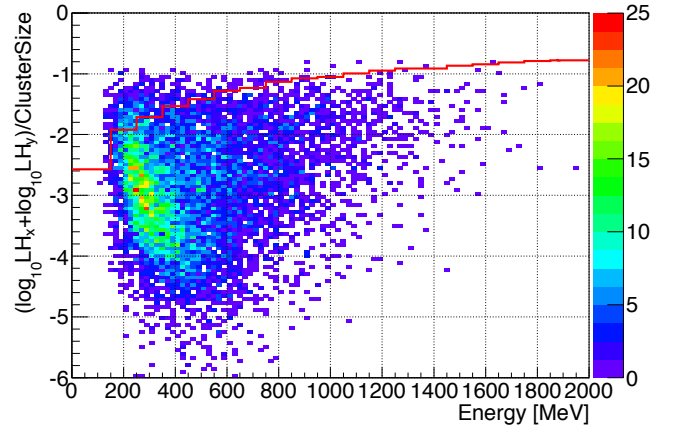
Figure 6.37: The correlation between the ClusterShapeLH and the energy of photon cluster in the neutron-rich samples with loose-cut. The red line represents the threshold for the case of incident angle $\theta = 0$.

Table 6.4: Number of events with Z_{vtx} >2900 mm and P_t >120 MeV/c in the neutron-rich samples for each cut condition

Cut Condition	w/o Cluster-shape Likelihood Cut	w/Cluster-shape Likelihood Cut	reduction(%)
Loosecut	5362	5	0.1±0.04
+ Pulse shape likelihood cut	5	0	0
$+NN_{kine}$ cut	594	0	0
$+NN_{shape}$ cut	778	5	0.6±0.29
$+NN_{kine}$ cut $+NN_{shape}$ cut	62	0	0
$+\chi^2_{shape}$ cut	19	0	0
All cut for $K_L \to \pi^0\nu\overline{\nu}$	2	0	0

to be 2.3 at the 90% confidence level (C.L.), based on Poisson statistics. The improvement by pulse-shape likelihood method after cluster shape likelihood cut was thus expected to be larger than by a factor of 2.1.

The correlation between the two likelihood method was studied for single cluster instead of two-cluster system. Figure 6.38 shows the fraction of clusters which passed the cluster shape likelihood cut as a function of $R_\gamma^{1cluster}$ in the neutron-rich sample. The cluster shape likelihood method could reject the neutron-induced clusters more efficiently for the cluster rejected by the pulse shape likelihood cut than for the cluster which passed the pulse shape likelihood cut.
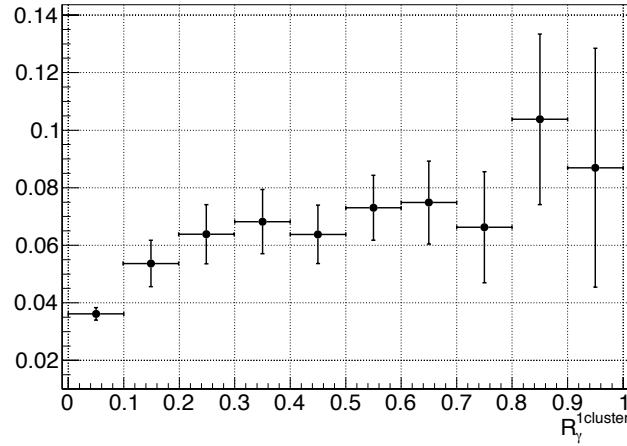
Figure 6.38: Fraction of cluster which passed cluster shape likelihood cut as a function of $R_\gamma^{1cluster}$ for the clusters in the neutron-rich sample.

The cluster-shape likelihood was also applied to physics data in the 2013 $K_L \to \pi^0\nu\overline{\nu}$ analysis.

The event remaining inside the signal region in the $K_L \to \pi^0\nu\overline{\nu}$ analysis could be rejected by the cluster-shape likelihood method. The ClusterShapeLH (threshold for ClusterShapeLH) for each cluster of that event was -1.364 (-1.394) and -1.635 (-1.498) for the cluster with the energy of 519 MeV and 357 MeV, respectively. Because the ClusterShapeLH of the lower energy cluster was smaller than the threshold, the lower energy cluster was regarded as the cluster with a hadronic interaction and thus the event was rejected. The higher energy cluster had the ClusterShapeLH higher than the threshold and regarded as the photon-induced cluster.

This result was consistent with that from the pulse shape likelihood method.

Table 5.6 shows the number of events in the physics data with $Z_{vtx} >$2900 mm and $P_t >$120 MeV/c for various cut condition. After cluster-shape likelihood cut 7 events in physics data

Table 6.5: Number of events in physics data with $Z_{vtx} >$2900 mm and $P_t >$120 MeV/c for each cut condition

Cut Condition	w/o Cluster-shape Likelihood Cut	w/Cluster-shape Likelihood Cut	reduction(%)
Loosecut	5150	7	0.1±0.05
+ Pulse shape likelihood cut	562	3	$(5.34 \pm 3.07) \times 10^{-1}$
$+NN_{kine}$ cut	940	1	0.1±0.11
$+NN_{shape}$ cut	387	6	1.5±0.63
$+NN_{kine}$ cut $+NN_{shape}$ cut	94	1	1.1±1.06
$+\chi^2_{shape}$ cut	7	0	0
All cut for $K_L \to \pi^0 \nu\overline{\nu}$	2	0	0

remained and 3 events out of them remained after applying cut on Pulse-shape likelihood method. The improvement by Pulse-shape likelihood method for physics data after cluster-shape likelihood cut was thus expected to be 2.3.

The improvement by Pulse-shape likelihood method after Cluster-shape likelihood cut was estimated to be about by a factor of 2 from neutron-rich sample and physics data. If we combine these two samples, 3 events remained after pulse shape likelihood method cut out of 12 events after cluster shape likelihood cut. This gives us the improvement by a factor of 4.

6.5.1.2 Shower-depth measurement capability

The shower depth can be a possible tool to discriminate hadron showers from electromagnetic showers.

The shower maximum of hadron showers tends to be located more downstream than that of electromagnetic shower because the interaction length (38.04 cm) is longer than the radiation length (1.86 cm) [14]. This tendency becomes more significant in the background events with single neutrons studied with the MC simulation. Figure 6.39 shows the maximum shower depth for two clusters in the $K_L \to \pi^0 \nu\overline{\nu}$ and 1-GeV neutron events with loose-cuts for $K_L \to \pi^0 \nu\overline{\nu}$ analysis studied with MC simulation. Among the two clusters used for π^0 reconstruction, the cluster with deeper shower depth tends to have the shower maximum in the downstream-half of the crystal for the neutron events. If we select the events with the maximum shower depth shorter than 180 mm, 92% of the neutron-induced background events were rejected while keeping the 95% of signal events.

With the current setup of the KOTO CsI calorimeter, the scintillation light from the CsI crystals are read out only from the downstream side and it is difficult to get the depth information. If we can add a photo sensor at the upstream end of the crystal, we can get the depth information by taking the timing difference between the both ends. Multi Pixel Photon Counter (MPPC) is being considered as the photo sensor for the additional readout because of its low mass thickness, The improvement with additional readout was estimated by Dr. H. Nanjo to be a factor 10 [50].
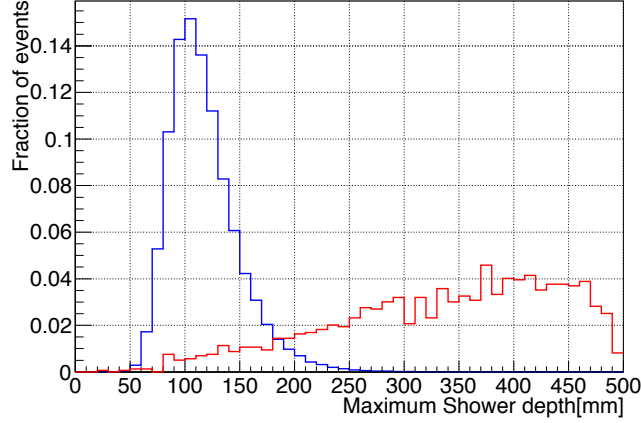
Figure 6.39: The maximum shower depth for two-cluster system in the $K_L \to \pi^0 \nu \overline{\nu}$ (blue line) and 1-GeV neutron events (red line) with the loose-cuts for $K_L \to \pi^0 \nu \overline{\nu}$ analysis studied with MC simulation.

Correlation between pulse shape difference and shower depth

If there is a correlation between pulse shape difference and shower depth, pulse shape discrimination method will have shower depth dependence and the additional improvement by shower depth measurement after pulse shape cut will be smaller than by a factor of 10.

As described in Section 2.3.2, most of CsI crystals were made from two crystals glued together and were covered by an aluminized mylar and a black mylar. These special properties may change the timing structure of scintillating light during the light propagation depending on the emission point and may change the pulse-shape. If the pulse-shape of the CsI crystal vary with the position of interaction, it will be sensitive to the position of shower maximum or shower depth. If the position dependences of fit parameters contributes to pulse-shape difference between photon and neutron samples, the positive correlation between the fit parameters and the position of activities is expected. To check the contribution of position dependence of fit parameters on the pulse-shape difference between photon and neutron samples, the z position dependence of the pulse-shape was studied with the cosmic-ray muons and also with a positron beam.

Test with cosmic ray muons

The z position dependence of the pulse-shape was studied with cosmic ray muons. The data of cosmic ray muons taken after the 2013 physics data taking were used for this study. The cosmic ray muons which penetrated through the MB, BCV, and the CsI calorimeter were used. As described in Section 4.3.2.3, the hit z position at each module of MB and BCV was measured from its timing information. The hit z positions at each CsI crystal were calculated from the track of cosmic ray muons reconstructed from the hit positions on the inner and outer modules of MB. Figure 6.40 shows the reconstructed track of the cosmic muon. The z position resolution with the reconstructed track was measured to be 56 mm [23].

The waveforms of the CsI calorimeter channels were fitted with the same method as described in Section 5.3.2. Figures 6.41 and 6.42 show example of correlations between the fit parameters and the hit z position of the cosmic ray muons.

The correlations between fit parameters and the hit z position were fitted with straight lines and the fit parameter differences between the activities at the upstream end ($z = 0$ mm) and the downstream end ($z = 500$ mm) were obtained from the fit result. Figures 6.43 and 6.44
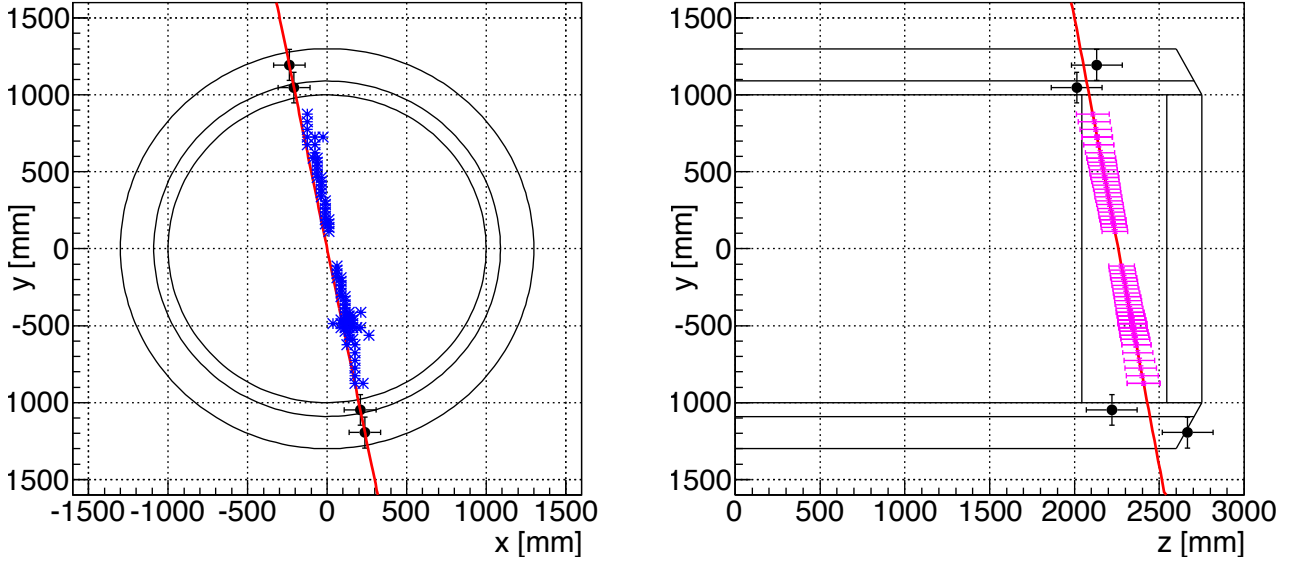
Figure 6.40: Left: The reconstruction of the track of a cosmic-ray muon. The black points represent the hit positions on the inner and outer modules of MB. The blue points represent the hit positions on the CsI calorimeter channels. The red line represents the reconstructed track of a cosmic-ray muon. Right: the estimation of hit z position in each CsI crystal using reconstructed track of a cosmic-ray muon. The red line represents the reconstructed track of a cosmic-ray muon. The magenta point represents the hit z positions on the CsI calorimeter channels expected from the track.
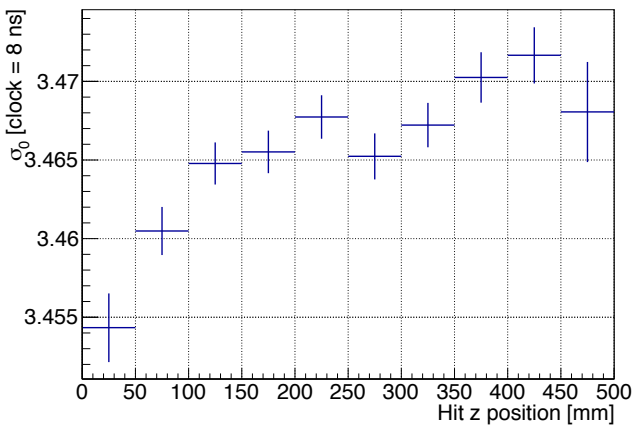
Figure 6.41: The correlation between σ_0 and the hit z position of the cosmic ray muon for the crystal with CsI ID=176.
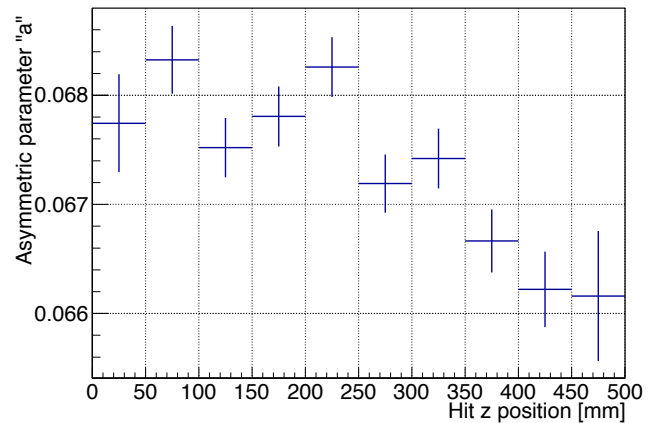
Figure 6.42: The correlation between asymmetric parameter "a" and the hit z position of the cosmic ray muon for the crystal with CsI ID=176.

show the correlation between the fit parameter difference measured with neutron and photon samples and the fit parameter difference expected from the cosmic ray muon measurement for each crystal. As shown in Fig. 6.43, most of crystals had larger σ_0 in the downstream region even though the amount of difference expected from the cosmic ray muon measurement (~ 0.01) were not large enough to explain the difference seen between the neutron and photon samples (~ 0.03). Figure 6.44 shows that most of crystals had smaller "a" in the downstream region while they had larger "a" in the neutron samples compared with the photon samples.

The measurement with cosmic ray muons shows that the position dependence of σ_0 can be one of the sources for the difference in pulse shapes, but the position dependence of "a" cannot explain the difference in "a" in the neutron sample.
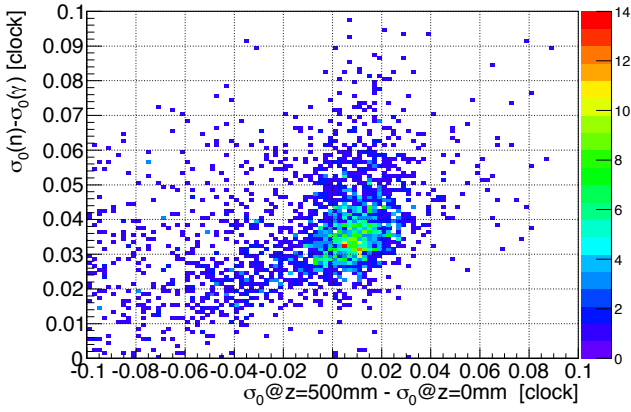
Figure 6.43: The correlation between the difference of σ_0 measured with neutron and photon samples and the difference between upstream and downstream ends measured with cosmic ray muons for each crystal.
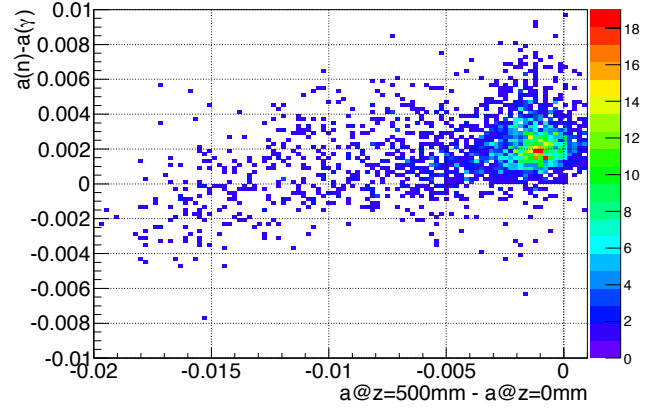
Figure 6.44: The correlation between the difference of "a" measured with neutron and photon samples and the difference between upstream and downstream ends measured with cosmic ray muons for each crystal.

Test with positron beam The position dependences of the fit parameters were studied also with the positron beam at the beam test. The beam test was held at the Research Center for Electron Photon Science (ELPH) in the Tohoku University on February 23rd and 24th, 2016. Figures 6.45 and 6.46 show the setup of the apparatus for the beam test. A small CsI calorimeter made of 8 large crystals and 4 small crystals was used to test the response of the CsI crystals against the hit z position. The small CsI calorimeter was placed on a movable stage. The z axis was defined to be parallel with the longitudinal direction of the crystals and the origin of z axis was defined to be the center of the crystal.

The 500-MeV positron beam was used to test the position dependence of the fit parameters. Positrons that penetrated through two 1 cm×1 cm trigger counters were used. The z position dependence was studied by changing the hit position of the beam by moving the calorimeter along the z direction.

The output from the PMTs connected to the CsI crystal was read out with the same type of 125-MHz ADC modules used in the KOTO experiment. The recorded waveforms of events were fitted with the same method as described in Section 5.3.2.

The correlation between the fit parameters and the hit z position was studied for four small CsI crystals. Figures 6.47 and 6.48 show the correlation with the hit z position for σ_0 and "a", respectively. Positive correlation can be seen between σ_0 and the hit z position for all four

Figure 6.45: A photograph of the beam test apparatus. A small CsI calorimeter was installed inside the box covered by black sheets. Two plastic scintillator tigger counter were placed in front of the CsI calorimeter.
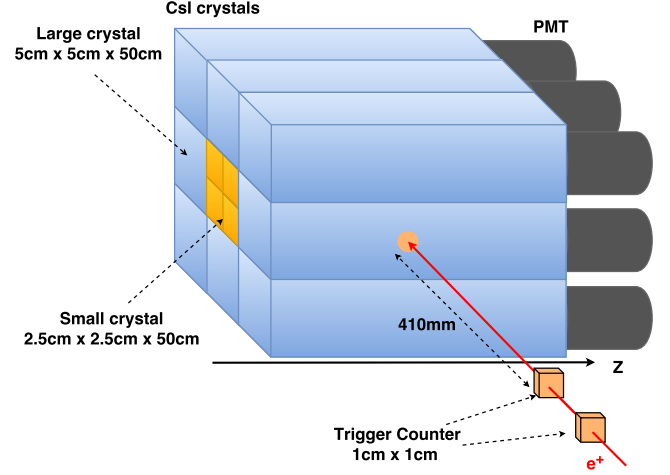
Figure 6.46: The CsI calorimeter used for the beam test. It consisted of 8 large crystals and 4 small crystals.
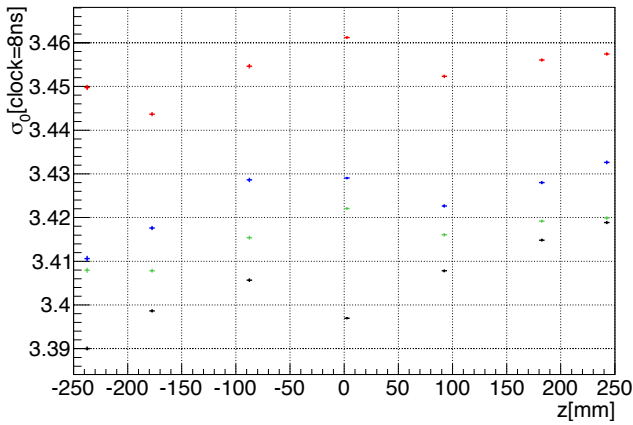
Figure 6.47: The correlation between fit parameter σ_0 and the hit z position of the positron beam. Points with different colors represent different crystals.
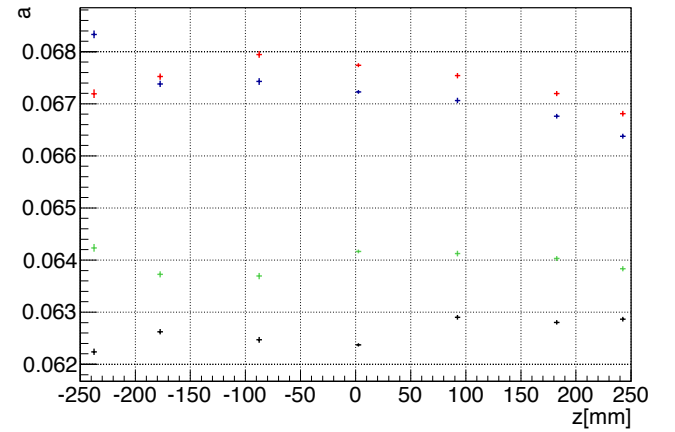
Figure 6.48: The correlation between fit parameter "a" and the hit z position of the positron beam. Points with different colors represent different crystals.

small crystals, while three crystals had negative correlation between "a" and the hit z position. These results from the beam test are consistent with the result with the cosmic ray muons.

Conclusion for study of interaction position dependence

The difference in σ_0 due to interaction position difference is smaller than that seen in photon and neutron samples. The interaction position dependences of fit parameters were inconsistent with the pulse shape difference seen in photon and neutron samples. The correlation between the pulse shape likelihood method and the shower depth is thus expected to be small.

6.5.2 K_L decay background rejection

The background events from K_L decay are caused by the intrinsic detection inefficiency of detector system and the inefficiency due to accidental hit.

6.5.2.1 Inefficiency due to accidental hit

The contribution of K_L background due to the inefficiency with accidental hits was estimated to be 0.014 events with the single event sensitivity of 1.29×10^{-8}. This means that signal to background ratio, S/N, with the background only from this decay is 1/7.

This inefficiency was caused by misidentification of pulses overlapping together. As shown in Fig. 4.15, the parabola fitting method cannot separate the two pulses if one comes after another one within 100 ns because it finds pulses by searching for local maxima in the smoothed waveform.

To improve pulse identification efficiency, I have developed a pulse identification method utilizing pulse shape template [61]. This method is called "Template fitting method". In the developed pulse identification method, waveform was fitted with pulse-shape template. After fitting waveform with pulse-shape template, the remaining pulse was searched for in the difference between waveform and pulse shape template. This procedure was iterated by increasing the number of pulses expected in the waveform until no significant difference was found between waveform and pulse shape template.

Figure 6.49 shows an example of the result of pulse identification with the template fitting method. The waveform shown in this figure is the same waveform used in Fig. 4.16 which parabola fitting could not identify correctly. With the template fitting method, the overlapping pulses in this waveform were correctly identified.

I studied the pulse identification efficiency of template fitting method for the two pulses, which were made from overlaying two waveform recorded in 2013.

The pulse identification efficiency for the waveform collected with 125-MHz ADC module was studied with the waveform of MB. Figure 6.50 shows the two-pulse separation efficiency for the pulses of MB against the distance of two pulses and the log of the ratio of the pulse heights between the later pulse and the earlier pulse. Pulse heights of both pulses were required to be larger than 100 ADC counts, which is equivalent to 2 MeV per channel. Two pulses could be separated if a latter pulse comes at least 30 ns after the earlier pulse and the height of the later pulse is larger than 5 % of the height of the earlier pulse.

The pulse identification efficiency for the waveform collected with 500-MHz ADC module was studied with the waveform of BHPV. Figure 6.51 shows the two-pulse separation efficiency for the pulses of BHPV against the distance of two pulses and the log of the ratio of the pulse heights between the later pulse and the earlier pulse. Pulse heights of both pulses were required
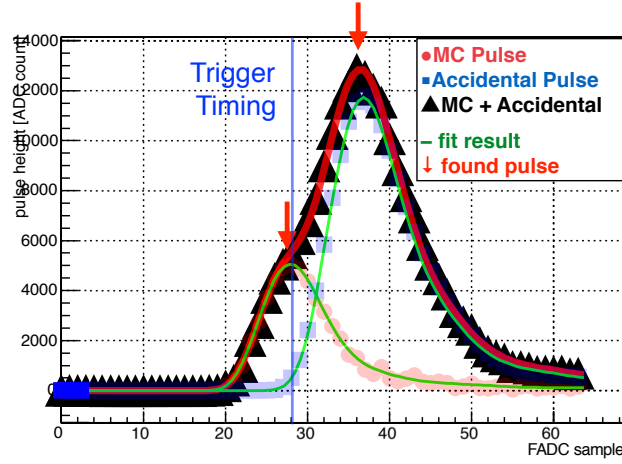
Figure 6.49: An example of identification of pulses from the waveform with overlapped pulses with template fitting method. The red and blue points represent the pulses of hit from Kaon decay and that of the accidental hit, respectively. The black points are the waveform with two pulses summed together. The green lines are the pulse shape of identified pulses

to be larger than 100 ADC counts. Two pulses could be separated if a later pulse comes at least 6 ns after the earlier pulse and the height of the later pulse is larger than 10 % of the height of the earlier pulse.

Figure 6.52 shows the two-pulse identification efficiency of template fitting method against the waveform of 125-MHz ADC modules and 500-MHz ADC modules. With the template fitting method, the pulse identification efficiency for overlapped pulses could be improved from parabola fitting method. The minimum distance for the separation of two pulses could be shortened from 100 ns with parabola fitting method to 30 ns with the template fitting method. If we use 500-MHz ADC modules for digitization, the minimum distance can be shortened down to 5 ns.

I estimated the number of background events due to the accidental hits in the case with template fitting method. The estimation was done in the same way as with parabola fitting method [39]. The same value as the current event selection cuts were used for size of veto window and the energy threshold for detectors. The effect of accidental hits was simulated by overlaying the waveform of accidental events on the simulated pulse. Table 6.6 shows the result of the estimation. No background event due to accidental hit was found in the signal region with the statistics $300 \sim 800$ times larger than the number of K_Ls recorded in the 2013 physics run.

In the case with current veto window size, we can reduce the background due to the accidental hits low enough with template fitting method. In the case with narrower veto window to reduce acceptance loss due to accidental hit, we can improve pulse identification efficiency and remove more background events with the template fitting method by replacing the current 125-MHz ADC modules equipped with Bessel filter with the 500-MHz ADC modules without the filter.

6.5.2.2 $K_L \to 2\pi^0, 3\pi^0$ background

The contribution of $K_L \to 2\pi^0, 3\pi^0$ background was estimated to be 0.069 events with the single event sensitivity of 1.29×10^{-8}. This means that signal to background ratio, S/N, with
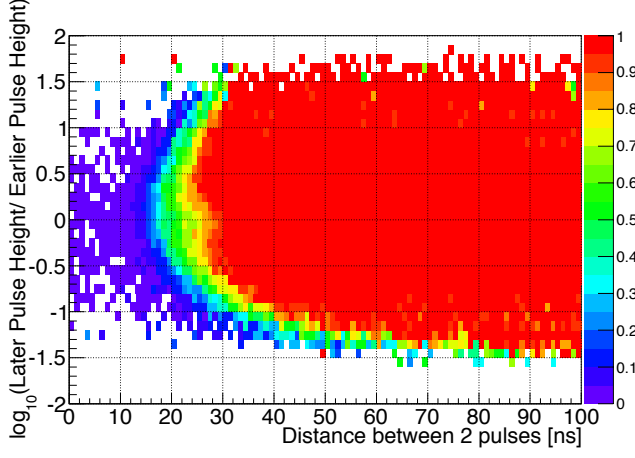
Figure 6.50: Two-pulse separation efficiency for the pulses of MB (z) against the distance of two pulses (x) and the log of the ratio of the pulse heights between the latter pulse and the earlier pulse (y). Pulse heights of both pulses were required to be larger than 100 ADC counts, which is equivalent to 2 MeV per channel.
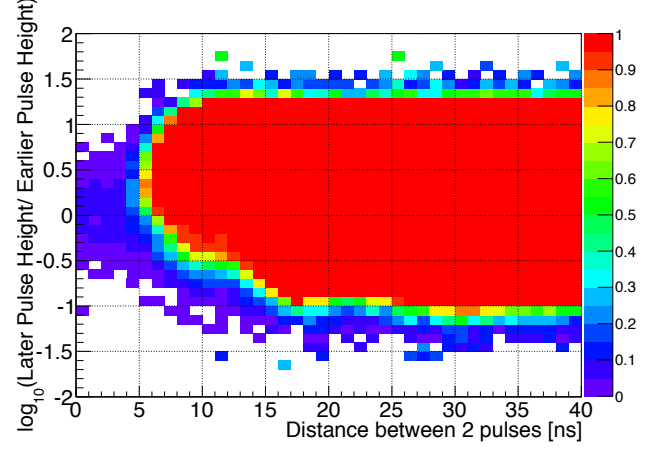
Figure 6.51: Two-pulse separation efficiency for the pulses of BHPV (z) against the distance of two pulses (x) and the log of the ratio of the pulse heights between the latter pulse and the earlier pulse (y). Pulse heights of both pulses were required to be larger than 100 ADC counts.
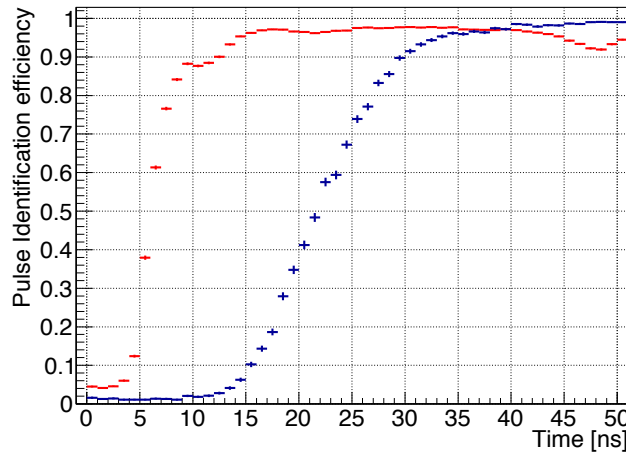
Figure 6.52: The two-pulse identification efficiency for the two pulses as a function of the distance between two pulses. Blue points represent the result of pulse identification for the waveform of 125-MHz ADC module. Red points represent the result of pulse identification for the waveform of 500-MHz ADC module.

Table 6.6: The summary of estimated number of background events. Statistics was defined as the number of K_Ls at the exit of beam line.

Decay Mode	Initial statistics	number of accidental events	Total statistics	Scale to #K_L in 2013 data	Estimated number of background events
$K_L \to 2\pi^0$	6.94×10^{11}	100	6.94×10^{13}	291	<0.008(90%C.L)
$K_L \to 3\pi^0$	7.68×10^{8}	100000	7.68×10^{13}	323	<0.0071(90%C.L)
$K_L \to \pi^+\pi^-\pi^0$	3.98×10^{8}	52000	2.07×10^{14}	868	<0.0025(90%C.L)
$K_L \to \pi^\pm e^\mp \nu$	3.94×10^{8}	52000	2.05×10^{14}	862	<0.0026(90%C.L)
$K_L \to \pi^\pm \mu^\mp \nu$	1.85×10^{8}	52000	9.61×10^{13}	403	<0.0057(90%C.L)

the background only from these decay is 1/34.5. The background events from $K_L \to 2\pi^0, 3\pi^0$ decays can be reduced by additional detector modules installed after 2013 physics run including four more BHPV module, BHGC modules, and additional Barrel-shaped photon detector called "Inner Barrel (IB)" with $5X_0$. With additional detector modules and tighten threshold for MB and BCV, S/N only with $K_L \to 2\pi^0, 3\pi^0$ background can be improved to 0.9 [39].

6.5.2.3 $K_L \to 2\gamma$ background

The contribution of $K_L \to 2\gamma$ background was estimated to be 0.069 events with the single event sensitivity of 1.29×10^{-8}. This means that signal to background ratio, S/N, with the background only from this decay is 1/15. This background can be rejected by discriminating the incident angle of photon. The method to the discriminate incident angle of photon based on the cluster was studied and an improvement by a factor of 53 was expected [43].

6.5.2.4 $K_L \to \pi^+\pi^-\pi^0$ background

The background events found in the low-$P_T^{\pi^0}$ region are regarded as the events from $K_L \to \pi^+\pi^-\pi^0$ decays with missing π^+ and π^- hitting the beam pipe. With the new beam pipe made of aluminum and BPCV modules, a reduction of $K_L \to \pi^+\pi^-\pi^0$ by a factor of 30 was expected [36].

6.5.3   Summary for further improvement

The background events from K_L decays can be reduced by the detectors added after 2013 physics data taking and by the pulse identification with template fitting method. The combination of the Pulse-shape and the Cluster-shape likelihood methods and the shower depth measurement will give us the improvement of the reduction of neutron-induced cluster by more than a factor of 100. These improvements will enable us to discover $K_L \to \pi^0\nu\bar{\nu}$ at the level of the branching ratio of SM prediction.

Chapter 7

Conclusion

I have developed the data acquisition system for the KOTO experiment. In particular, I have integrated veto detectors into the data acquisition system to reject events which have any activities on the veto detector subsystems. The system worked stably and achieved the required performance during the physics data taking in 2013 and 2015.

To suppress the background caused by neutrons, which was found in the $K_L \to \pi^0 \nu \bar{\nu}$ data taken in 2013, I studied the pulse shape of CsI calorimeter for photon-induced clusters. I found a difference in the pulse shapes for neutrons and photons in the CsI crystals. I have developed a new method to reject neutron-induced clusters by using the pulse shapes of the CsI calorimeter. The method can reject 67% of neutron-induced single clusters and 92% of neutron-induced two-cluster systems while keeping more than 90% of photon clusters. The developed method has no clear correlation with existing cut based on the cluster-shape.

Combined with an improved cluster-shape discrimination method and a proposed shower depth discrimination method, the background caused by neutrons will be supressed by more than a factor of 100. This will allow us to discover $K_L \to \pi^0 \nu \bar{\nu}$ at the level of the branching ratio predicted by SM.

Appendix A

Appendix

A.1 Detailed study about the correlation between the number of CsI crystal used in the calculation and $R_\gamma^{1cluster}$

The number of crystals used in the calculation should increase along with the energy deposit of incident particle. Figures A.1 and A.2 show the correlation between energy deposit and the number of crystals used in the calculation in the photon-rich sample and the neutron-rich sample, respectively. The number of crystals used in the calculation was less than 3 for energy deposit less than 400 MeV in the photon-rich sample and the neutron-rich sample.
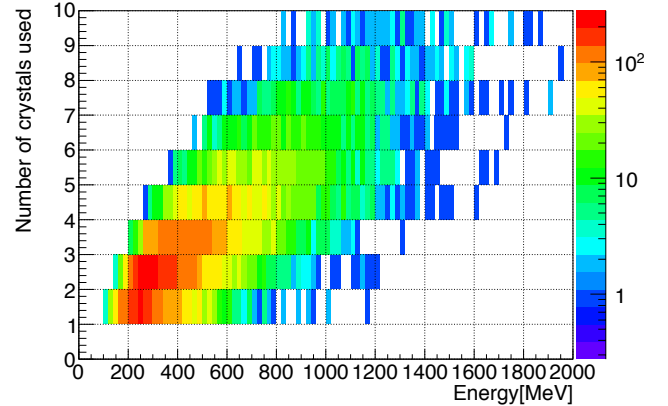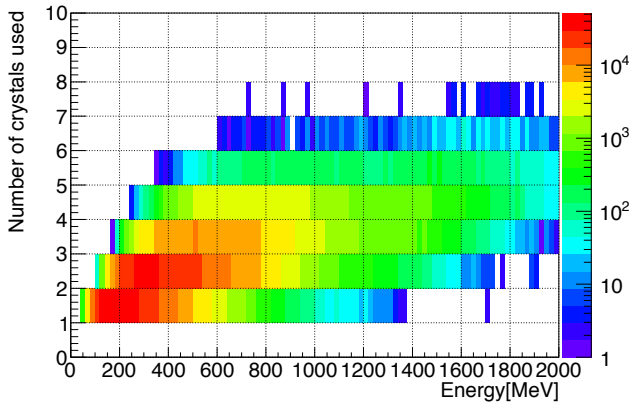
Figure A.1: Correlation between energy deposit in the cluster and the number of crystals used for its calculation in the photon-rich sample.

Figure A.2: Correlation between energy deposit in the cluster and the number of crystals used for its calculation in the neutron-rich sample.

In the calculation of the $R_\gamma^{1cluster}$, the crystals with energy deposit larger than the threshold were used. If we lower the energy threshold, more crystals are expected to be used. If the energy dependence of $R_\gamma^{1cluster}$ is caused by the number of crystal used in the calculation, the likelihood ratio with smaller energy threshold should have a different energy dependence. Figure A.3 shows the correlation between cluster energy and the number of crystals used for the calculation in photon-rich sample with energy threshold on crystal set at 10 MeV. By lowering the threshold, most of clusters have three or more crystals used in the calculation even in the low energy region. Figure A.4 shows the correlation between $R_\gamma^{1cluster}$ and the cluster

151

energy in photon-rich sample with a 10 MeV energy threshold on each crystal. There is no significant difference between Fig. 5.22 and Fig. A.4 even though the number of crystals used in the calculation increased.

The energy dependence of $R_\gamma^{1cluster}$ is thus determined not by the total number of crystals used in the crystals but by the total number of crystals with energy deposit larger than 50 MeV.
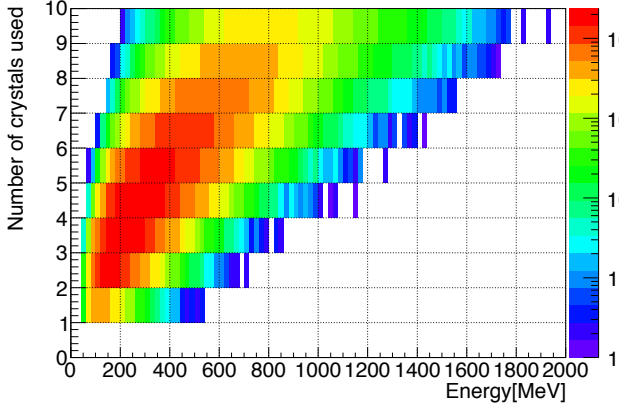
Figure A.3: Correlation between the number of crystals used in the calculation and the cluster energy in the photon-rich sample with energy threshold on crystal set at 10-MeV.
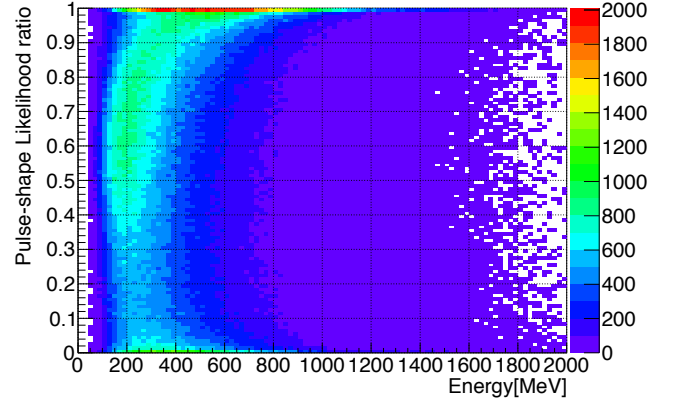
Figure A.4: Correlation between $R_\gamma^{1cluster}$ and the cluster energy in the photon-rich sample with energy threshold on crystal set at 10-MeV.

A.2   Energy threshold dependence

The effect of the energy threshold on the crystals on the performance of discrimination was studied.

Energy threshold dependence of $R_\gamma^{1cluster}$

Figures A.5 and A.6 show $R_\gamma^{1cluster}$ distribution for the photon-rich sample and the neutron-rich sample, respectively, with the energy threshold on crystal set to 10 MeV and 50 MeV. More clusters tend to have smaller likelihood ratio with 10-MeV than with 50-MeV threshold in both samples. As shown in Figs. 5.5 and 5.6, in the low energy region, the RMS values of fit parameter's template for the neutron-rich samples were larger than those for photon-rich samples. The larger RMS value can make the likelihood of neutron-assumption larger than that of photon-assumption in low energy region, and make the $R_\gamma^{1cluster}$ smaller. This is why we have smaller $R_\gamma^{1cluster}$ with smaller energy threshold on crystal. Figure A.7 shows the fraction of clusters with $R_\gamma^{1cluster}$ larger than 0.1 for the photon-rich sample and neutron-rich sample as a function of the energy threshold on crystal. By lowering the energy threshold on the crystals, neutrons are rejected more efficiently while keeping most of the photons.

Energy threshold dependence of $R_\gamma^{2cluster}$

The performance of discrimination depends the energy threshold on crystal. Figure A.8 shows the fraction of two-cluster system whose $R_\gamma^{2cluster}$ is larger than 0.1 for the photon-rich sample and the neutron-rich sample, as a function of the energy threshold on crystal. By
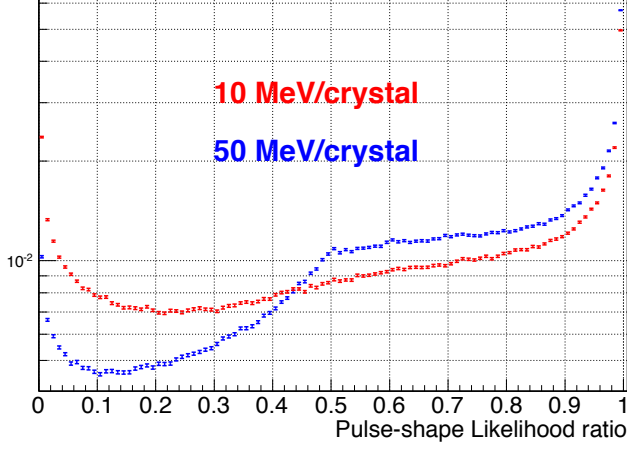
Figure A.5: $R_\gamma^{1cluster}$ distribution for clusters in the photon-rich sample with energy threshold on crystal set to 10 MeV (red) and 50 MeV (blue).
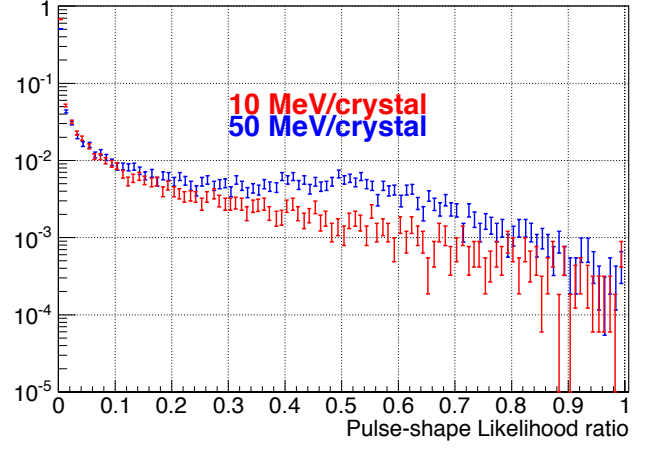
Figure A.6: $R_\gamma^{1cluster}$ distribution for the clusters in the neutron-rich sample with energy threshold on crystal set to 10-MeV (red) and 50-MeV (blue) .
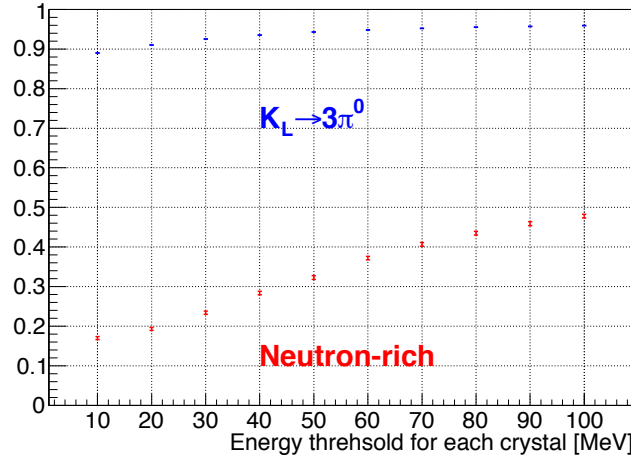
Figure A.7: Fraction of clusters with the single-cluster pulse-shape likelihood ratio larger than 0.1 in the photon-rich sample (blue) and the neutron-rich sample (red) as a function of the energy threshold on crystal.

lowering energy threshold on the crystals, two-cluster system induced by neutrons are rejected more efficiently while keeping most of two-cluster system with two real photons.
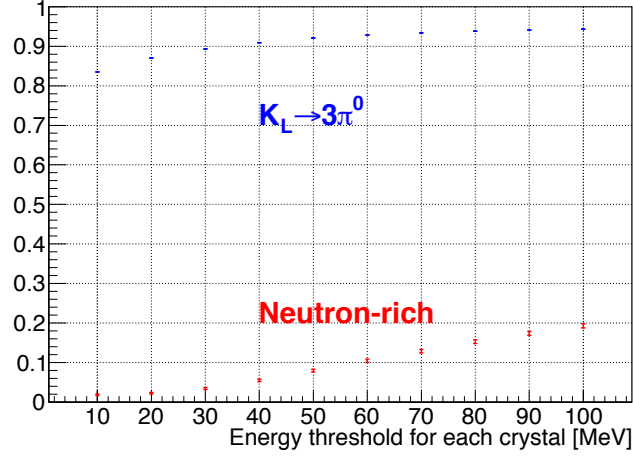
Figure A.8: Fraction of two-cluster system with the $R_\gamma^{2cluster}$ larger than 0.1 in the photon-rich sample (blue) and the neutron-rich sample (red) as a function of the energy threshold on crystal.

List of Tables

List of Figures

158

164

Bibliography

[1] N. Cabibbo, Unitary Symmetry and Leptonic Decays, Phys. Rev. Lett. **10**, 531 (1963).

[2] M. Kobayashi and T. Maskawa, C P -Violation in the Renormalizable Theory of Weak Interaction, Prog. Theor. Phys. **49**, 652 (1973).

[3] J. Comfort et al., Proposal for $K_L \rightarrow \pi^0\nu\overline{\nu}$ Experiment at J-Parc., http://koto.kek.jp/pub/p14.pdf.

[4] J-PARC, http://j-parc.jp/index-e.html.

[5] S. Nagamiya, Introduction to J-PARC, Prog. Theor. Exp. Phys. **2012**, 2B001 (2012).

[6] L. Wolfenstein, Parametrization of the Kobayashi-Maskawa Matrix, Phys. Rev. Lett. **51**, 1945 (1983).

[7] K. Shiomi, *Measurement ofK_L^0 flux at the J-PARC neutral-kaon beam line for the $K_L^0 \rightarrow \pi^0\nu\overline{\nu}$ experiment*, Ph.D. thesis, Kyoto University, 2012.

[8] J. Brod et al., Two-loop electroweak corrections for the $K \rightarrow \pi\nu\overline{\nu}$ decays, Phys. Rev. D **83**, 034030 (2011).

[9] Y. Grossman and Y. Nir, $K_L \rightarrow \pi^0\nu\overline{\nu}$ beyond the standard model, Phys. Lett. B **398**, 163 (1997).

[10] A. V. Artamonov et al., New Measurement of the $K^+ \rightarrow \pi^+\nu\overline{\nu}$ Branching Ratio, Phys. Rev. Lett. **101**, 191802 (2008).

[11] A. V. Artamonov et al., Study of the decay $K^+ \rightarrow \pi^+\nu\overline{\nu}$ in the momentum region $140 < P_\pi < 199$ MeV/c, Phys. Rev. D **79**, 092004 (2009).

[12] F. Mescia and C. Smith, $K \rightarrow \pi\nu\overline{\nu}$ decay in the Standard Model, http://www.lnf.infn.it/wg/vus/content/Krare.html.

[13] J. K. Ahn et al., Experimental study of the decay $K_L^0 \rightarrow \pi^0\nu\overline{\nu}$, Phys. Rev. D **81**, 072004 (2010).

[14] K. Olive, Review of Particle Physics, Chinese Phys. C **38**, 090001 (2014).

[15] M. Ikegami, Beam commissioning and operation of the J-PARC linac, Prog. Theor. Exp. Phys. **2012**, 2B002 (2012).

BIBLIOGRAPHY

[16] H. Hotchi *et al.*, Beam commissioning and operation of the Japan Proton Accelerator Research Complex 3-GeV rapid cycling synchrotron, Prog. Theor. Exp. Phys. **2012**, 2B003 (2012).

[17] T. Koseki *et al.*, Beam commissioning and operation of the J-PARC main ring synchrotron, Prog. Theor. Exp. Phys. **2012**, 2B004 (2012).

[18] T. Sekiguchi, Neutrino facility and neutrino physics in J-PARC, Prog. Theor. Exp. Phys. **2012**, 2B005 (2012).

[19] H. Takahashi *et al.*, Construction and beam commissioning of Hadron Experimental Hall at J-PARC, J. Phys. Conf. Ser. **312**, 052027 (2011).

[20] K. Agari *et al.*, Primary proton beam line at the J-PARC hadron experimental facility, Prog. Theor. Exp. Phys. **2012**, 2B008 (2012).

[21] H. Hotchi, Commissioning the 400 MeV Linac at J-PARC and High Intensity Operation of the J-PARC RCS, in *Proceedings, 5th Int. Part. Accel. Conf. (IPAC 2014)*, p. TUXA01, 2014.

[22] H. Takahashi *et al.*, Indirectly water-cooled production target at J-PARC hadron facility, J. Radioanal. Nucl. Chem. **305**, 803 (2015).

[23] T. Masuda, *Development and Experimental Study of the KOTO Detector System using Three K_L Neutral Decay Modes*, Ph.D. thesis, Kyoto University, 2014.

[24] T. Shimogawa, Design of the neutral K_L^0 beamline for the KOTO experiment, Nucl. Instrum. Meth. A **623**, 585 (2010).

[25] K. Shiomi *et al.*, Measurement of K_L^0 flux at the J-PARC neutral-kaon beam line, Nucl. Instrum. Meth. A **664**, 264 (2012).

[26] T. Matsumura *et al.*, Photon-veto counters at the outer edge of the endcap calorimeter for the KOTO experiment, Nucl. Instrum. Meth. A **795**, 19 (2015).

[27] A. Alavi-Harati *et al.*, Measurements of direct CP violation, CPT symmetry, and other parameters in the neutral kaon system, Phys. Rev. D **67**, 012005 (2003).

[28] R. E. Ray, The KTeV pure CsI calorimeter, Calorim. high-energy physics. Proceedings, 5th Int. Conf. Brookhaven, Upton, USA, Sept. 25 - Oct. 1, 1994 **C940925**, 110 (1994).

[29] M. B. Crisler, Review of calorimetry in Fermilab fixed target experiments, in *17th Int. Symp. Lepton-phot. Interact. Beijing, China, 10 - 15 Aug 1995*, 1995.

[30] A. Roodman, The KTeV CsI calorimeter, 28th Int. Conf. High-energy Physics, Warsaw, Poland, 25 - 31 Jul 1996 , 1684 (1996).

[31] L. Jong-won, *Energy Calibration Method for the KOTO CsI Calorimeter*, Ph.D. thesis, Osaka University, 2014.

[32] T. Masuda *et al.*, A vacuum tolerant high voltage system with a low noise and low power CockcroftWalton photomultiplier base, Nucl. Instrum. Meth. A **746**, 11 (2014).

[33] D. Naito *et al.*, Development of a low-mass and high-efficiency charged-particle detector, Prog. Theor. Exp. Phys. **2016**, 023C01 (2016).

[34] Y. Tajima *et al.*, Barrel photon detector of the KEK $K_L^0 \to \pi^0 \nu \bar{\nu}$ experiment, Nucl. Instrum. Meth. A **592**, 261 (2008).

[35] N.Kawasaki, Development of Undoped Cesium Iodide Counter with Wavelength- Shifting-Fiber Readout, to be Publ. in Prog. Theor. Exp. Phys. .

[36] K. Miyazaki, *J-PARC KOTO* $K_L^0 \to \pi^+ \pi^- \pi^0$, Master thesis, Osaka University, 2016.

[37] I. Kamiji, *KOTO* , Master thesis, Kyoto University, 2015.

[38] Y. Maeda *et al.*, An aerogel Cherenkov detector for multi-GeV photon detection with low sensitivity to neutrons, Prog. Theor. Exp. Phys. **2015**, 63H01 (2015).

[39] Y. Maeda, *Search for the Decay $K_L^0 \to \pi^0 \nu \bar{\nu}$ with a Neutron-Insensitive GeV-Energy Photon Detector*, Ph.d. thesis, Kyoto University, 2016.

[40] Y. Sugiyama *et al.*, The Data Acquisition System for the KOTO Experiment, IEEE Trans. Nucl. Sci. **62**, 1115 (2015).

[41] M. Bogdan *et al.*, Custom 14-Bit, 125MHz ADC/Data Processing Module for the KL Experiment at J-Parc, in *2007 IEEE Nucl. Sci. Symp. Conf. Rec.* Vol. 1, pp. 133–134, IEEE, 2007.

[42] M. Bogdan *et al.*, Custom 12-Bit, 500MHZ ADC/Data Processing Module for the KOTO Experiment at J-Parc, in *2010 17th IEEE-NPSS Real Time Conf.*, pp. 1–2, IEEE, 2010.

[43] E. Iwai, *CsI calorimeter for the J-PARC KOTO experiment*, Ph.D. thesis, Osaka University, 2012.

[44] E. Iwai *et al.*, Performance study of a prototype pure CsI calorimeter for the KOTO experiment, Nucl. Instrum. Meth. A **786**, 135 (2015).

[45] D. A. McFarland, *Measurement of the Branching Ratio of Klong to pi0 nu nubar*, Ph.D. thesis, Arizona State University, 2015.

[46] T. Koseki and K. Hasegawa, Present Status of J-PARC - after the Shutdown due to the Radioactive Material Leak Accident-, in *Proceedings, 5th Int. Part. Accel. Conf. (IPAC 2014)*, p. THPME061, 2014.

[47] M. Tomizawa *et al.*, Malfunction, Cause and Recurrence Prevention Measures of J-PARC Slow Extraction, in *Proceedings, 5th Int. Part. Accel. Conf. (IPAC 2014)*, p. THPME060, 2014.

[48] K. Shiomi, $K_L^0 \to \pi^0 \nu \bar{\nu}$ at KOTO, in *Proc. 8th Int. Work. CKM Unitarity Triangle (CKM 2014), Vienna, Austria, Sept. 8-12, 2014*, 2014, arXiv:1411.4250.

[49] K. Sato, *Measurement of the CsI calorimeter performance and K_L momentum spectrum for the J-PARC KOTO experiment*, Ph.D. thesis, Osaka Univeristy, 2015.

BIBLIOGRAPHY

[50] H. Nanjo, J-PARC K , in *JPS 2015 Autumn Meet.*, 2015.

[51] H. Klein and F. D. Brooks, Scintillation detectors for fast neutrons, in *Proc. Int. Work. Fast Neutron Detect. Appl. 2006*, p. 97, PoS, 2006.

[52] R. Novotny, Inorganic scintillators a basic material for instrumentation in physics, Nucl. Instrum. Meth. A **537**, 1 (2005).

[53] C. Bartle and R. Haight, Small inorganic scintillators as neutron detectors, Nucl. Instrum. Meth. A **422**, 54 (1999).

[54] T. Matulewicz *et al.*, Response of BaF2, CsI(Tl) and Pb-glass detectors to neutrons below 22 MeV, Nucl. Instrum. Meth. A **274**, 501 (1989).

[55] T. Yorita *et al.*, Response of CsI(pure) to electron and hadrons., in *Proc. Work. Scintill. Crystals, KEK, Tsukuba, Apr 24 - 25, 1997*, pp. 11–27, KEK Proceedings, 1997.

[56] A. Gektin *et al.*, Fast U.V. scintillations in CsI-type crystals, Nucl. Tracks Radiat. Meas. **21**, 11 (1993).

[57] P. Schotanus and R. Kamermans, Scintillation characteristics of pure and Tl-doped CsI crystals, IEEE Trans. Nucl. Sci. **37**, 177 (1990).

[58] H. Nishimura *et al.*, Origin of the 4.1-eV luminescence in pure CsI scintillator, Phys. Rev. B **51**, 2167 (1995).

[59] V. B. Mikhailik *et al.*, Luminescence and scintillation properties of CsI: A potential cryogenic scintillator, Phys. status solidi **252**, 804 (2015).

[60] G. Laustriat, The luminescence decay of organic scintillators, Mol. Cryst. **4**, 127 (1968).

[61] Y. Sugiyama *et al.*, Pulse Identification Method for Overlapped Pulses, in *Proc. 2nd Int. Symp. Sci. J-PARC Unlocking Myster. Life, Matter Universe*, Journal of the Physical Society of Japan, 2015.